Discovery and analysis of novel podosome components in human macrophages

Dissertation zur Erlangung des Doktorgrades
an der Fakultät für Mathematik Informatik, und Naturwissenschaften
Fachbereich Biologie der Universität Hamburg

vorgelegt von
Pasquale CERVERO
aus Neapel (Italien)

Hamburg, 2018

Die vorliegende Arbeit wurde von Februar 2010 bis Februar 2018 unter Anleitung von Prof. Dr. Stefan Linder am Institut für Medizinische Mikrobiologie, Virologie und Hygiene am Universitätsklinikum Hamburg-Eppendorf durchgeführt.

Die vorliegende kumulative Dissertation umfasst Arbeiten aus den folgenden drei Publikationen:

Proteomic analysis of podosome fractions from macrophages reveals similarities to spreading initiation centres.
Cervero P, Himmel M, Krüger M, Linder S.
Eur J Cell Biol. 2012 Nov-Dec;91(11-12):908-22.

Podosome reformation in macrophages: assays and analysis.
Cervero P, Panzer L, Linder S.
Methods Mol Biol. 2013;1046:97-121.

Lymphocyte-specific protein 1 regulates mechanosensory oscillation of podosomes and actin isoform-based actomyosin symmetry breaking.
Cervero P, Wiesner C, Bouissou A, Poincloux R, Linder S.
Nat Commun. 2018 Feb 6;9(1):515.

Dissertation zur Erlangung des Doktorgrades
Im Fachbereich Biologie der
Universität Hamburg
vorgelegt von
Pasquale CERVERO (M.Sc.)
aus Neapel (Italien)

Dissertationsgutachter: Prof. Dr. Stefan Linder
                          PD Dr. Andreas Pommerening-Röser

Disputationsgutachter: Prof. Dr. Stefan Linder
                          PD Dr. Andreas Pommerening-Röser
                          Prof. Dr. Julia Kehr

Tag der Disputation: 08.06.2018

TABLE OF CONTENTS

ABSTRACT

Macrophages are important cells of the innate immune system. They are highly specialized in the phagocytosis of pathogens and contribute to tissue homeostasis, remodelling and tumor progression or resolution. To address all these functions, macrophages have developed a very typical and highly dynamic cytoskeleton, which notably sustains cell locomotion and allows extracellular matrix degradation and remodelling. Essential structures of the macrophage actin cytoskeleton are podosomes. They are multipurpose organelles with the key abilities to adhere, degrade extracellular matrix by releasing proteolytic enzymes and sense the stiffness of the surrounding environment, all of which allows the cell to adapt to different tissues, from bones to brain. Like other cell-matrix contact, podosomes comprise several hundreds of proteins which contribute to their structure, dynamics and functions. However, no attempt has been made to map the whole, or even a substantial part of their proteome, in contrast to studies performed on focal adhesions, spreading initiation centres or invadopodia.

In the first part of my PhD project I tried to fill this gap, providing a list of 203 proteins, of which 33 were already known as podosome components, and that likely represents a good approximation of the real podosome proteome. By comparison with other adhesion structure, we found that podosomes have an intermediate position in terms of functions and molecular machineries, in addition to a set of 136 new potential candidates not shared with any other cell-matrix adhesion structure.

From an initial screening, we could already characterize some proteins as new podosome components and among them, in the second part of my PhD project, I decided to focus on lymphocyte-specific protein 1 (LSP1) for further evaluation. We found that LSP1 localizes at a newly discovered substructure of the podosome, the so-called cap, and that it regulates podosome dynamics and mechanosensing. Interestingly, LSP1 dysregulation can lead to severe defects in immune cell locomotion, such as neutrophil actin dysfunction (NAD47/89), where LSP1 overexpression causes immobility of neutrophils and, as consequence, recurrent infections in patients.

In particular, we discovered that LSP1 can moderately activate myosin IIA and compete with supervillin, a myosin hyper activating protein, for binding of myosin regulators and actin isoforms, especially β-actin. Moreover, we found that actin isoform shows specific gradients of distribution in macrophages and that such subcellular patterns form the molecular basis for the differential recruitment of two actomyosin regulators, namely LSP1 and supervillin, that significantly contribute to actomyosin symmetry breaking by supporting different levels of myosin activity.

In the last part of the thesis, I summarize the principles for creating an algorithm to semi-automatically detect podosomes in still images or time lapse videos of macrophages stained for F-actin. By exploiting specific tools for image processing is thus possible now to gather large numbers and robust statistics of certain podosome parameters, such as absolute number and density, which are very important to investigate the impact of certain components, including LSP1, on podosome dynamics.

INTRODUCTION

1. Macrophages

1.1. Origins

Macrophages (from Greek "makrós" = large, and "phageín" = to eat; big eaters) are cells of the immune system, first described in the 19th century by Élie Metchnikoff as highly specialised phagocytic cells with a substantial role in the innate immunity and tissue homeostasis [1].

These cells are professional sentinels, capable to sense and respond to microorganism infection and tissue injury by means of a vast array of tools, such as pattern recognition receptors (PRRs), nuclear hormone and cytokine receptors, scavenger activity and a highly developed lysosomal compartment with specific proteases and bactericidal activity [2]. In addition, their specific phagocytic machinery is also essential to sustain tissue remodelling during early embryogenesis, by pruning cellular structure, clearing cell debris and supporting vascularization [3, 4], and tissue homeostasis in adulthood, by clearing lipoproteins, debris and apoptotic cells [5].

For a long time, since the description of the "mononuclear phagocyte system" (MPS) concept by van Furth in 1968, macrophages were believed to only originate from the common myeloid progenitor (CMPs) in the bone marrow, which after consecutive stages differentiated into monocyte, with poor proliferative capacity, in the peripheral blood and eventually into macrophages once in specific tissue [6-8].

Different studies have now added more details and demonstrated that most tissue-resident macrophages are actually originated from the yolk sac and fetal liver during early phases of embryonic development. They develop without a monocyte intermediate stage and persist into adulthood thanks to longevity and self-renewal, independently of further blood monocyte input in the steady state [9-12], with the exception of certain tissue, such as skin and gut, that are extensively exposed to microbiota which may cause a constant state of alert in the "surveillance system" [5].

In those tissues (e.g. skin and gut) and in pathological conditions, such as infection, inflammation or tissue injury, the hematopoietic input becomes crucial and mono-

cyte-derived macrophages are recruited from the blood circulation, by means of chemo-attractants, and integrate the resident embryo-derived population to promote tissue repair and restore the correct homeostasis [2].

Depending on the organ they colonize, tissue-resident macrophages can develop characteristic transcriptional and epigenetic programs to set up and/or improve specific functions, in addition to pathogen phagocytosis [13]. These specialized macrophages can have different names, such as microglia in the brain, Kupffer cells in the liver, Langerhans cells in the skin, peritoneal macrophages in the peritoneum, alveolar macrophages in the lung, red pulp macrophages in the spleen or osteoclasts in the bone (**Figure 1**).
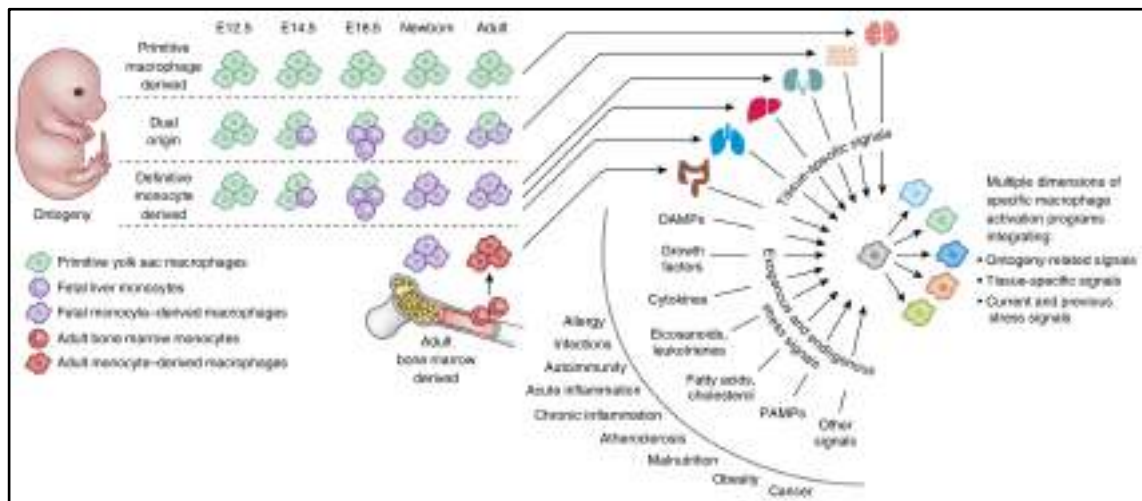
Figure 1. Integrative model of macrophage activation [14].
Ontogeny, local tissue microenvironment and stress signals, caused by pathological conditions, integrate to shape macrophage responses.

1.2. M1, M2 and tumor-associated macrophages (TAMs)

Quiescent macrophages can undergo different activation states, namely M1 and M2, depending on the response to various signals, similarly to the Th1-Th2 polarization of T-cells. Specifically, the M1 phenotype, also called classical activation, can be stimulated by TLR ligands, TNF-α or IFN-γ, and is characterized by a pro-inflammatory response with expression of high levels of specific cytokines, production of reactive nitrogen, oxygen intermediates and a strong microbicidal and tumoricidal activity.

On the other hand, the M2 phenotype, also called alternative activation, can be simulated by IL-4, IL-13, IL-1R ligands, IL-10, and based on the specific ligand / response they can be further categorized into 3 different subtypes: M2a, M2b and M2c [15]. These types of macrophages are characterized by anti-inflammatory response, high phagocytic activity, containment of parasites, wound healing and tissue repair but also angiogenesis and tumor progression [16, 17].

However, it is now clear that these different states of activation represent only extremes of a continuum of polarization[16, 18, 19] that most likely *in-vivo* macrophages continuously undergo in both directions throughout their existence (**Figure 2**).
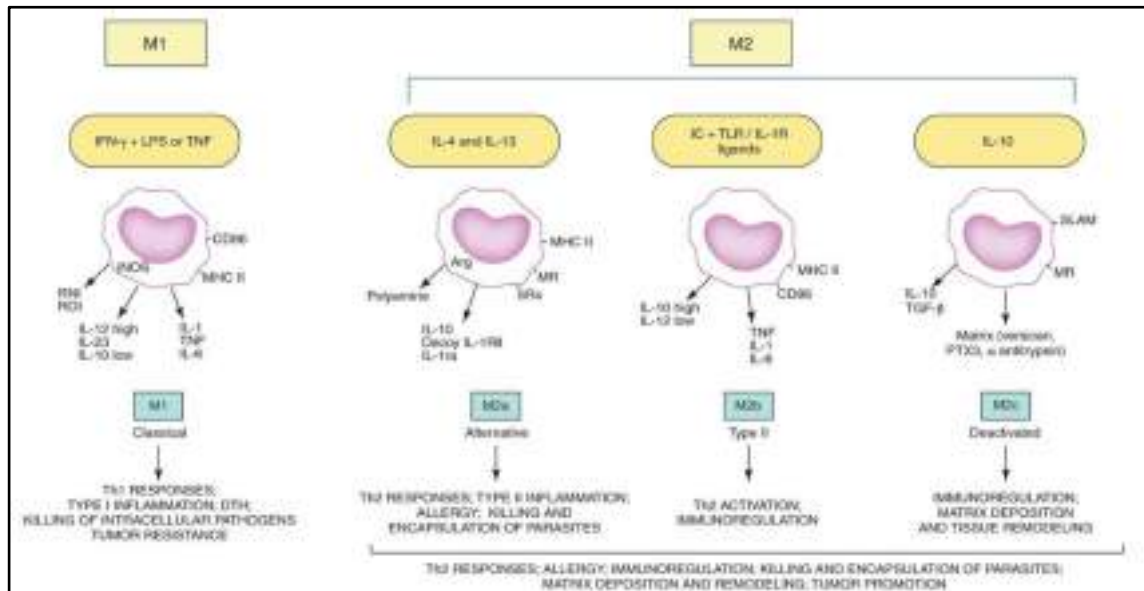
Figure 2. Model for M1/M2 macrophage activation [15].
Depending on the specific ligands, macrophages can activate and acquire different functional properties. INF-γ and LPS drives M1 polarization with strong cytotoxic and tumoricidal activity, whereas M2 polarized macrophages have more immunoregulatory, protumoral and tissue remodeling activity. In particular, the M2a response is promoted by IL-4 and IL-13, M2b by combined exposure to immune complexes and TLR or IL-1R agonists, and M2c by IL-10.

As mentioned earlier, macrophages have been described to be closely connected to tumors (Tumor Associated Macrophages, TAMs). Monocyte-derived macrophages can be recruited during the early stage of cancer-related inflammation and be classically activated to acquire a M1 phenotype [20, 21]. The pro-inflammatory and tumoricidal activity of M1 macrophages can potentially support the tumor disrup-

tion in cooperation with other immune cells recruited to the newly formed niche. However, in some cases a switch from M1 to M2 phenotype can take place, [22-24] setting up new conditions in the surrounding environment and new cross-talk pathways. The mechanism underlying this intricate phenomenon is hard to fully decipher and understand as it involves multiples cell types, especially macrophages, tumor cells, fibroblasts and endothelial cells, and interconnected pathways and feedbacks.

For this reason is not anymore surprising that TAMs infiltration has been observed and correlated with poor prognosis in different tumors, such as in Hodgkin disease, glioma, ovarian and breast carcinoma [16].

2. Actin cytoskeleton

The cytoskeleton is an essential structure present in all cells. It is responsible for cell shape, locomotion and intracellular organization, but also significantly involved in cell division, intracellular signalling and molecule trafficking [25]. In eukaryotic cells it consists of three main interconnected substructures, organized in 3D networks: 1) microtubules, which are polymers of α/β tubulin with a diameter of about 23 nm; 2) intermediate filaments, which consist of heterogeneous polymers composed of different proteins such as vimentin, keratin, desmin and lamin, with a diameter of about 10 nm; 3) microfilaments which are essentially polymers of actin, with a diameter about 7 nm [25, 26].

Actin is one of the most abundant protein in eukaryotic cells [27]. It is an ATPase with the ability to spontaneously polymerize when the concentration of globular actin monomers (G-actin) is above the critical concentration (Cc), whereas filaments depolymerize below the Cc.

Actin polymers have a specific orientation "head-to-tail" due to the intrinsic polarization of the monomers [28] . The nomenclature of the polymer extremities is based on the typical arrow-like shape that monomers acquire upon decoration with the myosin fragment S1 [29].

It is thus possible to define a "pointed-end" (-) and a "barbed-end" (+), which have different Cc (respectively 0.7 μM and 0.1 μM) [27]. Based on these different kinetic

constants, when the G-actin concentration is between 0.1 and 0.7 µM, the net effect is the polymerization occurring at the barbed-end (+) and simultaneous depolymerisation at the pointed-end (-), a phenomenon called treadmilling [27].

Interestingly, when the concentration of G-actin induces polymer growth and shrinkage at the same speed the treadmilling enters a steady-state[27]. This dynamic state is highly costly in terms of ATP, but, on the other hand, it provides the cell with a highly flexible machinery, capable of rapid adaptation to a variety of different cues and optimal for fine-tuning of cell locomotion.

In some nonmuscle cells the concentration of unpolymerized actin in the cytoplasm is estimated to be around 100 µM (or much higher in muscle cells), which is 100 to 1000-fold higher than the Cc needed for actin polymerization to occur [30]. In this condition and in physiological concentrations of Mg^{2+} (mM), ATP and Ca^{2+} (0.1 µM), the pure actin should polymerize almost completely in few seconds. However, to avoid spontaneous actin nucleation, a set of proteins have been positively selected through evolution to sequester actin monomers (such as profilin, which "regenerates" actin by replacing ADP with ATP, and thymosin-β4 which sequesters actin-ATP monomers, creating a reservoir of functional monomers) or cap the free barbed ends, thus blocking the addition of new monomers to filaments [30].

Very important to avoid continuous and uncontrolled actin assembly is also the control of F-actin depolymerisation and filament severing. Proteins like ADF (actin depolymerizing factor) or cofilin, for instance, are able to bind to the side of ADP-bound actin filaments and destabilize the structure, thus creating the conditions for filament severing and actin disassembly from the ADP-bound pointed end [31]. The process increases actin depolymerisation, but it also creates new uncapped barbed ends and new actin monomers, a phenomenon that leads to increased actin dynamics and eventually new F-actin assembly when needed [32].

Among all the proteins responsible for filament severing and barbed-end capping, those belonging to the gelsolin family have been extensively studied. This family includes protein like gelsolin, adseverin (also known as scinderin), villin, advillin, supervillin and CapG in mammalian cells [31]. These proteins contain multiple Ca^{2+}-regulated gelsolin-like domains and by capping barbed-ends of shortened filaments they favour pointed-end depolymerisation [31]. Interestingly, phospho-

inositides, especially PIP$_2$, are the only known agents able to inhibit gelsolin activity by favouring its dissociation from the barbed-end, and thus facilitating the new polymerization against the membrane [33].

The mechanisms controlling F-actin disassembly previously described are physiologically counterbalanced by factors that increase actin polymerization, generally called actin nucleators / elongators. Three major groups of actin nucleators have been described so far: 1) ARP 2/3 complex; 2) formins and 3) WH2 domain-containing proteins [34] (**Figure 3**).

Arp 2/3 complex is composed of seven subunits: actin-related proteins Arp2 and Arp3 and five additional subunits ARPC1, ARPC2, ARPC3, ARPC4 and ARPC5, with the first two (Arp 2 and Arp3) structurally resembling an actin-like dimer capable of incorporating on the side of a "mother" filament and start the nucleation of a new branch of "daughter" filament with an angle of 70° [35]. The complex is essential for the formation of the dense network of branched F-actin filaments, especially in the lamellipodium of migrating cells, less than 1 μm away from the plasma membrane [27].
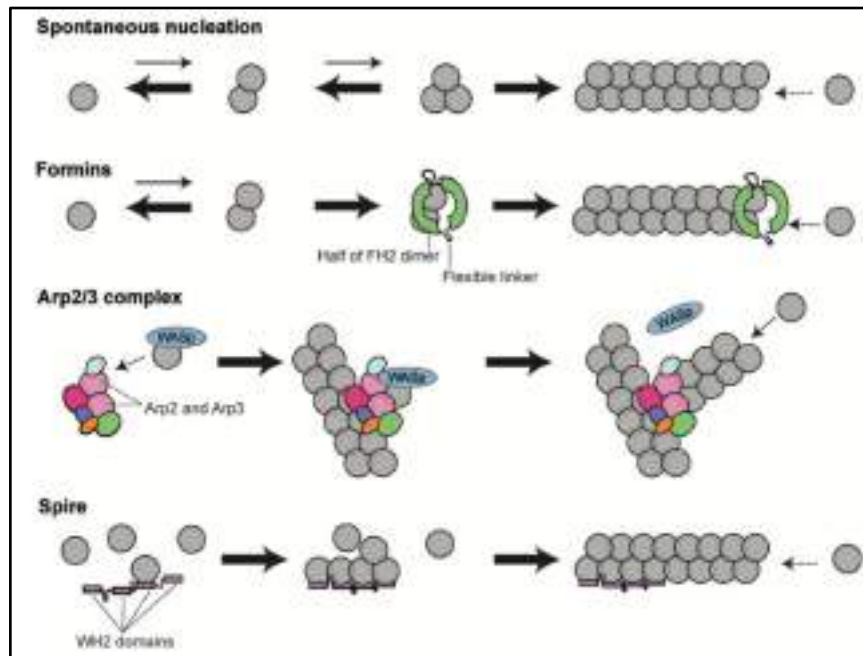

Figure 3. Mechanisms of actin polymerization mediated by ARP 2/3, formins and spire [36].

Noteworthy, Wiskott-Aldrich syndrome family proteins, such as WASP, N-WASP, WASH and WAVE are fundamental for the correct function of Arp 2/3 complex. These proteins, collectively called nucleation-promoting factors (NPFs), integrate downstream signals of many pathways including those initiated by cell receptors and carried out by Rho family GTPases, Rac and Cdc42, and eventually activate the nucleation core of Arp 2/3 complex. In this way, Arp 2/3 complex and in general the dynamics of the actin cytoskeleton are functionally linked to signalling cascade initiated by external stimuli such as chemo attractants [30] (**Figure 4**).
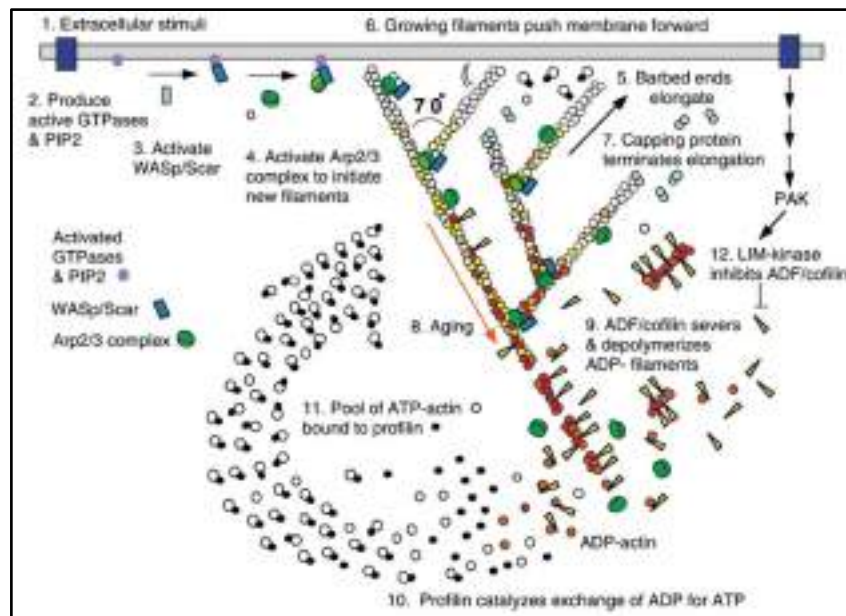
Figure 4. Branched actin nucleation and treadmilling model at leading edge [27].

The formin family is the second major group of actin nucleators and comprises 15 different proteins in human [37]. They can bind the barbed end through dimerization of the formin homology domain (FH) and sequentially add profilin-actin monomers. During polymer elongation, the formin dimer is firmly and processively associated to the barbed end for many cycles before dissociation, and this mechanism also avoid the binding of other F-actin capping proteins that would stop elongation [38]. As results formins will grow unbranched actin filaments very rapidly; a mechanism especially important during filopodia and stress fibres formation. In addition, two different modes of regulation have been described so far for formins:

autoinhibition by intramolecular binding between domains (DID and DAD) and Rho GTPase binding [36].

WH2 domain-containing proteins, like Spire, have a mechanism of nucleation different from Arp 2/3 and formins. Spire has four WH2-like domains, similar to those present in many actin binding proteins like WASP and thymosin β4 and is able to recruit and organize up to four actin monomers in tandem into a stable prenucleation complex [39]. It functions as a scaffold for polymerization of un-branched actin filaments and similarly to Arp 2/3 it stays associated to the pointed end preventing its depolymerisation [40].

The functional antagonism between actin assembly/disassembly is fundamental for keeping actin in the dynamic steady-state which is required for essential features like cytokinesis, migration, polarization and intracellular trafficking. However, actin filaments not only undergo growth/shrinkage but can also be rearranged in bundles and meshwork. At this purpose, F-actin bundling proteins, such as fimbrin and α-actinin can assemble tight or loose bundles, respectively, with filaments aligning parallel or antiparallel to each other, depending on the F-actin binding domain composition and position within the protein structure [41]. Similarly, some actin crosslinking proteins like spectrin or filamin can bind multiple filaments so loosely to form a network rather than bundles.

3. Actin isoforms

Although actin is generally thought as single protein, in mammals it is actually encoded by six different genes. The translated proteins are almost identical, with only slight variations in the amino acid sequence, especially at the N-terminus, and specific muscle expression for four of them : $\alpha_{cardiac}$-actin, α_{smooth}-actin, $\alpha_{skeletal}$-actin and γ_{smooth}-actin, whereas the other two show ubiquitous distribution: $\beta_{cytoplasmic}$-actin, and $\gamma_{cytoplasmic}$-actin [42] (**Figure 5**).

Data collected from different studies involving knockout (KO) mice or conditional KO models support the theory that isoactins share many functions, but also have specific features that cannot be totally compensated by each other [43], with β-actin being essential for life, as KO-mice die during early phases of embryogenesis [44, 45].
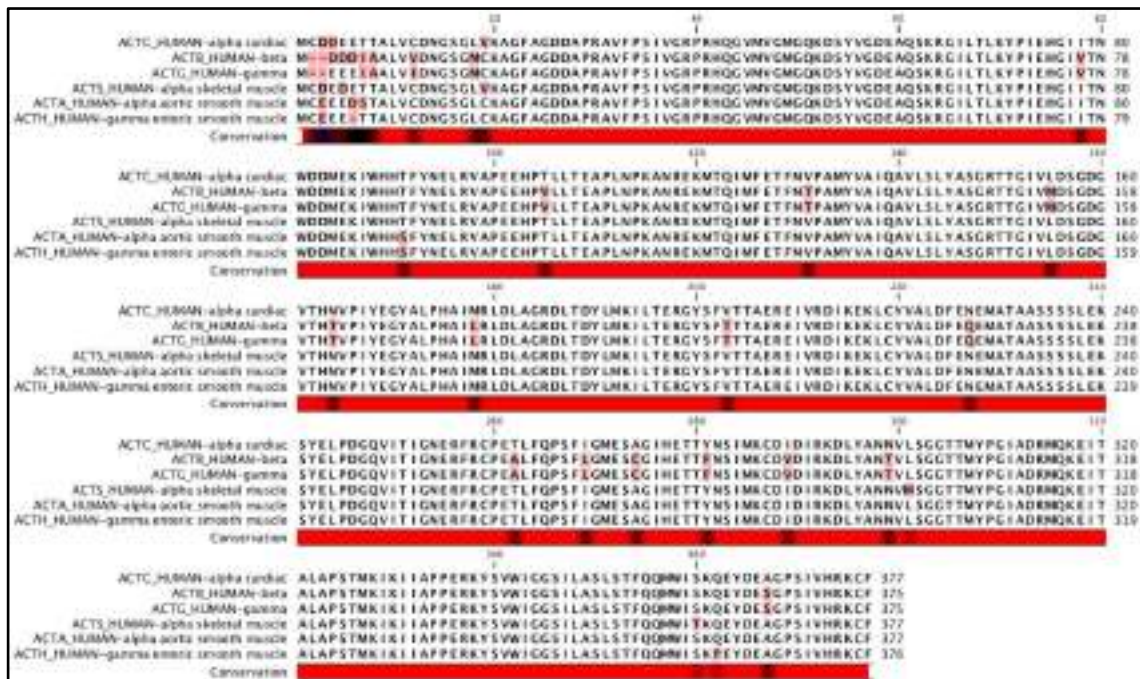
Figure 5. Comparison of aminoacid sequences of the six human actin isoforms.
Differences are highlighted with a red box on the background of the relative aminoacid. Conservation bar shows region of low homology between sequences as black spots. Note how most of the differences are located in the N-terminus.

Specific functions can be explained by many reasons like [46]: 1) different chemicophysical properties intrinsic in the amino acid composition; 2) variations in mRNA sequences and untranslated regions (UTRs) responsible for mRNA localization, stability and translatability via secondary structure, ribosome binding and codon usage; 3) differences in gene sequences like intron, promoter and enhancer regions which affect the overall regulation, expression and tissue specificity; 4) preferential binding of isoform specific actin-binding proteins resulting in changes of the overall F-actin dynamics.

For instance, isoactin polymers in vitro show different biophysical properties especially in terms of viscoelasticity and filaments length [47]. β-and $\gamma_{cytoplasmic}$-actins are characterized by different dynamics when bound to calcium, with β-actin showing higher polymerization / depolymerisation rates compared to $\gamma_{cytoplasmic}$-actin [48]. Interestingly, these isoactins can also copolymerize creating mixed filaments with polymerization / depolymerisation rates in line with respective ratios within filaments [43].

Recently, it has been shown that the ribosome densities on the mRNA and arginylation of β-actin play a very important role in fine tuning its translation and local/global rates of accumulation [46]. An additional feature of actin mRNA is located in the 3' UTR, which is isoform-specific and evolutionarily conserved. The 3' UTR of β-actin mRNA, for instance, contains a zipcode that binds to specific proteins such as ZBP1 (zipcode binding protein 1) and targets mRNA near the leading edge especially in those cells characterized by active migration [49] or the 3' UTR of $\alpha_{cardiac}$-actin, which is responsible for its perinuclear localization [50]. In line with this mechanism, many in situ hybridization and proteomic studies have described the association of granules containing mRNAs, ribosomal proteins and elongation factors with microfilaments and microtubules, which are responsible for active transport to specific cell structures, thus enabling localized protein synthesis [29, 49].

α-actins have been observed mostly associated with contractile structures in muscles, whereas γ-actins with dense unbranched network and stress fibers, and β-actin with branched network at cell cortex and leading edge [51], although it is highly challenging to draw a general conclusion, especially concerning β- and γ-actin, where specific localization seems to be dependent also on the cell type and sample preparation method used prior to imaging, as reported recently [43, 52].

Moreover, some actin-binding proteins have been shown to discriminate between muscle and cytoplasmic isoactins, such as cofilin, ezrin, l-plastin, thymosin β4 [43] and recently LSP1 [53] (see attached paper), thus providing additional regulation to specific functions of actin isoforms.

Collectively, all the aforementioned observations reveal a complex system involving isoactin proteins, mRNAs, genes and associated proteins, which is ultimately responsible of the fine tuning of the actin cytoskeleton and its functions.

4. Podosomes

Podosomes are F-actin rich dot-like structures distributed on the ventral side of many cell types, in close contact with the extracellular matrix (ECM), and capable of adhesion and extracellular matrix (ECM) degradation [54].

They were first observed in 1982 in osteoclasts and monocytes in physiological conditions, although in 1980 a similar rearrangement of the actin cytoskeleton was already noticed in chicken embryo fibroblasts transformed with Rous sarcoma virus [55]. Since then, podosomes have been observed and investigated in a variety of cell types, such as smooth muscle cells [56], endothelial cells [57], megakaryocytes [58] and eosinophils [59], normally upon specific stimulation, in addition to cells of the monocytic lineage (macrophages [60], dendritic cells [61] and microglia [62]) and osteoclasts [63], which constitutively and physiologically form several hundreds of podosomes per cell.

Interestingly podosomes also have a pathological counterpart represented by invadopodia, with the two structures collectively named invadosomes [64]. Invadopodia are formed by many cancer cell types, such as pancreatic, ovarian, prostate, brain, skin, bladder, head and neck, breast and melanoma [65]. They mainly contribute to tumor growth and dissemination (i.e. metastasis) by extensive ECM degradation [65]. Similarly to podosomes they are able to degrade ECM and partially overlap in protein composition, however they differ in other aspects, with invadopodia having longer lifetime (hours), lower number per cell (1-10), almost no mobility and peculiar structure characterized by thick and deep protrusion of mainly F-actin bundles, without an apparent ring of plaque proteins, and enriched in metabolic enzymes [66].

Podosomes are multipurpose organelles that combine several important features typical of cell migration and invasion. They are sites of cell-matrix adhesion through transmembrane proteins like integrins and CD44, and hot-spots for ECM degradation through microtubule-associated vesicle transport and secretion of matrix-lytic enzymes, especially matrix metalloproteinases (MMPs) [54, 67] (**Figure 6**).
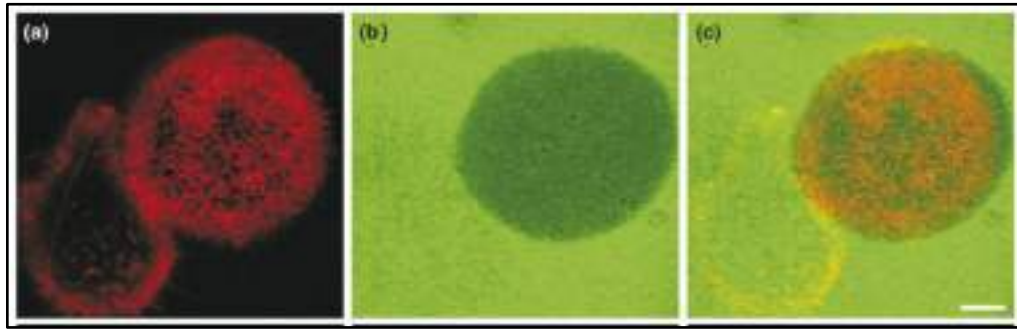
Figure 6. Matrix degradation by human primary macrophage [68].
Cells are seeded on Alexa488-labeled fibronectin (green) and stained for F-actin (red). Matrix degradation is visible as loss of fluorescence. Note degradation taking place only underneath the macrophage forming hundreds of podosomes.

The key ability of podosomes to adhere and degrade extracellular matrix is thus essential for bone remodelling, extravasation, migration, tissue invasion, sprouting of new blood vessels and antigen sampling, depending on the cell type involved [63, 64, 69, 70]. Important defects in podosome formation and / or function can lead to severe diseases like Wiskott-Aldrich syndrome, where WASP mutations harshly affect podosome formation and immune cell functionality [60].

Podosomes are classically described to consist of two main structures: 1) a cylinder-shaped core with a diameter of 0.5-1 μm and an average height of 0.6 μm [69, 71], which is mainly composed of F-actin and associated proteins involved in assembly (e.g. ARP 2/3 complex, formins), disassembly (e.g. gelsolin, cofilin), regulation (e.g. CDC42, WASP, cortactin) and bundling/crosslinking (e.g. α-actinin, caldesmon, fimbrin, fascin); 2) a ring-like shape surrounding the F-actin core and consisting of adhesion proteins like vinculin, talin, zyxin and paxillin organized in multiple clusters [72, 73]. Further studies have recently shown that the branched F-actin core is surrounded by unbranched actin filaments polymerized by formins and decorated by myosin IIA [74]. These actin filaments connect the top of the podosome to the ventral plasma membrane (lateral cables) and interconnect individual podosomes to each other, thus enabling tight coordination between closely interspaced podosomes [69] (**Figure 7**).
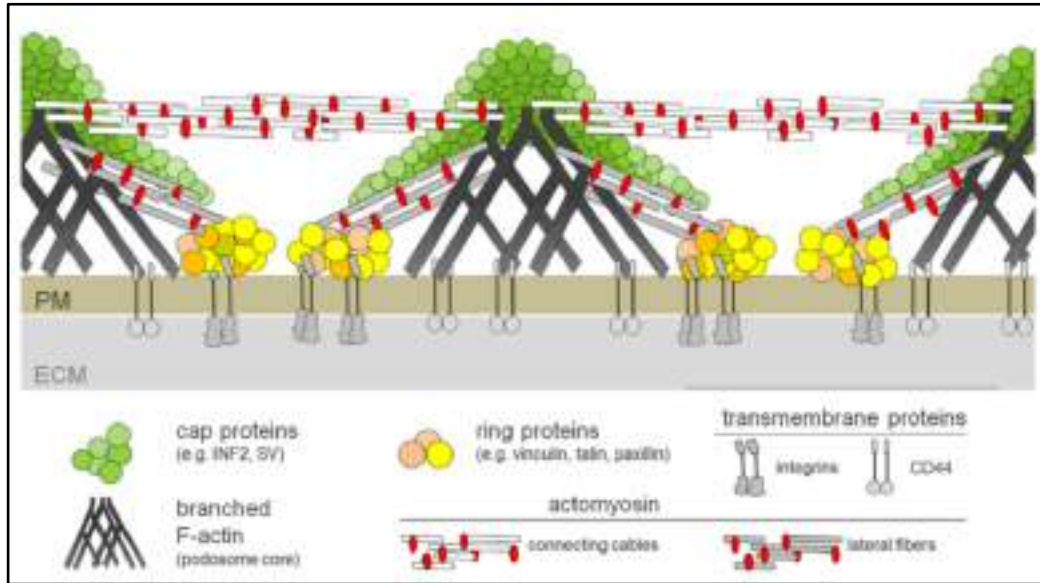
Figure 7. Podosome structure and interconnection [75].

A few years ago, a new cap-like structure, that decorates the top of the F-actin core [75], has also been observed and described for proteins like FMNL1, INF2 and supervillin. This structure is likely functioning as a hub for transported vesicles and as a regulator of podosome mechanosensing [69] (**Figure 7**). Although they have been observed in 3D settings with cells embedded in ECM, podosome distribution and the typical tripartite structure are less clear compared to 2D settings [75].

Podosomes also serve as mechanosensing devices, that is the ability to "sense" the mechanical properties of the surrounding environment (i.e. rigidity and topography) and adapt accordingly [76]. The current model assumes that ARP 2/3 complex-driven actin polymerization, taking place at the bottom of podosomes, induces a vertical growth of the F-actin core. As a consequence, actin polymerization generates increased stiffness of the F-actin core [71] and increased tension on lateral cables. Stretching tension is counterbalanced by actomyosin contractility and recruitment of tension-sensitive ring component, such as vinculin and talin. The mechanical coupling of the core polymerization with lateral cables contractility thus leads to the generation of coordinated vertical oscillations and rhythmic protrusion of the plasma membrane [75] on pliant substrates, allowing the cell to physically probe extracellular matrix, collect information about its mechanical properties and transduce them into biochemical signals [69] (**Figure 8**).
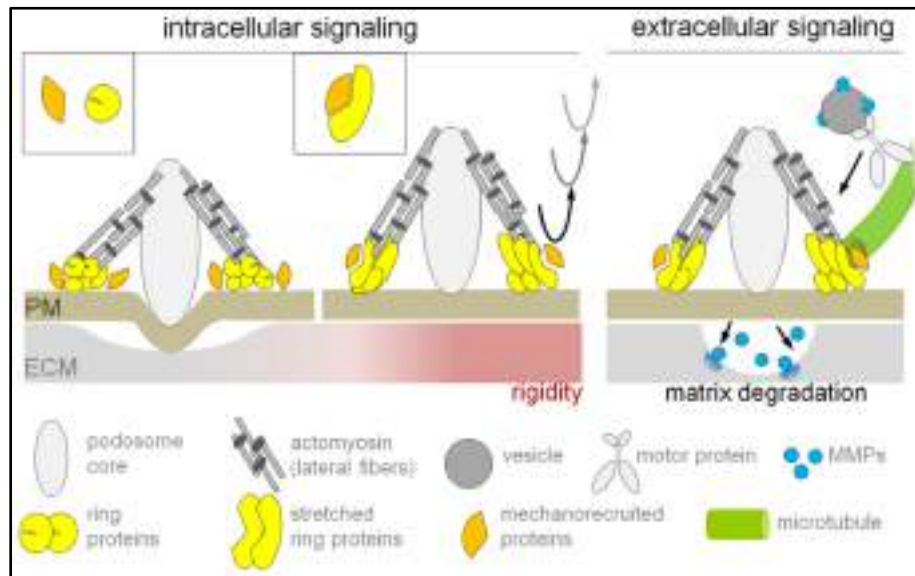
Figure 8. Podosome mechanosensing is regulated by intracellular and extracellular signalling [75].
Depending on the ECM rigidity podosomes can induce specific signalling, such as recruitment of tension-sensing molecules and delivery of vesicles containing matrix-lytic enzymes.

Podosomes are highly dynamic structures characterized by a lifetime ranging from 0.5 to 14 min, with a mode value of approximately 2.5 min, and rapid internal actin turnover of 20-40 sec [63]. According to differences in lifetime, size, dynamic behaviour and localization, two distinct population of podosomes can be defined, especially in monocyte-derived macrophages: 1) precursors, characterized by larger structures, higher rates of fission / fusion events (i.e. shorter lifetime) and normally present at the cell periphery, in particular at the leading edge of migrating cells; 2) successors, characterized by longer lifetime, increased stability (i.e. less fission / fusion events) and localizing in the middle of the cell or right behind precursors in migrating cells [77,78]. The molecular mechanisms responsible of such a difference and regulating these two subpopulations are not fully understood, however, two different podosomal proteins have been recently described to preferentially localize to either precursors (LSP1) [53] or successors (supervillin) [79] and a possible explanation will be further described in the Discussion section of this thesis.

AIMS OF THE STUDY

1. Identification and description of the podosome proteome.

Recently, many proteomic studies have focused on characterizing the molecular composition of integrin-based adhesions, such as focal adhesions [80-83], SICs [84] and invadopodia [85]. However, comparable studies on important adhesion structures such as podosomes have never been undertaken so far.

Lack of information about podosome proteomes and its comparison with the proteomes of other cell-matrix contacts were thus the main motivation of the first part of my PhD project.

2. Characterization of a new podosome component in macrophages: LSP1.

Based on the mass spectrometry score described in the podosome proteome paper we selected the most promising candidate, lymphocyte-specific protein 1 (LSP1), for further analysis. After confirming its presence at podosome cores by immunostaining I aimed to further characterized its role in podosome dynamics and mechanosensing. Moreover, based on previously published studies in other cell types [86-90], we also wanted to investigate the role of LSP1 in the regulation of macrophage migration in 2D and 3D.

3. Semi-automated analysis of podosome parameters using imageJ.

The analysis of podosome dynamics can provide insightful information about the functional role of novel components. Human primary macrophages, which constitutively form hundreds of podosomes, represent an optimal system to address this task. However, these large numbers cannot be fully exploited with statistics if the study has to be performed manually. The principal aim of this part of the project was to exploit the tools given by image analysis software (e.g. imageJ) to rapidly and carefully gather large numbers and perform robust statistics on important podosome parameters, such as absolute numbers and density, which are essential to describe podosome dynamics.

PUBLICATIONS

1. **Proteomic analysis of podosome fractions from macrophages reveals similarities to spreading initiation centres.**
   Cervero P, Himmel M, Krüger M, Linder S.
   Eur J Cell Biol. 2012 Nov-Dec;91(11-12):908-22.

2. **Lymphocyte-specific protein 1 regulates mechanosensory oscillation of podosomes and actin isoform-based actomyosin symmetry breaking.**
   Cervero P, Wiesner C, Bouissou A, Poincloux R, Linder S.
   Nat Commun. 2018 Feb 6;9(1):515.

3. **Podosome reformation in macrophages: assays and analysis.**
   Cervero P, Panzer L, Linder S.
   Methods Mol Biol. 2013;1046:97-121.

Proteomic analysis of podosome fractions from macrophages reveals similarities to spreading initiation centres

Pasquale Cervero[a], Mirko Himmel[a], Marcus Krüger[b], Stefan Linder[a,*]

[a] *Institut für Medizinische Mikrobiologie, Virologie und Hygiene, Universitätsklinikum Eppendorf, Martinistrasse 52, 20246 Hamburg, Germany*
[b] *Max-Planck-Institute for Heart and Lung Research, Parkstrasse 1, 61231 Bad Nauheim, Germany*

ARTICLE INFO

ABSTRACT

Podosomes are multifunctional organelles of invasive cells that combine several key abilities, including adhesion, matrix degradation and mechanosensing. The necessary spatiotemporal fine-tuning of podosome structure, turnover and function implies the existence of an intricate network of proteins, comparable to other integrin-based adhesions. However, no systematic effort has yet been made to map the podosome proteome. Here, we describe the purification of podosome-enriched fractions from primary human macrophages, labelled with isotopically stable amino acids, and the subsequent mass spectrometric analysis of these fractions. We present a consensus list of 203 proteins, comprising 33 known podosome proteins and 170 potential novel components. We also present second-level analyses of the podosome proteome, as well as proof-of-principle experiments by showing that the newly identified components WDR1/AIP-1 and hnRNP-K localise to the core structure of macrophage podosomes. Comparisons with other adhesion structure proteomes confirm that the podosome proteome shares components with focal adhesions and invadopodia, but also reveal an extensive overlap with spreading initiation centres (SICs). We suggest that the consensus list comprises a significant part of the podosome proteome and will be helpful for future studies on podosome structure, composition and function, and also for detailed classification of adhesion structure subtypes.

Introduction

Podosomes and invadopodia, collectively called "invadosomes", are a specialised group of cell-matrix contacts, with the signature ability to degrade extracellular matrix (ECM) material, and a typical dependence on Arp2/3 complex-based actin nucleation. These properties set them apart from other cell-matrix contacts such as focal adhesions or fibrillar adhesions (Linder, 2007, 2009; Caldieri et al., 2009; Saltel et al., 2011). Invadosomes are found in invasive cell types, with podosomes formed in monocytic cells such as macrophages (Linder et al., 1999), dendritic cells (Burns et al., 2001) and osteoclasts (Destaing et al., 2003), and also smooth muscle cells (Burgstaller and Gimona, 2004) or endothelial cells (Moreau et al., 2003; Osiak et al., 2005), and invadopodia in several types of cancer cells such as carcinoma (Lorenz et al., 2004) and melanoma cells (Monsky et al., 1994).

Podosomes are multifunctional organelles that combine several key functions of invasive cells, including adhesion, matrix degradation and mechanosensing (Linder et al., 2011), which is based on their abilities: (i) to contact the ECM through

matrix-binding proteins such as integrins (Zambonin-Zallone et al., 1989; Gimona et al., 2008) and CD44 (Chabadel et al., 2007), (ii) to locally degrade matrix material by accumulating matrix-lytic enzymes such as ADAM-12 (Abram et al., 2003) or MT1-MMP (Wiesner et al., 2010), and (iii) to transduce traction forces and thus function as mechanosensors (Collin et al., 2006, 2008), which is controlled by actomyosin contraction (Linder et al., 2011) and possibly by actin filament growth (Luxenburg et al., 2012).

Podosomes show a typical bipartite architecture, with a core structure of F-actin and actin-associated proteins such as Arp2/3 complex (Linder et al., 2000a; Kaverina et al., 2003), gelsolin (Chellaiah et al., 2000) or cortactin (Tehrani et al., 2006), which is surrounded by a ring of plaque proteins such as vinculin, talin and paxillin (Linder and Aepfelbacher, 2003). Recently, also a cap structure on top of the actin core has been described (Linder et al., 2011), which contains FMNL1 (Mersich et al., 2010) and supervillin (Bhuwania et al., 2012).

Podosomes display several levels of dynamic behaviour, including de novo formation, fusion and fission, growth and dissolution (Linder, 2007). Moreover, even under steady state conditions, podosomes also show internal dynamics, as (i) actin in the podosome core is turned over ca. 3 times within the life span of a single podosome (Destaing et al., 2003), and (ii) podosomes undergo internal cycles of stiffness, which is probably based

on actin bundling and myosin contractility (Labernadie et al., 2010).

Collectively, these findings show that podosomes are highly complex organelles that are composed of a plethora of proteins, and that the multiple aspects of podosome architecture and function have to be spatiotemporally fine-tuned on several levels. This indicates the existence of an intricately linked network of podosomal proteins, whose complexity is likely comparable to that of other integrin-based adhesions (Zaidel-Bar, 2009). Indeed, the list of podosome components and regulatory factors is growing steadily (compare Linder and Aepfelbacher, 2003 and Linder et al., 2011). However, a systematic effort to map the whole podosome proteome and to identify novel podosome components, comparable to studies on integrin-based adhesions in general (Zaidel-Bar et al., 2007; Zaidel-Bar and Geiger, 2010; Humphries et al., 2009; Kuo et al., 2011; Schiller et al., 2011) or invadopodia specifically (Attanasio et al., 2010), has not been undertaken yet.

In the present study, we purified and analysed podosome-enriched fractions from primary human macrophages. Macrophages present themselves as an excellent cell system for podosome proteomic studies, as they constitutively form numerous podosomes that often cover most of the adhesive surface (Linder et al., 1999). SILAC (stable isotope labelling by amino acids in cell culture) culture conditions were established that allowed optimal incorporation of isotopically labelled amino acids for subsequent mass spectrometric analysis. Based on these experiments, we present a consensus (overlap) list of 203 proteins, comprising 33 established podosome proteins and 170 potential novel components. We also present second-level analyses of the podosome proteome and also proof-of-principle experiments by showing that the newly identified components WDR1/AIP-1 and hnRNP-K localise to the core structure of macrophage podosomes.

Materials and methods

Cell isolation and cell culture

Human peripheral blood monocytes were isolated from buffy coats (kindly provided by Frank Bentzien, University Medical Center Hamburg-Eppendorf, Germany) and differentiated into macrophages as described previously (Linder et al., 1999). Cells were cultured in RPMI-1640 without arginine, lysine, leucine and phenol red (R1780, Sigma–Aldrich Corp. St. Louis, MO, USA), which was reconstituted with 0.45 mM arginine, 0.52 mM lysine and 0.72 mM leucine (corresponding to 0.1 µg/L each; Sigma–Aldrich Corp. St. Louis, MO, USA) in addition to 20% dialysed fetal bovine serum (Invitrogen, Carlsbad, USA). Considering that macrophages are mostly non-dividing cells and in order to increase the culture viability, cells were seeded in double amount (2×10^6/well in six-well plate) and 5 ng/mL M-CSF (RELIATech GmbH, Wolfenbüttel, Germany) was added to the culture medium beginning from the first day of culture.

Podosome disruption assay

Podosomes were disrupted by addition of tyrosine kinase inhibitor PP2 (Calbiochem, Merck KGaA, Darmstadt, Germany) at 25 µM for 30 min, as described earlier (Linder et al., 2000b).

Differential cell lysis

Differential cell lysis was performed on 7-d-old macrophages, cultured in 6-wells at a cell density of 2×10^6 cells/well, as described previously (Gringel et al., 2006), with some modifications. Cells were lysed by addition of 600 µL/well of lysis buffer A (20 mM Tris–HCl, pH 7.4, 5 mM EDTA, 1% Triton, 1 mM sodium ortho-vanadate, with Complete Mini protease inhibitor (Roche Diagnostics, Mannheim, Germany)) and incubated ca. 3 min on ice with gentle shaking. Cell bodies and cytoplasm were removed and saved. The remaining adhesive parts of the cells ("footplate") were washed two times, each time with 200 µL lysis buffer A, then the washing solution was completely removed, and the adhesive cell fraction was solubilised by addition of 100 µL/well of lysis buffer B (20 mM Tris–HCl, pH 7.4, 5 mM EDTA, 1% SDS, 0.1% sodium deoxycholate, with Complete Mini protease inhibitor (Roche Diagnostics, Mannheim, Germany)). Confocal microscopic imaging confirmed removal of the cell body fraction by the first lysis step, while the adhesive part of the cell containing the podosomes was still left on the substratum as shown by confocal yz-scans.

SILAC media and labelling

For the preparation of the SILAC media, L-Arg and L-Lys were replaced as follows, according to previously published protocols (Ong et al., 2002; Blagoev et al., 2003; Ong and Mann, 2006; Mann, 2006; Gruhler and Kratchmarova, 2008): "Light" SILAC medium with naturally stable L-Arg (Sigma–Aldrich Corp. St. Louis, MO, USA) and L-Lys (Sigma–Aldrich Corp. St. Louis, MO, USA), and "Heavy" SILAC medium with isotopically stable $[^{13}C_6\ ^{15}N_4]$-L-Arg and $[^{13}C_6\ ^{15}N_2]$-L-Lys (Silantes, Munich, Germany). Cells were cultured for 1 week in SILAC medium, washed with PBS and differentially lysed. Protein samples from footplates were run on 4–12% SDS-PAGE, with subsequent in-gel digestion and mass spectrometry analysis. After analysis with the MaxQuant software tool we detected a median incorporation rate of 86%, 87% and 88%, respectively, from experiment I, II and III. In the experiment I, the "Heavy" medium was added to the control culture, while the "Light" medium was added to the PP2-treated culture, and vice versa in experiment II and III.

Gel electrophoresis and in-gel digestion

Following differential cell lysis, footplate fractions (FF) from control (+DMSO) and 25 µM PP2 (dissolved in DMSO) treated cells were isolated and mixed in equal volumes. Mixtures were run on NuPAGE 4–12% BIS-TRIS gel (Invitrogen, Carlsbad, USA). Gels were stained with PageBlue Protein Staining Solution (Fermentas, Thermo Fisher Scientific), and evenly sized gel pieces were excised and processed for mass spectrometry. The gel pieces were subjected to in gel reduction and alkylation, followed by trypsin digestion as described previously (Shevchenko et al., 1996; Krüger et al., 2008). Briefly, gel pieces were washed twice with 50% (50 mM NH$_4$HCO$_3$ eluent additive for LC–MS (Sigma–Aldrich)/50% ethanol) for 20 min and dehydrated with 100% ethanol for 10 min and then vacuum centrifuged. Gel pieces were reduced with 10 mM DTT for 45 min at 56 °C and alkylated with 55 mM iodoacetamide (BioUltra-Sigma–Aldrich Corp.) for 30 min at RT in the dark. After two steps of washing/dehydration, samples were dehydrated twice with 100% ethanol for 15 min and vacuum centrifuged. Gel pieces were digested overnight at 37 °C in 50 µL of digestion buffer containing 12,5 ng/µL of Sequencing Grade Modified Trypsin (Promega Corp., Madison, USA). Released peptides were extracted (collecting separately the liquid mixture of each sample at each step) once by adding 100 µL of 30% acetonitrile LC/MS grade (Thermo Scientific)/3% trifluoroacetic acid (TFA, protein sequence analysis grade, Sigma–Aldrich) in water (LC/MS grade quality, Thermo Scientific), twice by adding 70% acetonitrile, followed by two final extractions with 100% acetonitrile. Extracts were vacuum centrifuged to remove acetonitrile and subsequently acidified with 0.5% TFA. Samples containing tryptic peptides were desalted and concentrated with homemade "STAGE" tips (Stop and Go extraction tips) filled

with C-18 (C18 Empore Disks, 3M, Minneapolis, MN) as described earlier (Rappsilber et al., 2003; Krüger et al., 2008).

Mass spectrometry

Reverse phase nano-LC–MS/MS was done by using an Agilent 1200 nanoflow LC system (Agilent Technologies, Santa Clara, CA) using a cooled thermostated 96-well autosampler. The LC system was coupled to LTQ-Orbitrap instrument (Thermo Fisher Scientific) equipped with a nanoelectrospray source (Proxeon, Denmark). Chromatographic separation of peptides was performed in a 10-cm long and 75-μm inner diameter capillary needle. The column was custom-made with methanol slurry of reverse-phase ReproSil-Pur C18-AQ 3-μm resin (Dr. Maisch GmbH). The tryptic peptide mixtures were autosampled at a flowrate of 0.5 μL/min and then eluted with a linear gradient at a flow rate 0.25 μL/min. The mass spectrometers were operated in the data-dependent mode to automatically measure MS and MS/MS spectra. LTQ-FT full scan MS spectra (from m/z 350–1750) were acquired with a resolution of $r = 60,000$ at m/z 400. The five most intense ions were sequentially isolated and fragmented in the linear ion trap by using collision-induced dissociation with collision energy of 35%. Further mass spectrometric parameters: spray voltage of 2.4 kV, no sheath gas flow, and the temperature of the heated capillary was 200 °C. For data analysis we used the MaxQuant software tool (Version 1.2.2.5). The measured raw data were processed and quantitated as follows: a peak list was generated using the following parameters: SILAC doublets with heavy labels Arg10+Lys8; maximum of 3 labelled AAs; maximum mass deviation for precursor ions was 20 ppm and 0.5 Da for CID fragment ions. A maximum of 2 missed cleavages was allowed and enzyme specificity was set to trypsin. In addition, carbamidomethyl (C) was chosen as fixed modification and variable modifications included Oxidation (M), and Acetyl (Protein N-term). The MaxQuant generated peak list was searched against the human International Protein Index (IPI) database v3.68 including a list of common contaminants such as keratins and concatenated with reverse copies of all sequences.

Transfection of cells and expression constructs

Cells were transiently transfected using the Microporator device (PeqLab, Erlangen, Germany) and Neon Transfection kits (Invitrogen, Carlsbad, USA). For transfection of primary human macrophages, the following parameters were used: 1000 V, 40 ms, 2 pulses, and 0.5 μg DNA per 1×10^5 cells. The WDR1-YFP expression construct was a kind gift from Kensaku Mizuno (Kato et al., 2008), hnRNP-K-GFP was a kind gift from Yu-Sun Chang (Chen et al., 2009).

Immunofluorescence microscopy

Cells were fixed for 15 min in 3.7% formaldehyde/PBS and subsequently permeabilised for 5 min in ice-cold acetone. F-actin was stained with Alexa Fluor568-labelled phalloidin (Invitrogen, Carlsbad, USA), and with Alexa Fluor647-labelled phalloidin in the case of WDR1-YFP overexpression. Vinculin was stained with specific primary mouse monoclonal antibody (V9264, Sigma–Aldrich Corp. St. Louis, MO, USA). Cells stained for WDR1 (goat polyclonal antibody (G-13) from Santa Cruz) were fixed in −20 °C cold methanol for 5 s, post-fixed with 3.7% formaldehyde/PBS for 15 min, and permeabilised in 0.5% Triton X-100 for 10 min. Cells stained for hnRNP-K (goat polyclonal antibody (P-20) from Santa Cruz) were fixed for 15 min in 3.7% formaldehyde/PBS and subsequently permeabilised in 0.5% Triton X-100 for 10 min. Secondary antibodies used were Alexa Fluor488-labelled goat anti-mouse, and Alexa Fluor488-labelled donkey anti-goat (Invitrogen, Carlsbad,

USA). Coverslips were mounted in Mowiol (Calbiochem, Darmstadt, Germany) containing *p*-phenylendiamine (Sigma–Aldrich Corp. St. Louis, MO, USA) as anti-fading reagent and sealed with nail polish.

Microscopy was performed as described previously (Kopp et al., 2006). Images of fixed samples were acquired with a confocal laser-scanning microscope (Leica DM IRE2 with a Leica TCS SP2 AOBS confocal point scanner) equipped with an oil-immersion HCX PL Apo 63x NA 1.4 lambda blue objective. Acquisition of images was performed with Leica Confocal Software (Leica Microsystems, Wetzlar, Germany), while image processing and 3D reconstruction was performed with Volocity 6.0 for Mac (PerkinElmer, Waltham, USA).

Software and statistical analysis

Initial mass spectrometry datasheets were streamlined by selecting only those entries with a number of Razor and unique identified peptides ≥ 1 and a Posterior Error Probabilities (PEP) score $\leq 10^{-5}$. Proteomes for comparison were obtained from published studies and reviews on invadopodia and podosome proteins (Buccione et al., 2004; Attanasio et al., 2010; Linder and Aepfelbacher, 2003; Linder et al., 2011) as well as spreading initiation centres (SICs) (de Hoog et al., 2004). The focal adhesion proteome lists were obtained from http://www.adhesome.org, a meta-study of the cell-adhesion literature (Zaidel-Bar et al., 2007; Zaidel-Bar and Geiger, 2010), and from a more recent publication (Kuo et al., 2011). In some cases, database entries of "hypothetical proteins" from other proteomes (e.g. SICs proteome) were updated and annotated to correspond to the current state of knowledge using the UniProt "best guess" function of the Protein Identifier Cross-Reference Service (PICR) on the EMBL website (Côté et al., 2007). Few entries with empty ID fields (unidentified proteins) were removed manually, and some established podosome components (e.g. Cdc42, cortactin, MMP-9, FMNL1, WASP and WIP) were filtered out from the datasets and marked with "n.d." (not detected) in Suppl. Table 2, because they lacked a given calculated ratio. Statistical analyses were performed with Graphpad Prism 5 for Mac, using an unpaired *t*-test. $P < 0.05$ was considered as statistically significant (single asterisk), $P < 0.01$ as highly statistically significant (double asterisks). For the Gene Ontology enrichment analysis, P was calculated automatically by the respective web based applications.

GO analysis and bioinformatic tools

The list of gene names from each dataset was used to generate Venn diagrams using BioVenn (Hulsen et al., 2008). The consensus list of proteins found in all three experiments was then used for the second level analysis, based on Gene Ontology (Ashburner et al., 2000) enrichment analysis, using web server applications including Panther (Thomas et al., 2003; Mi et al., 2010), GOrilla (Eden et al., 2007, 2009), WebGestalt (Zhang et al., 2005; Duncan et al., 2010), ToppCluster (Kaimal et al., 2010), and the open-source softwares Gephi (Bastian et al., 2009) for drawing protein network diagrams and iVici (Tarassov and Michnick, 2005) for the creation of heatmaps. For the comparison of four proteome dataset, the program Venny (Oliveros, 2007) was used to generate Venn diagrams.

Results

Preparation of podosome-enriched fractions from macrophages

In order to analyse the podosome proteome and identify novel podosome proteins, we generated podosome-enriched fractions from primary human macrophages, which constitutively form numerous (>100) podosomes per cell (Linder et al., 2011). We
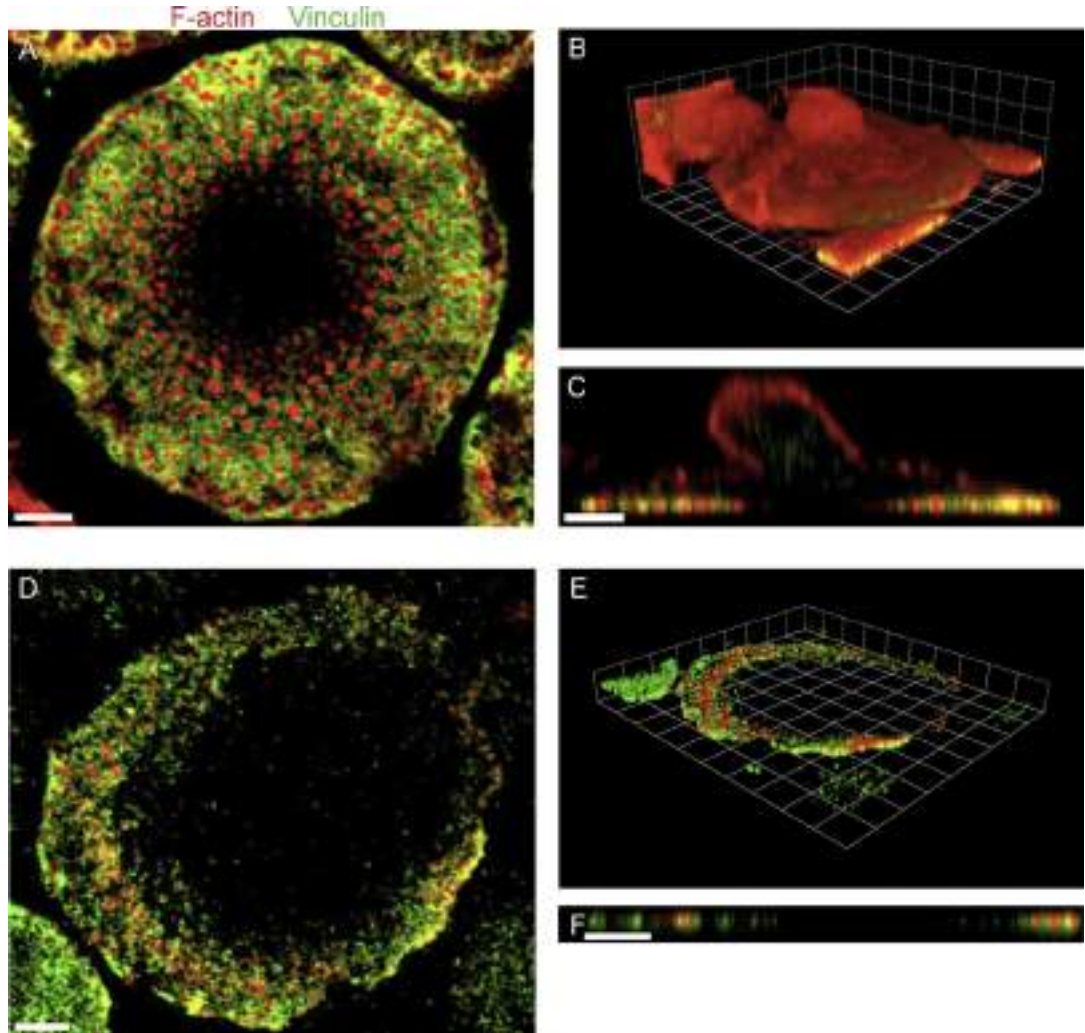
24

Fig. 1. Differential cell lysis of primary human macrophages. Confocal xy scans (A and D), 3D reconstructions (B and E) or confocal yz scans (C and F) of 7-d cultured primary human macrophages not lysed (A–C) or after differential cell lysis (D–F), and stained for F-actin (red) and vinculin (green). Note dome-shaped part of cell in (B and C), which contains the nucleus and most of the cytoplasm, and remaining adhesive part ("footplate") in (E and F) after differential lysis. White bars: 5 μm.

first optimised a protocol for the preparation of adhesive fractions from primary human macrophages (Materials and Methods; Gringel et al., 2006). This protocol is based on a two-step method for differential cell lysis, resulting in the removal of the apical cell part, which contains the cytoplasm and nucleus (Fig. 1A–C), and allowing enrichment of the ventral membrane of cells ("footplates"), containing podosomes (Fig. 1D–F). Enrichment of podosomes in the footplate fraction was checked by immunofluorescence labelling of both podosome core and ring components, shown exemplarily for F-actin and vinculin in Fig. 1.

SILAC labelling of primary macrophages

Analysis of podosome-containing vs. podosome-free footplates was performed using SILAC (stable isotope labelling of cells) labelling of macrophages, which allows direct comparison between two experimental conditions in a single run of mass spectrometry analysis. For SILAC-based analyses, cellular proteins are labelled by incorporation of stable isotopes, which is achieved by culturing cells in dialysed serum (devoid of free amino acids) and culture medium lacking amino acids such as L-Arg or L-Lys, and concomitant re-supplementation of the respective amino acids containing heavy carbon and nitrogen isotopes, here ($^{13}C_6$ $^{15}N_4$)-L-Arg and ($^{13}C_6$ $^{15}N_2$)-L-Lys (Ong et al., 2002). A comparison between signal intensities from "light" and "heavy" samples provides a ratio of their relative abundance in the mixture (Ong and Mann, 2006).

SILAC protocols are usually based on ca. 5 subsequent passages of cells to ensure proper labelling. However, as macrophages are slowly proliferating cells under standard cell culture conditions, sufficient overall labelling of their proteome is difficult. We thus developed a protocol for optimized SILAC labelling of macrophages, which includes (i) testing of dialysed sera for cell culture, (ii) addition of increasing concentrations of M-CSF (5–50 ng/mL) to enhance cell division and viability (van der Zeijst et al., 1978) in the presence of dialysed serum, and (iii) seeding cells at varying densities to increase cell viability. Best results were achieved with a combination of dialysed fetal bovine serum from a specific supplier (Invitrogen), addition of 5 ng/mL M-CSF to the culture medium,

25
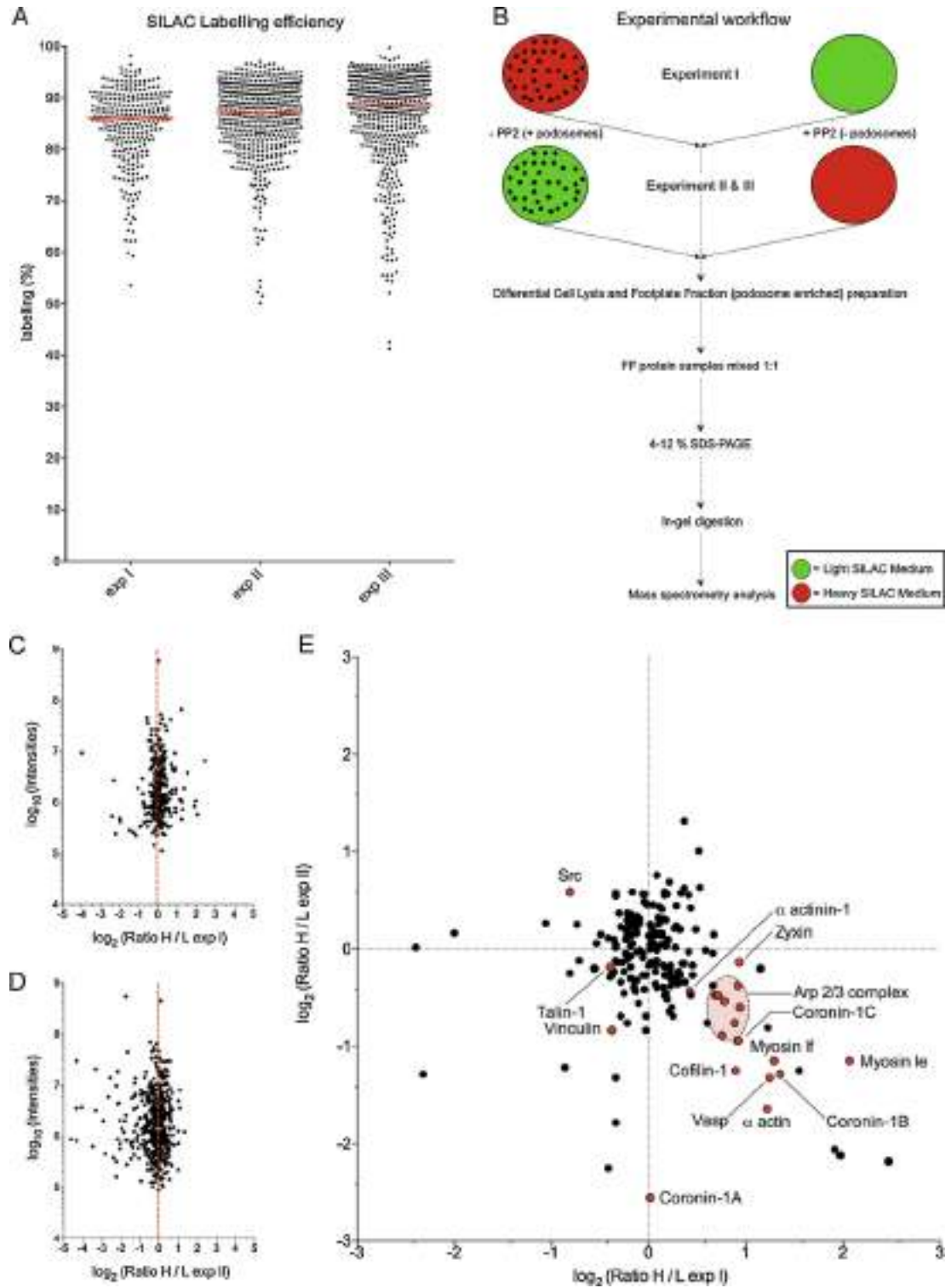
Fig. 2. SILAC labelling of primary macrophages. (A) Incorporation efficiency of isotopically labelled amino acids after 1 week of culture in "heavy" SILAC medium. Incorporation efficiency into specific proteins is indicated as labelling percentage for each experiment. (B) Experimental workflow. Differential cell lysis was performed on cells cultured in "heavy" medium or cells cultured in "light" medium. Footplates from cells grown in "heavy" medium with intact podosomes ("–PP2") were combined with footplates from cells grown in "light" medium after podosome disruption ("+PP2"; experiment I), and vice versa (experiments II–III). Respective samples were mixed 1:1 and run on SDS PAGE gels, with subsequent in-gel digestion of gel slices, followed by mass spectrometry analysis. (C–D) Log_2 SILAC ratios (H/L) plotted against the respective log_{10} sum

26

and seeding of freshly prepared monocytes in six-well plates at a density of 2×10^6 cells/well. Using this protocol, we achieved a medium labelling rate of 87% after 1 week of culture, as determined by mass spectrometry of footplate lysates from experiments I, II and III (Fig. 2 A).

Mass spectrometry analysis of footplate fractions

We next combined differential cell lysis and SILAC labelling to generate macrophage footplate fractions for subsequent mass spectrometric analysis. To distinguish between proteins that are potential podosome components and those that are more generally associated with the adhesive fraction, we analysed footplate fractions from 1 week cultured cells from two conditions: (i) cells that were treated with PP2 to disrupt podosomes ("+PP2") or control cells containing podosomes (treated with DMSO; "−PP2"), and (ii) cells grown in "heavy" or "light" medium (Fig. 2B). Two combinations of footplates were then analysed: footplates from cells grown in heavy medium and with intact podosomes ("heavy, −PP2") combined with footplates from cells grown in light medium and disrupted podosomes ("light, +PP2"; experiment I), and vice versa (done in duplicate; experiments II + III; Fig. 2B). Both times, lysates from the two conditions were mixed in equal volumes, and samples were processed for mass spectrometric analysis (see Materials and Methods).

Next we evaluated the suitability of this method to detect podosomal proteins. We plotted the log SILAC ratios (H/L) against the respective log sum intensities of detected SILAC pairs. In total, we identified more than 1000 proteins. As shown in Fig. 2C, ratios >1 indicate proteins which were enriched in the "heavy" untreated podosome fraction, compared to the "light" PP2 treated cells (without podosomes). Conversely, lower ratios (<1) in Fig. 2D indicate a decrease of podosomal proteins in the "heavy" fraction after PP2 treatment. We next plotted the ratios from the forward experiment I and the backward experiment II against each other (Fig. 2E). Proteins that are enriched in the footplate fraction due to the PP2 treatment are localised in the upper-left quadrant (e.g. Src), whereas proteins that are diminished (or lost) from footplates are mostly found in the lower-right quadrant. Note that this is the quadrant where podosome components that are lost from footplates after podosome disruption would be mostly expected. The localisation of several podosome components is indicated in Fig. 2E. For a diagram showing all known podosome components (from the consensus list in Fig. 3B, see Suppl. Fig. 2A).

Second level analysis of mass spectrometry datasets

We next compared the overlap of experiments I–III, to generate a consensus list of proteins. Two hundred and three proteins were shared between all three datasets, from 282 proteins in experiment I, 486 proteins in experiment II, and 503 proteins in experiment III (Fig. 3A; Suppl. Table 1). Comparing the proteins found in the three experiments with known podosome components, we identified 35 known components in experiment I, 46 in experiment II and 53 in experiment III, with an overlap of 33 proteins shared between all three datasets (Fig. 3B, Suppl. Table 2). The overlap comprises typical proteins of the podosome core such as Arp2/3 complex subunits, cofilin, CD44, coronin and gelsolin, and also components of the podosome ring structure including vinculin, zyxin,

talin-1, kindlin-3, β_2-integrin and myosin IIA. Several other typical podosome components were present only in one or two datasets, including cortactin, CDC42 or palladin, whereas some others were filtered out from each dataset (see Matherials and Methods) including MMP-9, WASP, WIP, supervillin and FMNL-1. For complete and detailed lists, see Suppl. Table 2. These initial comparisons show that a substantial fraction of known podosome components has been detected in the mass spectrometric analysis, 33 of which are present in all three datasets.

Interestingly, the intensity ratios (PP2/Ctrl) of these proteins were different for components of the podosome core (mean value: 0.68; Fig. 3C; e.g. 0.54 for Arp 2/3 complex subunit 3 (ARPC3), 1.07 for ezrin) or of the podosome ring structure (mean value: 0.91; Fig. 3C; e.g. 0.68 for vinculin or 1.49 for c-Src). This difference is even more apparent when intensity ratios (R) are fitted to a Gaussian distribution (median value of distribution: 0.61 for core proteins vs. 0.88 for ring proteins; Fig. 3D). Collectively, these findings point to possible differences in the behaviour of podosome components in response to PP2 treatment according to their localisation at a particular podosome substructure.

To streamline further analyses of both known and potentially novel podosome components, we concentrated on the consensus list of 203 proteins detected in all three datasets and performed Gene Ontology (GO) enrichment analysis. Using the Panther Classification System (Thomas et al., 2003; Mi et al., 2010), we grouped the consensus list by the Gene Ontology class of cellular components and compared it with the whole *Homo sapiens* genome as a reference list to statistically determine over- or under-represented categories. As expected, particular enrichment was found for intracellular proteins (22.3%; Fig. 4A), cytoskeletal proteins (19.3%; Fig. 4A), and here especially proteins of the actin cytoskeleton (14.9%; Fig. 4A). Surprisingly, also ribonuclear proteins were significantly enriched (6.93%; Fig. 4A), pointing to a possible contamination or to a previously unrecognised group of podosome components.

We next analysed the consensus list according to cellular components or molecular function, using GOrilla (Eden et al., 2007, 2009) and WebGestalt (Zhang et al., 2005; Duncan et al., 2010) web based applications. Resulting networks are shown as Directed Acyclic Graphs (DAG), colour-coded for *P* values (Fig. 4B and C). Consistent with the Panther analysis, particular enrichment was found for cytoskeleton- and actin-associated proteins, and also for focal adhesion and nucleoplasmic proteins (Fig. 4B). In addition, components common to lamellipodia, as well as those featuring ATPase or GTPase activity were highlighted, as well as RNA-binding proteins and structural components of ribosomes. (Fig. 4C).

A more detailed depiction of the complete network, comprising all identified proteins from the consensus list, and grouped according to molecular function, was made using ToppCluster (Kaimal et al., 2010) and Gephi software (Bastian et al., 2009), as depicted in Fig. 5 (a complete list of proteins, with descriptions, can be found in Suppl. Table 1). Similar to the previous analysis, the identified core groups comprise cytoskeletal proteins, especially those binding actin and F-actin such as coronin-2 (CORO1B) or VASP, cell adhesion molecules such as vinculin, proteins showing ATPase or GTPase binding, including myosin IIA (MYH9), dynamin-2 and Rac1, as well as proteins with a more structural role such as vimentin. Again, two additional major groups were structural components of ribosomes and proteins showing RNA binding.

---

intensities of detected SILAC pairs in experiments I and II. Note that proteins tend to cluster in half-right of the graph in (C) (ratios>1), indicating an enrichment of podosomal proteins in the "heavy" untreated sample (experiment I), or in the half-left of the graph in (D) (ratios < 1), indicating a loss of proteins from the "heavy" PP2 treated sample (experiment II). (E) Log$_2$ ratios (H/L) from experiments I and II plotted against each other. Proteins enriched in the footplate fraction due PP2 treatment are in the upper-left quadrant (e.g. Src), since they show a ratio (H/L) <1 in experiment I and >1 in experiment II, whereas proteins diminished (or lost) due to PP2 are in the lower-right quadrant. Some known podosome components are indicated in red. See also Suppl. Fig. 2A.
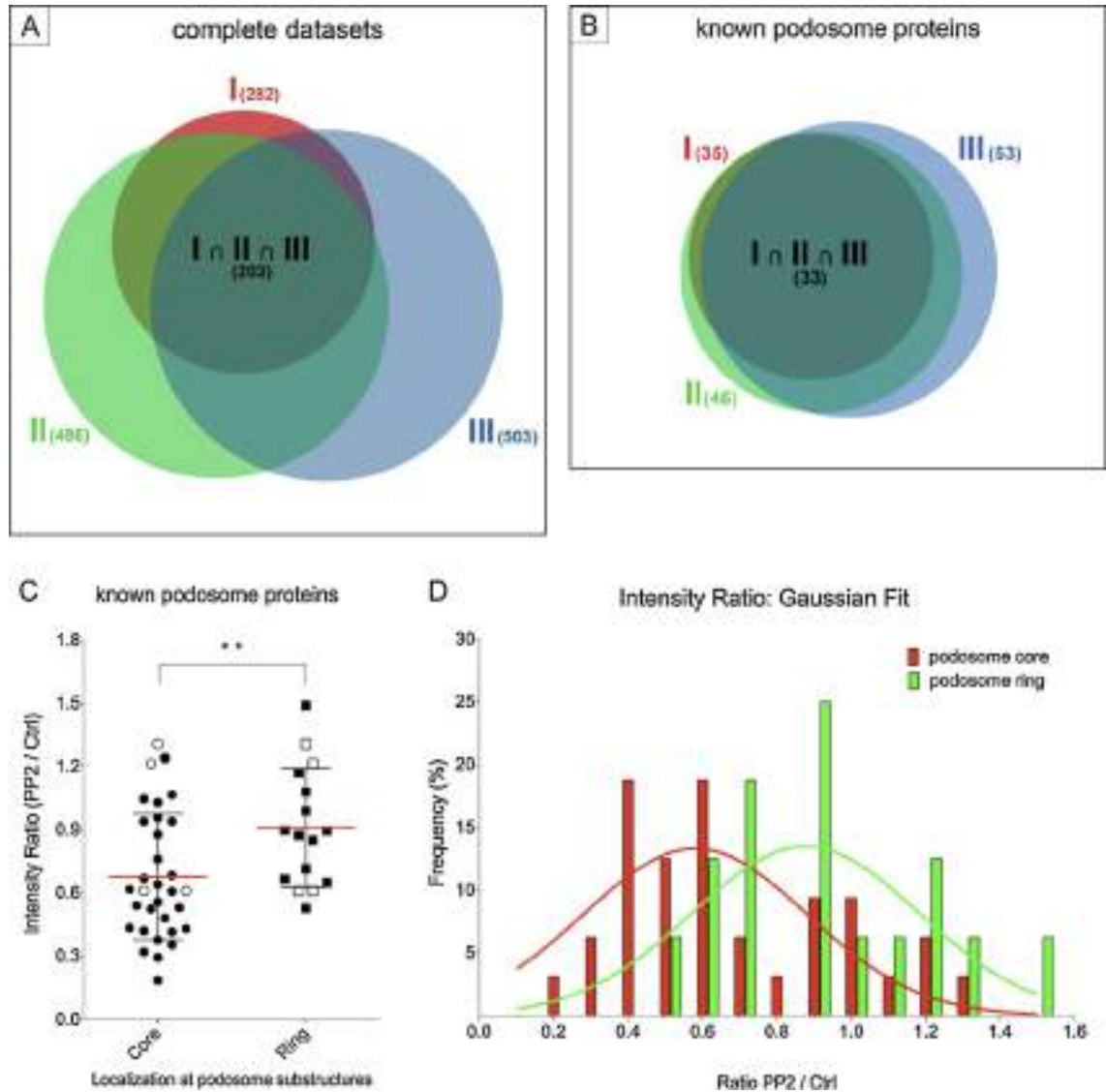
Fig. 3. Comparison and analysis of SILAC datasets. (A and B) VENN diagrams of proteins identified in different footplate preparations, with areas drawn to represent number of identified proteins. Numbers of proteins identified in each experiment, as well as number of common proteins (I∩II∩III) are indicated. (A) VENN diagram illustrating the complete three sets of proteins identified in experiments I–III. (B) VENN diagram of previously identified podosome components that were found in experiments I–III. (C) Mean of intensity ratios (PP2/Ctrl) of previously identified podosome components (found at least in two datasets), grouped according to their localisation to podosome core (black circles) or ring structure (black squares). Statistical significance indicated by double asterisks, with $P < 0.01$, as determined by unpaired t-test. Components that have been described with unclear localisation for either core or ring are included in both columns as white symbols (ACTN1, ACTN4, GSN and PTPN6). (D) Frequency distribution of intensity ratios of known podosome components and Gaussian fit.

WDR1/AIP-1 and hnRNP-K are novel components of podosome cores

To test the validity of the consensus list as a potential source for novel podosome components, we investigated the subcellular localisation of two newly identified proteins from the list: WDR (WD40 repeat protein)1, also known as AIP (actin interacting protein)-1, from the group of actin-associated proteins, and hnRNP-K (heterogeneous ribonucleoprotein-K), as a representative for the newly identified group of RNA-associated proteins (Fig. 5). hnRNP-K was also chosen to test whether RNA-binding proteins, in principle, can be validated as potential podosome components.

7-d-old primary human macrophages were fixed and stained using antibodies specific for WDR1 or hnRNP-K, and treated with Alexa568-labelled phalloidin, to detect F-actin-rich podosome cores. Strikingly, both proteins were found to localise to podosome cores (Fig. 6A–C, G–I). This finding was further corroborated by overexpression of respective YFP- or GFP-fusion constructs. Cells expressing WDR1-YFP or hnRNP-K-GFP showed clear localisation of the respective construct to podosome cores (Fig. 6D–F, J–O), comparable to the endogenous proteins. In accordance with its role as an RNA binding protein, hnRNP-K-GFP was also found in the nucleus, which was especially visible in xz sections of cells (Fig. 6M–O). We conclude from these findings that

28

Fig. 4. SILAC consensus list analysis according to cellular components and molecular functions. The consensus list of identified proteins was analysed according to Gene Ontology enrichment by Panther web server application (A), presenting enrichment of the consensus group in depicted categories, as opposed to general gene count in the human genome. Four asterisks indicate highly significant enrichment in respective groups, with $P < 0.0001$. (B) Enrichment analysis using GOrilla web server application or WebGestalt (C), presented as Directed Acylic Graphs (DAG), depicting enrichment of consensus list proteins according to GO:cellular components or GO:molecular functions (C). Colour code according to P values, as indicated.

29

Fig. 5. Network diagram of consensus list proteins. Diagram was drawn using Gephi software, based on enrichment analysis performed with ToppCluster. Individual proteins (small circles) are grouped according to depicted molecular functions (large circles) and colour-coded (red, blue, yellow). Proteins that can be attributed to several groups show intermediate colours (orange, purple, green), with final shade (e.g. deep or light orange) depending on the relative attribution to each group. For full protein names and database entries, see Suppl. Table 1.

the SILAC consensus list can indeed be used as a source for potential novel podosome components. Localisation of hnRNP-K to podosomes also indicates that the detected enrichment of RNA binding proteins in the footplate fractions is not an artefact, but might point to a potential relevance for RNA binding proteins in the regulation of podosome structure and/or function.

Comparisons between adhesion structure proteomes

In a next step, we compared the podosome proteome with published proteomes from focal adhesions (Zaidel-Bar et al., 2007; Zaidel-Bar and Geiger, 2010), invadopodia (Attanasio et al., 2010) and spreading initiation centres (SICs) (de Hoog et al., 2004). As expected, the list of known podosome components (from the

30
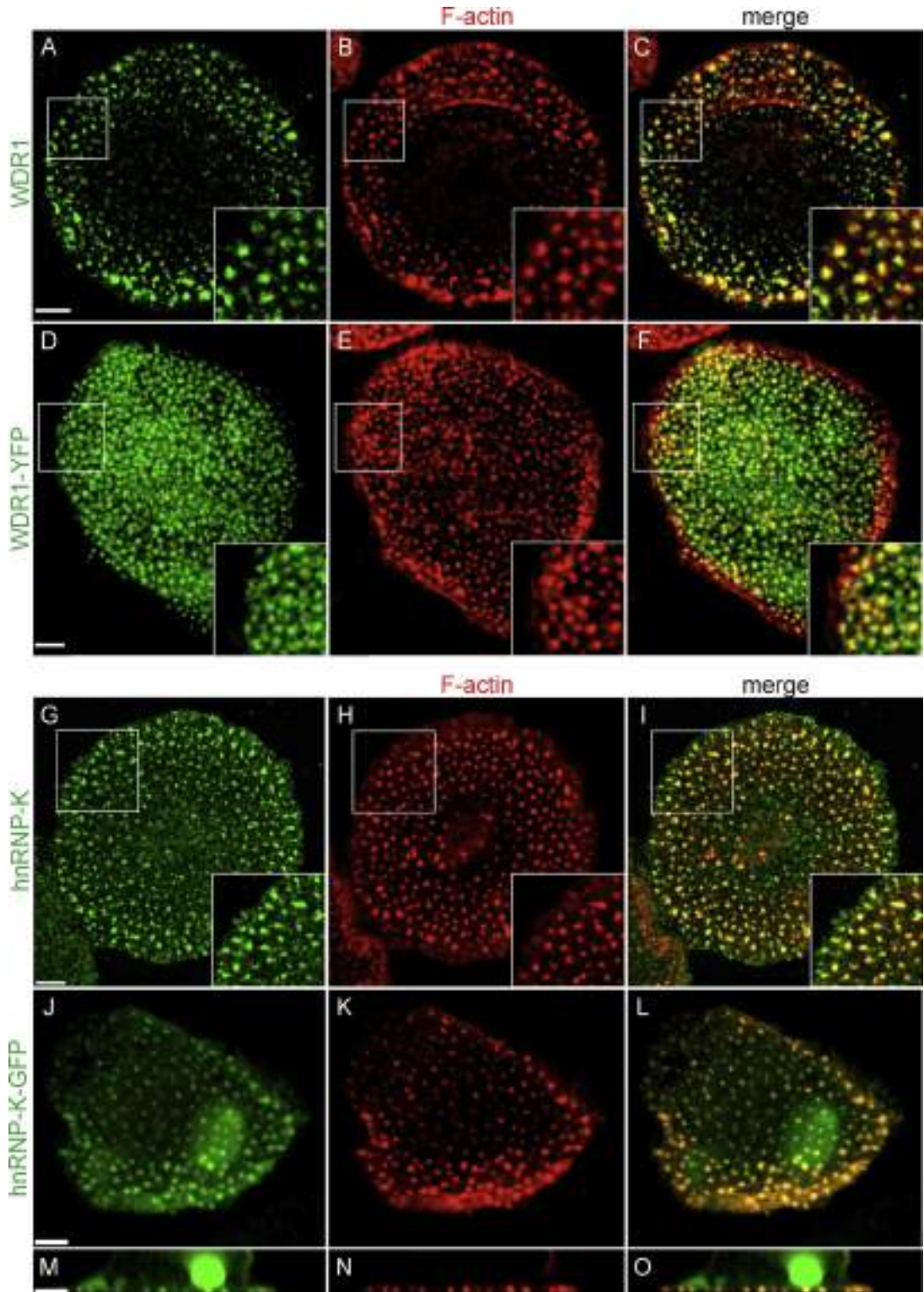
Fig. 6. The newly identified components WDR1 and hnRNP-K localise to podosome cores. xy confocal fluorescence micrographs of primary human macrophages stained for WDR-1 (A–C) or hnRNP-K (G–I) using specific antibodies, or expressing WDR-1-YFP (D–F) or hnRNP-K-GFP (J–O), with F-actin labelled using phalloidin-Alexa Fluor 568 (B, H, K and N) or phalloidin-Alexa Fluor 647 (E), with respective merges shown in (C, F, I, L and O). Note (i) localisation of both WDR1 and hnRNP-K to F-actin-rich core structures of podosomes, and also (ii) partial localisation of hnRNP-K to the nucleus, compatible with its role as an RNA binding protein, which is clearly visible in xz confocal sections (M–O) of the cell depicted in (J–L). Scale bars: 5 μm.

31

podosome consensus: 33 proteins) shows overlaps with both focal adhesion (13 proteins) and invadopodia proteomes (3 proteins; Suppl. Fig. 2B and C), but also with SICs (6 proteins) (Suppl. Fig. 2D). Interestingly, all four proteomes share only one common protein, the intermediate filament protein vimentin (Suppl. Fig. 2E). It is also noteworthy that the proteomes of focal adhesions and invadopodia show an overlap of only two proteins, vimentin and Grb2 (Suppl. Fig. 2B). For complete lists of overlapping proteins between the individual proteomes, see Suppl. Table 3.

We next compared the whole SILAC consensus list (203 proteins) with the other proteomes. Compared to the previous analyses using only known podosome components, we find a modest increase in the overlap with focal adhesions (17 proteins, up from 13 proteins; Fig. 7A and B), a higher increase in the overlap with invadopodia (19 proteins, up from 3 proteins; Fig. 7A and C), and an even higher increase in the overlap with SICs (40 proteins, up from 6; Fig. 7B and C). For complete lists of overlapping proteins, see Suppl. Table 3.

The podosome consensus proteome thus has extensive, but separate, overlaps with focal adhesions and invadopodia (Fig. 7D). Together with the newly identified AIP-1 and hnRNP-K, the overlap with invadopodia comprises 19 proteins, including annexin A5, gelsolin, several heat shock proteins, and enzymes such as glucose 6-phosphate dehydrogenase or enolase-1 (Suppl. Table 3). Overlap between podosomes and focal adhesions comprises 17 proteins, including actin-associated proteins such as filamin A, Arp2/3 complex subunits and cofilin, and as well as plaque proteins such as talin-1, vinculin and zyxin. The overlap between podosomes and invadopodia thus seems to consist mostly of proteins with enzymatic or metabolic function, whereas the overlap between podosomes and focal adhesions contains mostly cytoskeletal and structural components.

Comparisons between the consensus list of the 33 known podosome components with focal adhesions and invadopodia show that the SILAC consensus list adds 4 proteins to the overlap with focal adhesions, but 16 to the overlap with invadopodia. The new proteins in the overlap with focal adhesions comprise LASP-1, CSRP (cysteine and glycin rich protein)-1, Rac1 and syntenin-1 (SDCBP), while the 14 proteins in the overlap with invadopodia comprise mostly the newly identified heat shock proteins and enzymes.

A similar picture emerges upon exchange of the focal adhesion proteome analysed in Zaidel-Bar et al. (2007) and Zaidel-Bar and Geiger (2010) with the myosin II-responsive focal adhesion proteome detected in Kuo et al. (2011) (283 proteins of the so-called "expected focal adhesion list"). Including this proteome in the comparison, the number of unique overlapping proteins with the SILAC consensus list rises to 34 for the focal adhesome, the overlap with invadopodia drops to 8 proteins, while the overlap with SICs is slightly decreased to 25 proteins (Fig. 7E). Notable proteins newly included in the overlap between the myosin-responsive focal adhesion proteome and the SILAC consensus list include several Arp2/3 complex subunits, coronins 1B and 1C, and IQGAP. Among the proteins lost from the overlap are Src and ezrin. Interestingly, the overlap between all four proteomes now includes four proteins, comprising vimentin, hnRNP-K, the clathrin-associated ATPase HSPA8, and protein disulfide isomerase PDIA3. For a complete list of proteins in the overlap, as well as proteins gained or lost in respect to the first focal adhesome comparison, see Suppl. Table 3.

Collectively, these analyses show that, while focal adhesion, invadopodia and SIC proteomes share few components with each other, the podosome SILAC consensus proteome shows significant, but mostly separate, overlaps with each group. In addition to the group of established podosome proteins, the consensus list identifies 4 new components shared with focal adhesions, 16 new components shared with invadopodia, and 34 new components

shared with SICs. Moreover, the consensus list identifies 136 novel candidate proteins that appear to be unique to the podosome proteome (Fig. 7D).

Discussion

Cell-matrix contacts are organelles that enable cells to interact with the surrounding environment, most notably with the meshwork of the extracellular matrix. This group comprises diverse structures such as focal complexes, focal adhesions, fibrillar adhesions, spreading initiation centres (SICs), as well as invadopodia and podosomes, with each type presenting a unique combination of characteristics such as size, structure, dynamics and subcellular localisation. These defining differences also imply variations on the molecular level. Several efforts have therefore been made to characterise the proteomes of various cell matrix contacts, including those of focal adhesions (Zaidel-Bar et al., 2007; Zaidel-Bar and Geiger, 2010; Kuo et al., 2011; Schiller et al., 2011), SICs (de Hoog et al., 2004) and invadopodia (Attanasio et al., 2010). The lists of relevant proteins have thus grown constantly, for example from ca. 50 components known to be present in focal adhesions (Zamir and Geiger, 2001) to currently more than 150 (Zaidel-Bar et al., 2007). Comparable efforts have yielded lists of 58 components for invadopodia (out of 129 protein spots in gels; Attanasio et al., 2010) and 282 components for SICs (de Hoog et al., 2004), of which 240 have been classified so far in the Uniprot database. Adhesion structure proteomes thus seem consist of 150–200 different components. By contrast, 86 bona fide components have yet been described for podosomes.

Here, we present the first structured effort to identify a substantial part of the podosome proteome. We chose primary human macrophages, as these cells form numerous podosomes, which cover a sizable part of the ventral cell surface in 2D (Linder et al., 2011), and are thus amenable to enrichment of respective cell fractions. We compared ventral membranes containing podosomes ("footplates") with ventral membranes from cells in which podosomes were disrupted by treatment with the Src tyrosine kinase inhibitor PP2 (Linder et al., 2000b). This comparison allowed us to subtract footplate-associated background signals that are not due to enrichment at podosomes. SILAC labelling of cells enabled us to directly compare samples from these two conditions and analyse enrichment of respective proteins in subsequent mass spectrometric analyses. To eliminate donor- and set up-specific errors, three datasets were generated in independent experiments.

Comparisons between the different preparations show that a substantial fraction of known podosome components has been detected in our experiments, 33 of which are present in all three datasets. Our method to prepare podosome-enriched fractions thus appears to be, in principle, validated, and the complete consensus list of 203 proteins is likely to contain a variety of novel components. Moreover, as some known podosome components have only been detected in one or two experiments, it should also be worthwhile to evaluate the potential relevance of proteins outside of the consensus list. Typical podosome core components that have been detected only in one or two datasets (and are therefore not included in the consensus list) comprise, among others, calponin, cortactin, plectin and palladin. To streamline the following analysis, however, we concentrated on the consensus list of 203 proteins detected in all three datasets, as this list is most likely to contain novel podosome components.

An interesting finding concerns the intensity ratio (PP2/Ctrl) of proteins from footplate fractions. From the 33 previously known podosome components of the consensus list, podosome core components show a mean intensity ratio (PP2/Ctrl) of 0.68, while components of the ring structure show a ratio of 0.91. This is

32
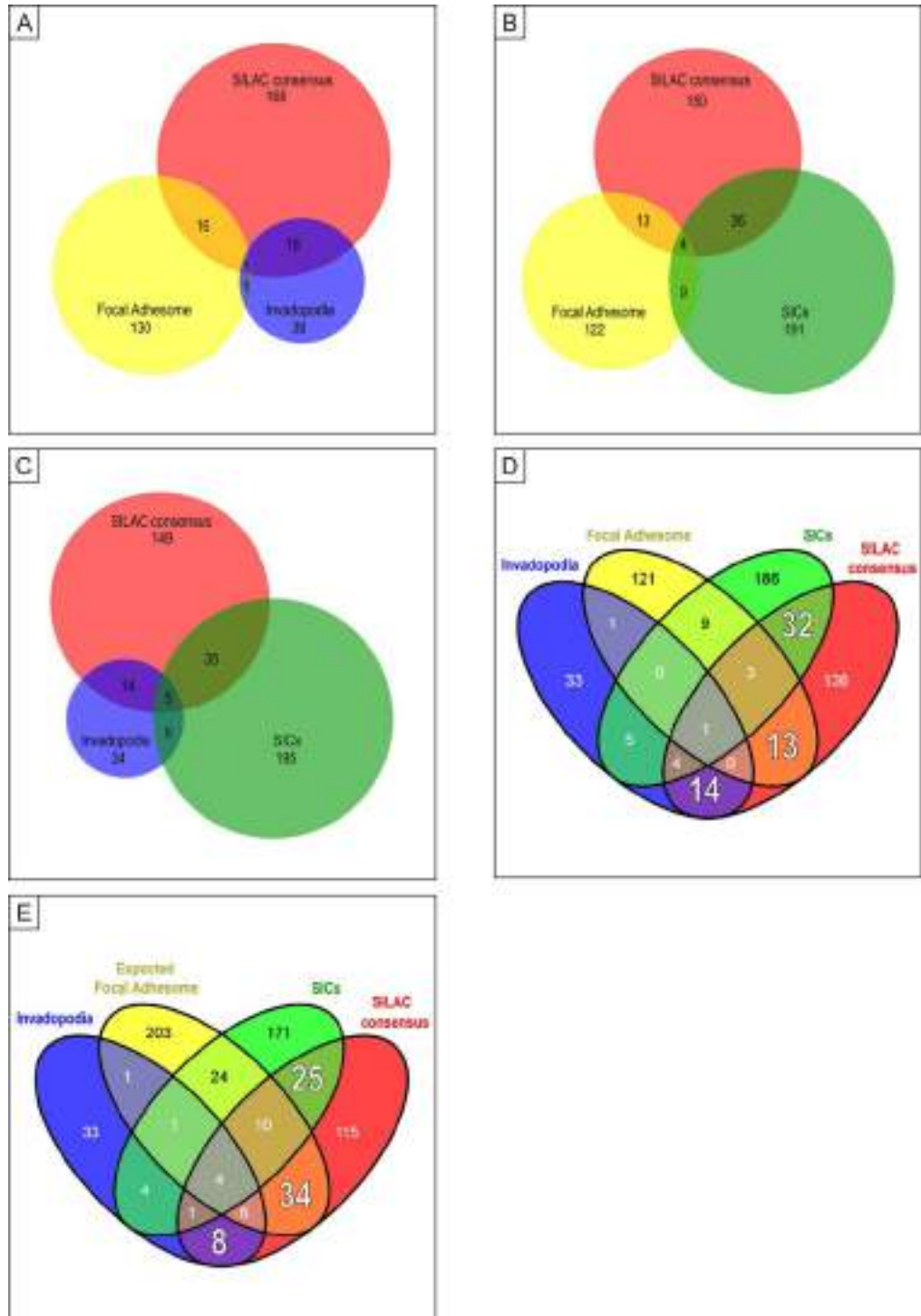
Fig. 7. Comparison of SILAC consensus list with other cell matrix contact proteomes. VENN diagrams showing overlaps between SILAC consensus list and proteomes of focal adhesions (www.adhesome.org list) and invadopodia (A), of focal adhesions and spreading initiation centres (SICs; B), of invadopodia and spreading initiation centres (C), and all proteomes together (D). In (E), the focal adhesion list was replaced with the "expected focal adhesion list" (Kuo et al., 2011), generated from the analysis of the myosin II-responsive focal adhesion proteome. Digits indicate the number of proteins found in the respective field. Large digits in (D;E) highlight the unique overlaps between the SILAC consensus list with other individual proteomes. Note that the SILAC consensus list has extensive overlaps with proteomes of focal adhesions, invadopodia and SICs. Overlap between these other proteomes is limited. For more detailed information about the proteins shared in the respective overlapping regions see Suppl. Table 3.

33

apparently based on the different behaviour of core and ring proteins due to PP2 treatment. A possible explanation may be that, although podosomes are destroyed by inhibition of Src kinase activity, ring/plaque proteins could still be recruited to other adhesion foci at the ventral membrane, whereas proteins of the actin core are mostly released into the cytoplasm. A prediction based on this finding is that proteins with a purification ratio of 0.6 or lower are likely to be core components, whereas those with a ratio of ca. 1.0 or higher probably reside in the podosome ring.

For proof-of-principle experiments, we chose two novel candidate proteins from the consensus list: WDR1/AIP-1, from the group of actin-associated proteins, and hnRNP-K as a representative for the newly identified group of RNA-associated proteins. Stainings of endogenous protein and overexpression of GFP/YFP-fused constructs showed that both proteins clearly localise to the F-actin rich core structure of podosomes, establishing them as bone fide podosome components. WDR1 is known to promote cofilin-mediated actin turnover by enhancing the severing activity of cofilin and by capping severed actin filaments (Okada et al., 2002; Balcer et al., 2003; Ono et al., 2004). Moreover, an vitro system of purified WDR1, coronin and cofilin has been shown to reconstitute actin filament disassembly (Kueh et al., 2008). It is thus very likely that WDR1, together with cofilin, is mediating actin filament turnover in podosomes.

Interestingly, hnRNP-K has also been identified as a component of the invadopodia proteome (Attanasio et al., 2010), and found to interact directly with N-WASP in mouse embryonic fibroblasts (Yoo et al., 2006). N-WASP is a central component of invadopodia (Yamaguchi et al., 2005), while its hematopoietic homologue WASP regulates podosomes in macrophages (Linder et al., 1999) and dendritic cells (Burns et al., 2001). Collectively, this may point to a potential role of hnRNP-K in (N-)WASP mediated formation of invadosome cores, although the localisation of hnRNP-K at invadopodia is currently unknown. Importantly, hnRNP-K is also a prominent component of spreading initiation centres (SICs) (de Hoog et al., 2004; Yoo et al., 2006).

Lasp-1, another member of the podosome consensus list, has also recently been identified as a podosome ring structure component, in both primary macrophages and smooth muscle cells, where it is involved in the regulation of podosome size and matrix degradation (Stölting et al., 2012). Collectively, these findings appear to validate the relevance of the podosomes proteome consensus list as a potential source for novel podosomes components.

We also compared the podosome consensus list with the previously published proteomes of focal adhesions (Zaidel-Bar et al., 2007; Zaidel-Bar and Geiger, 2010), invadopodia (Attanasio et al., 2010) and SICs (de Hoog et al., 2004). SICs are dot-like structures with a diameter of ca. 2 μm, containing RNA and associated proteins in a core that is sheated within an actin-rich zone, which is in contact with a patch of plaque proteins such as paxillin (de Hoog et al., 2004). SICs are short-lived structures that form at the cell periphery during spreading of primary cells. They regulate the rate of cell spreading (Yoo et al., 2006) and may be involved in local protein translation and/or folding (de Hoog et al., 2004).

Surprisingly focal adhesion, invadopodia, SIC, and podosome proteomes overlap in only one protein, the intermediate filament protein vimentin (Suppl. Fig. 2D), which is also a well-known contaminant in mass spectrometric analyses. The podosome proteome, on the other hand, has more extensive, but separate, overlaps with all three other proteomes. Overlap between podosomes and invadopodia seems to consist mostly of metabolic proteins, while podosomes and focal adhesions share mostly cytoskeletal and structural components. The most extensive overlap is between podosomes and SICs and consists mostly of ribonuclear components and RNA binding proteins. Although we cannot exclude that our footplate preparations also contains SICs, it has to be pointed out that (i) SICs have not been described in primary macrophages, (ii) SICs are only present during a short period in spreading cells, which is not applicable to our preparations, and (iii) clear and exclusive localisation of hnRNP-K to podosome cores argues for a specific enrichment at macrophage podosomes.

Exchanging the focal adhesion proteome (Zaidel-Bar et al., 2007; Zaidel-Bar and Geiger, 2010) with the myosinII-responsive focal adhesion proteome detected in Kuo et al. (2011), the overlap between all four proteomes now includes four proteins, among them hnRNP-K. This may point to a central role of hnRNP-K in the regulation of adhesion structures in general, although unequivocal localisation has so far been only demonstrated for SICs (de Hoog et al., 2004) and podosomes (this study).

Collectively, these analyses show that the podosome consensus proteome shows distinct overlaps with the proteomes of focal adhesions, invadopodia and SICs. Each of these overlaps is more extensive than the overlaps shared by the other three groups, which points to an "intermediate" position of podosomes in the group of matrix contact structures. Moreover, an extensive overlap was found between podosomes and SICs, which should make further investigations in this direction worthwhile.

Despite obvious differences in architecture, dynamics and subcellular localisation between the different cell matrix contacts, few clear molecular distinctions are available. For example, the adaptor protein Nck1 has been proposed as a marker for invadopodia, as opposed to podosomes (Oser et al., 2009), and WASP family proteins are typical for podosomes and invadopodia, but not for focal adhesions (Linder et al., 2011). The analyses of the different proteomes presented here should thus be helpful in developing individual "molecular fingerprints" that allow clear distinction between the different types of matrix contacts also on the protein level.

In sum, we present here techniques for the stable isotope labelling of primary human macrophages and for purification of podosome-enriched fractions from these cells. Using mass spectrometry analysis and database comparisons, we present a consensus list of 203 proteins, containing 33 known podosome proteins and 170 potential novel components. Software analyses show that particularly proteins involved in actin cytoskeleton regulation, adhesion mediation and those harbouring ATPase or GTPase activity are enriched. Surprisingly, we also identified a variety of ribosomal and RNA binding proteins. This was corroborated by proof-of-principle experiments, in which the newly identified RNA binding protein hnRNP-K, and also the actin binder WDR1/AIP-1, could be identified as novel bona fide podosome components that localise to the core structure of macrophage podosomes. Our results therefore point to the potential relevance of RNA binding proteins as additional regulators of podosome structure and/or function. They also indicate that the current consensus list might prove to be a useful and relevant source for the identification and study of novel podosome components and thus of novel regulators of macrophage adhesion and invasion.

Appendix A. Supplementary data

Supplementary data associated with this article can be found, in the online version, at http://dx.doi.org/10.1016/j.ejcb.2012.05.005.
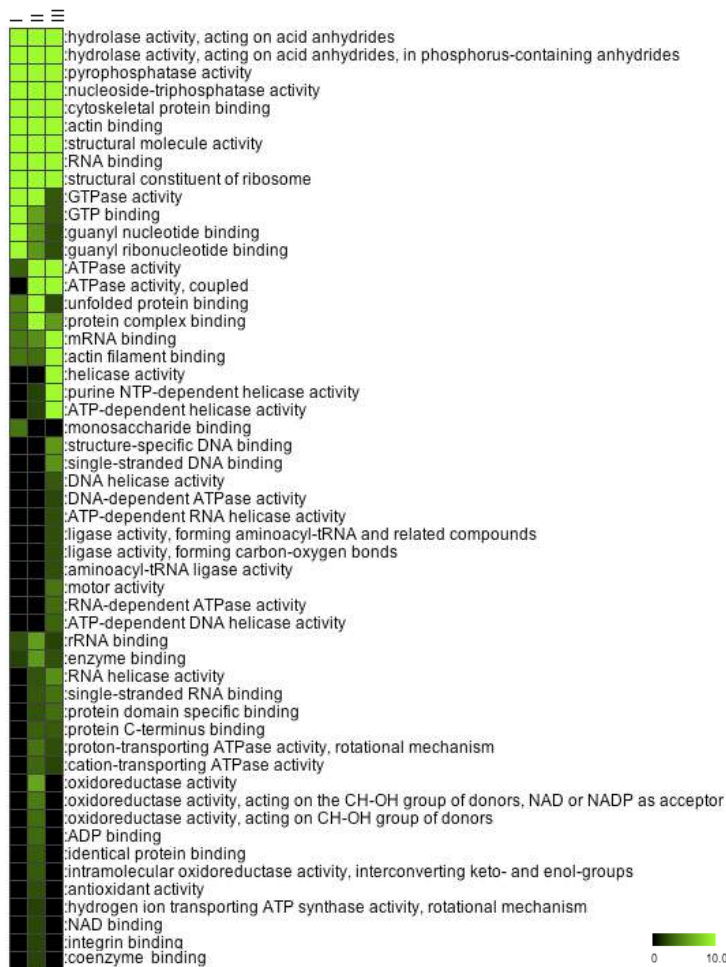
References

Abram, C.L., Seals, D.F., Pass, I., Salinsky, D., Maurer, L., Roth, T.M., Courtneidge, S.A., 2003. The adaptor protein fish associates with members of the ADAMs family and localizes to podosomes of Src-transformed cells. J. Biol. Chem. 278, 16844–16851.

Ashburner, M., Ball, C.A., Blake, J.A., Botstein, D., Butler, H., Cherry, J.M., Davis, A.P., Dolinski, K., Dwight, S.S., Eppig, J.T., Harris, M.A., Hill, D.P., Issel-Tarver, L., Kasarskis, A., Lewis, S., Matese, J.C., Richardson, J.E., Ringwald, M., Rubin, G.M., Sherlock, G., 2000. "The gene ontology consortium" gene ontology: tool for the unification of biology. Nat. Genet. 25, 25–29.

Attanasio, F., Caldieri, G., Giacchetti, G., van Horssen, R., Wieringa, B., Buccione, R., 2010. Novel invadopodia components revealed by differential proteomic analysis. Eur. J. Cell Biol. 90, 115–127.

Balcer, H.I., Goodman, A.L., Rodal, A.A., Smith, E., Kugler, J., Heuser, J.E., Goode, B.L., 2003. Coordinated regulation of actin filament turnover by a high-molecular-weight Srv2/CAP complex, Cofilin, Profilin, and Aip1. Curr. Biol. 13, 2159–2169.

Bastian, M., Heymann, S., Jacomy, M., 2009. Gephi: an open source software for exploring and manipulating networks. In: International AAAI Conference on Weblogs and Social Media, https://gephi.org/.

Bhuwania, R., Cornfine, S., Fang, Z., Krüger, M., Luna, E.J., Linder, S., 2012. Supervillin couples myosin-dependent contractility to podosomes and enables their turnover. J. Cell Sci. (Epub February 17).

Blagoev, B., Kratchmarova, I., Ong, S.-E., Nielsen, M., Foster, L.J., Mann, M., 2003. A proteomics strategy to elucidate functional protein–protein interactions applied to EGF signaling. Nat. Biotechnol. 21, 315–318.

Buccione, R., Orth, J.D., McNiven, M.A., 2004. Foot and mouth: podosomes, invadopodia and circular dorsal ruffles. Nature reviews. Mol. Cell. Biol. 5, 647–657.

Burgstaller, G., Gimona, M., 2004. Actin cytoskeleton remodelling via local inhibition of contractility at discrete microdomains. J. Cell Sci. 117, 223–231.

Burns, S., Thrasher, A.J., Blundell, M.P., Machesky, L., Jones, G.E., 2001. Configuration of human dendritic cell cytoskeleton by Rho GTPases, the WAS protein, and differentiation. Blood 98, 1142–1149.

Caldieri, G., Ayala, I., Attanasio, F., Buccione, R., 2009. Cell and molecular biology of invadopodia. Int. Rev. Cell Biol. 275, 1–34.

Chabadel, A., Bañon-Rodríguez, I., Cluet, D., Rudkin, B.B., Wehrle-Haller, B., Genot, E., Jurdic, P., Anton, I.M., Saltel, F., 2007. CD44 and β3 Integrin organize two functionally distinct actin-based domains in osteoclasts. Mol. Biol. Cell 18, 4899–4910.

Chellaiah, M., Kizer, N., Silva, M., Alvarez, U., Kwiatkowski, D., Hruska, K.A., 2000. Gelsolin deficiency blocks podosome assembly and produces increased bone mass and strength. J. Cell Biol. 148, 665–678.

Chen, L.-C., Liu, H.-P., Li, H.-P., Hsueh, C., Yu, J.-S., Liang, C.-L., Chang, Y.-S., 2009. Thymidine phosphorylase mRNA stability and protein levels are increased through ERK-mediated cytoplasmic accumulation of hnRNP K in nasopharyngeal carcinoma cells. Oncogene 28, 1904–1915.

Collin, O., Na, S., Chowdhury, F., Hong, M., Shin, M.E., Wang, F., Wang, N., 2008. Self-organized podosomes are dynamic mechanosensors. Curr. Biol. 18, 1288–1294.

Collin, O., Tracqui, P., Stephanou, A., Usson, Y., Clément-Lacroix, J., Planus, E., 2006. Spatiotemporal dynamics of actin-rich adhesion microdomains: influence of substrate flexibility. J. Cell Sci. 119, 1914–1925.

Côté, R.G., Jones, P., Martens, L., Kerrien, S., Reisinger, F., Lin, Q., Leinonen, R., Apweiler, R., Hermjakob, H., 2007. The protein identifier cross-referencing (PICR) service: reconciling protein identifiers across multiple source databases. BMC Bioinformatics 8, 401–414.

de Hoog, C.L., Foster, L.J., Mann, M., 2004. RNA and RNA binding proteins participate in early stages of cell spreading through spreading initiation cent. Cell 117, 649–662.

Destaing, O., Saltel, F., Geminard, J.-C., Jurdic, P., Bard, F., 2003. Podosomes display actin turnover and dynamic self-organization in osteoclasts expressing actin-green fluorescent protein. Mol. Biol. Cell 14, 407–416.

Duncan, D., Prodduturi, N., Zhang, B., 2010. WebGestalt2: an updated and expanded version of the Web-based Gene Set Analysis Toolkit. BMC Bioinformatics 11, P10, http://bioinfo.vanderbilt.edu/webgestalt.

Eden, E., Lipson, D., Yogev, S., Yakhini, Z., 2007. Discovering motifs in ranked lists of DNA sequences. PLoS Comp. Biol. 3, 0508–522.

Eden, E., Navon, R., Steinfeld, I., Lipson, D., Yakhini, Z., 2009. GOrilla: a tool for discovery and visualization of enriched GO terms in ranked gene lists. BMC Bioinformatics 10, 48–54.

Gimona, M., Buccione, R., Courtneidge, S.A., Linder, S., 2008. Assembly and biological role of podosomes and invadopodia. Curr. Opin. Cell Biol. 20, 235–241.

Gringel, A., Walz, D., Rosenberger, G., Minden, A., Kutsche, K., Kopp, P., Linder, S., 2006. PAK4 and aPIX determine podosome size and number in macrophages through localized actin regulation. J. Cell. Physiol. 209, 568–579.

Gruhler, A., Kratchmarova, I., 2008. Stable isotope labeling by amino acids in cell culture (SILAC). Methods Mol. Biol. 424, 101–111.

Hulsen, T., de Vlieg, J., Alkema, W., 2008. BioVenn – a web application for the comparison and visualization of biological lists using area-proportional Venn diagrams. BMC Genomics 9, 488–493, http://www.cmbi.ru.nl/cdd/biovenn/.

Humphries, J.D., Byron, A., Bass, M.D., Craig, S.E., Pinney, J.W., Knight, D., Humphries, M.J., 2009. Proteomic analysis of integrin-associated complexes identifies RCC2 as a dual regulator of Rac1 and Arf6. Sci. Signal. 2 (87), ra51.

Kaimal, V., Bardes, E.E., Tabar, S.C., Jegga, A.G., Aronow, B.J., 2010. ToppCluster: a multiple gene list feature analyzer for comparative enrichment clustering and network-based dissection of biological systems. Nucleic Acids Res. 38, W96–W102.

Kato, A., Kurita, S., Hayashi, A., Kaji, N., Ohashi, K., Mizuno, K., 2008. Critical roles of actin-interacting protein 1 in cytokinesis and chemotactic migration of mammalian cells. Biochem. J. 414, 261–270.

Kaverina, I., Stradal, T.E.B., Gimona, M., 2003. Podosome formation in cultured A7r5 vascular smooth muscle cells requires Arp2/3-dependent de-novo actin polymerization at discrete microdomains. J. Cell Sci. 116, 4915–4924.

Kopp, P., Lammers, R., Aepfelbacher, M., Woehlke, G., Rudel, T., Machuy, N., Steffen, W., Linder, S., 2006. The kinesin KIF1C and microtubule plus ends regulate podosome dynamics in macrophages. Mol. Biol. Cell 17, 2811–2823.

Krüger, M., Kratchmarova, I., Blagoev, B., Tseng, Y.-H., Kahn, C.R., Mann, M., 2008. Dissection of the insulin signaling pathway via quantitative phosphoproteomics. PNAS 105, 2451–2456.

Kueh, H.Y., Charras, G.T., Mitchison, T.J., Brieher, W.M., 2008. Actin disassembly by cofilin, coronin, and Aip1 occurs in bursts and is inhibited by barbed-end cappers. J. Cell Biol. 182, 341–353.

Kuo, J.-C., Han, X., Hsiao, C.-T., Yates III, J.R., Waterman, C.M., 2011. Analysis of the myosin-II-responsive focal adhesion proteome reveals a role for β-Pix in negative regulation of focal adhesion maturation. Nat. Cell Biol. 13, 383–393.

Labernadie, A., Thibault, C., Vieu, C., Maridonneau-parini, I., Charrière, G.M., 2010. Dynamics of podosome stiffness revealed by atomic force microscopy. PNAS 107, 21016–21021.

Linder, S., 2007. The matrix corroded: podosomes and invadopodia in extracellular matrix degradation. Trends Cell Biol. 17, 107–117.

Linder, S., 2009. Invadosomes at a glance. J. Cell Sci. 122, 3009–3013.

Linder, S., Aepfelbacher, M., 2003. Podosomes: adhesion hot-spots of invasive cells. Trends Cell Biol. 13, 376–385.

Linder, S., Higgs, H., Hüfner, K., Schwarz, K., Pannicke, U., Aepfelbacher, M., 2000a. The polarization defect of Wiskott–Aldrich syndrome macrophages is linked to dislocalization of the Arp2/3 complex. J. Immunol. 165, 221–225.

Linder, S., Hüfner, K., Wintergerst, U., Aepfelbacher, M., 2000b. Microtubule-dependent formation of podosomal adhesion structures in primary human macrophages. J. Cell Sci. 113 (Pt 23), 4165–4176.

Linder, S., Nelson, D., Weiss, M., Aepfelbacher, M., 1999. Wiskott–Aldrich syndrome protein regulates podosomes in primary human macrophages. PNAS 96, 9648–9653.

Linder, S., Wiesner, C., Himmel, M., 2011. Degrading devices: invadosomes in proteolytic cell invasion. Annu. Rev. Cell Dev. Biol. 27, 185–211.

Lorenz, M., Yamaguchi, H., Wang, Y., Singer, R.H., Condeelis, J., 2004. Imaging sites of N-WASP activity in lamellipodia and invadopodia of carcinoma cells. Curr. Biol. 14, 697–703.

Luxenburg, C., Winograd-katz, S., Addadi, L., Geiger, B., 2012. Involvement of actin polymerization in podosome dynamics. J. Cell Sci. (Epub. February 10).

Mann, M., 2006. Functional and quantitative proteomics using SILAC. Nat. Rev. Mol. Cell Biol. 7, 952–958.

Mersich, A.T., Miller, M.R., Chkourko, H., Blystone, S.D., 2010. The formin FRL1 (FMNL1) is an essential component of macrophage podosomes. Cytoskeleton 67, 573–585.

Mi, H., Dong, Q., Muruganujan, A., Gaudet, P., Lewis, S., Thomas, P.D., 2010. PANTHER version 7: improved phylogenetic trees, orthologs and collaboration with the Gene Ontology Consortium. Nucleic Acids Res. 38, D204–D210.

Monsky, W.L., Lin, C.-Y., Aoyama, A., Kelly, T., Akiyama, S.K., Mueller, S.C., Chen, W.-T., 1994. A potential marker protease of invasiveness Separase, is localized on invadopodia of human malignant melanoma cells. Cancer Res. 54, 5702–5710.

Moreau, V., Tatin, F., Varon, C., Genot, E., 2003. Actin can reorganize into podosomes in aortic endothelial cells, a process controlled by Cdc42 and RhoA. Mol. Cell. Biol. 23, 6809–6822.

Okada, K., Blanchoin, L., Abe, H., Chen, H., Pollard, T.D., Bamburg, J.R., 2002. Xenopus actin-interacting protein 1 (XAip1) enhances cofilin fragmentation of filaments by capping filament ends. J. Biol. Chem. 277, 43011–43016.

Oliveros, J.C., 2007. VENNY. An Interactive Tool for Comparing Lists with Venn Diagrams., http://bioinfogp.cnb.csic.es/tools/venny/index.ht.

Ong, S.-E., Blagoev, B., Kratchmarova, I., Kristensen, D.B., Steen, H., Pandey, A., Mann, M., 2002. Stable isotope labeling by amino acids in cell culture SILAC, as a simple and accurate approach to expression proteomics. Mol. Cell. Proteomics 1, 376–386.

Ong, S.-E., Mann, M., 2006. A practical recipe for stable isotope labeling by amino acids in cell culture (SILAC). Nat. Protoc. 1, 2650–2660.

Ono, S., Mohri, K., Ono, K., 2004. Microscopic evidence that actin-interacting protein 1 actively disassembles actin-depolymerizing factor/Cofilin-bound actin filaments. J. Biol. Chem. 279, 14207–14212.

Oser, M., Yamaguchi, H., Mader, C.C., Bravo-Cordero, J.J., Arias, M., Chen, X., Desmarais, V., van Rheenen, J., Koleske, A.J., Condeelis, J., 2009. Cortactin regulates cofilin and N-WASp activities to control the stages of invadopodium assembly and maturation. J. Cell Biol. 186, 571–587.
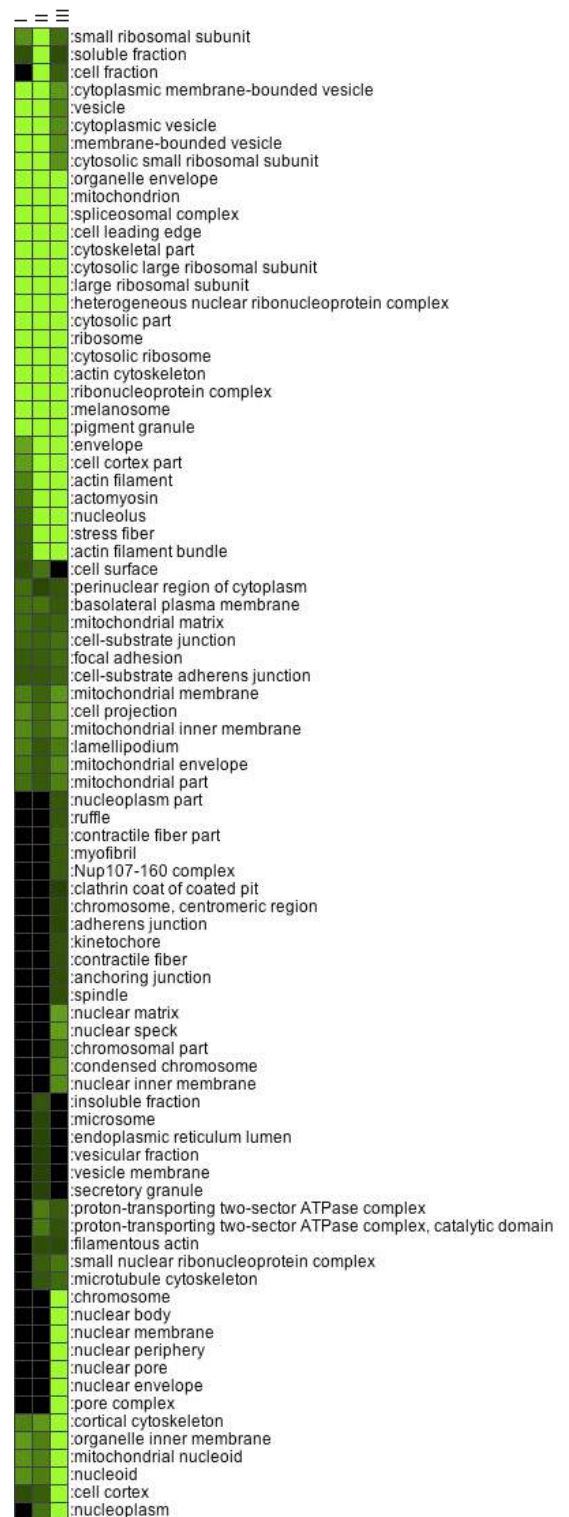
35

Osiak, A.-E., Zenner, G., Linder, S., 2005. Subconfluent endothelial cells form podosomes downstream of cytokine and RhoGTPase signaling. Exp. Cell Res. 307, 342–353.

Rappsilber, J., Ishihama, Y., Mann, M., 2003. Stop and go extraction tips for matrix-assisted laser desorption/ionization, nanoelectrospray, and LC/MS sample pretreatment in proteomics. Anal. Chem. 75, 663–670.

Saltel, F., Daubon, T., Juin, A., Ganuza, I.E., Veillat, V., Génot, E., 2011. Invadosomes: intriguing structures with promise. Eur. J. Cell Biol. 90, 100–107.

Shevchenko, A., Wilm, M., Vorm, O., Mann, M., 1996. Mass spectrometric sequencing of proteins silver-stained polyacrylamide gels. Anal. Chem. 68, 850–858.

Schiller, H.B., Friedel, C.C., Boulegue, C., Fässler, R., 2011. Quantitative proteomics of the integrin adhesome show a myosin II-dependent recruitment of LIM domain proteins. EMBO Rep. 12, 259–266.

Stölting, M., Wiesner, C., van Vliet, V., Butt, E., Pavenstädt, H., Linder, S., Kremer-skothen, J., 2012. Lasp-1 is involved in podosome dynamics. PLoS ONE 7 (4), e35340 (Epub April 13).

Tarassov, K., Michnick, S.W., 2005. iVici: interrelational visualization and correlation interface. Genome Biol. 6, R115–R127.

Tehrani, S., Faccio, R., Chandrasekar, I., Ross, F.P., Cooper, J.A., 2006. Cortactin has an essential and specific role in osteoclast actin assembly. Mol. Biol. Cell 17, 2882–2895.

Thomas, P.D., Kejariwal, A., Campbell, M.J., Mi, H., Diemer, K., Guo, N., Ladunga, I., Ulitsky-Lazareva, B., Muruganujan, A., Rabkin, S., Vandergriff, J.A., Doremieux, O., 2003. PANTHER: a browsable database of gene products organized by biological function, using curated protein family and subfamily classification. Nucleic Acids Res. 31, 334–341.

van der Zeijst, B.A., Stewart, C.C., Schlesinger, S., 1978. Proliferative capacity of mouse peritoneal macrophages in vitro. J. Exp. Med., 1253–1266.

Wiesner, C., Faix, J., Himmel, M., Bentzien, F., Linder, S., 2010. KIF5B and KIF3A/KIF3B kinesins drive MT1-MMP surface exposure CD44 shedding, and extracellular matrix degradation in primary macrophages. Blood 116, 1559–1569.

Yamaguchi, H., Lorenz, M., Kempiak, S., Sarmiento, C., Coniglio, S., Symons, M., Segall, J., Eddy, R., Miki, H., Takenawa, T., Condeelis, J., 2005. Molecular mechanisms of invadopodium formation: the role of the N-WASP-Arp2/3 complex pathway and cofilin. J. Cell Biol. 168, 441–452.

Yoo, Y., Wu, X., Egile, C., Li, R., Guan, J.-L., 2006. Interaction of N-WASP with hnRNPK and its role in filopodia formation and cell spreading. J. Biol. Chem. 281, 15352–15360.

Zaidel-Bar, R., 2009. Evolution of complexity in the integrin adhesome. J. Cell Biol. 186, 317–321.

Zaidel-Bar, R., Geiger, B., 2010. The switchable integrin adhesome. J. Cell Sci. 123, 1385–1388.

Zaidel-Bar, R., Itzkovitz, S., Ma'ayan, A., Iyengar, R., Geiger, B., 2007. Functional atlas of the integrin adhesome. Nat. Cell Biol. 9, 858–867.

Zambonin-Zallone, A., Teti, A., Grano, M., Rubinacci, A., Abbadini, M., Gaboli, M., Marchisio, P.C., 1989. Immunocytochemical distribution of extracellular matrix receptors in human osteoclasts: a beta 3 integrin is colocalized with vinculin and talin in the podosomes of osteoclastoma giant cells. Exp. Cell Res. 182, 645–652.

Zamir, E., Geiger, B., 2001. Molecular complexity and dynamics of cell-matrix adhesions. J. Cell Sci. 114, 3583–3590.

Zhang, B., Kirov, S., Snoddy, J., 2005. WebGestalt: an integrated system for exploring gene sets in various biological contexts. Nucleic Acids Res. 33, W741–W748.

A   Molecular function: heat map

_ = ≡

- hydrolase activity, acting on acid anhydrides
- hydrolase activity, acting on acid anhydrides, in phosphorus-containing anhydrides
- pyrophosphatase activity
- nucleoside-triphosphatase activity
- cytoskeletal protein binding
- actin binding
- structural molecule activity
- RNA binding
- structural constituent of ribosome
- GTPase activity
- GTP binding
- guanyl nucleotide binding
- guanyl ribonucleotide binding
- ATPase activity
- ATPase activity, coupled
- unfolded protein binding
- protein complex binding
- mRNA binding
- actin filament binding
- helicase activity
- purine NTP-dependent helicase activity
- ATP-dependent helicase activity
- monosaccharide binding
- structure-specific DNA binding
- single-stranded DNA binding
- DNA helicase activity
- DNA-dependent ATPase activity
- ATP-dependent RNA helicase activity
- ligase activity, forming aminoacyl-tRNA and related compounds
- ligase activity, forming carbon-oxygen bonds
- aminoacyl-tRNA ligase activity
- motor activity
- RNA-dependent ATPase activity
- ATP-dependent DNA helicase activity
- rRNA binding
- enzyme binding
- RNA helicase activity
- single-stranded RNA binding
- protein domain specific binding
- protein C-terminus binding
- proton-transporting ATPase activity, rotational mechanism
- cation-transporting ATPase activity
- oxidoreductase activity
- oxidoreductase activity, acting on the CH-OH group of donors, NAD or NADP as acceptor
- oxidoreductase activity, acting on CH-OH group of donors
- ADP binding
- identical protein binding
- intramolecular oxidoreductase activity, interconverting keto- and enol-groups
- antioxidant activity
- hydrogen ion transporting ATP synthase activity, rotational mechanism
- NAD binding
- integrin binding
- coenzyme binding

0   10.0

B   Cellular component: heat map

_ = ≡

- small ribosomal subunit
- soluble fraction
- cell fraction
- cytoplasmic membrane-bounded vesicle
- vesicle
- cytoplasmic vesicle
- membrane-bounded vesicle
- cytosolic small ribosomal subunit
- organelle envelope
- mitochondrion
- spliceosomal complex
- cell leading edge
- cytoskeletal part
- cytosolic large ribosomal subunit
- large ribosomal subunit
- heterogeneous nuclear ribonucleoprotein complex
- cytosolic part
- ribosome
- cytosolic ribosome
- actin cytoskeleton
- ribonucleoprotein complex
- melanosome
- pigment granule
- envelope
- cell cortex part
- actin filament
- actomyosin
- nucleolus
- stress fiber
- actin filament bundle
- cell surface
- perinuclear region of cytoplasm
- basolateral plasma membrane
- mitochondrial matrix
- cell-substrate junction
- focal adhesion
- cell-substrate adherens junction
- mitochondrial membrane
- cell projection
- mitochondrial inner membrane
- lamellipodium
- mitochondrial envelope
- mitochondrial part
- nucleoplasm part
- ruffle
- contractile fiber part
- myofibril
- Nup107-160 complex
- clathrin coat of coated pit
- chromosome, centromeric region
- adherens junction
- kinetochore
- contractile fiber
- anchoring junction
- spindle
- nuclear matrix
- nuclear speck
- chromosomal part
- condensed chromosome
- nuclear inner membrane
- insoluble fraction
- microsome
- endoplasmic reticulum lumen
- vesicular fraction
- vesicle membrane
- secretory granule
- proton-transporting two-sector ATPase complex
- proton-transporting two-sector ATPase complex, catalytic domain
- filamentous actin
- small nuclear ribonucleoprotein complex
- microtubule cytoskeleton
- chromosome
- nuclear body
- nuclear membrane
- nuclear periphery
- nuclear pore
- nuclear envelope
- pore complex
- cortical cytoskeleton
- organelle inner membrane
- mitochondrial nucleoid
- nucleoid
- cell cortex
- nucleoplasm

Supplementary table 1

				SILAC consensus list	
#	UniProt ID	Uniprot name	Gene name	Protein name	Intensity ratio (R) PP2 / DMSO
1	P49748	ACADV_HUMAN	ACADVL	Very long-chain specific acyl-CoA dehydrogenase, mitochondrial	1,40
2	P33121	ACSL1_HUMAN	ACSL1	Long-chain-fatty-acid--CoA ligase 1	1,87
3	P68032	ACTC_HUMAN	ACTC1	Actin, alpha cardiac muscle 1	0,48
4	P12814	ACTN1_HUMAN	ACTN1	Alpha-actinin-1	0,61
5	P61160	ARP2_HUMAN	ACTR2	Actin-related protein 2	0,96
6	P61158	ARP3_HUMAN	ACTR3	Actin-related protein 3	0,64
7	Q09666	AHNK_HUMAN	AHNAK	Neuroblast differentiation-associated protein AHNAK	1,38
8	P04075	ALDOA_HUMAN	ALDOA	Fructose-bisphosphate aldolase A	1,03
9	P04083	ANXA1_HUMAN	ANXA1	Annexin A1	0,86
10	P50995	ANX11_HUMAN	ANXA11	Annexin A11	1,34
11	A6NMY6	AXA2L_HUMAN	ANXA2P2	Putative annexin A2-like protein	1,40
12	P08758	ANXA5_HUMAN	ANXA5	Annexin A5	0,82
13	O95782	AP2A1_HUMAN	AP2A1	AP-2 complex subunit alpha-1	1,28
14	P63010	AP2B1_HUMAN	AP2B1	AP-2 complex subunit beta	1,10
15	P02649	APOE_HUMAN	APOE	Apolipoprotein E	1,48
16	P61204	ARF3_HUMAN	ARF3	ADP-ribosylation factor 3	0,87
17	O15143	ARC1B_HUMAN	ARPC1B	Actin-related protein 2/3 complex subunit 1B	0,68
18	O15144	ARPC2_HUMAN	ARPC2	Actin-related protein 2/3 complex subunit 2	0,52
19	O15145	ARPC3_HUMAN	ARPC3	Actin-related protein 2/3 complex subunit 3	0,54
20	P59998	ARPC4_HUMAN	ARPC4	Actin-related protein 2/3 complex subunit 4	0,56
21	O15511	ARPC5_HUMAN	ARPC5	Actin-related protein 2/3 complex subunit 5	0,61
22	P05023	AT1A1_HUMAN	ATP1A1	Sodium/potassium-transporting ATPase subunit alpha-1	1,87
23	P25705	ATPA_HUMAN	ATP5A1	ATP synthase subunit alpha, mitochondrial	1,79
24	P06576	ATPB_HUMAN	ATP5B	ATP synthase subunit beta, mitochondrial	1,79
25	P51572	BAP31_HUMAN	BCAP31	B-cell receptor-associated protein 31	1,68
26	Q01518	CAP1_HUMAN	CAP1	Adenylyl cyclase-associated protein 1	0,74
27	P52907	CAZA1_HUMAN	CAPZA1	F-actin-capping protein subunit alpha-1	0,96
28	P47756	CAPZB_HUMAN	CAPZB	F-actin-capping protein subunit beta	0,60
29	P16070	CD44_HUMAN	CD44	CD44 antigen	1,03
30	P23528	COF1_HUMAN	CFL1	Cofilin-1	0,38
31	Q9NX63	CHCH3_HUMAN	CHCHD3	Coiled-coil-helix-coiled-coil-helix domain-containing protein 3	1,02
32	O00299	CLIC1_HUMAN	CLIC1	Chloride intracellular channel protein 1	0,81
33	Q00610	CLH1_HUMAN	CLTC	Clathrin heavy chain 1	1,00
34	P31146	COR1A_HUMAN	CORO1A	Coronin-1A	0,42
35	Q9BR76	COR1B_HUMAN	CORO1B	Coronin-1B	0,35
36	Q9ULV4	COR1C_HUMAN	CORO1C	Coronin-1C	0,43
37	O75390	CISY_HUMAN	CS	Citrate synthase, mitochondrial	1,05
38	P21291	CSRP1_HUMAN	CSRP1	Cysteine and glycine-rich protein 1	0,69
39	P25774	CATS_HUMAN	CTSS	Cathepsin S	1,29
40	P04839	CY24B_HUMAN	CYBB	Cytochrome b-245 heavy chain	1,86
41	Q7L576	CYFP1_HUMAN	CYFIP1	Cytoplasmic FMR1-interacting protein 1	0,96
42	Q02318	CP27A_HUMAN	CYP27A1	Sterol 26-hydroxylase, mitochondrial	1,72
43	P39656	OST48_HUMAN	DDOST	Dolichyl-diphosphooligosaccharide--protein glycosyltransferase 48 kDa subunit	3,46
44	Q92841	DDX17_HUMAN	DDX17	Probable ATP-dependent RNA helicase DDX17	0,77
45	O00571	DDX3X_HUMAN	DDX3X	ATP-dependent RNA helicase DDX3X	1,34
46	P17844	DDX5_HUMAN	DDX5	Probable ATP-dependent RNA helicase DDX5	0,83
47	Q16698	DECR_HUMAN	DECR1	2,4-dienoyl-CoA reductase, mitochondrial	0,97
48	Q08211	DHX9_HUMAN	DHX9	ATP-dependent RNA helicase A	0,87
49	O75937	DNJC8_HUMAN	DNAJC8	DnaJ homolog subfamily C member 8	0,94
50	P50570	DYN2_HUMAN	DNM2	Dynamin-2	0,88
51	Q14204	DYHC1_HUMAN	DYNC1H1	Cytoplasmic dynein 1 heavy chain 1	1,12
52	P68104	EF1A1_HUMAN	EEF1A1	Elongation factor 1-alpha 1	0,99
53	P13639	EF2_HUMAN	EEF2	Elongation factor 2	0,92
54	Q96C19	EFHD2_HUMAN	EFHD2	EF-hand domain-containing protein D2	0,19
55	Q9H223	EHD4_HUMAN	EHD4	EH domain-containing protein 4	1,06
56	P06733	ENOA_HUMAN	ENO1	Alpha-enolase	0,76
57	Q9UI08	EVL_HUMAN	EVL	Ena/VASP-like protein	0,29
58	P15311	EZRI_HUMAN	EZR	Ezrin	1,07
59	P09467	F16P1_HUMAN	FBP1	Fructose-1,6-bisphosphatase 1	1,28
60	Q86UX7	URP2_HUMAN	FERMT3	Fermitin family homolog 3	1,08
61	Q14314	FGL2_HUMAN	FGL2	Fibroleukin	2,34
62	P21333	FLNA_HUMAN	FLNA	Filamin-A	0,65
63	P35637	FUS_HUMAN	FUS	RNA-binding protein FUS	0,75
64	P11413	G6PD_HUMAN	G6PD	Glucose-6-phosphate 1-dehydrogenase	0,94
65	Q99988	GDF15_HUMAN	GDF15	Growth/differentiation factor 15	1,61
66	Q9H4G4	GAPR1_HUMAN	GLIPR2	Golgi-associated plant pathogenesis-related protein 1	1,09

67	Q8NBJ5	GT251_HUMAN	GLT25D1	Procollagen galactosyltransferase 1	1,83
68	P04899	GNAI2_HUMAN	GNAI2	Guanine nucleotide-binding protein G	1,19
69	P06744	G6PI_HUMAN	GPI	Glucose-6-phosphate isomerase	0,79
70	P06396	GELS_HUMAN	GSN	Gelsolin	1,21
71	O75367	H2AY_HUMAN	H2AFY	Core histone macro-H2A.1	0,95
72	P40939	ECHA_HUMAN	HADHA	Trifunctional enzyme subunit alpha, mitochondrial	2,20
73	P55084	ECHB_HUMAN	HADHB	Trifunctional enzyme subunit beta, mitochondrial	1,98
74	P52790	HXK3_HUMAN	HK3	Hexokinase-3	0,95
75	P09651	ROA1_HUMAN	HNRNPA1	Heterogeneous nuclear ribonucleoprotein A1	0,79
76	P51991	ROA3_HUMAN	HNRNPA3	Heterogeneous nuclear ribonucleoprotein A3	0,74
77	P07910	HNRPC_HUMAN	HNRNPC	Heterogeneous nuclear ribonucleoproteins C1/C2	1,00
78	Q14103	HNRPD_HUMAN	HNRNPD	Heterogeneous nuclear ribonucleoprotein D0	0,81
79	P31943	HNRH1_HUMAN	HNRNPH1	Heterogeneous nuclear ribonucleoprotein H	0,76
80	P61978	HNRPK_HUMAN	HNRNPK	Heterogeneous nuclear ribonucleoprotein K	0,72
81	P14866	HNRPL_HUMAN	HNRNPL	Heterogeneous nuclear ribonucleoprotein L	0,75
82	P52272	HNRPM_HUMAN	HNRNPM	Heterogeneous nuclear ribonucleoprotein M	0,70
83	Q00839	HNRPU_HUMAN	HNRNPU	Heterogeneous nuclear ribonucleoprotein U	0,93
84	Q1KMD3	HNRL2_HUMAN	HNRNPUL2	Heterogeneous nuclear ribonucleoprotein U-like protein 2	0,78
85	Q53GQ0	DHB12_HUMAN	HSD17B12	Estradiol 17-beta-dehydrogenase 12	1,36
86	P51659	DHB4_HUMAN	HSD17B4	Peroxisomal multifunctional enzyme type 2	1,67
87	P07900	HS90A_HUMAN	HSP90AA1	Heat shock protein HSP 90-alpha	0,91
88	P08238	HS90B_HUMAN	HSP90AB1	Heat shock protein HSP 90-beta	0,91
89	P14625	ENPL_HUMAN	HSP90B1	Endoplasmin	0,92
90	P11021	GRP78_HUMAN	HSPA5	78 kDa glucose-regulated protein	1,56
91	P11142	HSP7C_HUMAN	HSPA8	Heat shock cognate 71 kDa protein	1,05
92	P38646	GRP75_HUMAN	HSPA9	Stress-70 protein, mitochondrial	1,91
93	P10809	CH60_HUMAN	HSPD1	60 kDa heat shock protein, mitochondrial	1,14
94	Q92743	HTRA1_HUMAN	HTRA1	Serine protease HTRA1	1,92
95	Q12905	ILF2_HUMAN	ILF2	Interleukin enhancer-binding factor 2	1,00
96	Q16891	IMMT_HUMAN	IMMT	Mitochondrial inner membrane protein	1,19
97	P46940	IQGA1_HUMAN	IQGAP1	Ras GTPase-activating-like protein IQGAP1	1,75
98	Q96CN7	ISOC1_HUMAN	ISOC1	Isochorismatase domain-containing protein 1	1,06
99	P20702	ITAX_HUMAN	ITGAX	Integrin alpha-X	1,24
100	P05107	ITB2_HUMAN	ITGB2	Integrin beta-2	1,17
101	Q13303	KCAB2_HUMAN	KCNAB2	Voltage-gated potassium channel subunit beta-2	0,98
102	Q92945	FUBP2_HUMAN	KHSRP	Far upstream element-binding protein 2	0,72
103	P83111	LACTB_HUMAN	LACTB	Serine beta-lactamase-like protein LACTB, mitochondrial	3,01
104	Q14847	LASP1_HUMAN	LASP1	LIM and SH3 domain protein 1	0,49
105	P13796	PLSL_HUMAN	LCP1	Plastin-2	0,62
106	P00338	LDHA_HUMAN	LDHA	L-lactate dehydrogenase A chain	0,68
107	P17931	LEG3_HUMAN	LGALS3	Galectin-3	0,92
108	O00182	LEG9_HUMAN	LGALS9	Galectin-9	1,02
109	P02545	LMNA_HUMAN	LMNA	Prelamin-A/C [Cleaved into: Lamin-A/C]	0,90
110	Q03252	LMNB2_HUMAN	LMNB2	Lamin-B2	0,95
111	P06858	LIPL_HUMAN	LPL	Lipoprotein lipase	1,13
112	P33241	LSP1_HUMAN	LSP1	Lymphocyte-specific protein 1	0,20
113	P09960	LKHA4_HUMAN	LTA4H	Leukotriene A-4 hydrolase	0,83
114	P43243	MATR3_HUMAN	MATR3	Matrin-3	0,82
115	P40926	MDHM_HUMAN	MDH2	Malate dehydrogenase, mitochondrial	1,03
116	P41218	MNDA_HUMAN	MNDA	Myeloid cell nuclear differentiation antigen	1,94
117	P26038	MOES_HUMAN	MSN	Moesin	0,94
118	Q14764	MVP_HUMAN	MVP	Major vault protein	1,32
119	Q96S97	MYADM_HUMAN	MYADM	Myeloid-associated differentiation marker	0,80
120	P35579	MYH9_HUMAN	MYH9	Myosin-9	0,88
121	P60660	MYL6_HUMAN	MYL6	Myosin light polypeptide 6	0,68
122	Q12965	MYO1E_HUMAN	MYO1E	Unconventional myosin-Ie	0,43
123	O00160	MYO1F_HUMAN	MYO1F	Unconventional myosin-If	0,53
124	Q9NZM1	MYOF_HUMAN	MYOF	Myoferlin	2,51
125	Q15233	NONO_HUMAN	NONO	Non-POU domain-containing octamer-binding protein	0,67
126	P06748	NPM_HUMAN	NPM1	Nucleophosmin	2,02
127	Q15365	PCBP1_HUMAN	PCBP1	Poly(rC)-binding protein 1	1,22
128	Q15366	PCBP2_HUMAN	PCBP2	Poly(rC)-binding protein 2	2,75
129	Q8WUM4	PDC6I_HUMAN	PDCD6IP	Programmed cell death 6-interacting protein	1,76
130	P30101	PDIA3_HUMAN	PDIA3	Protein disulfide-isomerase A3	1,45
131	P52209	6PGD_HUMAN	PGD	6-phosphogluconate dehydrogenase, decarboxylating	0,94
132	P00558	PGK1_HUMAN	PGK1	Phosphoglycerate kinase 1	0,71
133	P35232	PHB_HUMAN	PHB	Prohibitin	1,46
134	Q99623	PHB2_HUMAN	PHB2	Prohibitin-2	1,56
135	P62136	PP1A_HUMAN	PPP1CA	Serine/threonine-protein phosphatase PP1-alpha catalytic subunit	0,61

136	Q6NYC8	PPR18_HUMAN	PPP1R18	Phostensin	0,24
137	Q06830	PRDX1_HUMAN	PRDX1	Peroxiredoxin-1	0,97
138	P78527	PRKDC_HUMAN	PRKDC	DNA-dependent protein kinase catalytic subunit	0,82
139	P26599	PTBP1_HUMAN	PTBP1	Polypyrimidine tract-binding protein 1	0,73
140	P29350	PTN6_HUMAN	PTPN6	Tyrosine-protein phosphatase non-receptor type 6	1,30
141	P61026	RAB10_HUMAN	RAB10	Ras-related protein Rab-10	1,14
142	P51148	RAB5C_HUMAN	RAB5C	Ras-related protein Rab-5C	1,08
143	P51149	RAB7A_HUMAN	RAB7A	Ras-related protein Rab-7a	0,91
144	P61006	RAB8A_HUMAN	RAB8A	Ras-related protein Rab-8A	1,02
145	Q92930	RAB8B_HUMAN	RAB8B	Ras-related protein Rab-8B	1,08
146	P63000	RAC1_HUMAN	RAC1	Ras-related C3 botulinum toxin substrate 1	0,89
147	Q9UKM9	RALY_HUMAN	RALY	RNA-binding protein Raly	1,12
148	P62826	RAN_HUMAN	RAN	GTP-binding nuclear protein Ran	0,72
149	P38159	RBMX_HUMAN	RBMX	RNA-binding motif protein, X chromosome	0,80
150	P84095	RHOG_HUMAN	RHOG	Rho-related GTP-binding protein RhoG	1,00
151	P13489	RINI_HUMAN	RNH1	Ribonuclease inhibitor	0,96
152	P62913	RL11_HUMAN	RPL11	60S ribosomal protein L11	1,42
153	P26373	RL13_HUMAN	RPL13	60S ribosomal protein L13	1,34
154	P35268	RL22_HUMAN	RPL22	60S ribosomal protein L22	0,61
155	P61254	RL26_HUMAN	RPL26	60S ribosomal protein L26	1,30
156	P62888	RL30_HUMAN	RPL30	60S ribosomal protein L30	0,94
157	Q02878	RL6_HUMAN	RPL6	60S ribosomal protein L6	1,39
158	P62917	RL8_HUMAN	RPL8	60S ribosomal protein L8	0,94
159	P05388	RLA0_HUMAN	RPLP0	60S acidic ribosomal protein P0	2,07
160	P04843	RPN1_HUMAN	RPN1	Dolichyl-diphosphooligosaccharide--protein glycosyltransferase subunit 1	2,77
161	P62277	RS13_HUMAN	RPS13	40S ribosomal protein S13	1,36
162	P62244	RS15A_HUMAN	RPS15A	40S ribosomal protein S15a	1,54
163	P62269	RS18_HUMAN	RPS18	40S ribosomal protein S18	1,17
164	P39019	RS19_HUMAN	RPS19	40S ribosomal protein S19	1,50
165	P23396	RS3_HUMAN	RPS3	40S ribosomal protein S3	1,43
166	P62701	RS4X_HUMAN	RPS4X	40S ribosomal protein S4, X isoform	1,42
167	Q9NQC3	RTN4_HUMAN	RTN4	Reticulon-4	1,77
168	Q9Y3Z3	SAMH1_HUMAN	SAMHD1	SAM domain and HD domain-containing protein 1	0,99
169	O00560	SDCB1_HUMAN	SDCBP	Syntenin-1	1,39
170	Q9NVA2	SEP11_HUMAN	SEPT11	Septin-11	0,75
171	Q15019	SEPT2_HUMAN	SEPT2	Septin-2	1,00
172	Q16181	SEPT7_HUMAN	SEPT7	Septin-7	0,81
173	Q9UHD8	SEPT9_HUMAN	SEPT9	Septin-9	0,81
174	Q15393	SF3B3_HUMAN	SF3B3	Splicing factor 3B subunit 3	0,75
175	P23246	SFPQ_HUMAN	SFPQ	Splicing factor, proline- and glutamine-rich	0,65
176	Q9BWM7	SFXN3_HUMAN	SFXN3	Sideroflexin-3	1,15
177	Q00325	MPCP_HUMAN	SLC25A3	Phosphate carrier protein, mitochondrial	1,48
178	P05141	ADT2_HUMAN	SLC25A5	ADP/ATP translocase 2	1,34
179	P12236	ADT3_HUMAN	SLC25A6	ADP/ATP translocase 3	1,33
180	Q7KZF4	SND1_HUMAN	SND1	Staphylococcal nuclease domain-containing protein 1	1,15
181	Q9Y6N5	SQRD_HUMAN	SQRDL	Sulfide:quinone oxidoreductase, mitochondrial	1,25
182	P12931	SRC_HUMAN	SRC	Proto-oncogene tyrosine-protein kinase Src	1,49
183	O60506	HNRPQ_HUMAN	SYNCRIP	Heterogeneous nuclear ribonucleoprotein Q	0,93
184	P37837	TALDO_HUMAN	TALDO1	Transaldolase	1,06
185	P29401	TKT_HUMAN	TKT	Transketolase	0,87
186	Q9Y490	TLN1_HUMAN	TLN1	Talin-1	0,90
187	P57088	TMM33_HUMAN	TMEM33	Transmembrane protein 33	1,41
188	P60174	TPIS_HUMAN	TPI1	Triosephosphate isomerase	0,59
189	Q13263	TIF1B_HUMAN	TRIM28	Transcription intermediary factor 1-beta	0,70
190	Q9P0L0	VAPA_HUMAN	VAPA	Vesicle-associated membrane protein-associated protein A	1,65
191	P50552	VASP_HUMAN	VASP	Vasodilator-stimulated phosphoprotein	0,32
192	Q99536	VAT1_HUMAN	VAT1	Synaptic vesicle membrane protein VAT-1 homolog	1,26
193	P18206	VINC_HUMAN	VCL	Vinculin	0,66
194	P55072	TERA_HUMAN	VCP	Transitional endoplasmic reticulum ATPase	0,91
195	P21796	VDAC1_HUMAN	VDAC1	Voltage-dependent anion-selective channel protein 1	0,99
196	P45880	VDAC2_HUMAN	VDAC2	Voltage-dependent anion-selective channel protein 2	1,38
197	P08670	VIME_HUMAN	VIM	Vimentin	1,05
198	O75083	WDR1_HUMAN	WDR1	WD repeat-containing protein 1	0,42
199	P13010	XRCC5_HUMAN	XRCC5	X-ray repair cross-complementing protein 5	0,73
200	P12956	XRCC6_HUMAN	XRCC6	X-ray repair cross-complementing protein 6	0,81
201	P61981	1433G_HUMAN	YWHAG	14-3-3 protein gamma	0,70
202	P63104	1433Z_HUMAN	YWHAZ	14-3-3 protein zeta/delta	0,68
203	Q15942	ZYX_HUMAN	ZYX	Zyxin	0,53

Known podosome components	SILAC datasets and relative ratios						Podosome consensus
	I	Intensity ratio (R)	II	Intensity ratio (R)	III	Intensity ratio (R)	I ∩ II ∩ III overlap
PODOSOME CORE							
α-actinin	ACTN1	0,75	ACTN1	0,74	ACTN1	0,34	ACTN1
	ACTN3	**n.d.**					
	ACTN4	**n.d.**	ACTN4	0,95	ACTN4	0,27	
ADAMs			ADAM10	**n.d.**			
AFAP-110							
Arf6	ARF6	**n.d**	ARF6	0,86	ARF6	**n.d**	
Arp2/3 complex	ARPC1B	0,59	ARPC1B	0,54	ARPC1B	0,92	ARPC1B
	ARPC2	0,54	ARPC2	0,59	ARPC2	0,44	ARPC2
	ARPC3	0,52	ARPC3	0,66	ARPC3	0,44	ARPC3
	ARPC4	0,58	ARPC4	0,69	ARPC4	0,40	ARPC4
	ARPC5	0,53	ARPC5	0,77	ARPC5	0,52	ARPC5
	ACTR2	0,62	ACTR2	0,72	ACTR2	1,53	ACTR2
	ACTR3	0,61	ACTR3	0,72	ACTR3	0,59	ACTR3
ASAP1/AMAP1					ASAP1	0,72	
β-Dystroglycan							
Caldesmon							
Calponin			CNN2	**n.d**	CNN2	0,08	
CD44	CD44	1,10	CD44	1,21	CD44	0,78	CD44
CDC42	CDC42	**n.d**	CDC42	0,87	CDC42	1,01	
Cofilin	CFL1	0,54	CFL1	0,42	CFL1	0,17	CFL1
Coronin	CORO1A	0,99	CORO1A	0,17	CORO1A	0,10	CORO1A
	CORO1B	0,39	CORO1B	0,41	CORO1B	0,26	CORO1B
	CORO1C	0,53	CORO1C	0,52	CORO1C	0,24	CORO1C
					CORO7	0,50	
Cortactin (=EMS1)	CTTN	**n.d**	CTTN	**n.d**	CTTN	0,22	
Csk					CSK	**n.d.**	
Dynamin 2	DNM2	1,27	DNM2	1,03	DNM2	0,33	DNM2
Endophilin 2							
Eps8							
ERK1/2							
Ezrin	EZR	1,47	EZR	0,87	EZR	0,86	EZR
F-actin	ACTC1	0,43	ACTC1	0,32	ACTC1	0,69	ACTC1
			ACTG1	0,30	ACTG1	0,53	
Fascin	FSCN1	**n.d**	FSCN1	**n.d**			
FBP17 (formin-binding protein)							
Fimbrin (L-Plastin)	LCP1	0,73	LCP1	0,89	LCP1	0,23	LCP1
Gelsolin	GSN	0,89	GSN	1,23	GSN	1,52	GSN
Integrin αxβ2	ITGAX	0,82	ITGAX	1,36	ITGAX	1,54	ITGAX
Integrin β1							
Leupaxin	LPXN	**n.d**					
MMP-2							
MMP-9	MMP-9	**n.d**			MMP-9	**n.d**	
MT1-MMP							
Myosin I					MYO1B	0,88	
			MYO1C	0,61	MYO1C	0,91	
	MYO1E	0,24	MYO1E	0,45	MYO1E	0,61	MYO1E
	MYO1F	0,41	MYO1F	0,45	MYO1F	0,73	MYO1F
	MYO1G	**n.d**	MYO1G	0,22			
N-WASP							
p130Cas							
p190RhoGAP							
PAK4							
Palladin					PALLD	0,49	
PKC µ							

Supplementary table 2

Protein							
Profilin	PFN1	0,97	PFN1	0,37	PFN1	**n.d**	
PTP-PEST	PTPN6	0,97	PTPN6	1,11	PTPN6	1,84	PTPN6
RHAMM							
SHIP					SHIP	**n.d.**	
SM22α/Transgelin	TAGLN2	**n.d**	TAGLN2	0,31	TAGLN2	0,06	
STAT3							
Syk			SYK	1,06	SYK	0,82	
Tks4							
Tks5/Fish							
VASP	VASP	0,42	VASP	0,40	VASP	0,14	VASP
	EVL	0,34	EVL	0,42	EVL	0,12	EVL
Vimentin	VIM	0,98	VIM	1,06	VIM	1,10	VIM
WASp					WAS	**n.d**	
	WAVE2	**n.d**			WAVE2	0,97	
WIP					WIP	**n.d**	
PODOSOME RING							
α-actinin	ACTN1	0,75	ACTN1	0,74	ACTN1	0,34	ACTN1
	ACTN3	**n.d.**					
			ACTN4	0,95	ACTN4	0,27	
α-PIX							
c-src	SRC	1,74	SRC	1,50	SRC	1,23	SRC
Csk					CSK	**n.d.**	
Filamin	FLNA	0,63	FLNA	0,77	FLNA	0,55	FLNA
	FLNB	**n.d.**			FLNB	0,78	
Gelsolin	GSN	0,89	GSN	1,23	GSN	1,52	GSN
Kindlin-3 (FERM3)	FERMT3	0,91	FERMT3	1,10	FERMT3	1,23	FERMT3
Integrin $\alpha_M\beta_2$			ITGAM	0,30	ITGAM	1,68	
Integrin $\alpha_V\beta_3$	ITGAV	**n.d.**					
Integrin β_2	ITGB2	1,29	ITGB2	0,83	ITGB2	1,39	ITGB2
Integrin β_3							
Myosin IIA (non-muscle)	MYH9	0,94	MYH9	0,76	MYH9	0,92	MYH9
p130Cas							
Paxillin							
PI3K							
PKC α							
Plectin	PLEC	0,77	PLEC	1,02			
PTP-PEST	PTPN6	0,97	PTPN6	1,11	PTPN6	1,84	PTPN6
Pyk2							
RHAMM							
Spectrin					SPTA2	0,72	
					SPTB2	0,82	
Talin	TLN1	1,32	TLN1	0,88	TLN1	0,49	TLN1
Tensin	TNS3	**n.d.**			TNS3	1,44	
Tropomyosin	TPM3	**n.d.**	TPM3	0,83	TPM3	0,60	
	TPM4	**n.d.**	TPM4	1,01	TPM4	0,69	
TRPM7							
Vinculin	VCL	1,29	VCL	0,56	VCL	0,15	VCL
ZO-1							
Zyxin	ZYX	0,52	ZYX	0,91	ZYX	0,15	ZYX
PODOSOME CAP							
FMNL1 (formin-like)	FMNL1	**n.d.**	FMNL1	**n.d.**	FMNL1	**n.d.**	
Supervillin					SVIL	**n.d.**	

Supplementary table 3

Overlap lists		
Podosome consensus / Focal adhesome (Suppl. Fig. 2B, C)	**Podosome consensus / Invadopodia (Suppl. Fig. 2B, D)**	**Podosome consensus / SICs (Suppl. Fig. 2C, D)**
Alpha-actinin-1	Actin-related protein 3	Actin, alpha cardiac muscle 1
Actin-related protein 2/3 complex subunit 2	Gelsolin	Filamin-A
Cofilin-1	Vimentin	Myosin-9 (Non-muscle myosin heavy chain IIa)
Dynamin-2		Talin-1
Ezrin		Vinculin
Filamin-A		Vimentin
PTPN6		
SRC		
Talin-1		
VASP		
Vinculin		
Vimentin		
Zyxin		
SILAC consensus / Focal adhesome (Fig. 7A, B)	**SILAC consensus / Invadopodia (Fig. 7A, C)**	**SILAC consensus / SICs (Fig. 7B, C)**
Alpha-actinin-1	Actin-related protein 3	Actin, alpha cardiac muscle 1
Actin-related protein 2/3 complex subunit 2	Annexin A5	ATP synthase subunit beta, mitochondrial
Cofilin-1	ATP synthase subunit alpha, mitochondrial	ATP-dependent RNA helicase DDX3X
Cysteine and glycine-rich protein 1	Elongation factor 2	Elongation factor 1-alpha 1
Dynamin-2	Alpha-enolase	Alpha-enolase
Ezrin	G6PD	Filamin-A
Filamin-A	Gelsolin	RNA-binding protein FUS
LASP1	HNRNPK	Trifunctional enzyme subunit beta, mitochondrial
PTPN6	Heat shock protein HSP 90-beta	HNRNPH1
RAC1	Endoplasmin	HNRNPK
Syntenin-1	Heat shock cognate 71 kDa protein	HNRNPM
SRC	Stress-70 protein, mitochondrial	78 kDa glucose-regulated protein
Talin-1	Nucleophosmin	Heat shock cognate 71 kDa protein
VASP	Protein disulfide-isomerase A3	L-lactate dehydrogenase A chain
Vinculin	Prohibitin	Prelamin-A/C
Vimentin	Septin-2	Major vault protein
Zyxin	Triosephosphate isomerase	Myosin-9 (Non-muscle myosin heavy chain IIa)
	Vimentin	Myosin light polypeptide 6
	WDR1	Non-POU domain-containing octamer-binding protein
		Protein disulfide-isomerase A3
		Peroxiredoxin-1
		Polypyrimidine tract-binding protein 1
		RPL11
		RPL13
		RPL22
		RPL26
		RPL6
		RPL8
		RPS15A
		RPS19
		Splicing factor, proline- and glutamine-rich
		ADP/ATP translocase 2
		Heterogeneous nuclear ribonucleoprotein Q
		Talin-1
		Synaptic vesicle membrane protein VAT-1 homolog
		Vinculin

Supplementary table 3

		Vimentin
		X-ray repair cross-complementing protein 5
		X-ray repair cross-complementing protein 6
		14-3-3 protein zeta/delta

Unique overlap lists		
SILAC consensus / expected focal adhesome	**SILAC consensus / Invadopodia**	**SILAC consensus / SICs**
Alpha-actinin-1	(Actin-related protein 3)	(Actin, alpha cardiac muscle 1)
Actin-related protein 2	(Annexin A5)	ATP synthase subunit beta, mitochondrial
Neuroblast differentiation-associated protein AHNAK	ATP synthase subunit alpha, mitochondrial	ATP-dependent RNA helicase DDX3X
Annexin A1	Elongation factor 2	Elongation factor 1-alpha 1
Actin-related protein 2/3 complex subunit 1B	G6PD	RNA-binding protein FUS
Actin-related protein 2/3 complex subunit 2	(Gelsolin)	Trifunctional enzyme subunit beta, mitochondrial
Actin-related protein 2/3 complex subunit 3	Heat shock protein HSP 90-beta	HNRNPH1
Actin-related protein 2/3 complex subunit 5	(Endoplasmin)	HNRNPM
Adenylyl cyclase-associated protein 1	(Stress-70 protein, mitochondrial)	(78 kDa glucose-regulated protein)
CD44	(Nucleophosmin)	L-lactate dehydrogenase A chain
Cofilin-1	Prohibitin	Prelamin-A/C
Clathrin heavy chain 1	Septin-2	Major vault protein
Coronin-1B	Triosephosphate isomerase	Myosin-9 (Non-muscle myosin heavy chain Iia)
Coronin-1C	WDR1	Myosin light polypeptide 6
Cysteine and glycine-rich protein 1		Non-POU domain-containing octamer-binding protein
Cytoplasmic FMR1-interacting protein 1		Peroxiredoxin-1
Dynamin-2		Polypyrimidine tract-binding protein 1
(Ezrin)		RPL11
Ras GTPase-activating-like protein IQGAP1		RPL13
LASP1		(RPL22)
Moesin		RPL26
Poly(rC)-binding protein 2		(RPL6)
Programmed cell death 6-interacting protein		(RPL8)
(PTPN6)		RPS15A
RAB10		(RPS19)
RAC1		Splicing factor, proline- and glutamine-rich
RHOG		ADP/ATP translocase 2
RPL30		Heterogeneous nuclear ribonucleoprotein Q
RPLP0		Synaptic vesicle membrane protein VAT-1 homolog
RPS13		X-ray repair cross-complementing protein 5
RPS18		X-ray repair cross-complementing protein 6
RPS3		(14-3-3 protein zeta/delta)
RPS4X		
(Syntenin-1)		
(SRC)		
VASP		
14-3-3 protein gamma		
Zyxin		

Lymphocyte-specific protein 1 regulates mechanosensory oscillation of podosomes and actin isoform-based actomyosin symmetry breaking

Pasquale Cervero [1], Christiane Wiesner[1], Anais Bouissou[2], Renaud Poincloux [2] & Stefan Linder [1]

Subcellular fine-tuning of the actomyosin cytoskeleton is a prerequisite for polarized cell migration. We identify LSP (lymphocyte-specific protein) 1 as a critical regulator of actomyosin contractility in primary macrophages. LSP1 regulates adhesion and migration, including the parameters cell area and speed, and also podosome turnover, oscillation and protrusive force. LSP1 recruits myosin IIA and its regulators, including myosin light chain kinase and calmodulin, and competes with supervillin, a myosin hyperactivator, for myosin regulators, and for actin isoforms, notably β-actin. Actin isoforms are anisotropically distributed in myosin IIA-expressing macrophages, and contribute to the differential recruitment of LSP1 and supervillin, thus enabling an actomyosin symmetry break, analogous to the situation in cells expressing two myosin II isoforms. Collectively, these results show that the cellular pattern of actin isoforms builds the basis for the differential distribution of two actomyosin machineries with distinct properties, leading to the establishment of discrete zones of actomyosin contractility.

[1] Institut für Medizinische Mikrobiologie, Virologie und Hygiene, Universitätsklinikum Eppendorf, Martinistr. 52, 20246 Hamburg, Germany. [2] Institut de Pharmacologie et Biologie Structurale, IPBS, CNRS, UPS, Université de Toulouse, 205 route de Narbonne, 31077, Toulouse BP64182, France. Correspondence and requests for materials should be addressed to S.L. (email: s.linder@uke.de)

46

Macrophages constitute a crucial part of the innate immune system and are involved in counteracting infections and maintaining tissue homeostasis[1]. The ability of macrophages to migrate and to invade the extracellular matrix (ECM)[2] is based on their adaptable morphology[3], and the local degradation of matrix components[4]. Both functions are regulated by the actin cytoskeleton, especially by actomyosin-based contractility. To induce polarized migration, a break in cellular symmetry, especially in the pattern of actomyosin activity, is necessary. This can include differential recruitment of myosin isoforms, such as myosin IIA and IIB[5] or local relaxation of the actomyosin cortex[6]. However, as macrophages express predominantly myosin IIA[7], the respective mechanism is unclear.

A symmetry break in macrophages involves reorganization of the actin cytoskeleton, notably the recruitment of podosomes to the leading edge. Podosomes constitute prominent actomyosin-based organelles of the cell cortex, in monocytic cells such as macrophages[8], immature dendritic cells[9] and osteoclasts[10], and also in endothelial[11], smooth muscle[12] and neural crest cells[13]. Podosomes feature an extensive repertoire of functions such as cell–matrix adhesion, extracellular matrix degradation, topography and rigidity sensing, and others, which makes them crucial regulators of macrophage migration and invasion[14].

Podosomes contain an F-actin-rich core, surrounded by a ring of adhesion plaque proteins such as talin[15] or vinculin[16]. Both substructures are anchored to the ECM by transmembrane proteins such as CD44[17] and integrins[18]. Unbranched lateral actin filaments surround the podosome core[19], while a second set of unbranched actin filaments connects podosomes into higher-ordered clusters[19,20]. Recent research points to the existence of a cap structure on top of the podosome[14]. Identified cap components comprise the formins FMNL1[21] and INF2[22], and also supervillin[20], a member of the villin family. Supervillin forms a hub for actomyosin[23] at the cell cortex, by binding directly to myosin IIA and actin through regions within its N-terminal half[23,24], and to myosin regulators such as the long form of myosin light chain kinase (L-MLCK)[25]. Supervillin is a myosin IIA hyperactivator, as it binds activated myosin and also induces activation, leading to a feed-forward cycle and to podosome dissolution[20].

We now identify leukocyte-specific protein 1 (LSP1) as a myosin IIA-associated regulator of macrophage migration and invasion, and a novel component of the podosome cap. LSP1 is recognized as a regulator of immune cell migration in inflammation and phagocytosis[26,27], with aberrant LSP1 overexpression in neutrophil actin dysfunction (NAD47/89) leading to reduced motility of neutrophils and severe recurrent infections[28–31], and LSP1 deficiency leading to enhanced T cell migration, contributing to the development of rheumatoid arthritis[32]. However, LSP1´s molecular modes of action, and its interplay with other regulators of the actomyosin cortex are unclear. We now show that LSP1 interacts with actin, myosin IIA, and specific regulators of myosin activity, including L-MLCK and calmodulin. Importantly, LSP1 competes with supervillin for binding of these regulators in cells, leading to the formation of distinct zones of myosin contractility.

We further show that differential recruitment of LSP1 and supervillin correlates with the subcellular patterning of actin isoforms. Mammalian cells can express several of up to six actin isoforms that are grouped into three clusters, comprising α-skeletal muscle, α-smooth muscle and α-cardiac actin, β-cytoplasmic actin, as well as γ-smooth muscle and γ-cytoplasmic actin[33,34], with the α/β/γ isoform designation based on variant electrophoretic mobility, due to the number and type of acidic residues in their N-termini[35]. Studies from knock out mice indicated that, despite overlapping functions,

actin isoforms can not fully compensate for each other[33,34]. In consequence, impairment of specific isoforms can lead to pathologies, such as hearing loss, based on compromised stereocilia maintenance in the case of γ-cytoplasmic actin[36]. Actin isoform function has been speculated to involve differential binding of specific interaction partners, such as cofilin[37] or profilin[38]. Moreover, actin isoforms were shown to be differentially distributed, for example β- and γ-cytoplasmic actin in fibroblasts and endothelial cells[39]. However, the validity of both concepts is under discussion.

Our data provide a molecular explanation for the reported effects of LSP1 in immune cell dysregulation. We also show how competitive binding for actin isoforms and myosin regulators between LSP1 and supervillin, two actomyosin modulators with different activity, can lead to an actomyosin symmetry break and enable polarized migration of immune cells.

Results

LSP1 is enriched at podosomes and the macrophage leading edge. A proteomic screen of podosome-enriched fractions of primary human macrophages pointed to LSP1 as a potential new podosome component (Supplementary Fig. 1A)[40]. This was confirmed by staining of endogenous LSP1, F-actin and vinculin (Fig. 1a–d). Z-sections showed that LSP1 forms a cap structure on top of the core that extends along the sides of the podosome, thus partially overlapping with both core and ring (Fig. 1a′–d′), depending on the plane of imaging (Fig. 1d′, e). To analyse LSP1 localization at higher resolution, macrophages were stained for LSP1 and F-actin and analysed by STED (stimulated emission depletion) microscopy (Supplementary Fig. 1B–D). Z-sections (Supplementary Fig. 1E) and 3D reconstructions (Fig. 1f) confirmed that LSP1 is enriched at the podosome cap and also at lateral fibers.

Macrophages harbour two subpopulations of podosomes, larger and highly dynamic precursors at the cell periphery and the leading edge[41], and smaller successors at the inner region of cells[20]. Consistent with its general enrichment at the cell periphery, LSP1 localized mostly at precursors, and to a lesser degree at successors in migrating cells (Supplementary Fig. 1F–J). Analysis of the respective LSP1/F-actin intensity confirmed that LSP1 is especially enriched in a 5–10 µm wide zone at the cell periphery in both resting and migratory macrophages (Supplementary Fig. 1K–M). This preferential enrichment at the cell periphery was also observed in live cell analysis of resting macrophages coexpressing GFP-LSP1 and lifeact-RFP (Supplementary Fig. 2A–L). Interestingly, GFP-LSP1 and lifeact-RFP followed similar dynamics during formation and dissolution of single podosomes (Supplementary Fig. 2M–O).

To identify the domains of LSP1 that determine its subcellular localization, GFP-fused deletion constructs were created, comprising constructs containing only the N-terminal half ("N-terminal"), only the C-terminal half ("C-terminal"), only the caldesmon-like domains ("C1C2"), and only the villin headpiece-like domains ("V1V2") (Fig. 1g). Confocal analysis (Supplementary Fig. 3A–O) showed that the C-terminal half of LSP1 (Supplementary Fig. 3G–I), and especially the villin headpiece-like domains (Supplementary Fig. 3M–O), determine LSP1's localization to podosomes and to the actin cortex.

LSP1 depletion enhances dynamics of podosomes and cells. SiRNA-targeting of LSP1 led to depletion of 48 and 56% for two individual sequences (Supplementary Fig. 4A). Side-by-side stainings of cells treated with LSP1-specific or control siRNA showed that these reductions were also visible on the single cell-level, while the ability for podosome formation was not impaired

(Supplementary Fig. 4B–G). Podosome dynamics were analysed by confocal live cell imaging of cells expressing lifeact-RFP. Each frame of a respective video (1 h duration) was color coded for time, moving structures thus appear in multiple colors, while static ones are white. Accordingly, stationary macrophages treated with control siRNA showed mostly podosomes in white, while migrating cells showed progressive coloration of podosome clusters from the trailing to the leading edge, consistent with dissolution of podosomes in the back, and formation of new podosomes at the front (Fig. 2a). Strikingly, cells treated with
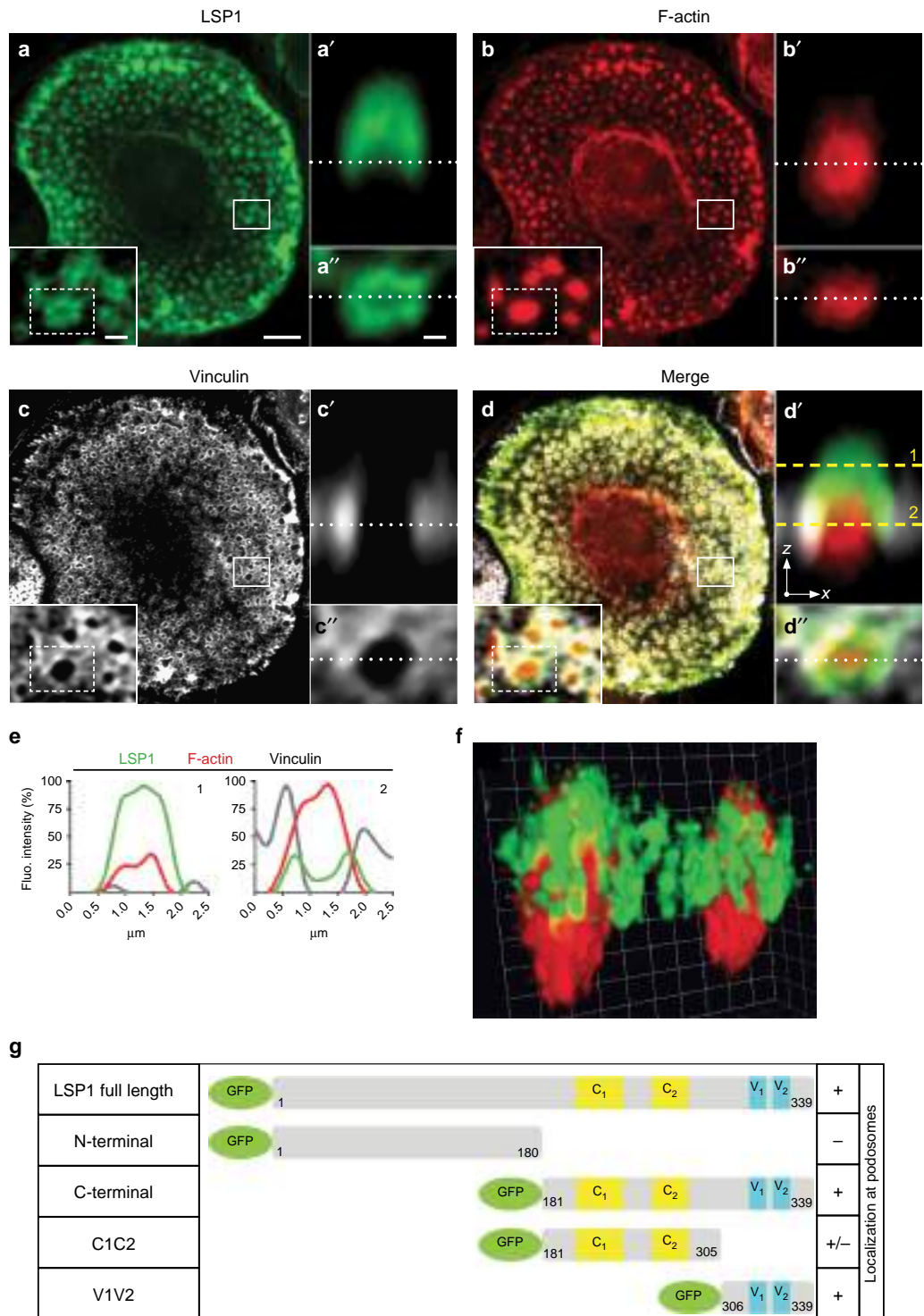
LSP1-specific siRNA showed strongly enhanced dynamics of podosome clusters (Fig. 2b, c). Podosome clusters, tracked by their centers of mass, were mostly static or showed persistent trajectories in controls (Fig. 2d), whereas clusters in cells treated with LSP1 siRNA were highly motile and showed non-directional trajectories (Fig. 2e, f), accompanied by an increased velocity of clusters in cells treated with LSP1 siRNA ($0.87 \pm 0.12\,\mu m/min$ and $0.73 \pm 0.1\,\mu m/min$), corresponding to a relative increase of 281 and 236% (Fig. 2g).

Live cell analyses showed that podosomes in LSP1 siRNA-treated cells have reduced lifetimes (6.6 ± 0.5 min and 6.6 ± 0.3 min; "$\pm$" indicating s.e.m.), compared to controls (9.9 ± 0.6 min), corresponding to a reduction of 33% (Fig. 2h), which was based on a general shift to shorter life times (Fig. 2i). Of note, macrophages transfected with LSP1-specific siRNA often showed longer trajectories (Fig. 2j–l), based on an increase (38 and 46%) of cell speed ($0.33 \pm 0.05\,\mu m/min$ and $0.35 \pm 0.05\,\mu m/min$ for LSP-1 siRNA vs. $0.24 \pm 0.02\,\mu m/min$ for controls) (Fig. 2m), while net displacement of cells was not significantly altered. Interestingly, LSP1 knockdown also led to a pronounced increase (53 and 90%) in cell area ($2226 \pm 209\,\mu m^2$ and $2771 \pm 307\,\mu m^2$ for LSP1 siRNA vs. $1456 \pm 83\,\mu m^2$ for controls), pointing to a role of LSP1 in cortex stabilization and/or contractility (Fig. 2n).

To further evaluate changes in podosome distribution upon LSP1 knockdown, cells were scored in groups, according to evenly spaced distribution of podosomes ("uniform"), recruitment of podosomes to a single leading edge ("polarized") and formation of clusters ("clusters"). In line with live cell imaging observations (Fig. 2a–c), LSP1 knockdown cells showed prominent formation of podosome clusters ($40.2 \pm 6.3\%$ and $48.2 \pm 5.2\%$ for LSP1 siRNAs vs. $19.1 \pm 7.1\%$ for controls) (Fig. 2o). To assess changes in overall cell morphology, cells were evaluated for circularity, a measure for equidistance of all points on the cell perimeter to the center, and also for aspect ratio, a measure for cell elongation, by determining the ratio of longest versus shortest axis[42] (see Materials). Frequency distribution analysis showed that aspect ratio was enhanced in LSP1 knockdown cells, with ~40–50% of cells showing values between 1.5 and 2.5, compared to ~20% of controls (Fig. 2p), while circularity was strongly decreased, with ~20% of LSP1 knockdown cells showing values between 0.85 and 0.95, compared to ~60% of controls (Fig. 2q). Scatter plots of both values (Fig. 2r) further showed that only ~20% of control cells displayed extreme values, for aspect ratio above 1.3, and for circularity below 0.8 (Fig. 2s), in contrast to ~60% of LSP1 knockdown cells (Fig. 2t–w). Collectively, these data indicate that LSP1 knockdown macrophages were more elongated and less circular. Moreover, they also showed an increased tendency to deviate from the inverse correlation between aspect ratio and circularity observed in control cells (Fig. 2s–u), indicating an uncoupling of localized cell protrusion and overall cell polarization.

To investigate subcellular localization of LSP1 in a 3D context, macrophages expressing LSP1-GFP and Lifeact-RFP were embedded in 3D collagen gels and analysed by confocal microscopy. LSP1-GFP was strongly enriched in F-actin-rich protrusions (Supplementary Fig. 5A–C), pointing to a potential role of LSP1 also in macrophage invasion. To test this, invasion was analysed in a collagen plug invasion assay[4] (Supplementary Fig. 5D–F). The invaded area was comparable for cells treated with LSP1-specific and control siRNA (Supplementary Fig. 5H). However, the number of invading cells was increased in case of LSP1 depletion ($166 \pm 13\%$ for siRNA1, $150 \pm 4\%$ for siRNA2, compared to controls; Supplementary Fig. 5G), showing that LSP1 also has a regulatory role in 3D invasion of macrophages.

LSP1 regulates oscillatory protrusion of podosomes. Podosomes are contractile organelles, with growth of the Arp2/3 complex-generated actin core[43] exerting forces on the formin-based lateral actin cables[22,44], and mechanical coupling of both systems enabling protrusion into the matrix[45–48]. To analyse the impact of LSP1 on podosome protrusion, F-actin levels at podosomes were measured in a confocal plane over time. As reported for dendritic cells[49], Lifeact-RFP-based fluorescence of individual podosomes varied in an oscillatory fashion, indicating podosome movement in the Z axis (Fig. 3a, a′, c). Overexpression of LSP1-GFP (Fig. 3b, b′, d) led to an increased number (by 49%) of local peaks (4.3 ± 0.2 for LSP1-GFP cells, vs. 2.9 ± 0.1 for controls) (Fig. 3e), while peak height was only slightly reduced (by 15%) (17.4 ± 1.0 for LSP1-GFP cells, vs. 20.5 ± 1.0 for controls) (Fig. 3f), and the frequency distribution of peak height was slightly shifted to smaller values (Fig. 3g). In contrast, depletion of LSP1 (Fig. 3i, i′, k) led only to a slight decrease (by 17%) in the number of local peaks (2.6 ± 0.2 for LSP1 siRNA cells, vs. 3.1 ± 0.1 for controls) (Fig. 3l), while peak height was strongly increased (by 53%) (32.8 ± 2.3 for LSP1 siRNA cells, vs. 21.4 ± 1.3 for controls) (Fig. 3m), and the frequency distribution of peak height showed broader deviation from control values, towards higher maximal values, indicative of a pronounced irregularity in peak height (Fig. 3n).

To measure the forces podosomes impose on the matrix, protrusion force microscopy was used. This technique applies atomic force microscopy to cells that are seeded on pliable membrane sheets (Fig. 3o)[48]. Protrusion force was determined for macrophages treated 4 days previously with LSP1-specific siRNA or control siRNA. Cells treated with LSP1 siRNA showed a 32% reduction of the evaluated protrusion force (1.7 ± 0.2 nN), compared to controls (2.5 ± 0.2 nN) (Fig. 3p). Collectively, these results show that LSP1 is a crucial regulator of mechanosensory oscillation of podosomes, ensuring both the regularity of this process and also the generation of protrusive force.

LSP1 recruits myosin IIA to the cell cortex and to podosomes. The influence of LSP1 on podosome dynamics and function, both of which are based on actomyosin contractility[48–50], pointed

Fig. 1 LSP1 is a component of the podosome cap structure. **a–d** Confocal micrographs of a macrophage stained for LSP1 using specific primary antibody and Alexa 488-labeled secondary antibody (**a**, green), for F-actin using Alexa405-labeled phalloidin (**b**, red), and for vinculin using specific primary antibody and Alexa568-labeled secondary antibody (**c**, white), with merge (**d**). White boxes in **a–d** indicate detail images shown as insets. Dashed boxes in insets indicate single podosome shown in x–z section in **a′–d′** and in x–y section in **a″–d″** with respective cross-section planes shown as white dotted lines. Dashed yellow lines in **d′** indicate confocal planes used for measurements of respective fluorescence intensities shown in **e**. Note the cap-like localization of LSP1 on top of the F-actin core (1), which can appear ring-like in a lower optical section (2) Scale bars: 5 μm in **a–d**, 1 μm in insets, 0.5 μm in **a″–d″**. **f** 3D reconstruction of two podosomes from STED micrographs macrophages stained for LSP1 (green) and F-actin (red), scale unit: 0.25 μm. See also Supplementary Movie 1. **g** Domain structure of LSP1 full length and deletion mutants. LSP1 features an acidic N-terminal half containing a hypothetical Ca^{2+} binding domain, two caldesmon-like F-actin binding domains (C1, C2) and two villin-headpiece-like F-actin binding domains (V1, V2). First and last amino acid residues are indicated. "+" and "−" indicate the presence or absence of the respective construct at podosomes
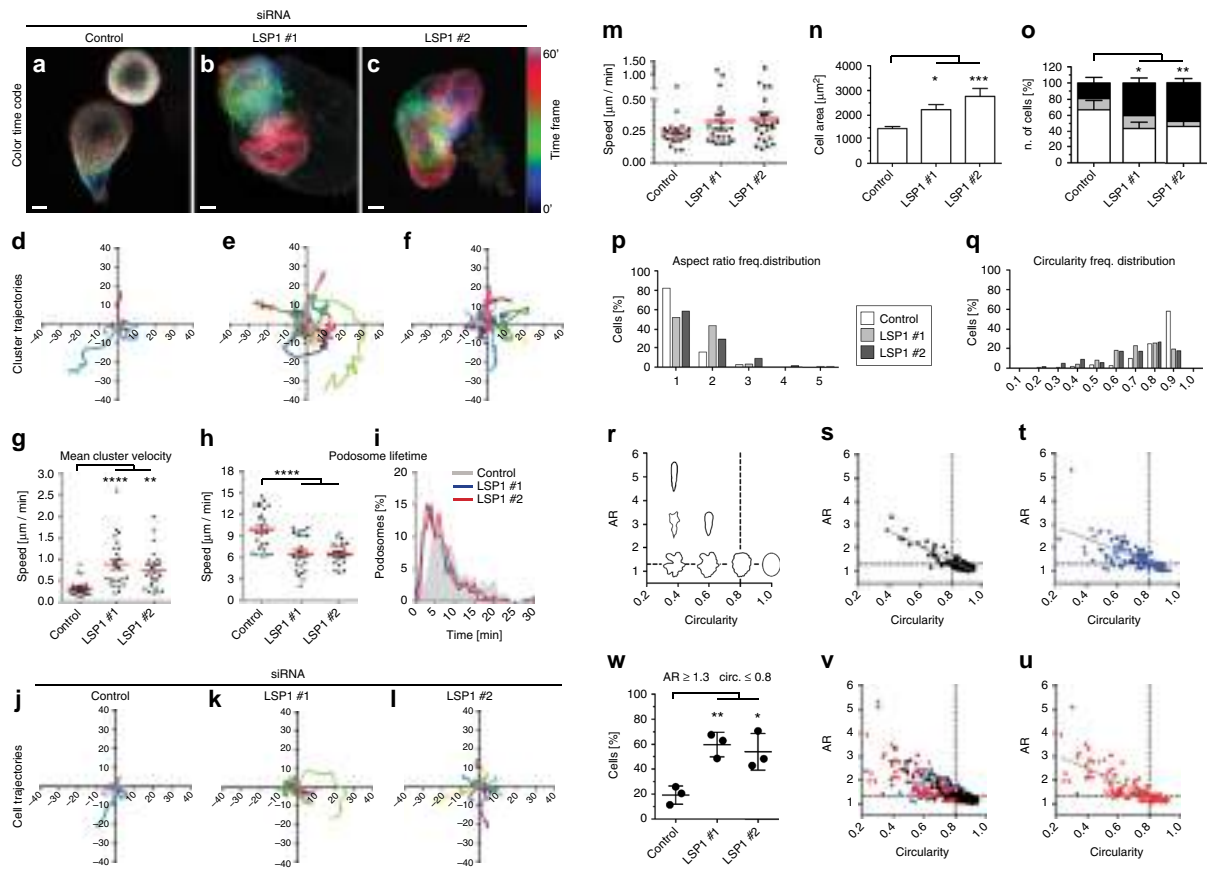
49

Fig. 2 LSP1 depletion leads to enhanced dynamics of podosomes, podosome clusters and cells. **a**–**c** Still images from confocal time lapse videos, frames were progressively colored along the spectrum, with final merges presented. Scale bars: 10 μm. See Supplementary Movies 2–4. **d**–**f** Colored lines track centers of mass of podosome clusters from cells of four different donors. Axes indicate relative position in μm. **g** Velocity of podosome clusters (μm min^{-1}), in 24 cells from four different donors. Dots represent mean cluster velocity of single cells. **h**, **i** Podosome lifetime, with 240 podosomes evaluated per condition. Dots in **h** represent mean values of 10 podosomes in single cells. **i** Frequency distribution of podosome lifetime. **j**–**l** Coloured lines track centers of mass of cells from four different donors. Axes indicate relative position in μm. **m**, **n** Graphs show speed (μm min^{-1}) (**m**), or total area (μm^2) (**n**) of cells treated with indicated siRNAs. Dots represent mean value of single cells (n = 24), each bar represents mean value of 24 cells from four different donors. **o**–**w** Cell morphology in control and LSP1 knockdown cells. **o** Podosome distribution, with cells scored in groups, according to even distribution (white), recruitment of podosomes to single leading edge (grey) and formation of clusters (black). Values represent the percentage of at least 50 cells per donor (N = 3). **p**, **q** Frequency distribution for aspect ratio (**p**) or circularity (**q**), with 123 cells from three different donors evaluated. **r**–**v** Scatter plots of circularity (x-axes) and aspect ratio (y-axes), with schematic graph depicting respective cell shapes (**r**), and plots for cells treated with control siRNA (**s**), LSP1-specific siRNAs (**t**, **u**), and merge (**v**). Cut-off values of 1.3 for aspect ratio and 0.8 for circularity: dashed lines, regression line in grey. Dots represent single cells (N = 123) from three donors. (**w**) Percentage of cells showing aspect ratio ≥1.3 and circularity ≤0.8. Dots represent mean percentages calculated with at least 35 cells per donor (N = 3). **a**–**w** Treatment with specific siRNAs is indicated. Values are given as mean ± s.e.m. Statistical test: one-way ANOVA. *P < 0.05, **P < 0.01, ***P < 0.001, ****P < 0.0001. For specific values, see Supplementary Data 1

to a functional connection between LSP1 and myosin IIA, the predominant form of myosin in macrophages[7] and at podosomes[20,51]. Fluorescence intensity measurements of F-actin at podosome cores (Fig. 4b, d) and myosin IIA levels at regions surrounding and including podosomes cores (Fig. 4a, c) showed a reduction of myosin IIA, but not of F-actin levels, for LSP1 siRNA-treated cells (myosin IIA intensity of LSP1-siRNA treated cells: 31.8 ± 16.3 and 35.9 ± 11.9 %, vs. 54.1 ± 21.3 for controls) (Fig. 4e, f), with measured areas being comparable between treatments (Fig. 4g, h).

To test a potential interaction between LSP1 and myosin IIA, and to determine the respective subcellular sites, proximity ligation assays (PLA) were performed, which report close spatial proximity (<40 nm) between two proteins. Control cells showed

PLA background levels (2.4 ± 0.4 spots per cell; Fig. 4i–l), whereas cells stained with LSP1 and myosin IIA-specific antibodies showed a strong increase in PLA spots (73 ± 7.8 spots per cell; Fig. 4m–o, l), with respective areas being comparable (Fig. 4p). PLA signals were enriched at the cell periphery, where precursor podosomes are located[41], and at the cell cortex. Similar results were gained with a PLA analysis of LSP1 and pan-actin, indicating interaction of LSP1 and actin especially in the cell periphery (Supplementary Fig. 6A–H). STED microscopy (Supplementary Fig. 6K–N) confirmed the close spatial proximity of myosin IIA and LSP1 in the cell periphery. Of note, podosomes in this zone showed colocalizing pixels especially at their periphery-facing side (Supplementary Fig. 6M), and LSP1 and myosin IIA colocalized at discrete spots along the whole podosome cap

50
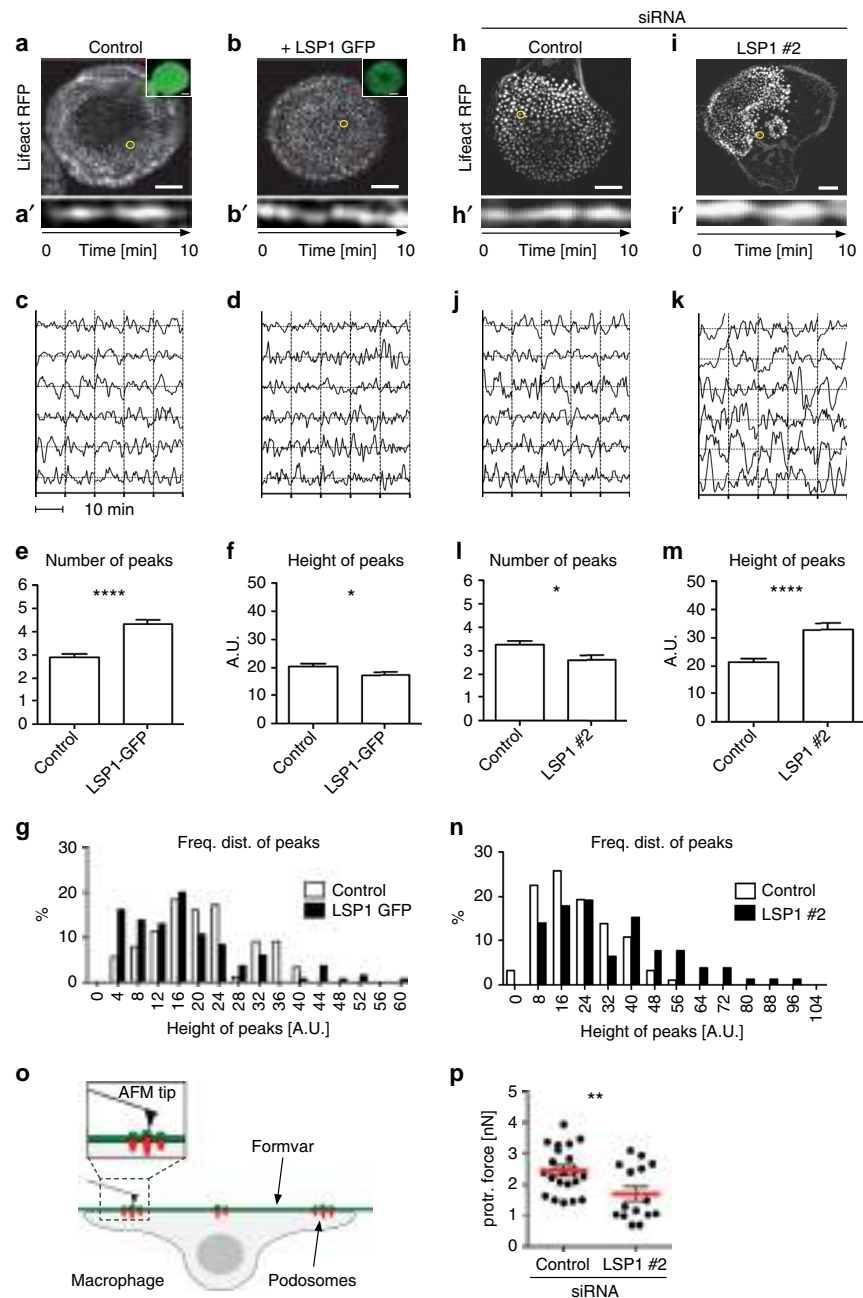
Fig. 3 LSP1 is a regulator of oscillatory podosome protrusion. **a**, **b**, **h**, **i** Podosome oscillation, determined by F-actin intensity measurements. Confocal micrographs of cells expressing lifeact-RFP and coexpressing EGFP (**a**) or LSP1-GFP (**b**), the latter shown as small insets in green, or treated with control (**h**) or LSP1-specific siRNA (**i**). **a′**–**b′**, **h′**–**i′** Kymographs of F-actin intensities at single podosomes indicated by yellow circles in **a**, **b**, **h**, **i**. Time is indicated in min. **c**, **d**, **j**, **k** Normalized F-actin intensities at single podosomes in a fixed plane of focus from EGFP control cells (**c**), LSP1-GFP expressing cells (**d**), or cells treated with control siRNA (**j**) or LSP1-specific siRNA (**k**). Each row shows F-actin intensity curves of five podosomes from a single cell, with 6 cells from from different donors analysed. Duration of each individual measurement: 10 min. **e**, **f**, **l**, **m** Statistical evaluation of F-actin based fluorescence intensity fluctuations, with **e**, **l** showing number of peaks and **f**, **m** showing height of peaks Data shown are Mean ± s.e.m.; *P < 0.05, ****P < 0.0001; two-tailed unpaired t-test. **g**, **n** Frequency distribution of peak height from graphs shown in **c**, **d** and **j**, **k**. Note different scale on x-axes due to broader frequency distributon in LSP1 kockdown cells. **o** Principle of protrusion force microscopy. A primary human macrophage is seeded on pliable Formvar matrix. Inversion of the setup allows probing of ventral macrophage surface, including oscillatory protruding podosomes, by atomic force microscopy (AFM). Modified from[48]. **p** Measurement of protrusion forces generated by single podosomes from cells treated with control or LSP1-specific siRNA. Each dot represents the mean protrusion force of at least 23 podosomes (max 245) in a single cell. Data collected from two donors. Values are given as mean ± s.e.m. **P < 0.01, two-tailed unpaired t-test. For specific values, see Supplementary Data 1
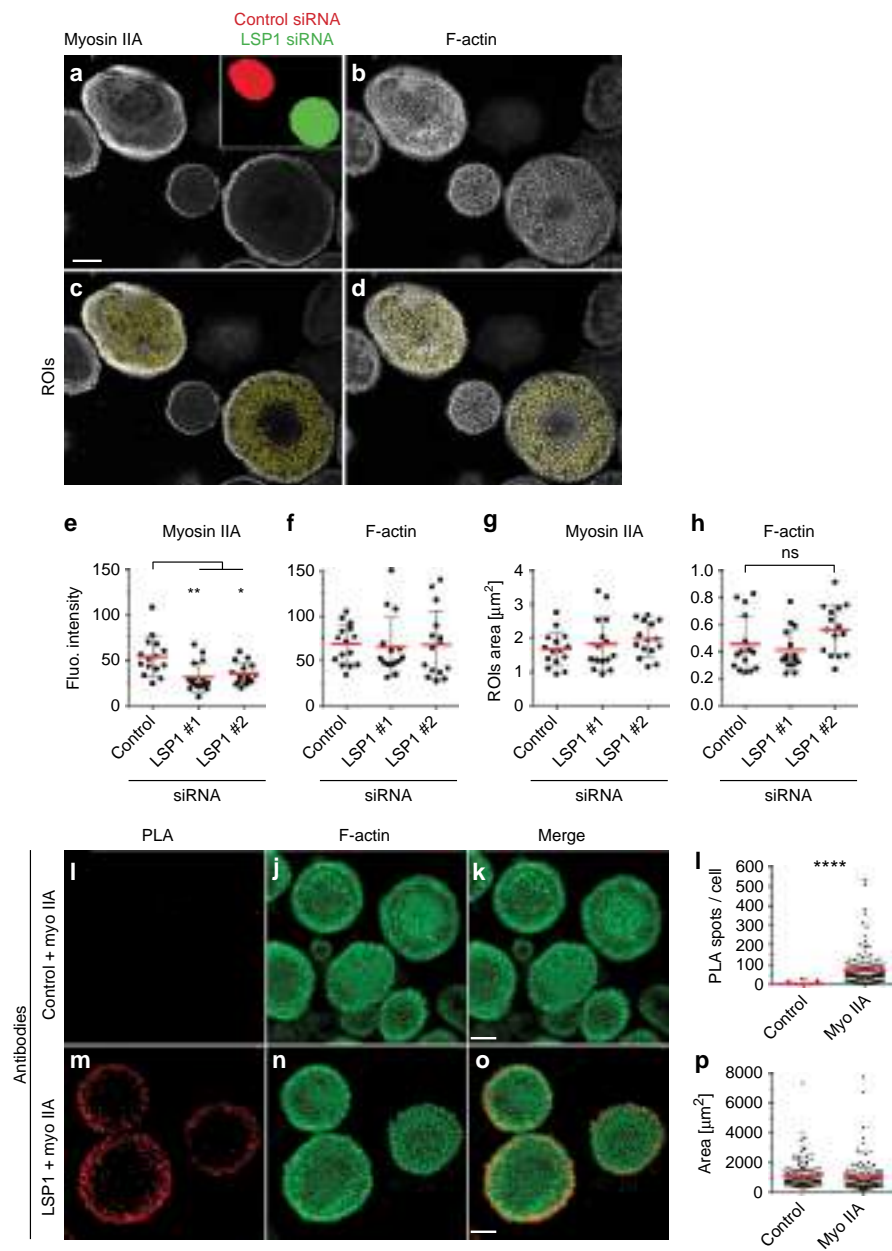
Fig. 4 LSP1 interacts with myosin IIA and regulates its recruitment to podosomes. **a**, **b** Confocal micrographs of mixed populations of macrophages, stained for myosin IIA using specific primary antibody (**a**) or for F-actin using Alexa-405-labeled phalloidin (**b**). Cells treated with LSP1 siRNA express GFP, cells treated with control siRNA express mCherry, as shown in inset in **a**. **c**, **d** ImageJ-based macros were used to identify myosin IIA at podosomes (**c**) and F-actin-rich podosome cores (**d**). Scale bar: 10 μm. **e**–**h** Statistical evaluation of (**e**) myosin-based fluorescence at podosomes, (**f**) F-actin-based fluorescence at podosomes and size of areas analysed for podosomal myosin IIA (**g**) and F-actin (**h**) podosome-covered area. Each dot represents the mean intensity of all the individual podosomes detected in a single cell (~500 podosomes/cell on average), five cells from three different donors. Values are given as mean ± SD. *$P < 0.05$, **$P < 0.01$, one-way ANOVA test. **i**–**k**, **m**–**o** Confocal micrographs of macrophages subjected to a proximity ligation assay (PLA), using myosin IIA-specific antibody, together with control IgG (**i**) or LSP1-specific antibody (**m**) and stained for F-actin (**j**, **n**), with merges (**k**, **o**). Scale bars: 10 μm. Note low background in **i** and PLA signals, especially at the cell cortex, in **m**. **l**, **p** Statistical evaluation of number of PLA spots per cell (**l**) and cellular area analysed for respective PLAs (**p**). Each dot represents one cell. Data collected from two different donors. Values are given as mean ± s.e.m. ****$P < 0.0001$, two-tailed unpaired t-test. For specific values, see Supplementary Data 1

52
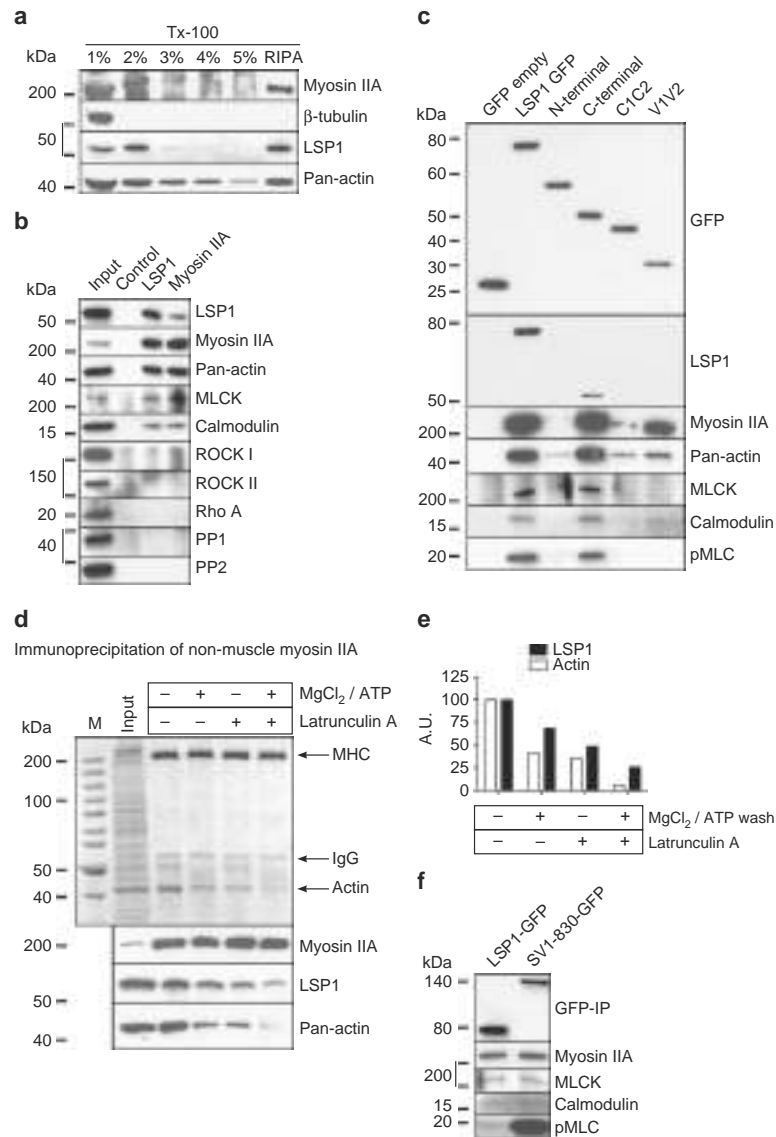
Fig. 5 LSP1 and supervillin interact with a similar subset of myosin IIA regulators. **a** Western blots of macrophage lysates progressively extracted by increased concentration of TritonX-100 (1–5%), or in RIPA buffer. Note that LSP1, and also myosin IIA, are mostly extracted in the 2% and RIPA fractions. **b** Western blot of immunoprecipitation of endogenous LSP1 or myosin IIA from macrophage lysates, with control IgG and input. Blots were probed with indicated antibodies. Note cross-coprecipitation of LSP1 and myosin IIA, accompanied by coprecipitation of myosin regulators MLCK and calmodulin. Molecular weight in kDa is indicated. **c** Western blots of anti-GFP immunoprecipitation of lysates from macrophages expressing LSP1 full length or LSP1 domains fused to GFP (For inputs, see Supplementary Fig. 7A). Blots were probed with indicated antibodies. Note coprecipitation of myosin IIA with full length LSP1, and also with the C-terminal and the villin headpiece-like domains (V1V2) of LSP1. Interestingly only the full length and the C-terminal constructs, but not V1V2, are also able to bind MLCK, pMLC and calmodulin. An LSP1-positive band in the lane of the C-terminal construct probably reflects the fact that the anti-LSP1 antibody recognizes an epitope in the C-terminal half of LSP1. **d** Immunoprecipitation of myosin IIA from macrophage lysates, with addition of Mg^{2+}/ATP and/or latrunculin A (10 µM), as indicated. Upper panel: colloidal Coomassie stained SDS PAGE gel, lower panels: corresponding western blots developed with indicated antibodies. Molecular weight is indicated in kDa. **e** Quantification of coprecipitated amounts of actin and LSP1, normalized to precipitations performed without addition of Mg^{2+}/ATP and/or latrunculin A. **f** Western blots of anti-GFP immunoprecipitations from lysates of macrophages expressing LSP1-GFP or supervillin construct SV1-830-GFP developed with indicated primary antibodies. Molecular weight in kDa is indicated. Note that LSP1 and SV1-830 coprecipitate comparable amounts of myosin IIA, MLCK and calmodulin, but that supervillin-coprecipitated myosin is more activated, as indicated by pMLC signal

(Supplementary Fig. 6N). The preferential association of LSP1 with the actin cortex was substantiated by detergent extraction of cell lysates, with the majority of the cellular LSP1 pool being present in the detergent-resistant fraction, which also contained actin and myosin IIA (Fig. 5a).

The LSP1 C-terminus recruits myosin IIA and its regulators. Confirming the PLA analysis (Fig. 4m–o), LSP1 and myosin IIA were cross-immunoprecipitated from macrophage lysates (Fig. 5b). This also resulted in the co-precipitation of a subset of myosin regulators, including the long form of myosin light

53
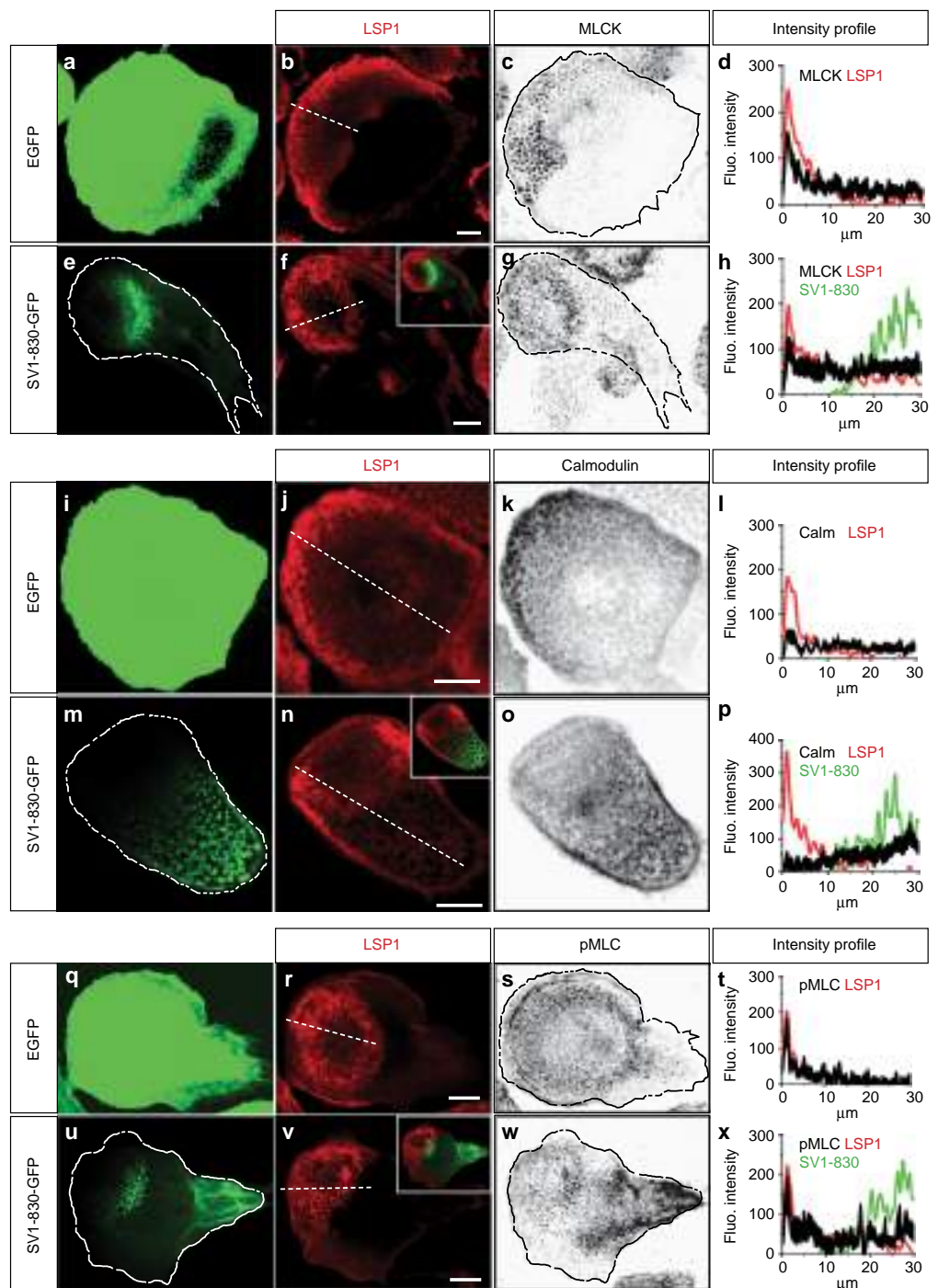
Fig. 6 LSP1 and supervillin compete for myosin regulators in cells. Confocal micrographs of control cells expressing EGFP (**a**, **i**, **q**) or SV1-830-GFP (**e**, **m**, **u**), and stained for endogenous LSP1 **b**, **f**, **j**, **n**, **r**,**v** both stained for MLCK (**c**, **g**), calmodulin (**k**, **o**) or pMLC (**s**, **w**). Dashed white lines in **b**, **f**, **j**, **n**, **r**, **v** indicate pixels used for generation of intensity profiles shown in **d**, **h**, **l**, **p**, **t**, **x**, gained from analysis of 10 cells from three different donors. Graphs for LSP1 and supervillin show respective mean intensities, while graphs for MLCK, calmodulin and pMLC also include error bars. Note localization of SV1-830 to the trailing edges of cells, accompanied by redistribution of MLCK (**d**, **h**), calmodulin (**l**, **p**), and pMLC (**t**, **x**) to the rear of respective cells, and also to rearward-facing podosomes. Scale bars: 10 μm

54

chain kinase (L-MLCK) and calmodulin, but not of RhoA, Rho kinase (ROCK) 1 and 2 or protein phosphatase (PP) 1 and 2 (Fig. 5b), pointing to the potential existence of a complex consisting of LSP1, myosin IIA, as well as L-MLCK and caldmodulin.

To dissect the interaction sites of LSP1 with its partners in more detail, GFP-fused full length and truncation constructs of LSP1 (Fig. 1g), were expressed in macrophages and precipitated by anti-GFP immunoprecipitation. The C-terminal construct coprecipitated actin, myosin IIA, MLCK, phospho-MLC and calmodulin, comparable to full length LSP1 (Fig. 5c). The N-terminal and C1C2 constructs did not lead to significant co-precipiation of the probed LSP1 interaction partners, whereas the V1V2 construct retained partial binding to actin, myosin IIA and calmodulin (Fig. 5c; Supplementary Fig. 7A).

Immunoprecipitations of myosin IIA from macrophage lysates showed that depletion of actin from myosin-containing precipitates using Mg^{2+}/ATP and/or latrunculin A was accompanied by a reduction of coprecipitated LSP1 (Fig. 5d, e). In order to test whether the binding of myosin IIA by LSP1 is direct or indirect, myosin cosedimentation experiments using purified rabbit skeletal muscle myosin were performed. As expected, myosin formed filaments in vitro that were pelleted by ultracentrifugation[23]. However, neither full length nor C-terminal constructs of LSP1 were found to cosediment to a significant degree (Supplementary Fig. 7B). Collectively, these results suggest an indirect interaction of LSP1 and myosin IIA that is apparently mediated by F-actin.

LSP1 and supervillin recruit the same myosin regulators. The data pointed to LSP1 being in a complex with actin, myosin IIA and its regulators at the cell cortex and at podosomes. Of note, supervillin has been described as a similar regulator of myosin IIA activity both at podosomes[20], and at the cell cortex[25], by recruiting actin, myosin IIA and L-MLCK through its N-terminal region (SV 1-830)[20,23]. To investigate whether LSP1 and supervillin bind the same subset of myosin regulators, macrophages were transfected with LSP1-GFP or SV1-830-GFP, and anti-GFP immunoprecipitations were performed. The amount of coprecipitated myosin IIA was ×1.6 higher for supervillin, compared to LSP1. However, the level of myosin light chain phosphorylated at the Ser19 residue of pMLC was even more enhanced (×9.0), leading to a ×5.6 increase in the overall level of myosin activation, thus confirming the role of supervillin as a myosin hyperactivating protein[20] (Fig. 5f). In addition, supervillin was found to interact with L-MLCK, as reported[25], as well as calmodulin (Fig. 5f).

LSP1 and supervillin present as, respectively, moderate or strong regulators of myosin II activity. Next, we explored the consequences of their binding to a similar subset of myosin regulators in cells. Macrophages were transfected with SV1-830-GFP or GFP as controls, stained for endogenous LSP1 and co-stained for MLCK, calmodulin or pMLC. In both controls and SV1-830 expressing cells, LSP1 was localized to the leading edge of polarized cells (Fig. 6b, f, j, n, r, v). In contrast, expression of SV1-830 led to a redistribution of MLCK (Fig. 6c, d), calmodulin (Fig. 6k, l) and pMLC (Fig. 6s, t) from the leading edge and precursor podosomes towards the trailing edge of cells and successor podosomes (Fig. 6g, h, o, p, w, x), at sites of supervillin-driven myosin hyperactivation. (Note: based on Western blot densitometry and transfection rates, LSP1-GFP and SV1-830-GFP were calculated to be overexpressed by a factor of 6.5 and 11.0, respectively, compared to endogenous proteins, and by a factor of 1.6 relative to each other.)

LSP1 and supervillin bind differentially to actin isoforms. We next investigated the potential cause underlying this asymmetry, and in particular, whether differential binding and distribution of actin isoforms could be involved. Interestingly, α-cardiac actin was found to localize only at podosomes, and especially at the rearward part of podosome groups (Fig. 7a), where successor podosomes are found[20]. By contrast, β-actin was detected at cortical actin structures (Fig. 7b), including precursor podosomes[41], with γ-actin showing a similar distribution, however, with less enrichment at the cell cortex (Fig. 7c). (Note: α-cardiac actin was detected in the macrophage podosome proteome[40], in contrast to α- smooth muscle actin, which was also not detectable by Western blots or immunofluorescence in the present study). This could be corroborated by fluorescence intensity graphs of podosome fields from different cells ($n = 10$) (Fig. 7d, e) and by ratiometric analysis of α-cardiac actin over β- or γ-actin (Fig. 7f, g). This differential distribution of actin isoforms mirrors the localization of LSP1 and supervillin, with LSP1 localizing to the leading edge or periphery of cells (Fig. 6b, f, j, n, r, v), which are enriched in β- and γ-actin (Fig. 7b, c, i, l), and supervillin (GFP-SV1-830) localizing to the inner part of cells, where it closely follows the α-cardiac actin gradient (Fig. 7h, k), being especially enriched at sites of a high α-cardiac over β- or γ-actin ratio (Fig. 7j, m).

To further investigate the potential differences in actin isoform binding by LSP1 and supervillin, anti-GFP immunoprecipitates (Fig. 5d) were re-probed for α-cardiac, β-, and γ-actin (Fig. 7n). Densitometry showed that, while the LSP1 construct coprecipitated only ~2/3 of total actin, compared to SV1-830-GFP, the levels of coprecipitated α-cardiac actin were even lower, corresponding to a further reduction of ~50% (Fig. 7o). Altogether with the immunofluorescence data, these biochemical experiments thus pointed to a potential role of the α-cardiac-versus β-actin binding in the establishment of distinct subcellular zones that are respectively enriched in LSP1 or supervillin.

To test the potentially differential binding of LSP1 and supervillin to individual actin isoforms, LSP1 full length and the three actin binding regions of supervillin (SV171-342, SV 343-571, SV570-830)[23] were expressed in E. coli as 6xHis or GST fusions, respectively, purified and added to pure actin isoforms in F-actin cosedimentation assays, which are based on ultracentrifugation of polymerized actin. Controls showed that both β-actin from human platelets and bovine α-cardiac actin were almost completely pelleted, while 100% of LSP1 6xHis and >50% of the individual purified GST-fused F-actin binding fragments of supervillin remained in the supernatant when not mixed with pure actin isoforms (Fig. 8a; Supplementary Fig. 7C). Of note, addition of LSP1 6xHis to β-actin resulted in 84% of cosedimentation of the fusion protein, in contrast to only 45% cosedimentation with α-cardiac actin (Fig. 8a, b). Importantly, all supervillin GST constructs were found to coprecipitate to a comparable degree with either β- or α-cardiac actin (Supplementary Fig. 7C,D). Collectively, these results showed that LSP1 has a preference for the binding of β-actin, with a comparably ~50% reduced binding to α-cardiac actin, while supervillin F-actin binding regions exhibit no such preference for a specific actin isoform. Furthermore, live cell imaging showed that the preferential localization of LSP1-GFP to the β-actin-rich leading edge and of SV1-830 to the α-actin-rich inner regions of the cell, respectively, is very persistent, and even in a cell changing direction, respective subcellular zones are rapidly reestablished (Supplementary Fig. 8; Supplementary Movie 5).

To explore potential consequences of depletion of actin isoforms, we established siRNA-mediated knockdown of α-cardiac actin and β-actin. Treatment of macrophages with α-cardiac actin-specific siRNA led to a global ~1/3 reduction of α-
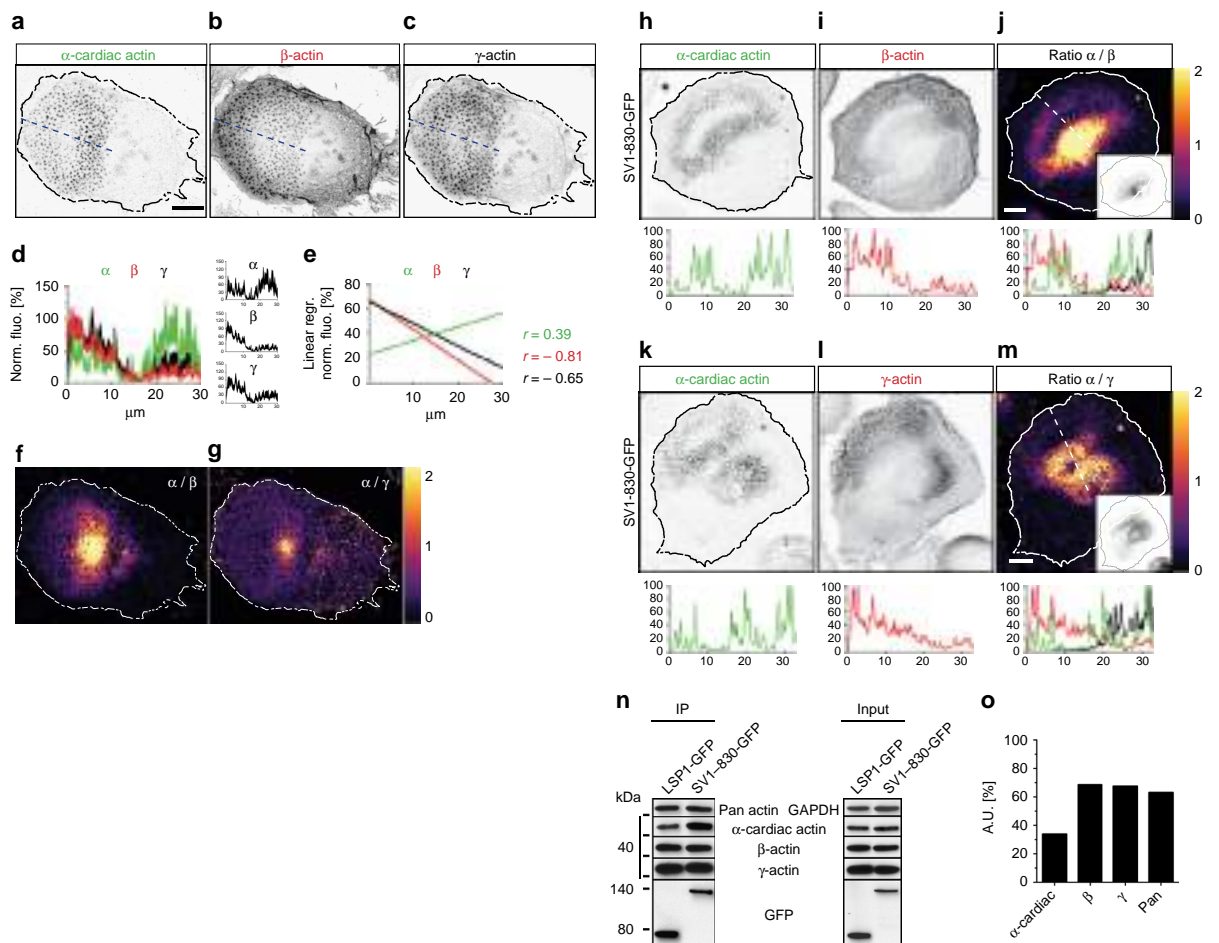
Fig. 7 LSP1 and supervillin localize to different subcellular zones that are enriched in distinct actin isoforms. **a**–**c** Confocal micrographs of primary human macrophage, co-stained for endogenous α-cardiac (**a**), β- (**b**), and γ- (**c**) actin, shown in inverted grey scale. Bar: 10 μm. Dashed line indicates pixels used for respective fluorescence intensity graphs, with relative maximums set to 100%. **d** Fluorescence intensity diagram of α-cardiac, β- and γ-actin, average from 10 cells with comparable podosome-covered areas, with standard errors. Individual graphs are shown in diagrams on the right. **e** Linear regressions of graphs shown in (**d**) with respective Pearson correlation values (**r**). **f**, **g** Ratiometric analysis of stainings in **a**–**c**, showing enrichment of α-cardiac-actin over β-actin (**f**) or γ-actin (**g**). Fold enrichment is indicated by colour scale on the right. **h**–**m** Confocal micrographs of primary human macrophage overexpressing GFP-SV1-830 and co-stained for endogenous α-cardiac (**h**), and β-actin (**i**), or for α-cardiac (**k**) and γ-actin (**l**), shown in inverted grey scale. **j**, **m** Ratiometric analysis with fold enrichment indicated by colour scale on the right. Bar: 10 μm. Dashed lines indicates pixels used for respective fluorescence intensity graphs, with relative maximums set to 100%. Small insets show respective supervillin (SV 1-830-GFP) signals, with cell circumference indicated by black line. Note close correlation between α-cardiac actin enrichment and supervillin localization. **n** Western blots of anti-GFP immunoprecipitations (left panel) from lysates of macrophages expressing LSP1-GFP or supervillin construct SV1-830-GFP, with respective inputs (right panel), developed with indicated primary antibodies. Molecular weight in kDa is indicated. **o** Quantification of precipitated actin isoform bands from LSP1 GFP-IP lysates shown in **n** in comparison to SV1-830-GFP-IP set to 100%

cardiac actin levels (Supplementary Figure 9A, B), and a wide range of reduction on the individual cell level. Strikingly, cells depleted for α–cardiac actin, but still forming peripheral podosomes enriched in β-actin, and expressing SV1-830-GFP showed a shift of the supervillin construct towards the cell periphery (Supplementary Figure 9C–F). This was reminiscent of the phenotype of the isolated, myosin II-binding region of supervillin (SV1-174), which also localizes to unbranched, myosin IIA-enriched actin filaments at the cortex (Supplementary Figure 9G–J)[20]. Treatment with β-actin specific siRNA led to a reduction of ~ 60% of β-actin levels, again with varying effects on the individual cell level. Also, while global levels of the remaining actin isoforms, and also of LSP1, were unchanged in case of α-

cardiac actin or β-actin knockdown (Supplementary Figure 9B), individual β-actin depleted cells frequently also showed reduced staining for α-cardiac actin (Fig. 8g). Importantly, the peripheral localization of LSP1 was not discernibly affected as a result of β-actin knockdown (Fig. 8h), indicating that additional molecular mechanisms are involved in cortical localization of LSP1.

Combining these results, we reasoned that the preferred binding of β-actin by LSP1 could restrict the access of supervillin to the cell periphery and to precursor podosomes. To test this hypothesis, SV1-830 distribution was analysed in control (Fig. 9a–d) and LSP1-depleted cells (Fig. 9e–h). Indeed, the SV1-830 construct was no longer restricted to rearward podosomes in LSP1 knockdown cells, instead showing a much

56
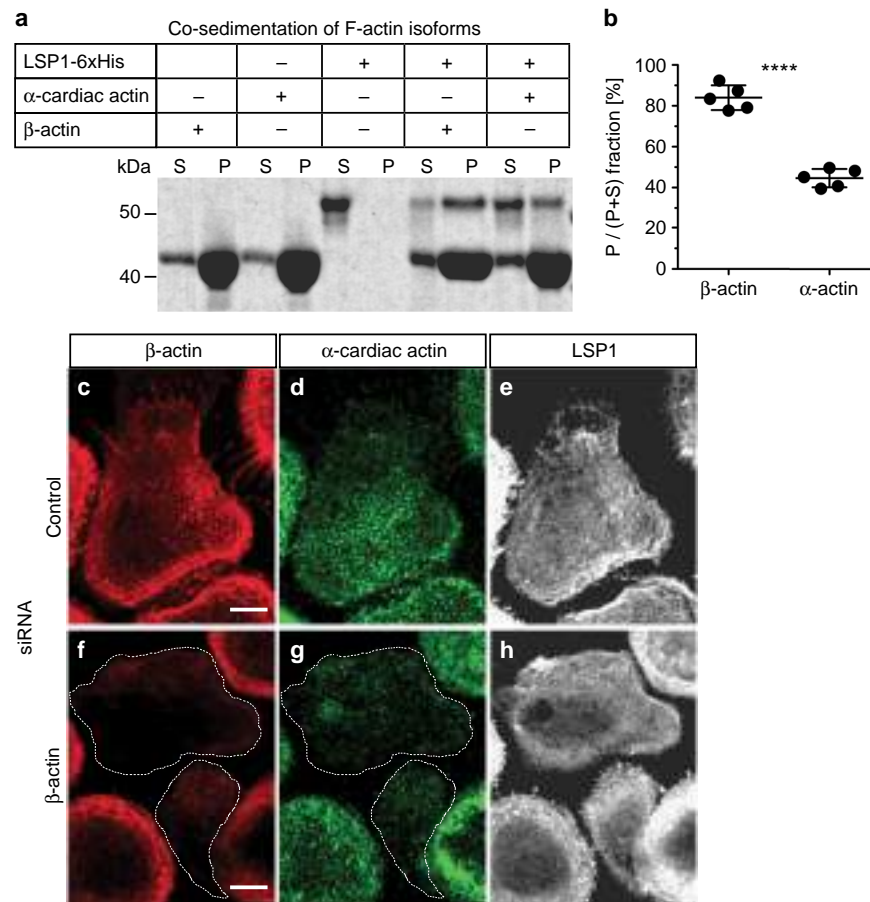
Fig. 8 Differential subcellular recruitment of LSP1 and supervillin is based on the preferential binding of LSP1 to β-actin. **a** Comassie blue staining of gel showing actin cosedimentation assays with pure β-actin, α-cardiac actin, or LSP1 6xHis, alone as control, or in combination with actin isoforms, as indicated. Lanes showing supernatant and pellet fractions are labelled with "S" and "P", accordingly. Molecular weight is indicated in kDa. **b** Quantification of copelleted material as ratios of pelleted fraction versus input. Values are given as mean ± S.D.; ****$P < 0.0001$, two-tailed unpaired t-test. **c–h** Confocal micrographs of macrophages treated with control siRNA (**c–e**) or β-actin-specific siRNA (**f–h**), stained for β-actin (**c**, **f**), α-cardiac actin (**d**, **g**), and LSP1 (**e**, **h**). (Note: staining conditions required especially for α-cardiac actin are not optimal for staining of LSP1.) Scale bars: 10 μm. For specific values, see Supplementary Data 1

broader localization that extended towards the cell periphery (Fig. 9e–h). This was further corroborated by analysis of respective fluorescence intensities that showed a shift in the recruitment of SV1-830 towards the cell periphery in LSP1-depleted cells (Fig. 9i–l). Further analyses showed that SV1-830 overexpression led to a reduction of the morphological changes observed upon LSP1 knockdown. Accordingly, cell area of LSP1 depleted cells overexpressing SV1-830 (Fig. 9m) did not increase compared to control cells and to cells only depleted of LSP1 (Fig. 2n). Also, formation of podosome clusters was unchanged, compared to control cells (Fig. 9n), which was in contrast to LSP1 knockdown cells (Fig. 2m, n). Furthermore, both aspect ratio and circularity index were comparable to control values (Fig. 9o, p) and also showed a close correlation (Fig. 9q–t), in clear distinction to the deviation observed for LSP1 knockdown cells (Fig. 2s–v). Moreover, the number of cells showing more extreme values (AR ≥ 1.3; C ≤ 0.8) was reduced to ~ 10–15%, in contrast to values of ~ 60% for cells only treated with LSP1 siRNA, but without SV1-830 overexpression. Collectively, these results show that supervillin overexpression leads to a rescue of the morphological aberrancies observed upon LSP1 knockdown.

Discussion

The data presented reveal new roles for two myosin IIA regulatory proteins in structural and sensory functions of primary macrophages that are crucial for migration and invasion of these cells. In particular, we identify LSP1 as a central regulator of the actomyosin cortex and show that LSP1 interacts with myosin IIA and its regulators, including L-MLCK, calmodulin and MLC. We also show that LSP1 competes with supervillin, a myosin hyper-activator[20], for these regulators, leading to discrete zones of myosin activity, and that establishment of these subcellular zones is based on the differential distribution of actin isoforms.

Consistent with earlier data[52–54], LSP1 was found to localize to the actin cortex and to podosomes. LSP1 regulates cell dynamics on multiple levels, as siRNA-induced knockdown of LSP1 led to enhanced dynamics of cells, podosome clusters and also of individual podosomes. LSP1 knockdown increased cell speed and migration track length, which is in line with leukocytes from LSP1-deficient mice showing faster migration to sites of inflammation[55], and overexpression of LSP1 in neutrophil actin dysfunction syndrome (NAD47/89) being based on reduced chemotactic motility of neutrophils[56]. LSP1 knockdown
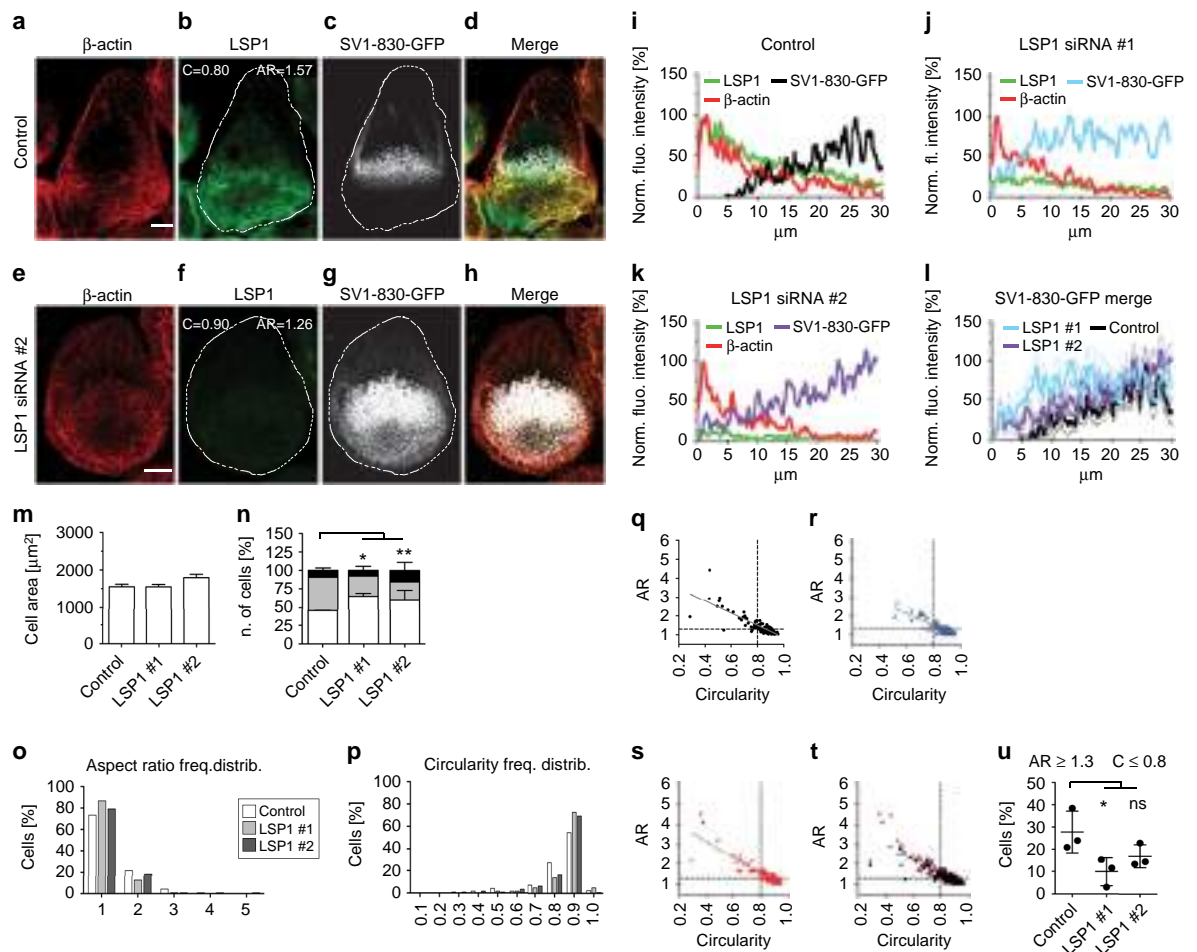
Fig. 9 Supervillin overexpression rescues morphological aberrancies due to LSP1 depletion. **a–l** LSP1 blocks access of supervillin to β-actin-rich podosomes in the cell periphery. **a–h** Confocal micrographs of macrophages treated with control siRNA (**a–d**) or LSP1-specific siRNA (**e–h**) and overexpressing SV1-830-GFP, stained for β-actin (**a, e**), LSP1 (**b, f**), SV1-830-GFP signal (**c, g**), with merges (**d, h**). "C" and "AR" in (**b, f**) indicate circularity and aspect ratio. Scale bars: 10 μm. (**i–l**) Fluorescence intensity scans of β-actin, LSP1 and SV1-830-GFP in cells treated with control siRNA (**i**) or with two individual LSP1-specific siRNAs (**j, k**), or all SV1-830-GFP intensity scans shown together (**l**). Graphs show mean intensities from 30 μm long line scans taken from the cell periphery towards the rear in 10 cells from three donors. **m** Total area (μm²) of cells treated with indicated siRNAs and overexpressing SV1-830-GFP. Each bar represents mean value of 120 cells collected from three different donors. Values are given as Mean ± s.e.m. **n** Podosome distribution in cells treated with indicated siRNAs and overexpressing SV1-830-GFP. Cells were scored in groups, according to even distribution (white), recruitment of podosomes to a single leading edge (grey) and formation of clusters (black). Values are given as Mean ± S.D and represent the percentage calculated with at least 30 cells per donor (N = 3). *P < 0.05, **P < 0.01, one-way ANOVA test. **o–u** Evaluation of cell morphology in control and LSP1 knockdown cells that overexpress SV1-830-GFP. **o, p** Frequency distribution for cells grouped according to aspect ratio (**o**) or circularity (**p**) with 120 cells collected from three different donors evaluated. **q–t** Scatter plots of circularity (x-axes) and aspect ratio (y-axes), with plots for cells treated with control siRNA (**q**), LSP1-specific siRNAs (**r, s**), and merge (**t**). Cut-off values of 0.8 for circularity and 1.3 for aspect ratio are indicated by dashed lines. Regression line shown in grey. Each dot represents a single cell (N = 120) from three different donors. **u** Evaluation of cells expressing SV1-830-GFP, treated with indicated siRNAs and showing values for aspect ratio ≥1.3 and for circularity ≤0.8; Values are given as Mean ± S.D.,*P < 0.05, one-way ANOVA test. For specific values, see Supplementary Data 1

macrophages also showed an increase in cell size, consistent with LSP1 negatively regulating T-cell spreading[32], and pointing to relaxation of cortical tension as a possible result of LSP1 depletion. Conceivably, relaxation of cortical tension could also be involved in the enhanced 3D invasion of LSP1 knockdown macrophages, as it could facilitate squeezing of cells through ECM pores or formation of blebs to drive locomotion.

Using confocal and STED microscopy, we show that endogenous LSP1 localizes on top of the podosome core and partially extends along its side. Our data thus confirm and extend previous

observations of a cap-like structure on top of the podosome core. Remarkably, all of the identified components of the podosome cap, including FMNL1[21], INF2[22], and supervillin[20] are involved in the regulation of unbranched actin filaments and of myosin IIA, pointing to a function of the podosome cap in actomyosin-based contractility. This concept is supported by the role of LSP1 in podosome oscillation and protrusive force generation. Podosomes have been described as contractile organelles, in which growth of the core leads to exertion of forces on the lateral actin cables[44,45,47], resulting in oscillatory movement of podosomes in

the z direction that can be blocked by the myosin II inhibitor blebbistatin[22,49]. Our data show that LSP1-GFP overexpression leads to enhanced "frequency" of podosome oscillations, while LSP1 depletion results in a more irregular "amplitude". Furthermore, atomic force measurements showed that siRNA-induced depletion of LSP1 led to a ~30% reduction of podosome protrusive force.

As podosome oscillation is thought to be a central mechanism in detecting and reporting the rigidity of the extracellular matrix[45,46], LSP1 and the cap structure in general likely fulfil a critical function in mechanosensing, which would also tie in with the role of myosin IIA in this process[22,49], which we now identify as an interaction partner of LSP1. Of note, LSP1 binds to F-actin[57], but not to G-actin and also does not directly influence the rate of actin polymerization[31].

Endogenous LSP1 and myosin IIA were cross-precipitated in immunoprecipitations of macrophages lysates. Importantly, proximity ligation assays showed that both proteins closely colocalize at podosomes and at the cell cortex, compatible with a potential interaction. Similar results were gained for LSP1 and actin, pointing to the existence of a complex of LSP1, myosin IIA and actin. Myosin cosedimentation assays, and also myosin immunoprecipitation in the presence of latrunculin and Mg^{2+}/ATP, reducing the amount of coprecipitated actin filaments, showed that the interaction between LSP1 and myosin II is probably indirect and mediated by F-actin. SiRNA-induced depletion of LSP1 resulted in a ~50% reduction of podosome-localized myosin IIA, but not of cellular myosin IIA levels. LSP1 thus seems to be crucial for the recruitment of myosin IIA to actin structures, possibly based on its actin bundling activity[31]. Immunoprecipitations from lysates of cells expressing LSP1 truncation constructs showed that for efficient binding of actin and myosin IIA, the complete LSP1 C-terminus, comprising both caldmodulin- and villin headpiece-like F-actin binding domains, is required. These results reflect the ability of LSP1 truncation constructs to localize to podosomes. Interestingly, LSP1 was reported to bind Myo1e during Fcγ receptor-driven phagocytosis in macrophages[27], which could suggest a more widespread ability of LSP1 to interact with myosins. This would also be in line with the presence of calmodulin in LSP1 immunoprecipitates, as calmodulin can also function as a light chain for unconventional myosins, including Myo1e[58]. Of note, the LSP1 C-terminal half is more conserved (85% identity) than the N-terminal half (53% identity) between mice and humans[59], pointing to less conserved regulatory functions of the N-terminus.

Interestingly, previous results showed that siRNA-induced depletion of myosin IIA led to enhanced lifetime of podosomes, similar to depletion of supervillin[20]. Reduced recruitment of myosin IIA subsequent to LSP1 depletion would thus also be expected to lead to higher lifetimes of podosomes. However, we now show that depletion of LSP1 leads to reduced lifetime of podosomes. Possible explanations for this could be that (1) LSP1 supports actin bundling, and its depletion thus affects podosome architecture/stability and indirectly also actin turnover due to an increase of available actin filaments; (2) LSP1 depletion also results in enhanced recruitment of supervillin to peripheral podosomes, which could contribute to their enhanced turnover; (3) LSP1 might also play an additional role in podosome formation and/or stabilization through recruitment of an interaction partner such as WASP[54] that is crucial for these processes[8]. Apparently, LSP1 does not perform the same role as supervillin in myosin II activation and podosome turnover. Supervillin is a myosin II hyperactivator, is prominently recruited to dissolving podosomes and leads to enrichment of phospho-myosin light chain at these podosomes. Podosome dissolution is thus likely to depend on supervillin-

induced myosin IIA hyperactivation. In contrast, LSP1 is associated with only moderate myosin II activation (see Fig. 5f), and even the high enrichment of LSP1 at precursors does not trigger podosome dissolution.

The presence of several myosin regulators was tested in cross-immunoprecipitations of LSP1 and myosin IIA. Indeed, L-MLCK, calmodulin and Ser19 phosphorylated myosin light chain (pMLC), but not ROCK1, ROCK2, RhoA, protein phosphatase 1 or 2, were coprecipitated. These results showed that LSP1 interacts with a variety of specific myosin regulators. The membrane-associated protein supervillin forms another hub for actomyosin[23] and also binds regulators of myosin activity, including L-MLCK[20], and calmodulin, as shown here. Of note, pMLC levels in supervillin (SV1-830) precipitates were significantly higher compared to LSP1 precipitates, confirming supervillin's role as a myosin IIA hyperactivating protein[20], and indicating that LSP1 does not share this ability. Importantly, LSP1 and supervillin not only interact with the same subset of myosin regulators but can also compete for them, as expression of SV1-830 led to a redistribution of L-MLCK, calmodulin and pMLC in cells, from the leading edge towards the trailing edge. This competition results in the formation of subcellular zones of different pMLC levels, leading to a symmetry break in actomyosin activity. Of note, actomyosin symmetry breaking can be achieved by differential recruitment of myosin II isoforms A and B[5]. As macrophages express predominantly myosin IIA[7], an alternative way would be differential recruitment of myosin II regulators with different activities, as shown here for LSP1 and supervillin[20].

Interestingly, cell polarization was recently shown to emerge as a result of competition for G-actin between two actin networks, branched filaments at protrusive sites and unbranched actin bundles of the cortex, which also act as a sink for myosin II. Moreover, only intermediary, but not extreme, levels of myosin II were shown to support cell polarization, with insufficient levels of cortical myosin II activity resulting in the formation of multiple protrusions and thus in loss of overall polarization[42]. Considering that LSP1 functions as an actin bundler[31] that supports moderate levels of myosin II activity, the observed formation of multiple protrusive sites upon LSP1 knockdown seems to be in line with this model and could be explained by the respective reduction of cortical myosin contractility.

It is thus noteworthy that (1) LSP1 knockdown leads to more extreme values for circularity and aspect ratio of macrophages, indicating an uncoupling of local protrusion from cell elongation and thus from productive cell polarization, and (2) these aberrancies in cell morphology can be rescued by expression of SV1-830, which shows a more widespread localization, also extending to the cell periphery, upon LSP1 knockdown. It is thus conceivable that the altered distribution of overexpressed supervillin in LSP1 knockdown cells helps to restore the necessary levels of myosin contractility at the cortex that contribute to proper cell polarization.

Investigating the underlying basis for the differential localization of LSP1 and supervillin, we found that actin isoforms show distinct cellular patterning in macrophages, as previously reported for neurons[60], fibroblasts and endothelial cells[39]. Specifically, β- and γ-cytoplasmic actin show a decreasing gradient from the cell periphery or leading edge towards the cell center or trailing edge, consistent with earlier results[33]. In contrast, α-cardiac actin shows an inverse gradient. These distributions were reminiscent of those of LSP1 and supervillin, respectively. Indeed, supervillin mostly colocalized to rearward regions of polarized cells that show a high α-cardiac over β- or γ-actin ratio.

Quantification of LSP1 and supervillin immunoprecipitations showed that LSP1 bound only ~2/3 of the overall amount of actin, compared to supervillin, probably reflecting the fact that
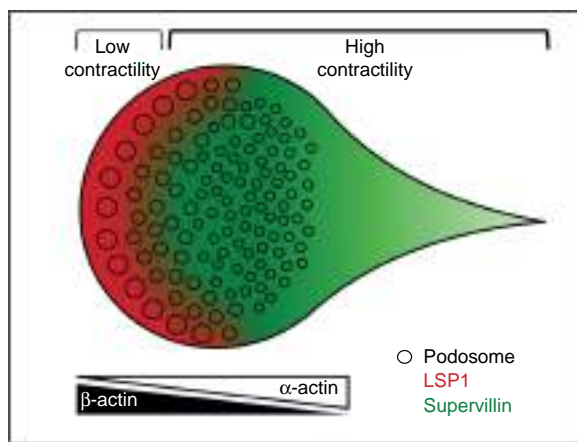
Fig. 10 Model of actin isoform-based actomyosin symmetry break in macrophages. Actin isoforms localize along inverse gradients in macrophages, with β-actin enriched at the cell periphery and α-actin enriched at the cell interior. Preferential binding of β-actin leads to LSP1 recruitment to structures with a high β- over α-actin ratio, while supervillin is recruited to structures showing a high α− over β-actin ratio. As LSP1 is associated with moderate levels of myosin II activation, whereas supervillin is a myosin II hyperactivator, this leads to a symmetry break in actomyosin-based contractility and to polarization of the cell, establishing zones of low contractility at the front and of high contractility at the back. Large precursor podosomes at the front and smaller successor podosomes at the back show respective enrichments of β-actin and LSP1 versus α-actin and supervillin, which is likely crucial for their different dynamic behaviour

supervillin contains three functional actin-binding sites[23], whereas LSP1 likely contains two. Importantly, LSP1 bound even less of α-cardiac actin, resulting in ~1/3 of α-cardiac actin levels, compared to those coprecipitated with supervillin. This differential binding to actin isoforms by LSP1 was confirmed by cosedimentation assays using pure proteins, with LSP1 preferentially binding to β-actin filaments, and only binding at ~50% reduced levels to α-cardiac actin filaments. Similar experiments performed with the three isolated, GST-fused actin binding regions of supervillin, on the other hand, showed no difference in cosedimenation with β- or α-cardiac actin filaments. Collectively, these results pointed to LSP1, its preferential binding of β-actin, and the presence of subcellular regions containing different ratios of actin isiforms, as the drivers of the observed asymmetry in LSP1 and supervillin distribution in cells. Indeed, interfering with the pattern of subcellular actin isoform distribution by depletion of α-cardiac actin resulted in a redistribution of supervillin away from successor podosomes to myosin IIA-positive filaments at the cell cortex. A possible explanation for this phenomenon could be that, in the absence of α−actin-rich successor podosomes, and in the presence of endogenous LSP1, which blocks the access to β-actin-rich precursor podosomes, supervillin is recruited to the cell cortex through its myosin II binding region. Of note, depletion of β-actin did not result in discernibly altered distribution of LSP1, indicating additional mechanisms that stabilize LSP1 at the cell periphery. Still, the altered distribution of supervillin upon LSP1 knockdown clearly shows that preferential binding of β-actin by LSP1 restricts the access of supervillin to this actin pool at the cell periphery. Collectively, these data suggest that the cellular pattern of actin isoforms forms the basis for the differential distribution of both myosin regulatory proteins in cells, thus leading to the establishment of distinct zones of actomyosin activity (Fig. 10).

Different actin isoform ratios are also likely to impact on podosome subpopulations, namely precursors at the leading edge[41] and the more rearward-localized successors[20]. Considering the different biochemical activities of actin isoforms, e.g., differences in polymerization and depolymerization rates, with especially β-actin showing higher dynamics[61,] and also in rheological properties[62], this could, in part, explain the different dynamic behavior of podosomes, with β-actin-rich precursors being more prone to growth and fission, and α-cardiac actin-rich successors being smaller and longer-lived.

In this context, it should be noted that podosome clusters in control cells contain both leading edge-associated, large and highly dynamic precursors and also smaller and more stable successors. In contrast, LSP1 knockdown cells form several clusters, which are often not leading edge-associated, and contain podosomes that show high dynamics and comparatively small size, thus combining characteristics of both precursors and successors. A further contributing factor could be the reduction of LSP1 and myosin IIA at podosome-connecting actin filaments, potentially leading to less coherence within the podosome array and thus giving rise to increased cluster formation. It should thus be worthwhile to investigate these points in detail by using live cell imaging and superresolution microscopy.

Differences between actin isoforms are especially found in their N-termini, the most notable being addition of an aspartic acid residue at the start of the α-cardiac actin sequence[34,35], which is exposed on the surface of the filament[63]. It would thus be interesting to model the F-actin binding regions of supervillin[24] and LSP1 and to determine the structural basis especially for the preferred binding of LSP1 for β-actin. Furthermore, the differential distribution of actin isoforms is likely to impact not only on LSP1 and supervillin, but also on other actin-associated proteins, as hypothesized previously for cofilin[37] and profilin[38].

Another interesting point concerns the establishment of the differential pattern of actin isoforms. One possibility would be localized translation of respective mRNAs. Indeed, the 3′UTR of the β- but not of the γ-actin transcript contains a sequence that binds to zipcode binding protein (ZBP1), which facilitates transcript targeting[34,64]. However, considering that local enrichment of LSP1 and supervillin to the leading and trailing edges is highly dynamic (Supplementary Fig. 8; Supplementary Movie 5), also other mechanisms such as anisotropic self-organization of the cytoskeleton[65], are likely to contribute. Moreover, flow of components such as actin and vinculin has been demonstrated to organize podosomes on the mesoscale[66]. Conceivably, anisotropic flow of actin isoforms during podosome turnover could form a pattern that is used for differential recruitment of LSP1 and supervillin.

Collectively, we show here that LSP1 is a multiple-level regulator of macrophage migration, mechanosensing and invasion, and provide a detailed molecular explanation for the reported effects of LSP1 in immune cell (dys-)regulation. LSP1 competes with supervillin, another actomyosin hub protein, for binding of myosin regulators, and also for actin isoforms, in particular β-actin. Actomyosin symmetry breaking in macrophages is thus achieved by differential recruitment of two actomyosin machineries that support different levels of myosin activity, with the underlying pattern generated by the distribution of actin isoforms.

Methods

Isolation and culture and transfection of cells. Human peripheral blood monocytes were isolated from buffy coats (kindly provided by Frank Bentzien, University Medical Center Eppendorf, Hamburg, Germany) and differentiated into macrophages, as described. Briefly, human heparinized blood is carefully added to Lymphocyte Separation Medium (LSM, PAA Laboratories, Cat. No. J15-004) and

60

centrifuged for 30 min at 4 °C and $450 \times g$ of speed. Buffy coat containing mononuclear cells and platelets is carefully recovered and monocytes are then isolated using magnetic anti-CD14 beads and separation columns (Miltenyi Biotec, Cat. No. 139-050-201). Approval for the analysis of anonymized blood donations was obtained by the Ethical Committee of the Ärztekammer Hamburg (Germany). Cells were cultured in RPMI-1640 (containing 100 units/ml penicillin, 100 µg/ml streptomycin, 2 mM glutamine and 20% autologous serum) at 37 °C, 5% CO_2 and 90% humidity. Monocytes were differentiated in culture for at least seven days, under addition of 20% human autologous serum. For transfection experiments, differentiated macrophages, at days 10–14 of culture, were transiently transfected using the Neon® Transfection System (Thermo Fisher Scientific, Waltham, MA), an electroporation-based system, with standard settings (1000 V, 40 ms, 2 pulses) and a concentration of (100 nM) for LSP1 siRNA, (50 nM) for α-cardiac actin siRNA, (50 nM) for β-actin siRNA and 0.5 µg per 1×10^5 cells for plasmids.

Expression constructs and siRNA. The human cDNA of LSP1 (Accession No. for NCBI sequence BC001785) was purchased from Open Biosystem (Catalog Number MHS4771-99611141). LSP1 full length and subdomains were subcloned into pEGFP-C1 empty vector (Clontech) by using the following primers: forward 1 (5-AAATTTAAACTCGAGCCATGGCGGAGGCTTCG AG-3′) and reverse 1 (5′-AAATTTAAAGAATTCCTAGGGAGCCGGGCCCCC-3′) for the full length; forward 1 and reverse 2 (5-AAATTTAAAGAATTCCTAGACCA AGGGGCTGGGTG-3′) for the N-terminus; forward 2 (5′-AAATTTAAACTC-GAGC CTTGGAG GGGACCATCGAACAG-3) and reverse 1 for the C-terminus; forward 2 and reverse 3 (5-AAATTTAAA-GAATTCCTAGGTCTTGGAGCCTCCCTTC-3) for the caldesmon 1/2; forward 3 (5′-AAATTTAAACTCGAGCCTCATCAACAATTAAGAG CACCC-3) and reverse 1 for the villin-headpiece 1/2, containing *Xho*I (#FD0694, Fermentas) and *Eco*RI (#FD0274, Fermentas) sites for forward and reverse primers, respectively. The C-terminus was also subcloned into pmCherry-C1 empty vector using the above mentioned restriction sites. The GFP-supervillin 1-174, 1-830 and supervillin-RFP constructs were a kind gift of E. Luna (University of Massachusetts, USA)[67]. pLifeact-TagGFP2 and pLifeact-TagRFP were purchased from Ibidi (Martinsried, Germany). siRNAs specific for human LSP1 were purchased from Eurofins Genomics (#1, 5′-UGGAGACAUGAGCAAGAAA-3)[68], and from Dharmacon (#2, ON-TARGETplus individual siRNA J-012640-05), with siRNA targeting firefly luciferase mRNA (D-001210-02-20, Dharmacon) used as negative control. Knockdowns were achieved 96 h post transfection. siRNA specific for α-cardiac actin was purchased from Dharmacon (ON-TARGETplus individual siRNA J-012015-05) and knockdown was achieved after 72 h. siRNA specific for β-actin was purchased from Ambion (Silencer Select Pre-designed individual siRNA ID # s230680) and knockdown was achieved after 72 h.

For protein expression in *E.coli*, LSP1 full length and C-terminal subdomain were subcloned into pEXP5-CT/TOPO TA vector (V960-06, Invitrogen, Thermo Fisher Scientific) with a C-terminal fused 6xHis-tag using the following primers: forward 1 (5′- ATGGCGGAGGCTTCGAGTGACCC-3′) and reverse 1 (5′-GGGAGCCGGGCCCCCT TCCACAA-3′) for the full length; forward 2 (5′-ATGTTGGAGGGGACCA TCGAACAGAG-3′) and reverse 1 for the C-terminus. GST-fused supervillin fragments (171-342; 343-571 and 570-830) were a kind gift of E.Luna (University of Massachusetts, USA)[67]. GST empty vector pGEX-2T was purchased from GE-Healthcare (Buckinghamshire, UK) and used as control for in vitro assay.

Proteins for in vitro assays. GST and 6xHis fusion proteins/fragments were expressed after induction in *E.coli* (BL21) cells, purified with gluthathione-Sepharose™ (GE-Healthcare, Buckinghamshire, UK) or Ni-NTA agarose beads (Qiagen, Hilden, Germany) and dialyzed overnight at 4 °C respectively against the following dialysis buffer (100 mM KCl, 2 mM $MgCl_2$, 1 mM DTT, 40 mM PIPES pH 7.0 and 3 mM NaN_3) or (10 mM imidazole pH 7.0, 75 mM KCl, 0.2 mM DTT, 0.2 mM EGTA, 0.01% NP-40 and 3 mM NaN_3). Following dialysis, purified proteins/fragments were snap-frozen in liquid nitrogen and stored at −80 °C. Human platelet non-muscle actin (85% β/15% γ, 99% pure, # APHL99) and rabbit skeletal muscle myosin motor protein (full length, 90% pure, # MY02) were purchased from Cytoskeleton, Inc. (Denver, USA), whereas bovine α-cardiac actin 99% pure (# 8201-01) was purchased from Hypermol (Bielefeld, Germany).

Antibodies and staining reagents. The following antibodies were used for immunofluorescence (1:100 dilution for primary and 1:200 for secondary, unless otherwise stated), immunoprecipitation, Western blots (1:2000 dilution for primary and 1:5000 for secondary, unless otherwise stated) or PLA assays, as indicated: rabbit polyclonal- (HPA019693), goat polyclonal- (PAB18566) or mouse monoclonal (610734) LSP1 antibodies were purchased, respectively, from Atlas Antibodies (Stockholm, Sweden), Abnova (Taipei, Taiwan) and BD Transduction Laboratories; mouse monoclonal anti-pan actin antibody (MAB1501, 1:5000 for WB) was purchased from Merck Millipore; mouse IgG1 monoclonal anti-human cytoplasmic β-actin (β-CYA)(MCA5775GA) and mouse IgG2b monoclonal anti-human cytoplasmic γ-actin (γ-CYA) (MCA5776GA) antibodies from AbD Serotec (Biorad) and diluted 1:5000 for WB; rabbit polyclonal anti-α cardiac actin (PA5-21396, 1:5000 for WB and 1:50 for IF) and rabbit polyclonal anti-α smooth muscle

actin antibodies (ABT1487) from Invitrogen (ThermoFisher Scientific) and Merck Millipore respectively; rabbit polyclonal (M8064) and mouse monoclonal anti-myosin IIA (60233-1-Ig) antibodies from Sigma-Aldrich (St Louis, MO) and Proteintech, respectively and diluted 1:5000 for WB; rabbit polyclonal phospho-specific (pS20) anti-myosin light chain antibody (ab2480) from Abcam; rabbit polyclonal anti-myosin light chain kinase (MLCK) (ST1657) antibody from Calbiochem (1:50 dilution for IF, 1:1000 for WB); mouse monoclonal anti-calmodulin (# 05–173) antibody from Merck Millipore; rabbit polyclonal anti-ROCK1 (#4035) and mouse monoclonal anti-ROCK2 (610623) antibodies from Cell Signaling and BD Transduction Laboratories, respectively; mouse monoclonal anti-human PP1α catalytic subunit (MAB6105) and polyclonal rabbit anti-PP2α catalytic subunit (#2038) antibodies from R&D Systems and Cell Signaling respectively and diluted 1:1000 for WB; rabbit monoclonal anti-RhoA (ab187027) antibody from Abcam; mouse monoclonal anti-vinculin (V9264) and mouse monoclonal anti-β tubulin (T4026) antibodies from Sigma-Aldrich; rabbit polyclonal anti-GAPDH (10494-1-AP, 1:5000 for WB) antibody from Proteintech; monoclonal mouse anti-GFP antibody (632380, 1:5000 for WB) from Clontech; normal mouse (sc-2025) and rabbit (sc-2027) IgG were purchased from Santa Cruz and used as negative control for PLA assay and immunoprecipitation. HRP-conjugated AffiniPure donkey anti-goat IgG (H + L) (705-035-147) from Jackson ImmunoResearch Laboratories, whereas HRP-linked F(ab′)₂ fragment donkey-anti rabbit (NA9340v) and HRP-linked sheep-anti mouse IgG (H + L) (NA931v) from GE Healthcare. Alexa Fluor-488 AffiniPure goat anti-rabbit IgG (H + L) (111-545-003) from Jackson ImmunoResearch Laboratories whereas Alexa Fluor-568 goat anti-rabbit IgG (H + L) (A-11011), Alexa Fluor-647 goat anti-rabbit IgG (H + L) (A-21244), Alexa Fluor-568 goat anti-mouse IgG1 (A-21124), Alexa Fluor-647 goat anti-mouse IgG1 (A-21240) and Alexa Fluor-568 goat anti-mouse IgG2b (A-21144) from Invitrogen (Thermo Fisher Scientific). F-actin was stained using Alexa-Fluor-405 (ab176752, Abcam), Alexa Fluor-488 (A12379, Molecular Probes) or Alexa Fluor-568 (A12380, Molecular Probes) phalloidin, as indicated. Coverslips were mounted in Mowiol (Calbiochem) containing DABCO (25 mg/ml; Sigma-Aldrich) as anti-fading reagent and sealed with nail polish. The following antibodies and immunofluorescence reagents were purchased from Abberior and used specifically for STED imaging: Abberior STAR 580-conjugated goat anti-mouse IgG (2-0002-005-1), Abberior STAR RED-conjugated goat anti-rabbit IgG (2-0012-011-9), Abberior STAR 635P-conjugated phalloidin (2-0205-007-0) and Abberior Mount Liquid Antifade (4-0100-005-0).

Protein sample preparation and immunoblotting. To evaluate the association of LSP1 with the cortical cytoskeleton, protein lysates were progressively extracted by increasing concentrations of Triton X-100. Cells were washed twice in prewarmed PBS and scraped from dishes in buffer (150 mM NaCl, 1% Triton X-100, 50 mM Tris-HCl (pH 8.0), with protease and phosphatase inhibitors (Roche)). After 5 min on ice with constant agitation, samples were collected in tubes and rotated at 4 °C for 10 min before centrifugation (15 min, 10.000 × g, 4 °C). Supernatants were collected, whereas pellets were resuspended in the same volume used in the first step with the addition of 1% Triton X-100 to the initial lysis buffer, for a final concentration of 2% Triton X-100. Samples were pipetted thoroughly and let rotate at 4 °C for 10 min before centrifugation (15 min, 10.000 × g, 4 °C). This procedure was sequentially repeated until a final concentration of 5% Triton X-100 was reached, and supernatants were saved. Last pellets were resuspended in RIPA buffer (150 mM NaCl, 1% Triton X-100, 0.5% sodium deoxycholate, 0.1% SDS, 50 mM Tris–HCl (pH 8.0)) and vortexed. Equal volumes of protein samples were then mixed with 4× Laemmli sample loading buffer and examined by standard immunoblotting procedure using NuPAGE 4–12% Bis-Tris gels (Invitrogen, Thermo Fisher Scientific), iBlot2 dry blotting system (Thermo Fisher Scientific) and the above-mentioned primary and HRP-conjugated antibodies, as indicated. When needed, nitrocellulose membranes were mild-stripped by extensive washing with buffer (200 mM glycine, 3.5 mM SDS, 1% tween20, (pH 2.2)) before reblocking and reprobing membranes with primary and secondary HRP-conjugated antibodies. Protein bands were visualized by using Super Signal Pico or Femto kit (Pierce) and X Omat AR films (Kodak). Results were scanned and protein band intensities quantified with Fiji distribution of ImageJ (NIH, Bethesda, MD).

Actin co-sedimentation assay. Co-sedimentation binding assays were performed by adding LSP1-6xHis or GST-supervillin fragments to pre-polymerized F-actin according to manufacturer's instructions (Actin binding protein biochem kit™, # BK001, Cytoskeleton, Inc.). Briefly, 20 µM of G-actin was polymerized for 1 h at 24 °C, then mixed to respective purified tagged proteins and left 30 min at 24 °C. The F-actin: protein molar ratio was respectively 16 µM: 4 µM for LSP1-6xHis and 10 µM: 2 µM for GST-supervillin fragments. Samples were then centrifuged at 100,000 × g for 1 h at 24 °C with a Sorvall Discovery M120 ultracentrifuge (Thermo Fisher Scientific) and supernatant and pellet resuspended in SDS loading buffer to reach equal volumes. For direct comparability, equal amounts of sample volumes were analyzed by SDS-PAGE, and bands were visualized by Coomassie blue staining using the Colloidal Blue Staining kit (LC6025, Invitrogen, Thermo Fisher Scientific). Gels were then scanned and protein band intensities quantified with Fiji distribution of ImageJ (NIH, Bethesda, MD).

Myosin co-sedimentation assay. For co-sedimentation assay with sedimentable rabbit skeletal muscle myosin, BSA and purified LSP1- fl or C-terminus-6xHis were mixed together with myosin in the following buffer[23] (50 mM KCl, 10 mM MgCl₂, 20 mM HEPES pH 7.1, 0.1% β-mercaptoethanol, 0.01 mM EGTA) to a molar ratio of 1: 7 (myosin: purified protein) and incubated for 90 min at 24 °C. Samples were then centrifuged at $100,000 \times g$ for 90 min at 24 °C and processed, as described above (see actin co-sedimentation assay).

Immunoprecipitation. Immunoprecipitation of endogenous protein, as well as of GFP constructs was performed according to manufacturer's instructions (Miltenyi Biotech) with modifications. Cells were washed twice in prewarmed PBS and scraped from dishes in buffer (500 mM NaCl, 2% Triton X-100, 50 mM Tris-HCl (pH 8.0), with protease and phosphatase inhibitors (Roche)). After 20 min on ice with constant agitation, samples were collected in tubes and let rotate at 4 °C for 10 min before centrifugation (30 min, $10,000 \times g$, 4 °C). Supernatants were collected and protein concentration measured with Pierce BCA assay (Thermo Fisher Scientific). Equal amount of protein samples were precleared with a mixture of µMACS Protein A/G Microbeads, rotated for 30 min at 4 °C and loaded into prewashed µMACS columns. Eluates were collected and incubated with a mixture of µMACS Protein A/G Microbeads+specific antibody as indicated or µMACS anti-GFP Microbeads, for 2 h with constant rotation at 4 °C. After incubation, protein samples were loaded into prewashed µMACS columns, washed once with starting lysis buffer, twice with RIPA buffer [150 mM NaCl, 1% Triton X-100, 0.5% sodium deoxycholate, 0.1% SDS, 50 mM Tris-HCl (pH 8.0)], twice with high-salt RIPA buffer (500 mM NaCl, 1% Triton X-100, 0.5% sodium deoxycholate, 0.1% SDS, 50 mM Tris–HCl (pH 8.0)) and once with 20 mM Tris-HCl (pH 7.5) before elution with buffer (50 mM Tris–HCl (pH 6.8), 50 mM DTT, 1% SDS, 0.005% bromphenol blue, 10% glycerol). Samples were then mixed with 4× Laemmli sample loading buffer, heated 10 min at 95 °C and examined by standard immunoblot. Normal mouse and rabbit IgG, matching the isotype species of the tested primary antibody, were used as control for immunoprecipitation of endogenous protein, whereas GFP-IP of pEGFP-C1 empty vector was used as control for immunoprecipitation of GFP overexpressed constructs. To test the role of F-actin in the binding of LSP1 to non-muscle myosin IIA, untreated macrophages were scraped in lysis buffer (2% Triton X-100, 150 mM NaCl, 50 mM Tris-HCl (pH 8.0), 5 mM ATP, 5 mM MgCl₂) in the presence of protease inhibitor cocktail (Roche). The sample was subsequently centrifuged at $10,000 \times g$ for 30 min at 4 °C and the supernatant (input) was split into four different samples, two of which were loaded with latrunculin A to a final concentration of 10 µM. All tubes were then incubated with a mixture of µMACS Protein A/G Microbeads+rabbit polyclonal anti-myosin IIA (M8064, Sigma-Aldrich), rotated at 4 °C for 1 h, loaded into prewashed µMACS columns, washed three times with µMACS lysis buffer (1% Triton X-100, 150 mM NaCl, 50 mM Tris–HCl (pH 8.0)) + 10 mM ATP/MgCl₂ where needed, once with 20 mM Tris–HCl (pH 7.5) + 10 mM ATP/MgCl₂ where needed, and then eluted with buffer (50 mM Tris–HCl (pH 6.8), 50 mM DTT, 1% SDS, 0.005% bromphenol blue, 10% glycerol). Samples were then mixed with 4× Laemmli sample loading buffer, heated 10 min at 95 °C and examined by Coomassie blue staining and standard immunoblot.

Proximity ligation assay. Two weeks-old human primary macrophages were seeded on glass coverslips and incubated overnight. Coverslips were pre-fixed in −20° C cold methanol for 1 sec prior to actual fixation with 3.7% formaldehyde/ PBS for 15 min, and permeabilisation in 0.5% Triton X-100 for 5 min. The assay was performed according to manufacturer's instructions (Duolink In Situ, Sigma Aldrich), with an antibody concentration of (0.4 ng/µL).

Immunostaining. Macrophages seeded on glass coverslips were pre-fixed in −20 °C cold methanol for 1 sec prior to actual fixation with 3.7% formaldehyde/PBS for 15 min, and permeabilisation in 0.5% Triton X-100 for 5 min. For better visualization of the podosomal F-actin network for STED imaging, cells were partially extracted/fixed using a solution of 3.7% formaldehyde/0.2% Triton X-100 for 5 min prior to actual fixation with 3.7% formaldehyde/PBS for 10 min and permeabilisation in 0.5% Triton X-100 for 5 min. After fixation samples were blocked with antibody diluting solution (0.05% Triton X-100/PBS + 2% BSA + 0.1% Sodium Azide) + 5% NGS. After staining with specific antibodies or labelling reagents, coverslips were mounted in Mowiol (Calbiochem) containing DABCO (25 mg/ml; Sigma-Aldrich) as anti-fading reagent and sealed with nail polish. The staining of actin isoforms was performed according to the protocol previously by Dugina et al.[39], with minor modifications. Briefly, macrophages seeded on glass coverslips were fixed in 1% formaldehyde dissolved in prewarmed RPMI for 30 min and then permeabilised with methanol for 5 min at −20 °C. Primary antibodies against specific actin isoforms were mixed 1:100 and probed in combination, as indicated. Images of actin isoform staining represent the Z-projection of the several confocal planes that comprise podosomes.

Microscopy. Images of fixed samples were acquired with a Leica TCS SP5 AOBS confocal laser scanner equipped with an oil-immersion HCX PL APO lambda blue 63× NA 1.4 objective and 3× HyD, 1× PMT detectors. Microscope control and image acquisition were performed with Leica LAS AF software (Leica). Time lapse movies were acquired using the above mentioned Leica TCS SP5 AOBS or with UltraVIEW VoX system (Perkin Elmer) equipped with a Nikon Eclipse Ti

microscope body with perfect focus function, a Yokogawa CSU X1 confocal spinning disk, an oil-immersion 60× Apo TIRF (corr.) NA 1.49 objective and a Hamamatsu EM-CCD C9100-50 camera. Microscope control and image acquisition were performed with Volocity 6.1.1 software (Perkin Elmer). The above-mentioned microscopes were equipped with environmental chambers to allow temperature, humidity and CO₂ control. 3D STED imaging of fixed samples were carried out with Abberior 4 channel easy 3D STED superresolution microscope. This system comprises a Nikon Ti-E microscope body, and an oil-immersion 60× P-Apo NA 1.40 objective. For excitation, 561 and 640 nm pulsed lasers were combined with the 775 nm STED pulsed laser. For detetection, 4 avalanche photodiodes (APD) were used in gated mode. Microscope control and image acquisition were performed with Abberior Inspector software (Abberior Instruments).

Protrusion force measurements. Protrusion force measurements were performed as described[50,69]. Briefly, Atomic Force Microscopy (AFM) measurements were performed using silicon nitride cantilevers (MLCT-AUHW, Veeco Instruments) with a nominal spring constant of 0.01 N/m mounted on a NanoWizard III AFM (JPK Instruments) coupled to an inverted optical microscope (Axiovert 200, Carl Zeiss). To prepare Formvar sheets, ethanol-cleaned glass slides were dipped into a Formvar solution of 0.5% (w/v) ethylene dichloride (Electron Microscopy Science) for a few seconds and the solution was emptied from the film casting device using a calibrated flow. A Formvar film was detached from dried slides by contact with water and was left floating at the surface. Acetone-washed 200-mesh nickel grids (EMS) were arranged on the floating film, picked up coated with the film onto another glass slide and then air-dried. To evaluate the thickness of the Formvar sheet, the border of the Formvar that remained on the glass slide after removing the grids was imaged in contact mode by AFM. For AFM experiments of living cells seeded on Formvar-coated grids, a temperature-controlled chamber was used (Petri dish heaterTM, JPK Instruments) and the culture medium was supplemented with 10 mM HEPES (pH 7.4) (Sigma-Aldrich). Images were recorded in contact mode in liquid at scanning forces lower than 1 nN. Cell-induced protrusions were imaged with a pixel resolution of 256 or 512 pixels at line rate around 2 Hz. Forces exerted by single podosomes were derived from the topographical data of podosome-induced protrusions[69] and each cell was attributed the median force value of its podosomes. Briefly, the deformation profile of each protrusion was measured on the AFM image using an ImageJ macro and, combined with the ring radius values, led to the determination of the deformation height h. This was converted to force for each podosome by the relation $F = C_0 \frac{E}{1-\nu^2} \frac{h_f^3}{r_t^2} h$ where the biaxial Young's modulus of Formvar $E/(1-\nu^2)$ is 2.3 GPa[50], $C_0 \approx 2.7$ is a geometric coefficient evaluated from numerical simulations[69] and the film thickness h_f and ring radius r_t were measured for each series of experiments by AFM and immunofluorescence respectively.

Live cell imaging. For live cell imaging, cells were transfected with respective constructs, as indicated, seeded on glass bottom live cell dishes (Ibidi) at subconfluent concentration and incubated overnight before starting live cell imaging acquisition. To evaluate podosome cluster and cell movement together with podosome lifetime in LSP1 depletion conditions, cells were transfected with control siRNA and siRNA against LSP1. After 72 h, cells were re-transfected with pLifeact-TagGFP2 or pLifeact-TagRFP and seeded on glass bottom live cell dishes (Ibidi) at subconfluent concentration. After overnight incubation cells were imaged for at least 1 h. 24 cells from four different donors were evaluated.

Macrophage 3D invasion and LSP1 localization. 3D collagen I invasion of LSP1-depleted macrophages was performed and analysed as described. Briefly, primary human macrophages were transfected with specific siRNA, copolymerised with rat tail collagen (2.5 mg/ml; Becton Dickinson) and embedded in rat tail collagen I (2 mg/ml) containing 10 ng/ml Macrophage-Colony Stimulating Factor (M-CSF, Relia Tech, Wolfenbüttel, Germany). Four days after transfection, brightfield micrographs of invaded areas were acquired (4 images per well) and the number of cells that invaded the surrounding matrix was counted using Fiji cell counter. Four wells per donor and three donors in total were analysed ($n = 16$). For LSP1 3D localization, macrophages were cotransfected with GFP-LSP1 and pLifeact-TagRFP, embedded in rat tail collagen I (2 mg/ml) and incubated overnight before confocal imaging.

Image analysis. Images were post-processed and analysed using Volocity 6.1.1 for Mac (Perkin Elmer) and/or Fiji distribution of ImageJ version 1.51. For color-coded analysis (Fig. 2), each single frame from a time-lapse video was color-coded using the "Temporal color code" tool of Fiji and according to the "Rainbow RGB" LUT. Podosome clusters/cells tracks of LSP1-depleted cells were generated by plotting the XY coordinates of the center of mass of podosome cluster or cells, as calculated by Volocity. The coordinates were imported into GraphPad, and the XY values pruned by subtracting the first time-point XY values in order to have all trajectories starting at $X = 0$, $Y = 0$. Podosome lifetime of LSP1-depleted cells was evaluated by calculating the difference between the time of appearance (fission event or de novo formation) and disappearence (fusion event or dissolution) of ten podosomes per cell (24 cells from four different donors per condition). Cell shape descriptors such as "aspect ratio" (AR), "circularity" (C) and "cell area" were measured using Fiji. Specifically, aspect ratio is calculated as (major axis×minor

axis^{-1}) therefore representing solely the degree of elongation, whereas circularity is calculated as [$4\pi^*$(area × perimeter^{-2})], thus representing the degree of similarity to a circumference with a value ranging from 0 to 1 (perfect circle). To analyze podosome oscillations upon GFP-LSP1 overexpression or knockdown (Fig. 3), the intensities of five individual podosomes per cell (6 cells from two different donors per condition) were measured at every timepoint (20 sec) of a 10 min-long video, using Fiji; intensity values were normalized by subtracting the respective avarage intensity. The number and height of peaks were measured using the "Area under the curve" tool from GraphPad by setting the normalized average intensity as baseline. A single peak was defined as the highest Y-value between two consecutive Y-values below the baseline and the peak height was measured as difference between the highest Y-value of a peak and respective baseline; peak within the shoulder of another peak were not taken in consideration. F-actin core and myosin IIA knockdown experiments (Fig. 4) were measured based on an ImageJ macro[70]. In addition, myosin IIA ROIs were generated by applying the "dilate" tool of Fiji to the previously detected F-actin core ROIs. For proximity ligation assay analysis, images of fixed samples were acquired with confocal Leica TCS SP5 microscope and PLA spots counted using the "FindMaxima" tool of Fiji. 30 μm-long intensity profiles of proteins in Figs. 6,7,9 were measured starting from cell cortex toward the inside of 10 cells from three different donors. In order to allow direct comparability among different protein profiles, the values were interpolated using the "cubic spline" tool from GraphPad and setting the same number of values for all curves; values were then corrected for respective average intensity and normalized to F-actin (or β-actin) intensity values when needed. Ratiometric analysis of actin isoforms was performed with Fiji: confocal Z-planes comprising podosomes were projected onto a single focal plane with averaged intensities, with contrast normalized and enhanced to include max 0.3% of saturated pixels in the podosome area; the "α-cardiac isoform channel was then divided by "β-" or"γ-actin isoform" channel, respectively, and the output calculated as 32-bit floating point values. Ratiometric values of generated images were thresholded from 0 to 2 after applying the "mpI-inferno" LUT. For better visualization, the ratiometric images were "smoothened" by running a 1 pixel Median filter.

Statistical analysis and softwares used. All data were processed with Microsoft Excel 2011 and GraphPad Prism 5 for Mac OSX. Data are presented as mean ± s.e. m. if not otherwise stated in the respective legends. Statistical comparisons are performed using one-sample t-test, two-tailed unpaired t-test or one-way ANOVA with Bonferroni's multiple comparison test as appropriate. Detailed descriptions and values can be found in respective legends and Suppl. Data 1. Statistically significant differences are indicated by single/multiple asterisks (****$P < 0.0001$; ***$P < 0.001$; **$P < 0.01$; and *$P < 0.05$). Correlation analysis was calculated and plotted using a correlation plot and linear regression line. Pearson correlation coefficients (r) are shown in the plots.

Data availability. The authors declare that the data supporting the findings of this study are available within the paper and its supplementary information files, and are available from the authors upon reasonable request.

References

1. Lavin, Y., Mortha, A., Rahman, A. & Merad, M. Regulation of macrophage development and function in peripheral tissues. *Nat. Rev. Immunol.* **15**, 731–744 (2015).
2. Hynes, R. O. The extracellular matrix: not just pretty fibrils. *Science* **326**, 1216–1219 (2009).
3. Dovas, A., Patsialou, A., Harney, A. S., Condeelis, J. & Cox, D. Imaging interactions between macrophages and tumour cells that are involved in metastasis in vivo and in vitro. *J. Microsc.* **251**, 261–269 (2013).
4. Wiesner, C., Le-Cabec, V., El Azzouzi, K., Maridonneau-Parini, I. & Linder, S. Podosomes in space: macrophage migration and matrix degradation in 2D and 3D settings. *Cell Adhes. Migr.* **8**, 179–191 (2014).
5. Vicente-Manzanares, M., Newell-Litwa, K., Bachir, A. I., Whitmore, L. A. & Horwitz, A. R. Myosin IIA/IIB restrict adhesive and protrusive signaling to generate front-back polarity in migrating cells. *J. Cell Biol.* **193**, 381–396 (2011).
6. Paluch, E., van der Gucht, J. & Sykes, C. Cracking up: symmetry breaking in cellular systems. *J. Cell Biol.* **175**, 687–692 (2006).
7. Maupin, P., Phillips, C. L., Adelstein, R. S. & Pollard, T. D. Differential localization of myosin-II isozymes in human cultured cells and blood cells. *J. Cell Sci.* **107**, 3077–3090 (1994). Pt 11.
8. Linder, S., Nelson, D., Weiss, M. & Aepfelbacher, M. Wiskott-Aldrich syndrome protein regulates podosomes in primary human macrophages. *Proc. Natl Acad. Sci. USA* **96**, 9648–9653 (1999).
9. Burns, S., Thrasher, A. J., Blundell, M. P., Machesky, L. & Jones, G. E. Configuration of human dendritic cell cytoskeleton by Rho GTPases, the WAS protein, and differentiation. *Blood* **98**, 1142–1149 (2001).
10. Destaing, O., Saltel, F., Geminard, J. C., Jurdic, P. & Bard, F. Podosomes display actin turnover and dynamic self-organization in osteoclasts expressing actin-green fluorescent protein. *Mol. Biol. Cell.* **14**, 407–416 (2003).
11. Moreau, V., Tatin, F., Varon, C. & Genot, E. Actin can reorganize into podosomes in aortic endothelial cells, a process controlled by Cdc42 and RhoA. *Mol. Cell Biol.* **23**, 6809–6822 (2003).
12. Gimona, M., Kaverina, I., Resch, G. P., Vignal, E. & Burgstaller, G. Calponin repeats regulate actin filament stability and formation of podosomes in smooth muscle cells. *Mol. Biol. Cell* **14**, 2482–2491 (2003).
13. Murphy, D. A. et al. A Src-Tks5 pathway is required for neural crest cell migration during embryonic development. *PLoS ONE* **6**, e22499 (2011).
14. Linder, S. & Wiesner, C. Tools of the trade: podosomes as multipurpose organelles of monocytic cells. *Cell Mol. Life Sci.* **72**, 121–135 (2015).
15. Tarone, G., Cirillo, D., Giancotti, F. G., Comoglio, P. M. & Marchisio, P. C. Rous sarcoma virus-transformed fibroblasts adhere primarily at discrete protrusions of the ventral membrane called podosomes. *Exp. Cell. Res.* **159**, 141–157 (1985).
16. Zambonin-Zallone, A., Teti, A., Carano, A. & Marchisio, P. C. The distribution of podosomes in osteoclasts cultured on bone laminae: effect of retinol. *J. Bone Miner. Res.: Off. J. Am. Soc. Bone Miner. Res.* **3**, 517–523 (1988).
17. Chabadel, A. et al. CD44 and beta3 integrin organize two functionally distinct actin-based domains in osteoclasts. *Mol. Biol. Cell* **18**, 4899–4910 (2007).
18. Teti, A., Grano, M., Carano, A., Colucci, S. & Zambonin Zallone, A. Immunolocalization of beta 3 subunit of integrins in osteoclast membrane. *Boll. Soc. Ital. Biol. Sper.* **65**, 1031–1037 (1989).
19. Luxenburg, C. et al. The architecture of the adhesive apparatus of cultured osteoclasts: from podosome formation to sealing zone assembly. *PLoS ONE* **2**, e179 (2007).
20. Bhuwania, R. et al. Supervillin couples myosin-dependent contractility to podosomes and enables their turnover. *J. Cell Sci.* **125**, 2300–2314 (2012).
21. Mersich, A. T., Miller, M. R., Chkourko, H. & Blystone, S. D. The formin FRL1 (FMNL1) is an essential component of macrophage podosomes. *Cytoskeleton* **67**, 573–585 (2010).
22. Panzer, L. et al. The formins FHOD1 and INF2 regulate inter- and intra-structural contractility of podosomes. *J. Cell Sci.* **129**, 298–313 (2016).
23. Chen, Y. et al. F-actin and myosin II binding domains in supervillin. *J. Biol. Chem.* **278**, 46094–46106 (2003).
24. Fedechkin, S. O. et al. An N-terminal, 830 residues intrinsically disordered region of the cytoskeleton-regulatory protein supervillin contains Myosin II- and F-actin-binding sites. *J. Biomol. Struct. Dyn.* **31**, 1150–1159 (2013).
25. Takizawa, N., Ikebe, R., Ikebe, M. & Luna, E. J. Supervillin slows cell spreading by facilitating myosin II activation at the cell periphery. *J. Cell Sci.* **120**, 3792–3803 (2007).
26. Jongstra-Bilen, J., Harrison, R. & Grinstein, S. Fcgamma-receptors induce Mac-1 (CD11b/CD18) mobilization and accumulation in the phagocytic cup for optimal phagocytosis. *J. Biol. Chem.* **278**, 45720–45729 (2003).
27. Maxeiner, S. et al. Crucial role for the LSP1-myosin1e bimolecular complex in the regulation of Fcgamma receptor-driven phagocytosis. *Mol. Biol. Cell* **26**, 1652–1664 (2015).
28. Howard, T. H., Hartwig, J. & Cunningham, C. Lymphocyte-specific protein 1 expression in eukaryotic cells reproduces the morphologic and motile abnormality of NAD 47/89 neutrophils. *Blood* **91**, 4786–4795 (1998).
29. Coates, T. D., Torkildson, J. C., Torres, M., Church, J. A. & Howard, T. H. An inherited defect of neutrophil motility and microfilamentous cytoskeleton associated with abnormalities in 47-Kd and 89-Kd proteins. *Blood* **78**, 1338–1346 (1991).
30. Howard, T., Li, Y., Torres, M., Guerrero, A. & Coates, T. The 47-kD protein increased in neutrophil actin dysfunction with 47- and 89-kD protein abnormalities is lymphocyte-specific protein. *Blood* **83**, 231–241 (1994).
31. Jongstra-Bilen, J. & Jongstra, J. Leukocyte-specific protein 1 (LSP1): a regulator of leukocyte emigration in inflammation. *Immunol. Res.* **35**, 65–74 (2006).
32. Hwang, S. H. et al. Leukocyte-specific protein 1 regulates T-cell migration in rheumatoid arthritis. *Proc. Natl Acad. Sci. USA* **112**, E6535–E6543 (2015).
33. Ampe, C. & Van Troys, M. Mammalian actins: isoform-specific functions and diseases. *Handbook Exp. Pharmacol.* **235**, 1–37 (2017).
34. Perrin, B. J. & Ervasti, J. M. The actin gene family: function follows isoform. *Cytoskeleton* **67**, 630–634 (2010).
35. Vandekerckhove, J. & Weber, K. At least six different actins are expressed in a higher mammal: an analysis based on the amino acid sequence of the amino-terminal tryptic peptide. *J. Mol. Biol.* **126**, 783–802 (1978).
36. Perrin, B. J., Sonnemann, K. J. & Ervasti, J. M. Beta-actin and gamma-actin are each dispensable for auditory hair cell development but required for Stereocilia maintenance. *PLoS Genet.* **6**, e1001158 (2010).
37. De La Cruz, E. M. Cofilin binding to muscle and non-muscle actin filaments: isoform-dependent cooperative interactions. *J. Mol. Biol.* **346**, 557–564 (2005).

38. Larsson, H. & Lindberg, U. The effect of divalent cations on the interaction between calf spleen profilin and different actins. *Biochim. Biophys. Acta* **953**, 95–105 (1988).

39. Dugina, V., Zwaenepoel, I., Gabbiani, G., Clement, S. & Chaponnier, C. Beta and gamma-cytoplasmic actins display distinct distribution and functional diversity. *J. Cell Sci.* **122**, 2980–2988 (2009).

40. Cervero, P., Himmel, M., Kruger, M. & Linder, S. Proteomic analysis of podosome fractions from macrophages reveals similarities to spreading initiation centres. *Eur. J. Cell Biol.* **91**, 908–922 (2012).

41. Evans, J. G., Correia, I., Krasavina, O., Watson, N. & Matsudaira, P. Macrophage podosomes assemble at the leading lamella by growth and fragmentation. *J. Cell Biol.* **161**, 697–705 (2003).

42. Lomakin, A. J. et al. Competition for actin between two distinct F-actin networks defines a bistable switch for cell polarization. *Nat. Cell Biol.* **17**, 1435–1445 (2015).

43. Linder, S., Hufner, K., Wintergerst, U. & Aepfelbacher, M. Microtubule-dependent formation of podosomal adhesion structures in primary human macrophages. *J. Cell Sci.* **113**, 4165–4176 (2000). Pt 23.

44. Bouissou, A. et al. Podosome force generation machinery: a local balance between protrusion at the core and traction at the ring. *ACS Nano* **11**, 4028–4040 (2017).

45. Linder, S. & Wiesner, C. Feel the force: Podosomes in mechanosensing. *Exp. Cell Res.* **343**, 67–72 (2016).

46. van den Dries, K., Bolomini-Vittori, M. & Cambi, A. Spatiotemporal organization and mechanosensory function of podosomes. *Cell Adhes. Migr.* **8**, 268–272 (2014).

47. Luxenburg, C., Winograd-Katz, S., Addadi, L. & Geiger, B. Involvement of actin polymerization in podosome dynamics. *J. Cell. Sci.* **125**, 1666–1672 (2012).

48. Labernadie, A. et al. Protrusion force microscopy reveals oscillatory force generation and mechanosensing activity of human macrophage podosomes. *Nat. Commun.* **5**, 5343 (2014).

49. van den Dries, K. et al. Interplay between myosin IIA-mediated contractility and actin network integrity orchestrates podosome composition and oscillations. *Nat. Commun.* **4**, 1412 (2013).

50. Labernadie, A., Thibault, C., Vieu, C., Maridonneau-Parini, I. & Charriere, G. M. Dynamics of podosome stiffness revealed by atomic force microscopy. *Proc. Natl Acad. Sci. USA* **107**, 21016–21021 (2010).

51. van Helden, S. F. et al. PGE2-mediated podosome loss in dendritic cells is dependent on actomyosin contraction downstream of the RhoA-Rho-kinase axis. *J. Cell. Sci.* **121**, 1096–1106 (2008).

52. Hannigan, M., Zhan, L., Ai, Y. & Huang, C. K. Leukocyte-specific gene 1 protein (LSP1) is involved in chemokine KC-activated cytoskeletal reorganization in murine neutrophils in vitro. *J. Leukoc. Biol.* **69**, 497–504 (2001).

53. Klein, D. P., Jongstra-Bilen, J., Ogryzlo, K., Chong, R. & Jongstra, J. Lymphocyte-specific Ca2+-binding protein LSP1 is associated with the cytoplasmic face of the plasma membrane. *Mol. Cell Biol.* **9**, 3043–3048 (1989).

54. Prasad, A. et al. Slit2N/Robo1 inhibit HIV-gp120-induced migration and podosome formation in immature dendritic cells by sequestering LSP1 and WASp. *PLoS ONE* **7**, e48854 (2012).

55. Jongstra-Bilen, J. et al. LSP1 modulates leukocyte populations in resting and inflamed peritoneum. *Blood* **96**, 1827–1835 (2000).

56. Southwick, F. S., Dabiri, G. A. & Stossel, T. P. Neutrophil actin dysfunction is a genetic disorder associated with partial impairment of neutrophil actin assembly in three family members. *J. Clin. Invest.* **82**, 1525–1531 (1988).

57. Jongstra-Bilen, J., Janmey, P. A., Hartwig, J. H., Galea, S. & Jongstra, J. The lymphocyte-specific protein LSP1 binds to F-actin and to the cytoskeleton through its COOH-terminal basic domain. *J. Cell Biol.* **118**, 1443–1453 (1992).

58. Jang, D. J., Guo, M. & Wang, D. Proteomic and biochemical studies of calcium- and phosphorylation-dependent calmodulin complexes in Mammalian cells. *J. Proteome Res.* **6**, 3718–3728 (2007).

59. Jongstra-Bilen, J., Young, A. J., Chong, R. & Jongstra, J. Human and mouse LSP1 genes code for highly conserved phosphoproteins. *J. Immunol.* **144**, 1104–1110 (1990).

60. Bassell, G. J. et al. Sorting of beta-actin mRNA and protein to neurites and growth cones in culture. *J. Neurosci.: Off. J. Soc. Neurosci.* **18**, 251–265 (1998).

61. Bergeron, S. E., Zhu, M., Thiem, S. M., Friderici, K. H. & Rubenstein, P. A. Ion-dependent polymerization differences between mammalian beta- and gamma-nonmuscle actin isoforms. *J. Biol. Chem.* **285**, 16087–16095 (2010).

62. Allen, P. G. et al. Phalloidin binding and rheological differences among actin isoforms. *Biochemistry* **35**, 14062–14069 (1996).

63. Oda, T., Iwasa, M., Aihara, T., Maeda, Y. & Narita, A. The nature of the globular- to fibrous-actin transition. *Nature* **457**, 441–445 (2009).

64. Condeelis, J. & Singer, R. H. How and why does beta-actin mRNA target? *Biol. Cell.* **97**, 97–110 (2005).

65. Winkelman, J. D. et al. Fascin- and alpha-Actinin-Bundled networks contain intrinsic structural features that drive protein sorting. *Curr. Biol.* **26**, 2697–2706 (2016).

66. Meddens, M. B. et al. Actomyosin-dependent dynamic spatial patterns of cytoskeletal components drive mesoscale podosome organization. *Nat. Commun.* **7**, 13127 (2016).

67. Wulfkuhle, J. D. et al. Domain analysis of supervillin, an F-actin bundling plasma membrane protein with functional nuclear localization signals. *J. Cell Sci.* **112**, 2125–2136 (1999). Pt 13.

68. Smith, A. L. et al. Leukocyte-specific protein 1 interacts with DC-SIGN and mediates transport of HIV to the proteasome in dendritic cells. *J. Exp. Med.* **204**, 421–430 (2007).

69. Proag, A. et al. Working together: spatial synchrony in the force and actin dynamics of podosome first neighbors. *ACS Nano* **9**, 3800–3813 (2015).

70. Cervero, P., Panzer, L. & Linder, S. Podosome reformation in macrophages: assays and analysis. *Methods Mol. Biol.* **1046**, 97–121 (2013).

Author contributions

P.C. designed and performed experiments and co-wrote the manuscript, C.W. performed 3D invasion experiments, A.B. and R.P. performed protrusion force microscopy, S.L. designed experiments and wrote the manuscript.

Additional information

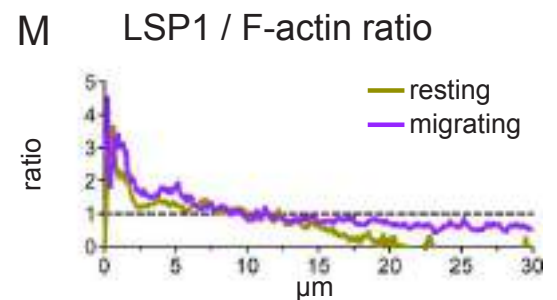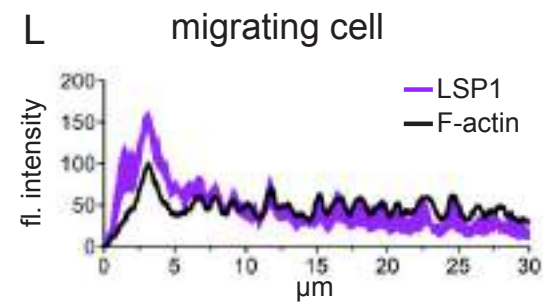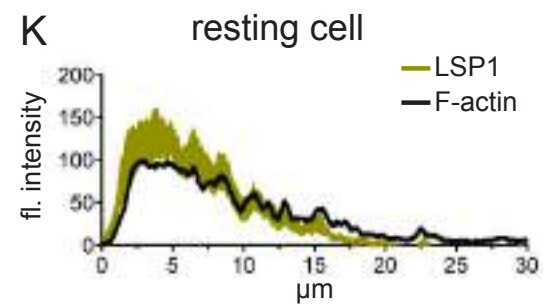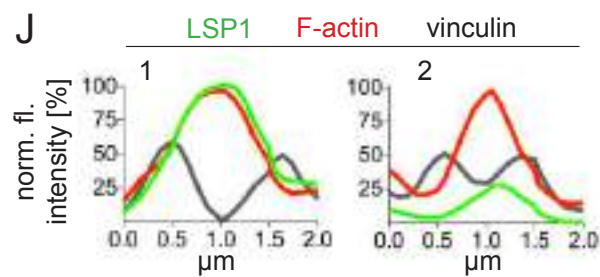**Supplementary Information** accompanies this paper at https://doi.org/10.1038/s41467-018-02904-x.
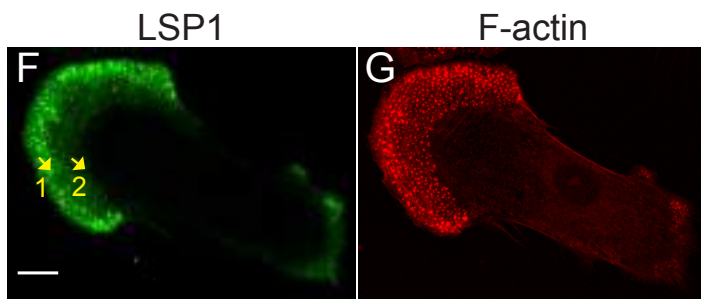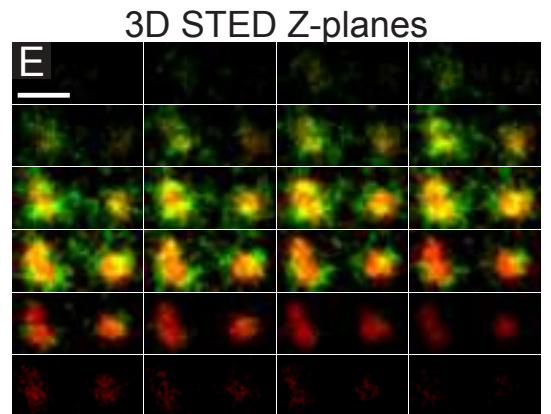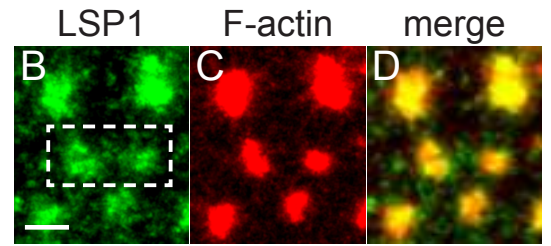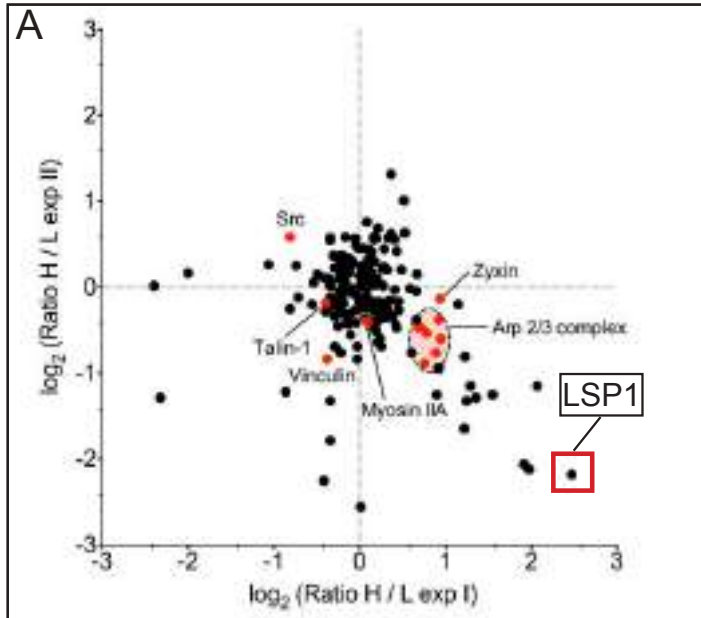
Competing interests: The authors declare no competing financial interests.

Reprints and permission information is available online at http://npg.nature.com/reprintsandpermissions/

Publisher's note: Springer Nature remains neutral with regard to jurisdictional claims in published maps and institutional affiliations.

64

A

B LSP1   C F-actin   D merge

3D STED Z-planes

E

F LSP1   G F-actin

H vinculin   I merge

J   LSP1   F-actin   vinculin

K resting cell

L migrating cell

M LSP1 / F-actin ratio

Supplementary Figure 1. SILAC analysis identifies LSP1 as a potential component of podosomes; STED analysis of podosomes; LSP1 is enriched at the leading edge of cells.

(A) Log2 ratios from SILAC analysis of podosome-enriched cell fractions from human macrophages. Proteins that are sensitive to inhibition of Src tyrosine signalling, and thus potentially podosome-associated, are enriched in the lower quadrant. Note respective enrichments of typical podosome components such as Arp2/3 complex, myosin IIA and vinculin, and highlighted position of LSP1. Modified, with permission, from (Cervero et al., 2012). (B-D) STED micrographs in extended focus mode of macrophage podosomes stained for LSP1 (B, green) and F-actin (C, red), with merge (D). Scale bars: 1 µm. Dashed box in (B) indicates detail region shown in several optical z planes from the apical to the ventral side in (E), which were used for 3D STED reconstruction shown in Fig. 1F. Note localization of LSP1 to the podosome cap and to podosome-connecting cables. Scale unit: 1 µm. (F-I) Confocal micrographs of a migratory macrophage stained for LSP1 using specific primary antibody and Alexa 488-labeled secondary antibody (F, green), for F-actin using Alexa 405-labeled phalloidin (G, red), and for vinculin using specific primary antibody and Alexa568-labeled secondary antibody (H, white), with merge (I). Scale bar: 10 µm. Yellow lines (1,2) in (F) indicate confocal planes used for measurements of respective fluorescence intensities shown in (J), with respective maximal fluorescence intensities set to 100%. Note enrichment of LSP1 at precursor podosome at the leading edge, compared to lower abundance at more internal successor podosome. (K-L) Analysis of LSP1 and F-actin intensities. Endogenous LSP1 and F-actin were stained with respective antibodies or Alexa 568-labeled phalloidin. Respective pixel intensities were measured along 30 µm starting with the cell edge, in both resting (K) and migratory (L) cells. Y-axis indicate relative fluorescence intensities, normalized to F-actin intensity values. (M) Respective LSP1/F-actin ratios based on graphs from (K,L). Note enrichment of LSP1 over F-actin in the cell periphery (5-10 µm from cell edges).

67
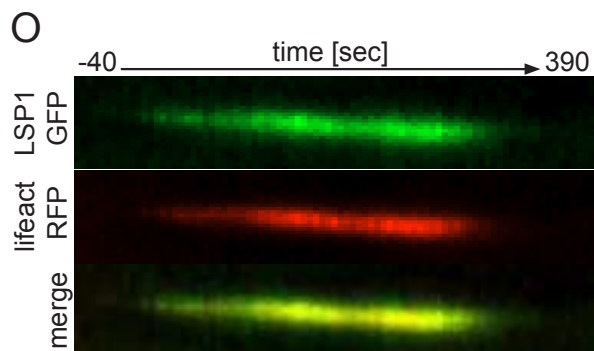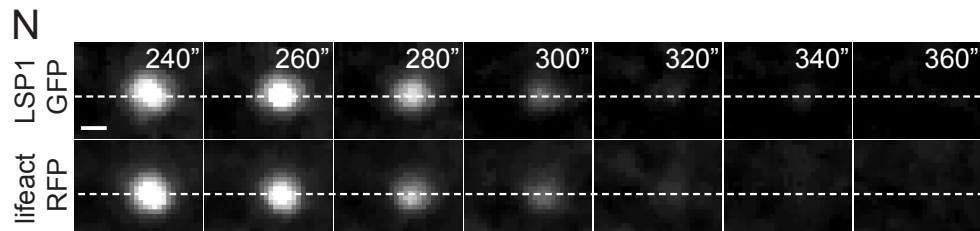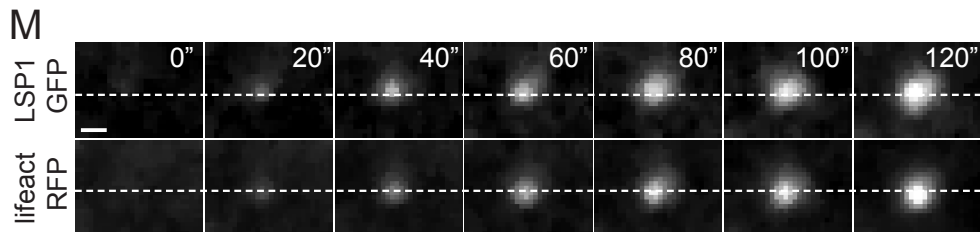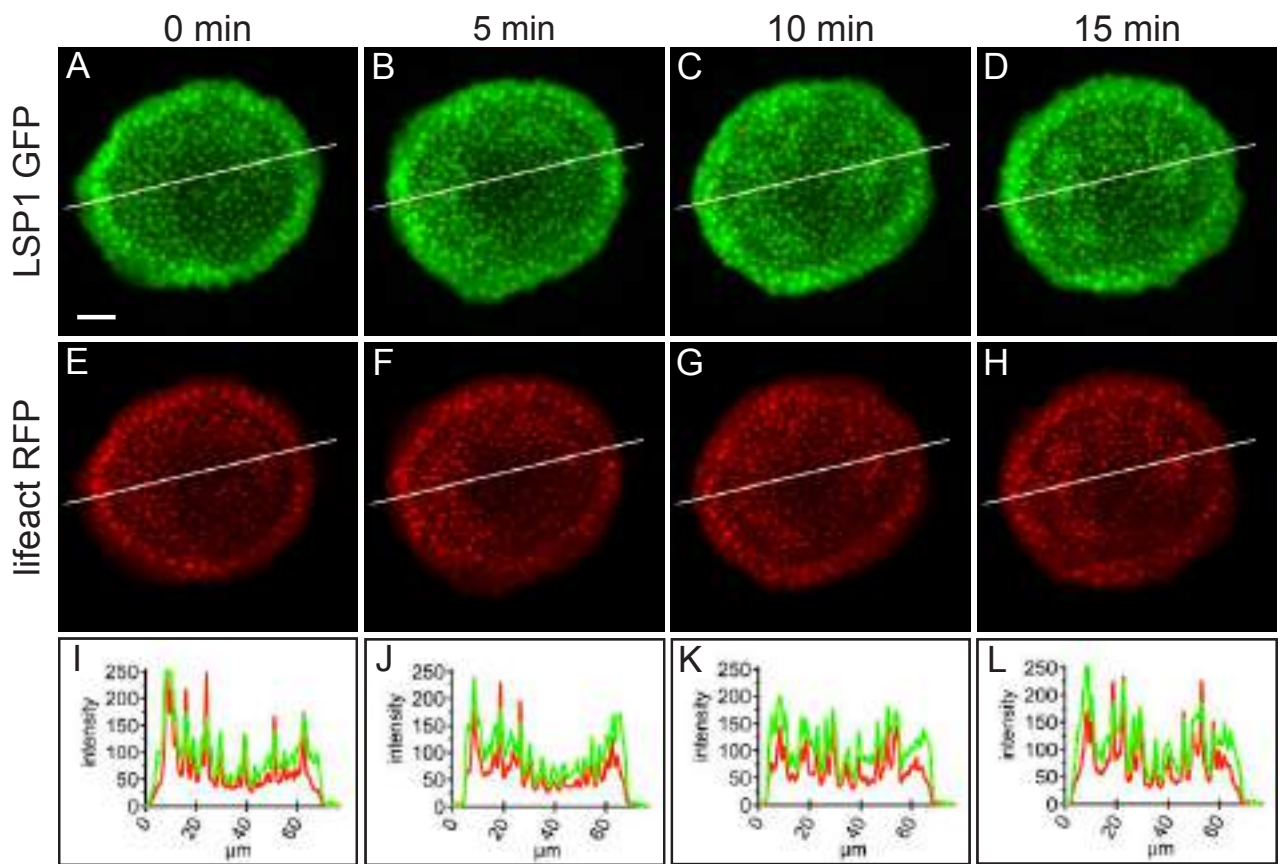
Supplementary Figure 2. LSP1 and F-actin show comparable dynamics in quiescent macrophages.

(A-H) Still images from confocal live cell video of macrophage expressing LSP1-GFP (A-D, green) and lifeact-RFP (E-H) to label podosome cores. White lines in (A-H) indicate plane of pixels used for evaluation of fluorescence intensities shown in (I-L). Note comparable enrichment of LSP1-GFP at the periphery of quiescent cell, and also at individual podosomes Scale bar: 10 μm.

(M-O) LSP1-GFP and F-actin show similar dynamics during podosome lifetime. Still images from TIRF live cell video (time resolution of 5 sec/ frame) of LSP1-GFP (upper rows) and lifeact-RFP (lower rows) expressing macrophage showing de novo formation of single podosome (M) and dissolution of the same podosome (N). Respective fluorescence signals are shown in inverted greyscale. Scale bar: 1 μm. Time since start of experiment is indicated in sec. (O) Kymograph of podosome shown in (M,N), with time indicated in sec. Pixels used for generation of kymograph are indicated by dashed white line in (M-N).
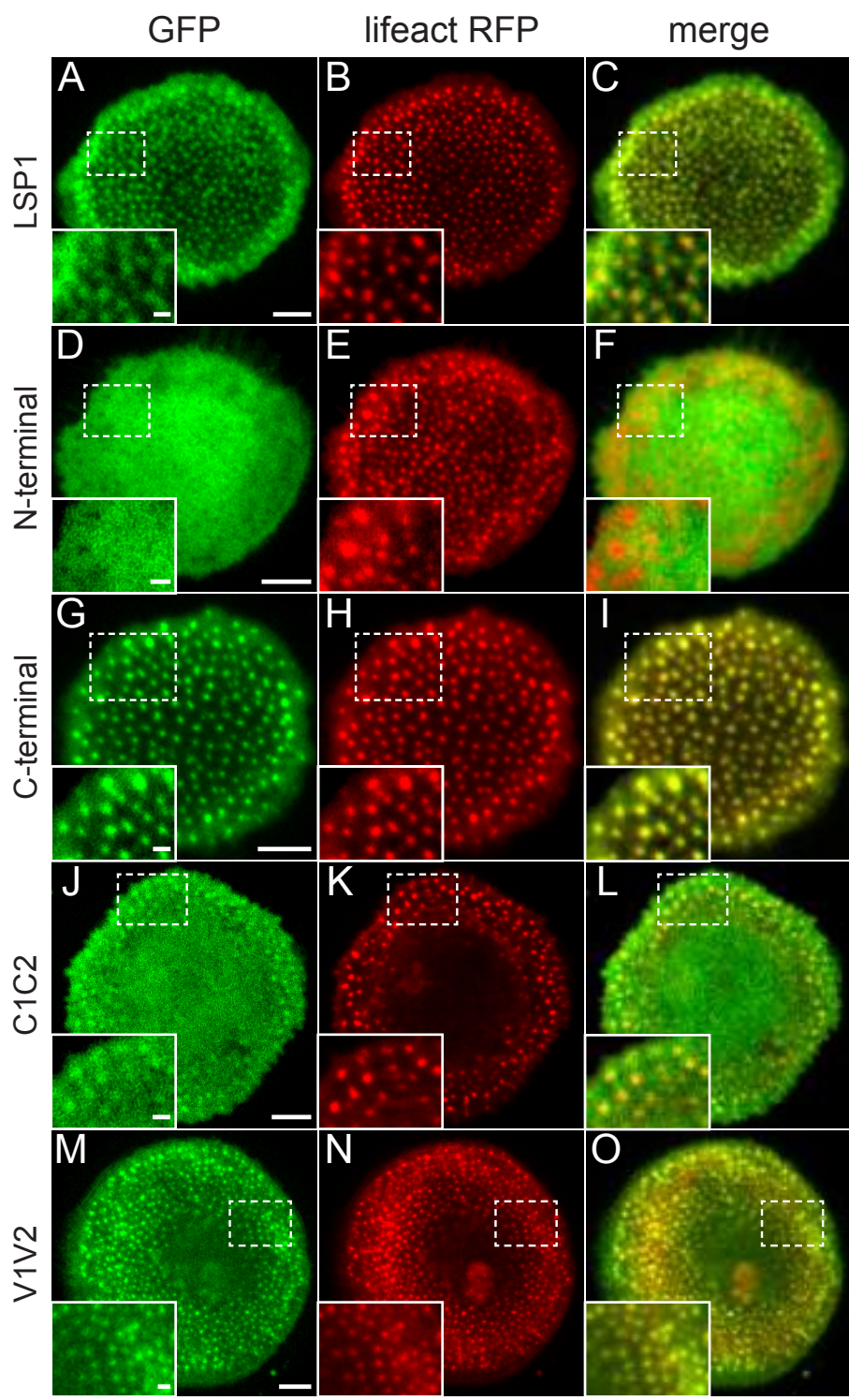
Supplementary Figure 3. The C-terminal villin-like domains of LSP1 are crucial for the localization to podosomes.

Confocal micrographs of macrophages expressing indicated constructs, with GFP signal in (A,D,G,J,M), and coexpressing lifeact-RFP to label podosome cores (B,E,H,K,N), with merges (C,F,I,L,O). Dashed boxes indicate detail regions shown as insets. Note unspecific localization of the N-terminal construct (D-F), but clear localization to podosomes of the C-terminal constructs, especially the V1/V2 containing ones (G-I,M-O). Scale bars: 10µm and 2µm for insets.
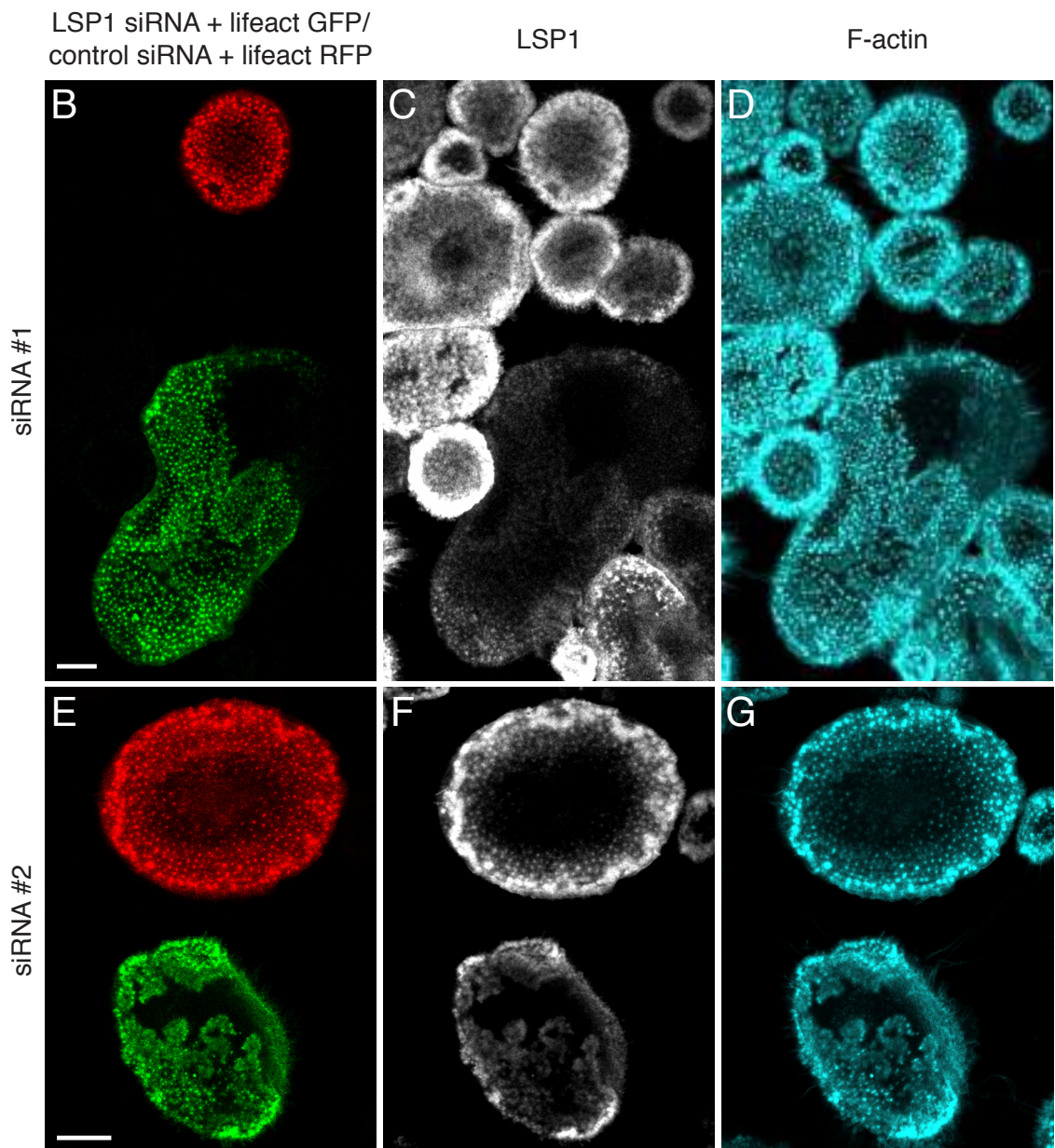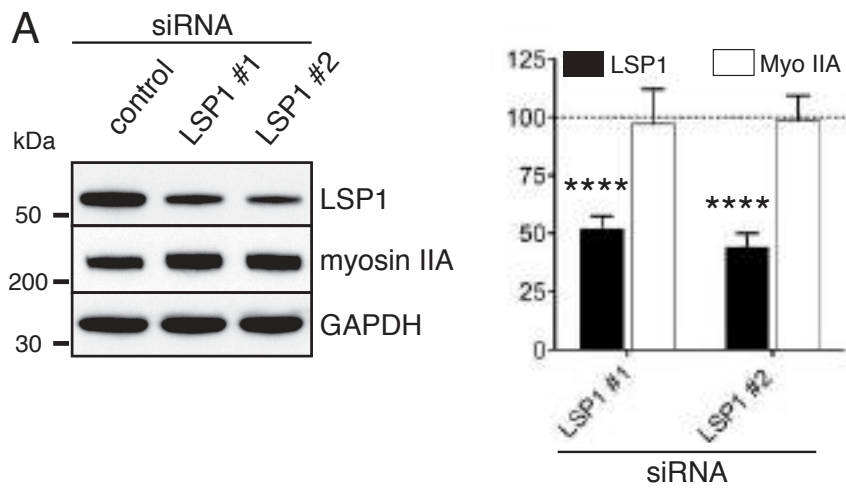
Supplementary Figure 4. LSP1 knockdown does not change myosin IIA protein levels.

(A) Western blots from lysates of cells treated with either of two LSP1-specific siRNAs or luciferase siRNA as control, developed with anti-LSP1 or anti-myosin II antibodies and quantified as shown in the respective graph, with control set to 100%. Molecular weight indicated in kDa on left. Values are given as mean ± s.e.m. N=8, independent experiments; one-sample t-test; ****: P<0.0001. For specific values, see Suppl. Table S1. (B-G) Confocal micrographs of mixed macrophage populations. Cells treated with LSP1 siRNA are labeled by co-transfection and expression of lifeact-GFP (B,E; green), cells treated with control siRNA by co-transfection and expression of lifeact-RFP (B,E; red). Cells were stained for LSP1 using specific primary antibody (C,F; white) and Alexa 647-labeled secondary antibody, and for F-actin using Alexa 405-labeled phalloidin (D,G; blue). Scale bars: 10 µm.
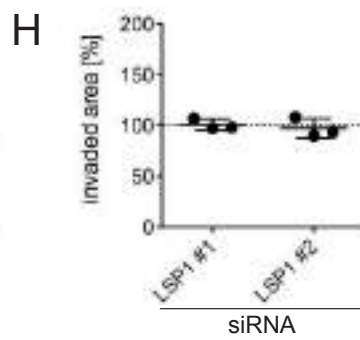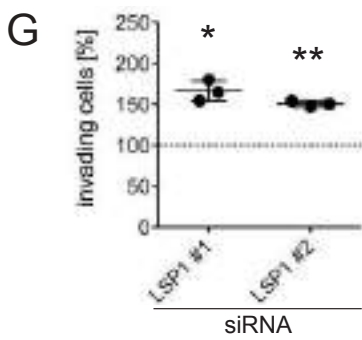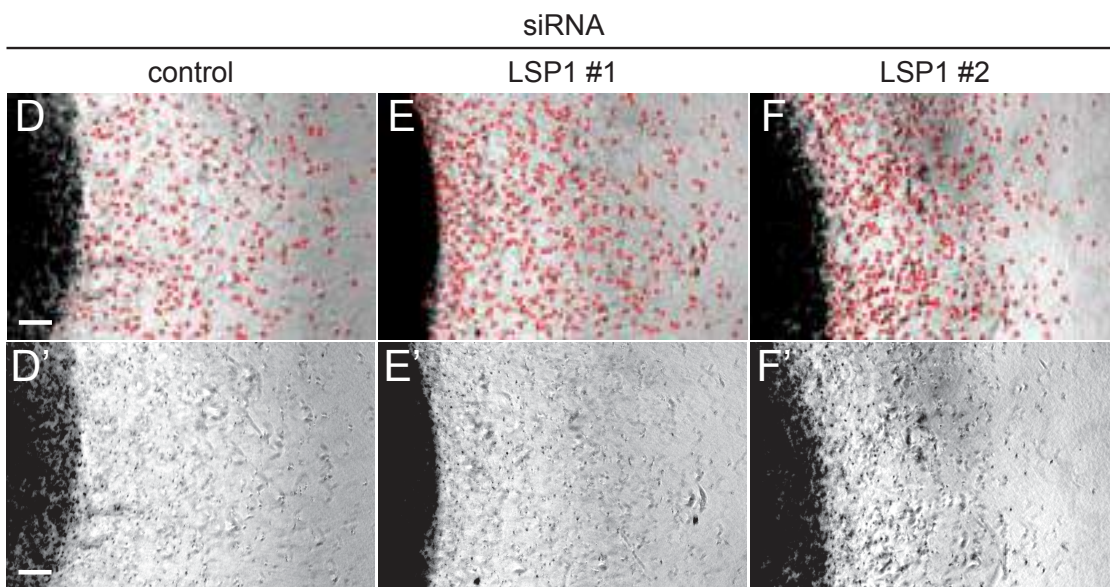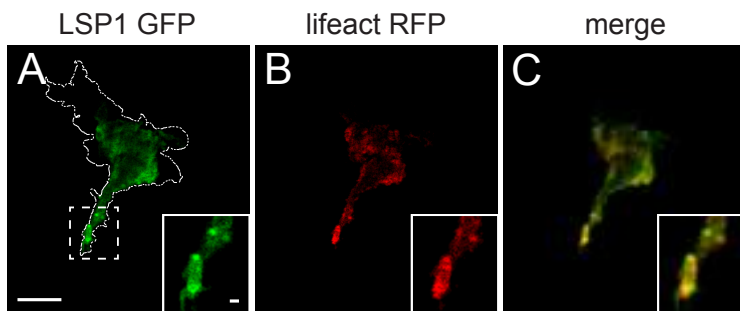
**Supplementary Figure 5. LSP1 is a regulator of macrophage 3D invasion.**

(A-C) LSP1 localizes to F-actin-rich protrusions in a 3D environment. Confocal micrograph of macrophage expressing LSP1-GFP (A) and lifeact-RFP (B), with merge (C), embedded in 3D collagen I matrix. Dashed line in (A) indicates cell outline in extended focus mode. Dashed box in (A) indicates detail region shown as insets. White bars: 10 µm and 1 µm in insets. (D-H) Evaluation of 3D macrophage invasion in a collagen plug invasion assay. (D-F) Brightfield micrographs of invading cells treated with indicated siRNA. Note dark zone of central plug with embedded macrophages, and bright zone of collagen matrix with invaded cells, visible as dark dots and highlighted by red circles. Scale bar: 100 µm. (D´-D´) Respective micrographs without red dot labelling. (G-H) Quantification of cell invasion into collagen matrix, at day 4 after seeding, with evaluation of cell numbers (G) and invaded area (H). Values for control siRNA were set to 100 %. Note enhanced number of invaded cells in case of LSP1 knockdown. Values are given as Mean ± S.D; 16 pictures per donor (N=3) were evaluated in each treatment; one-sample t-test; *: P<0.05, **: P<0.01. For specific values, see Suppl. Table S1

75
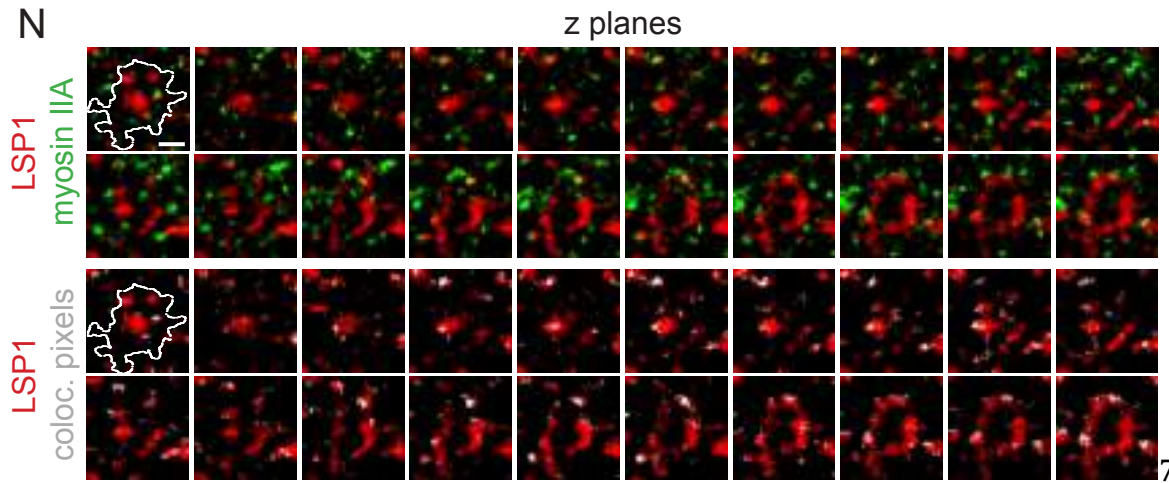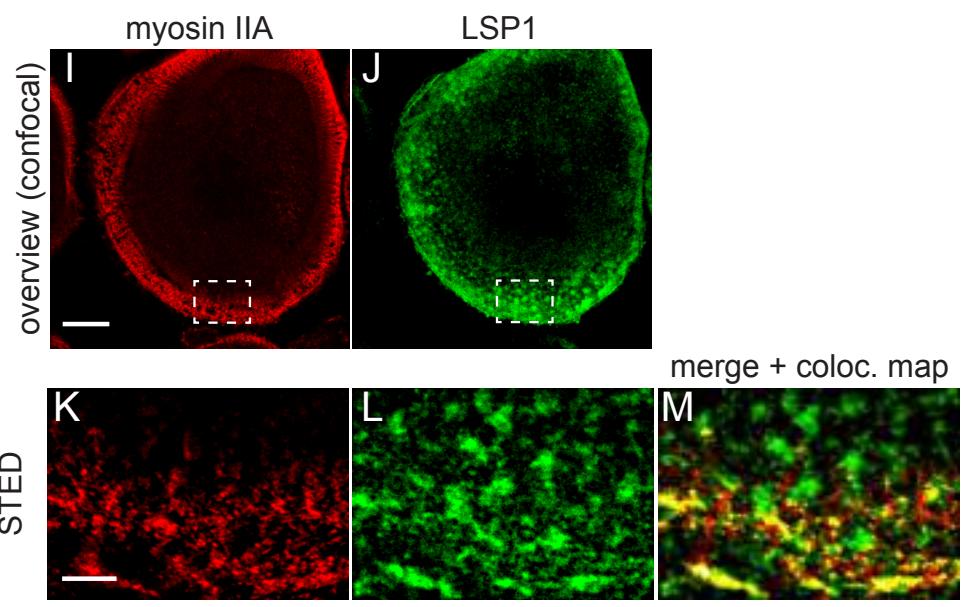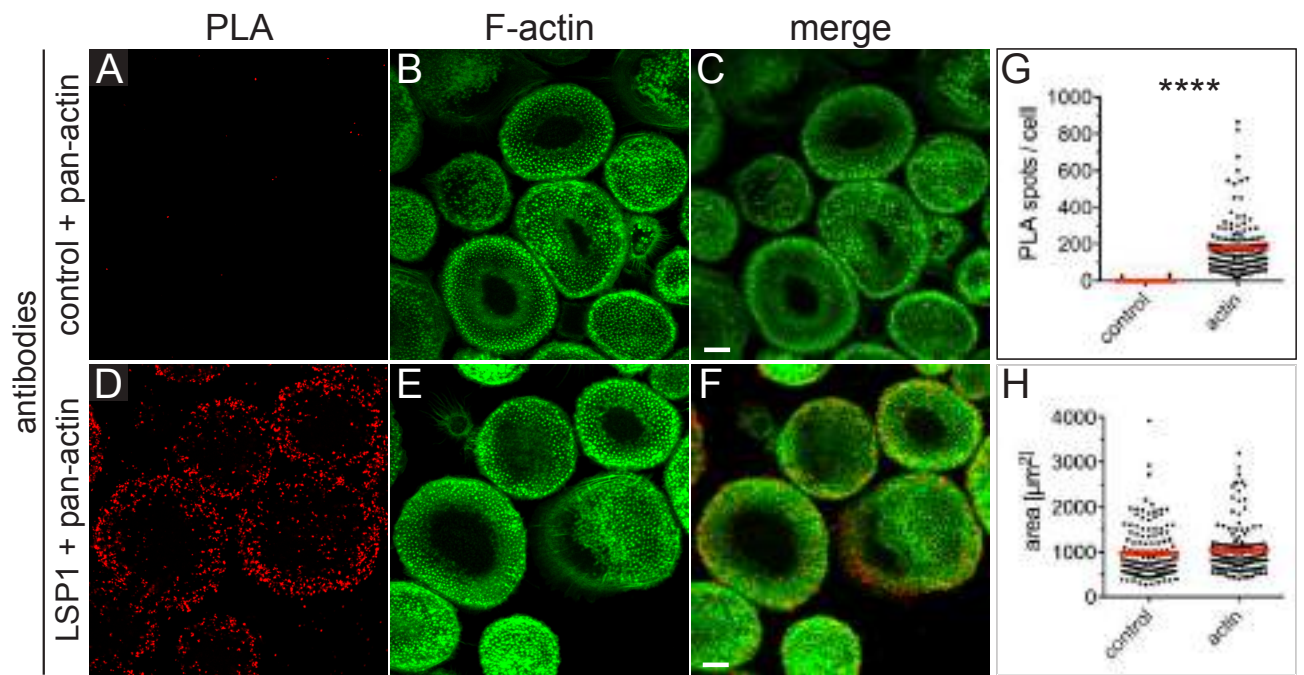
Supplementary Figure 6. Subcellular interaction of LSP1 and actin.

(A-F) Confocal micrographs of macrophages subjected to a proximity ligation assay (PLA), using pan-actin-specific antibody, together with control IgG (A) or LSP1-specific antibody (D) and stained for F-actin (B,E), with merges (C,F). Scale bars: 10 µm. Note low background in (A) and PLA signals, especially in the cell periphery, in (D). (G,H) Statistical evaluation of number of PLA spots per cell (G) and cellular area analysed for respective PLAs (H). Each dot represents one cell. Data collected from 2 different donors. Values are given as mean ± s.e.m. ****: P<0.0001. For specific values, see Suppl. Table S1. (I-M) LSP1 and myosin IIA colocalize especially in the cell periphery of macrophages. (I,J) Confocal micrographs of macrophage stained for myosin IIA and LSP1 using specific antibodies. Scale bar: 10 µm. Dashed white boxes indicate detail region analysed by STED microscopy, as shown in (K,L), with merge of LSP1 signal (green), myosin IIA (red) and myosin IIA/LSP1 map of colocalizing pixels (yellow) (M). Scale bar: 2 µm. (N) Merges of STED micrographs of macrophage podosomes stained for LSP1 (red) and myosin IIA (green). Gallery shows optical z planes from apical to ventral side of the podosome. Dashed box in first image indicates circumference of a single podosome in extended focus mode. Lower rows: corresponding merges of LSP1 staining (red) and LSP1/myosin IIA colocalization pixels (white). Scale bar: 0.5 µm.
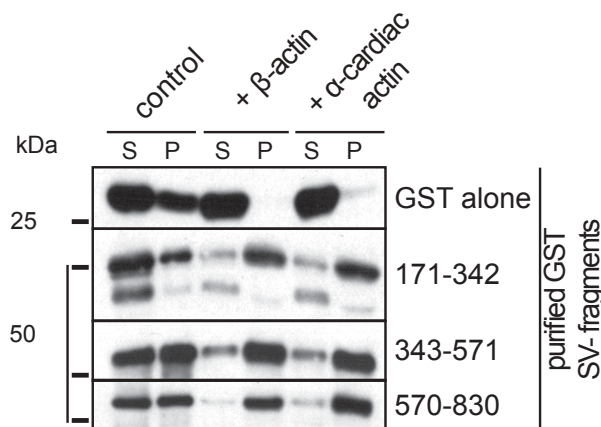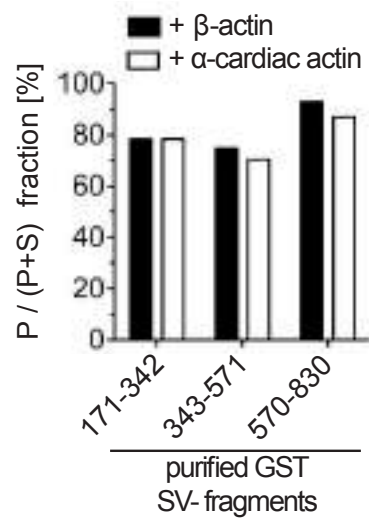
A GFP-IP inputs
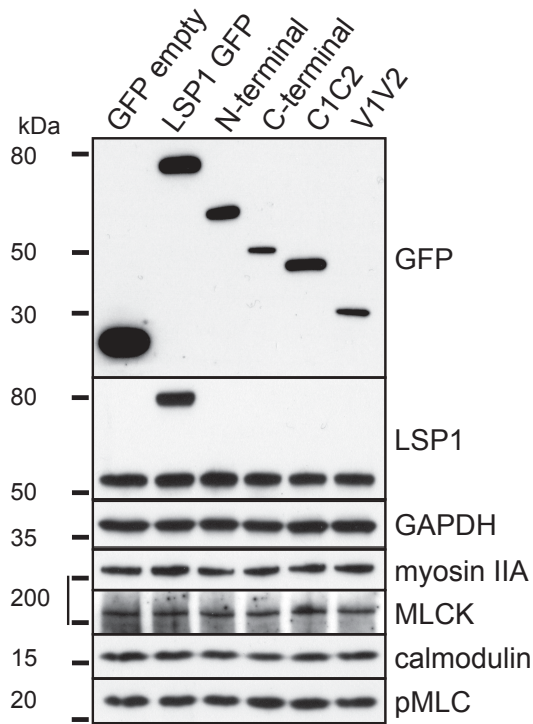
B co-sedimentation of rabbit skeletal muscle myosin
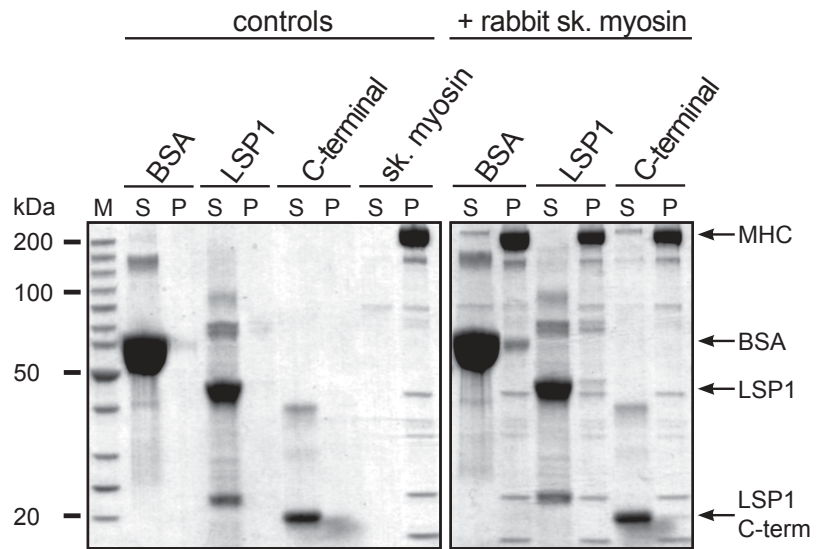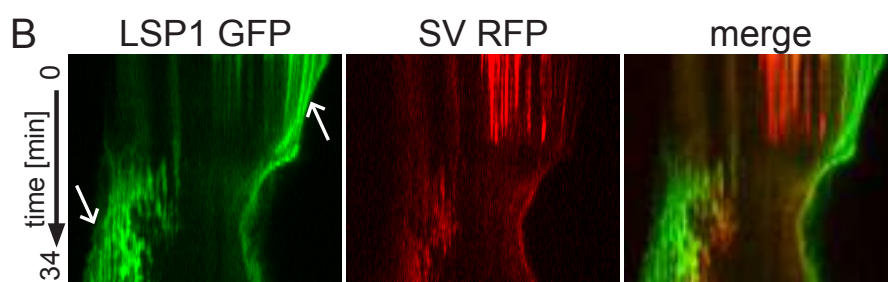
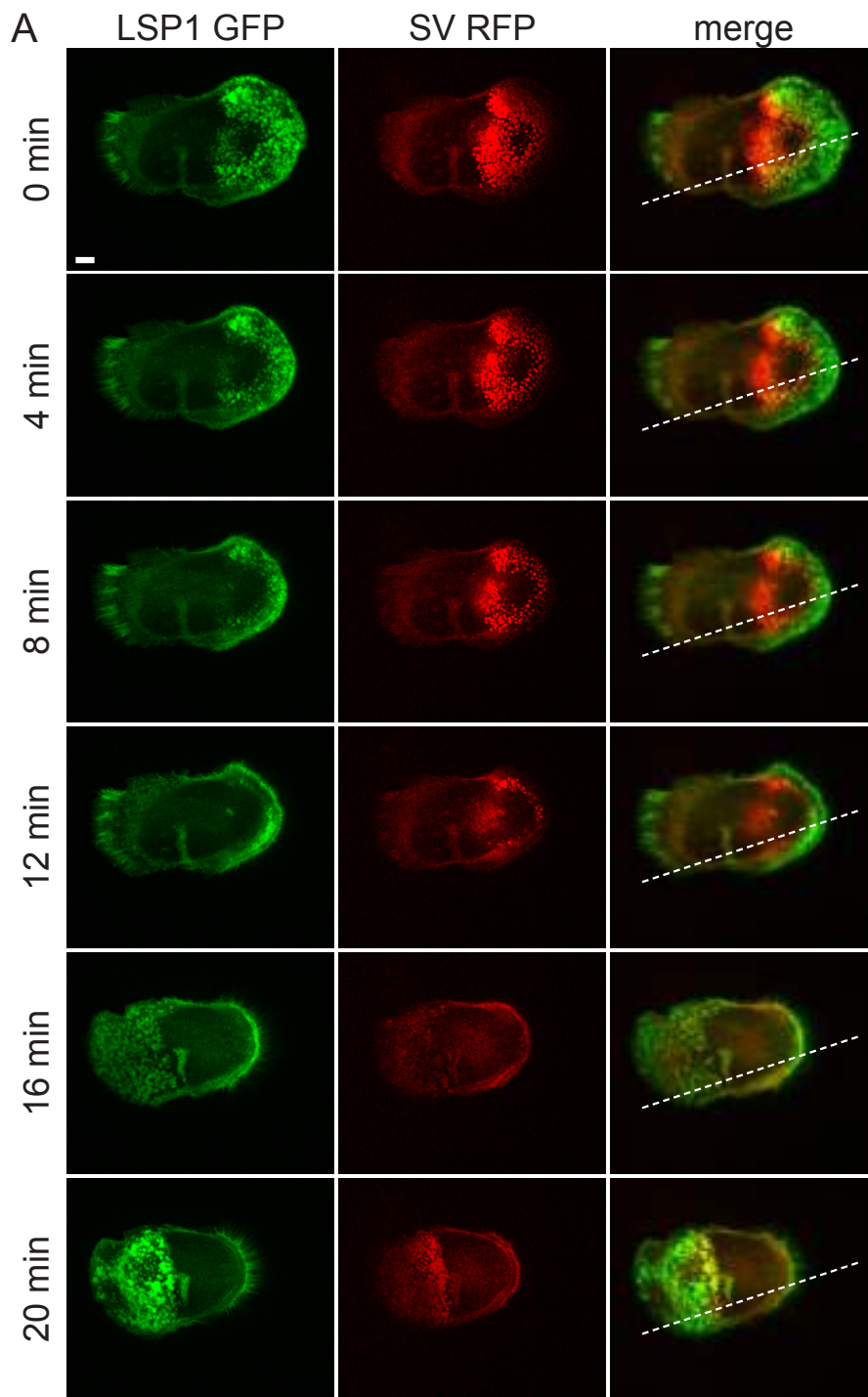**C** co-sedimentation of F-actin isoforms

D

Supplementary Figure 7. Cosedimentation assays.

(A-B) LSP1 and myosin IIA binding is mediated by actin. (A). Inputs from immunoprecipitations shown in Fig. 5C. (B) Myosin cosedimentation assay. SDS PAGE gels from rabbit skeletal muscle myosin precipitation by ultracentrifugation in the presence of BSA, LSP1 full length or C-terminal constructs (right panel), with controls of individual proteins (left panel). Molecular weight is indicated in kDa. (C-D) Supervillin actin-binding regions cosediment to a comparable degree with β-actin and α-cardiac actin filaments. (C) Western blots from actin cosedimentation assays using pure β-actin or α-cardiac actin, in combination with GST as a control, or with GST fused constructs of the actin-binding regions of supervillin (SV171-342, SV343-571, SV570-830), as indicated. Lanes showing supernatant and pellet fractions are labelled with "S" and "P", accordingly. Molecular weight is indicated in kDa. (D) Quantification of copelleted material as ratios of pelleted fraction versus input.

A

	LSP1 GFP	SV RFP	merge
0 min			
4 min			
8 min			
12 min			
16 min			
20 min			

B

	LSP1 GFP	SV RFP	merge
time [min] 0 → 34			

Supplementary Figure 8. LSP1 and supervillin dynamically localize to different zones of migrating macrophages.

(A) Still images from confocal time lapse videos of macrophage coexpressing LSP1-GFP (green) and supervillin-RFP (red) with respective merges. White line in merges indicates pixels used to generate the respective kymograph shown in (B). Note localization of LSP1-GFP to the leading edge and leading edge-associated podosomes (precursors), whereas supervillin-RFP is mostly localized to more internally localized podosomes (successors). Note establishment of a new leading edge at timepoint 16 min, accompanied by formation of LSP1-GFP positive podosomes, with subsequent formation of a new zone of supervillin-RFP positive successor podosomes. Arrows in kymograph indicate LSP1-GFP positive leading edges. Time is indicated in min. Scale bar = 10 µm. See also Suppl. Video 5.
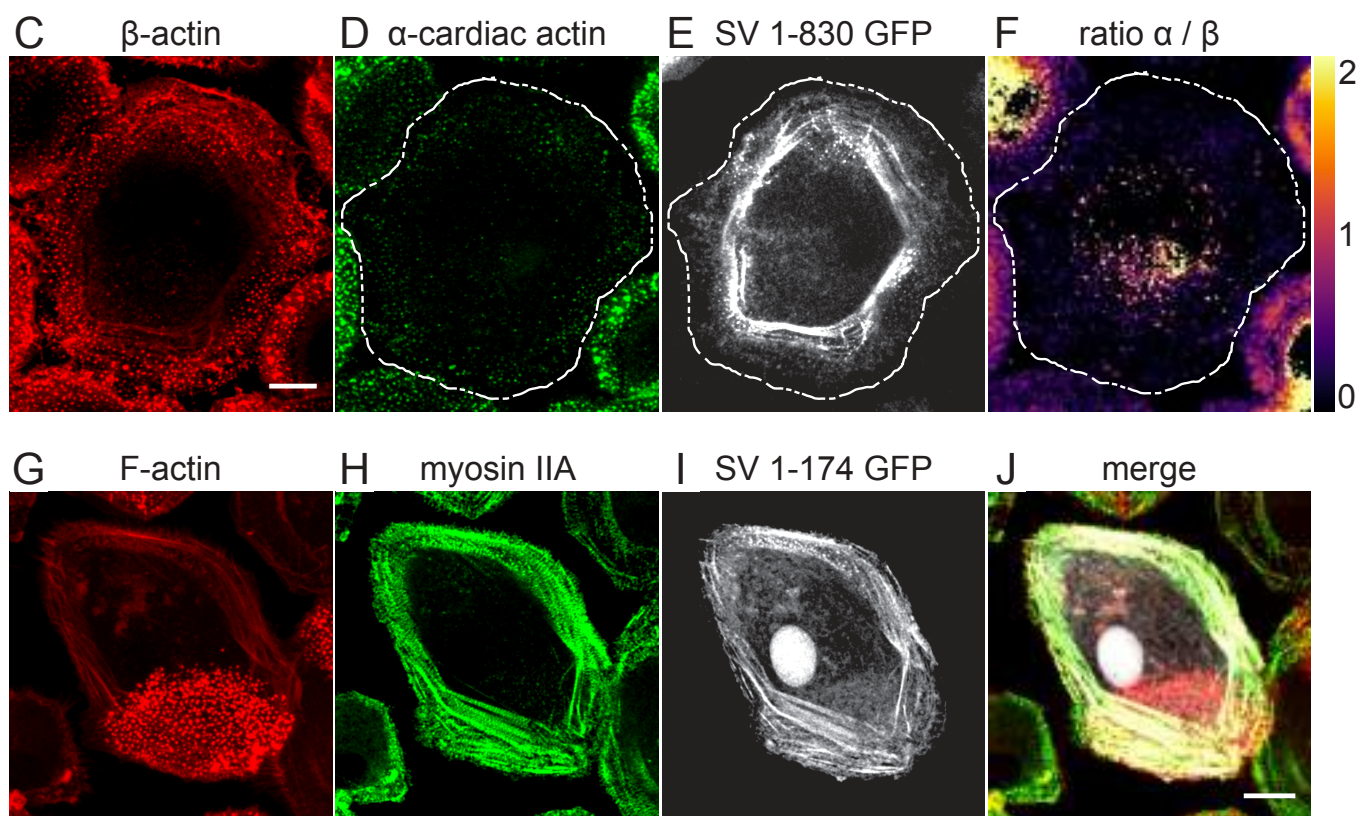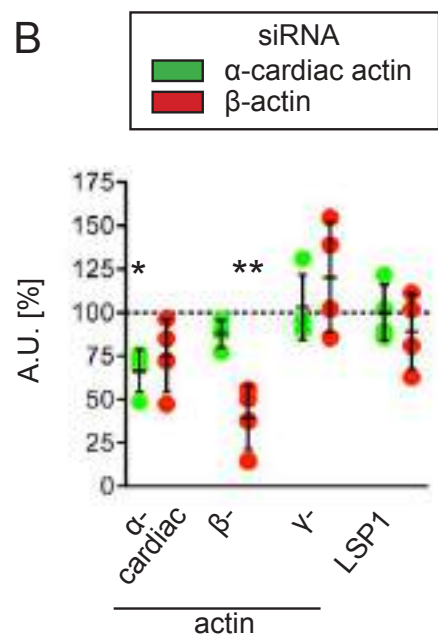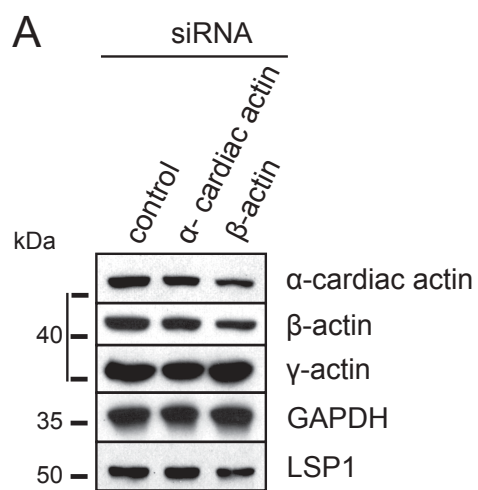
Supplementary Figure 9. SiRNA-induced depletion of α-cardiac actin leads to relocalization of supervillin to the cell cortex.

(A-B) Western blot of lysates from macrophages treated with control siRNA, α-cardiac actin- or β-actin-specific siRNA, as indicated. Molecular weight is indicated in kDa. (B) Quantification of actin isoform and LSP1 levels in cells treated with indicated siRNAs. Values are given as Mean ± S.D; N=4; one-sample t-test; *: P<0.05, **: P<0.01. For specific values, see Suppl. Table S1. (C-F) Confocal micrographs of macrophages treated with α-cardiac actin specific siRNA and over-expressing SV1-830-GFP construct, stained for β-actin (C), α-cardiac actin (D), SV1-830 GFP signal (E), and ratio of α/β-actin, as indicated by colour scale (F). (G-J) Confocal micrographs of macrophages expressing the myosin II-binding region of supervillin (SV1-174-GFP), stained for F-actin (G), myosin IIA (H), SV1-174-GFP signal (I), with merge (J).

Description of Additional Supplementary Files

File Name: Supplementary Movie 1
Description: **3D STED animation.** 3D animated reconstruction of two podosomes from STED micrographs of macrophage stained for LSP1 (green) and F-actin (red), as shown in Fig. 1F.

File Name: Supplementary Movie 2
Description: **Podosome cluster dynamics, control cell.** Live imaging of macrophages targeted with control siRNA and expressing pLifeact-tagRFP (gray scale) to visualize F-actin, as shown in Fig. 2A. Experiment performed with Ultra*VIEW* VoX system (Perkin Elmer) spinning disk microscope, at 37° C and controlled atmosphere. Frames were acquired every 60 sec for 1h. Scale bar = 10 μm

File Name: Supplementary Movie 3
Description: **Podosome cluster dynamics, LSP1 knockdown cell (siRNA #1).** Live imaging of macrophage targeted with LSP1 siRNA #1 and expressing pLifeact-tagRFP (gray scale) to visualize F-actin, as shown in Fig. 2B. Experiment performed with Ultra*VIEW* VoX system (Perkin Elmer) spinning disk micrscope, at 37° C and controlled atmosphere. Frames were acquired every 60 sec for 1h. Scale bar = 10 μm

File Name: Supplementary Movie 4
Description: **Podosome cluster dynamics, LSP1 knockdown cell (siRNA #2).** Live imaging of macrophage targeted with LSP1 siRNA #2 and expressing pLifeact-tagRFP (gray scale) to visualize F-actin, as shown in Fig. 2C. Experiment performed with Ultra*VIEW* VoX system (Perkin Elmer) spinning disk microscope, at 37° C and controlled atmosphere. Frames were acquired every 60 sec for 1h. Scale bar = 10 μm

File Name: Supplementary Movie 5
Description: **Localization of LSP1 and supervillin in macrophage changing direction.** Live imaging of macrophage overexpressing GFP-LSP1 and supervillin-RFP, as shown in Suppl. Fig. 7A. Experiment performed with Ultra*VIEW* VoX system (Perkin Elmer) spinning disk microscope, at 37° C and controlled atmosphere. Frames were acquired every 35 sec. for 35 min. Scale bar = 10 μm
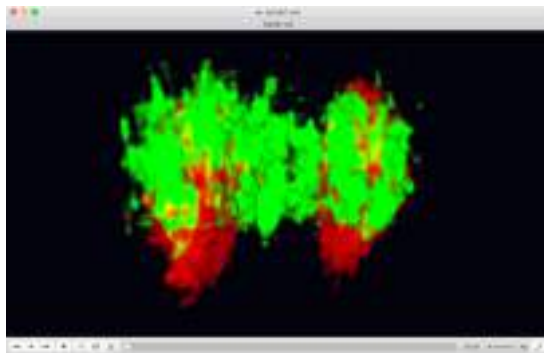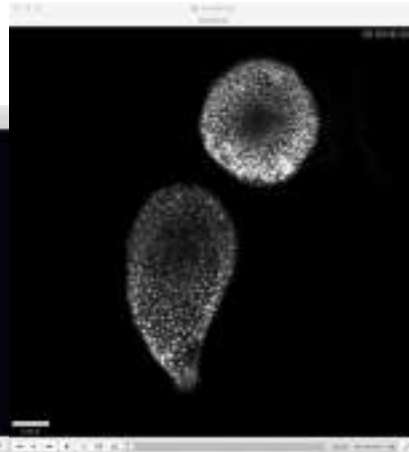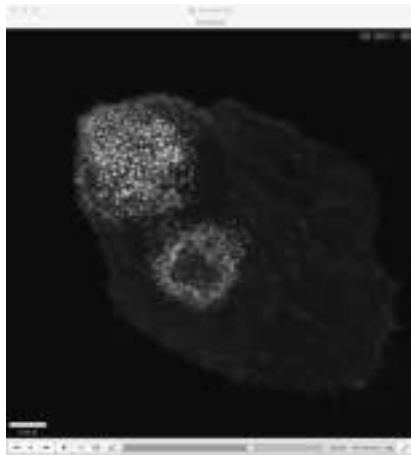
Supplementary movie 1

Supplementary movie 2

Supplementary movie 3
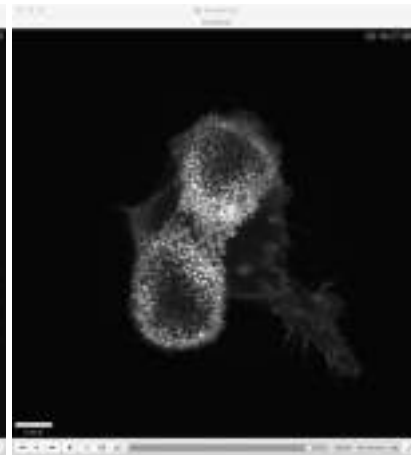
Supplementary movie 4
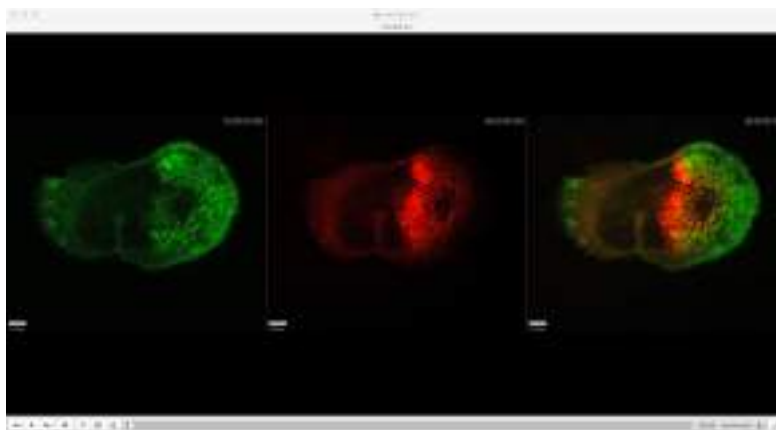
Supplementary movie 5

Supplementary Data 1. Values for podosome and cell analysis

Fig. 2G	Mean velocity of podosome clusters [µm/min]		
Sample	**Values**	**Mean ± SD**	
control siRNA	24	0.3099 ± 0.1841	
LSP1 siRNA #1	24	0.8719 ± 0.5838	
LSP1 siRNA #2	24	0.7312 ± 0.4697	
One-way analysis of variance			
P value			0.0001
P value summary			***
Are means signif. different? (P < 0.05)			Yes
Number of groups			3
F			10.34
R square			0.2307
ANOVA Table	**SS**	**df**	**MS**
Treatment (between columns)	4.105	2	2.053
Residual (within columns)	13.69	69	0.1984
Total	17.8	71	
Bonferroni's Multiple Comparison Test	**Mean Diff,**	**t**	**Summary**
control vs LSP1 #1	-0.562	4.37	****
control vs LSP1 #2	-0.4213	3.276	**

Fig. 2H	Podosome lifetime [min]		
Sample	**Values**	**Mean ± SD**	
control siRNA	24	9.921 ± 2.843	
LSP1 siRNA #1	24	6.560 ± 2.465	
LSP1 siRNA #2	24	6.554 ± 1.441	
One-way analysis of variance			
P value			< 0.0001
P value summary			****
Are means signif. different? (P < 0.05)			Yes
Number of groups			3
F			16.72
R square			0.3264
ANOVA Table	**SS**	**df**	**MS**
Treatment (between columns)	181	2	90.51
Residual (within columns)	373.5	69	5.413
Total	554.5	71	
Bonferroni's Multiple Comparison Test	**Mean Diff,**	**t**	**Summary**
control vs LSP1 #1	3.360	5.003	****
control vs LSP1 #2	3.367	5.013	****

Fig. 2M	Mean velocity of cells [µm/min]		
Sample	**Values**	**Mean ± SD**	
control siRNA	24	0.2380 ± 0.0977	
LSP1 siRNA #1	24	0.3329 ± 0.2569	
LSP1 siRNA #2	24	0.3521 ± 0.2486	
One-way analysis of variance			
P value			0.1488
P value summary			ns
Are means signif. different? (P < 0.05)			No
Number of groups			3
F			1.958
R square			0.05372
ANOVA Table	**SS**	**df**	**MS**
Treatment (between columns)	0.00004982	2	0.00002491
Residual (within columns)	0.0008776	69	0.00001272
Total	0.0009274	71	
Bonferroni's Multiple Comparison Test	**Mean Diff,**	**t**	**Summary**
control vs LSP1 #1	-0.001582	1.537	ns
control vs LSP1 #2	-0.001903	1.848	ns

Fig. 2N	Mean cell area [µm^2]		
Sample	**Values**	**Mean ± SD**	
control siRNA	24	1456 ± 407	
LSP1 siRNA #1	24	2226 ± 1025	
LSP1 siRNA #2	24	2771 ± 1506	
One-way analysis of variance			
P value			0.0003
P value summary			***
Are means signif. different? (P < 0.05)			Yes
Number of groups			3
F			9.020
R square			0.2073
ANOVA Table	**SS**	**df**	**MS**
Treatment (between columns)	20950000	2	10480000
Residual (within columns)	80140000	69	1161000
Total	101100000	71	
Bonferroni's Multiple Comparison Test	**Mean Diff,**	**t**	**Summary**
control vs LSP1 #1	-770.4	2.476	*
control vs LSP1 #2	-1315	4.227	***

Fig. 2O	Podosome distribution (clusters) [%]		
Sample	**Values**	**Mean ± SD**	
control siRNA	3	19.07 ± 7.067	
LSP1 siRNA #1	3	40.17 ± 6.250	
LSP1 siRNA #2	3	48.17 ± 5.244	
One-way analysis of variance			
P value			0.0032
P value summary			**
Are means signif. different? (P < 0.05)			Yes
Number of groups			3
F			17.46
R square			0.8534
ANOVA Table		**SS**	**df**	**MS**
Treatment (between columns)	1356	2	678.0
Residual (within columns)	233.0	6	38.84
Total	1589	8	
Bonferroni's Multiple Comparison Test	**Mean Diff,**	**t**	**Summary**
control vs LSP1 #1	-21.10	4.147	*
control vs LSP1 #2	-29.10	5.719	**

Fig. 2W	Cell shape analysis (AR ≥ 1.3 , circ. ≤ 0.8) [%]		
Sample	**Values**	**Mean ± SD**	
control siRNA	3	19.21 ± 7.285	
LSP1 siRNA #1	3	59.73 ± 9.941	
LSP1 siRNA #2	3	53.87 ± 8.454	
One-way analysis of variance			
P value			0.0084
P value summary			**
Are means signif. different? (P < 0.05)			Yes
Number of groups			3
F			11.78
R square			0.7971
ANOVA Table		**SS**	**df**	**MS**
Treatment (between columns)	2877	2	1439
Residual (within columns)	732.6	6	122.1
Total	3610	8	
Bonferroni's Multiple Comparison Test	**Mean Diff,**	**t**	**Summary**
control vs LSP1 #1	-40.52	4.491	**
control vs LSP1 #2	-34.66	3.842	*

Fig. 3E, 3L	Podosome oscillations [number of peaks]			
Sample	**Values**	**Mean ± SD**	**Unpaired t-test**	
			t	**df**
control GFP	30	2.900 ± 0.8030		
LSP1-GFP	30	4.333 ± 0.9942	6.143	58
control siRNA	30	3.133 ± 0.7761		
LSP1 siRNA #2	30	2.600 ± 1.133	2.128	58

Fig. 3F, 3M	Podosome oscillations [height of peaks]			
Sample	**Values**	**Mean ± SD**	**Unpaired t-test**	
			t	**df**
control GFP	87	20.46 ± 9.525		
LSP1-GFP	130	17.36 ± 11.77	2.046	215
control siRNA	93	21.42 ± 12.22		
LSP1 siRNA #2	78	32.78 ± 20.55	4.473	169

Fig. 3P	Podosome protrusion force [nN]			
Sample	**Values**	**Mean ± SD**	**Unpaired t-test**	
			t	**df**
control siRNA	21	2.451 ± 0.7480		
LSP1 siRNA #2	15	1.704 ± 0.8811	2.742	34

Fig. 4E	Myosin IIA fluorescence intensity at podosomes		
Sample	**Values**	**Mean ± SD**	
control siRNA	15	54.14 ± 21.31	
LSP1 siRNA #1	15	31.81 ± 16.25	
LSP1 siRNA #2	15	35.91 ± 11.93	
One-way analysis of variance			
P value			0.0018
P value summary			**
Are means signif. different? (P < 0.05)			Yes
Number of groups			3
F			7.394
R square			0.2604
ANOVA Table	**SS**	**df**	**MS**
Treatment (between columns)	4241	2	2121
Residual (within columns)	12045	42	286.8
Total	16286	44	
Bonferroni's Multiple Comparison Test	**Mean Diff,**	**t**	**Summary**
control vs LSP1 #1	22.34	3.612	**
control vs LSP1 #2	18.23	2.948	*

Fig. 4F	F-actin fluorescence intensity at podosomes		
Sample	**Values**	**Mean ± SD**	
control siRNA	15	68.34 ± 22.16	
LSP1 siRNA #1	15	65.01 ± 33.07	
LSP1 siRNA #2	15	68.10 ± 37.43	
One-way analysis of variance			
P value			0.9492
P value summary			ns
Are means signif. different? (P < 0.05)			No
Number of groups			3
F			0.05224
R square			0.002481
ANOVA Table	**SS**	**df**	**MS**
Treatment (between columns)	104.0	2	51.99
Residual (within columns)	41799	42	995.2
Total	41903	44	
Bonferroni's Multiple Comparison Test	**Mean Diff,**	**t**	**Summary**
control vs LSP1 #1	3.339	0.2898	ns
control vs LSP1 #2	0.2420	0.02101	ns

Fig. 4G	Myosin IIA ROI area [μm^2]		
Sample	**Values**	**Mean ± SD**	
control siRNA	15	1.669 ± 0.5050	
LSP1 siRNA #1	15	1.824 ± 0.7771	
LSP1 siRNA #2	15	1.968 ± 0.5040	
One-way analysis of variance			
P value			0.4118
P value summary			ns
Are means signif. different? (P < 0.05)			No
Number of groups			3
F			0.9063
R square			0.04137
ANOVA Table	**SS**	**df**	**MS**
Treatment (between columns)	0.6723	2	0.3362
Residual (within columns)	15.58	42	0.3709
Total	16.25	44	
Bonferroni's Multiple Comparison Test	**Mean Diff,**	**t**	**Summary**
control vs LSP1 #1	-0.1557	0.7001	ns
control vs LSP1 #2	-0.2993	1.346	ns

Fig. 4H	F-actin ROI area [μm^2]		
Sample	**Values**	**Mean ± SD**	
control siRNA	15	0.4534 ± 0.2088	
LSP1 siRNA #1	15	0.4103 ± 0.1533	
LSP1 siRNA #2	15	0.5610 ± 0.1795	
One-way analysis of variance			
P value			0.0766
P value summary			ns
Are means signif. different? (P < 0.05)			No
Number of groups			3
F			2.733
R square			0.1151
ANOVA Table	**SS**	**df**	**MS**
Treatment (between columns)	0.1810	2	0.09048
Residual (within columns)	1.391	42	0.03311
Total	1.572	44	
Bonferroni's Multiple Comparison Test	**Mean Diff,**	**t**	**Summary**
control vs LSP1 #1	-0.04311	0.6488	ns
control vs LSP1 #2	-0.1077	1.621	ns

Fig. 4L	PLA spots / cell			
Sample	**Values**	**Mean ± SD**	**Unpaired t-test**	
			t	**df**
IgG + myo IIA	130	2.43 ± 4.76		
LSP1 + myo IIA	130	72.98 ± 88.84	9.04	258

Fig. 7E	Correlation and linear regression of actin isoforms	
Sample	**Pearson r**	**R^2**
α-cardiac actin	0.3934	0.1548
β-actin	- 0.8055	0.6488
γ-actin	- 0.6515	0.4244

Fig. 8B	F-actin co-sedimentation [P / (S+P)] [%]			
Sample	**Values**	**Mean ± SD**	**Unpaired t-test**	
			t	**df**
LSP1 + β-actin	5	84.00 ± 6.015		
LSP1 + α-cardiac actin	5	44.58 ± 4.465	11.77	8

Fig. 9M	Mean cell area [μm^2]		
Sample	**Values**	**Mean ± SD**	
control siRNA	120	1552 ± 747.1	
LSP1 siRNA #1	120	1548 ± 728.0	
LSP1 siRNA #2	120	1794 ± 1000	
One-way analysis of variance			
P value			0.0341
P value summary			*
Are means signif. different? (P < 0.05)			Yes
Number of groups			3
F			3.411
R square			0.01880
ANOVA Table	**SS**	**df**	**MS**
Treatment (between columns)	4743000	2	2372000
Residual (within columns)	247600000	356	695377
Total	252300000	358	
Bonferroni's Multiple Comparison Test	**Mean Diff,**	**t**	**Summary**
control vs LSP1 #1	4.116	0.03823	ns
control vs LSP1 #2	-242.1	2.244	ns

Fig. 9N	Podosome distribution (polarised) [%]		
Sample	**Values**	**Mean ± SD**	
control siRNA	3	45.70 ± 3.940	
LSP1 siRNA #1	3	27.30 ± 7.467	
LSP1 siRNA #2	3	24.00 ± 6.065	
One-way analysis of variance			
P value			0.0091
P value summary			**
Are means signif. different? (P < 0.05)			Yes
Number of groups			3
F			11.39
R square			0.7915
ANOVA Table	**SS**	**df**	**MS**
Treatment (between columns)	820.3	2	410.2
Residual (within columns)	216.1	6	36.02
Total	1036	8	
Bonferroni's Multiple Comparison Test	**Mean Diff,**	**t**	**Summary**
control vs LSP1 #1	18.40	3.755	*
control vs LSP1 #2	21.70	4.428	**

Fig. 9U	Cell shape analysis (AR ≥ 1.3 , circ. ≤ 0.8) [%]		
Sample	**Values**	**Mean ± SD**	
control siRNA	3	27.74 ± 9.415	
LSP1 siRNA #1	3	9.963 ± 6.314	
LSP1 siRNA #2	3	16.98 ± 5.114	
One-way analysis of variance			
P value			0.06
P value summary			ns
Are means signif. different? (P < 0.05)			No
Number of groups			3
F			4.662
R square			0.6085
ANOVA Table	**SS**	**df**	**MS**
Treatment (between columns)	480.8	2	240.4
Residual (within columns)	309.3	6	51.56
Total	790.1	8	
Bonferroni's Multiple Comparison Test	**Mean Diff,**	**t**	**Summary**
control vs LSP1 #1	17.77	3.031	*
control vs LSP1 #2	10.75	1.834	ns

Suppl. Fig. 4A	Western blot quantification of LSP1 knockdown [% vs control]				
Sample	**Values**	**Mean ± SD**	**One sample t-test (theor.mean = 100)**		
			t	**df**	**P value**
LSP1 #1	8	51.89 ± 15.78	8.622	7	< 0.0001
LSP1 #2	8	44.17 ± 16.30	9.687	7	< 0.0001

Suppl. Fig. 5G	Mean number of cells invading into 3D collagen I [% vs control]				
Sample	**Values**	**Mean ± SD**	**One sample t-test (theor.mean = 100)**		
			t	**df**	**P value**
LSP1 siRNA #1	3	166.00 ± 12.73	9.030	2	0.0120
LSP1 siRNA #2	3	150.60 ± 3.69	23.75	2	0.0018

Suppl. Fig. 5H	Mean value of invaded area [% vs control]				
Sample	**Values**	**Mean ± SD**	**One sample t-test (theor.mean = 100)**		
			t	**df**	**P value**
LSP1 siRNA #1	3	100.70 ± 5.508	0.2097	2	0.8534
LSP1 siRNA #2	3	97.00 ± 9.644	0.5388	2	0.6440

Suppl. Fig. 6G	PLA spots / cell			
Sample	**Values**	**Mean ± SD**	**Unpaired t-test**	
			t	**df**
IgG + pan-actin	140	1.12 ± 3.37		
LSP1 + pan-actin	140	175.90 ± 148.50	13.92	278

Suppl. Fig. 9B	Western blot quantification of α-cardiac actin knockdown [% vs control]				
Sample	**Values**	**Mean ± SD**	**One sample t-test (theor.mean = 100)**		
			t	**df**	**P value**
α-card act. /GAPDH	4	66.44 ± 12.16	5.522	3	0.0117
β-act. /GAPDH	4	87.68 ± 7.881	3.128	3	0.0522
γ-act. /GAPDH	4	103.0 ± 18.84	0.3159	3	0.7728
LSP1 /GAPDH	4	99.84 ± 16.15	0.02010	3	0.9852

Suppl. Fig. 9B	Western blot quantification of β-actin knockdown [% vs control]				
Sample	**Values**	**Mean ± SD**	**One sample t-test (theor.mean = 100)**		
			t	**df**	**P value**
α-card act. /GAPDH	4	75.19 ± 21.15	2.346	3	0.1006
β-act. /GAPDH	4	39.58 ± 18.36	6.580	3	0.0071
γ-act. /GAPDH	4	120.3 ± 31.99	1.270	3	0.2937
LSP1 /GAPDH	4	89.14 ± 21.67	1.002	3	0.3901

Chapter 6

Podosome Reformation in Macrophages: Assays and Analysis

Pasquale Cervero, Linda Panzer, and Stefan Linder

Abstract

Podosomes are multifunctional organelles of invasive cells that combine several key abilities including cell–matrix adhesion, extracellular matrix degradation, and mechanosensing. In combination with their high turnover rates that allow quick adaptation to the pericellular environment, podosomes are likely to play important roles during invasive migration of cells. Primary human macrophages constitutively form numerous podosomes and are thus an ideal system for the quantitative study of podosome dynamics. This protocol describes assays for the study of podosome dynamics, namely, reformation of podosomes, in fixed and living cells, with subsequent software-based analyses allowing the extraction of quantitative parameters such as the number of podosomes per cell, podosome density, and half times for podosome disruption and reformation. Moreover, we describe the preparation of podosome-enriched cell fractions and their analysis by immunoblotting.

Key words Podosomes, Podosome reformation, Macrophages, F-actin, Lifeact, Actin dynamics, Live cell imaging, Image analysis, PP2

1 Introduction

Podosomes and invadopodia, collectively called "invadosomes" [1–3], are actin-rich cell–matrix contacts that are characterized by their ability to locally degrade components of the extracellular matrix [4]. Podosomes are mostly formed in a physiological context in cells comprising monocytic cells such as macrophages [5], dendritic cells [6], and osteoclasts [7], endothelial cells [8], or smooth muscle cells [9], while invadopodia are found in pathological contexts comprising cancer cells such as carcinoma [10] or melanoma cells [11].

Podosomes are multifunctional organelles that combine several key abilities of invasive cells including cell–matrix adhesion, localized matrix degradation, and mechanosensing [2, 12, 13]. They are thus thought to be of key importance for invasive cell
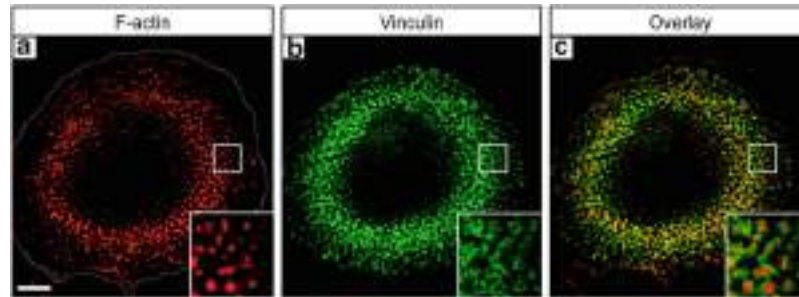
Fig. 1 Image of macrophage with podosomes, stained for F-actin and vinculin. Confocal micrograph of 7 day cultured primary human macrophage showing the typical bipartite architecture of podosomes, consisting of an F-actin-rich core (stained with Alexa568-labeled phalloidin) (**a**) and a ring structure of adhesion plaque proteins (stained for vinculin) (**b**). *Dotted line* shows the cell outline. White scale bar = 10 μm, with merge shown in (**c**)

migration. In fluorescence micrographs, podosomes present as dot-like structures with a diameter of ca. 0.5–1.0 μm and display a typical bipartite architecture consisting of an F-actin-rich core structure and a ring structure of adhesion plaque proteins such as talin or vinculin ([14]; Fig. 1). Recently, a cap-like structure on top of the actin core has also been described [2, 15, 16], while ultra-structural analysis has revealed that the "ring" structure is actually composed of individual clusters that surround the core [17].

Comparable to other adhesion structures, podosomes consist of a variety of structural and regulatory components, and recent mass spectrometric analysis revealed that the podosome proteome consists of at least 203 proteins [18], which is in the range of the proteome size for focal adhesions (ca. 150 components; [19]) and invadopodia (ca. 130 components; [20]). Key regulators of podosome formation and turnover include RhoGTPases [14, 21], actin-regulatory proteins [22], microtubule-dependent transport [2] and signalling by Src kinases [23, 24].

Podosomes are highly dynamic structures with a life time of 2–12 min [7, 25]. They display several levels of actin-based dynamics including de novo formation, fission and fusion, growth and dissolution [2]. Moreover, even in steady state podosomes show internal dynamics, as the actin-rich core (1) is turned over ca. three times within the life span of an individual podosome [7], and (2) shows internal cycles of stiffness, which are probably based on actomyosin contractility [26]. These multiple dynamics are probably key for quick adaptation of podosome formation and podosome-dependent function to a changing pericellular environment. At the same time, they implicate an intricate network of podosome components and regulators which ensures spatiotemporal fine-tuning of podosomes and their functions.

Analysis of podosome dynamics can yield important insights on the impact of novel podosome components or regulators. Primary human macrophages constitutively form numerous (>100)

podosomes per cell, and thus present as an excellent system for the study of podosome dynamics. Here, we describe assays that enable the measurement of podosome dynamics, namely, reformation of podosomes, in fixed and living cells. These assays are based on the key influence of Src kinases on podosome formation and turnover [14, 24] and use the general Src kinase inhibitor PP2 as a tool to disrupt podosomes, which enables the analysis of synchronized reformation of podosomes [27]. Subsequent software-based image analysis facilitates quantification of cells and podosomes and allows statistical analysis, yielding parameters such as the number of podosomes per cell, podosome density, and half times for podosome disruption and reformation. Moreover, we describe how these microscope-based assays can be coupled with a biochemical assay of podosome reformation, allowing one to monitor recruitment of proteins from the cell body fraction into the podosome fraction following PP2 treatment.

2   Materials

2.1   Isolation of Primary Human Monocytes

1. Buffy coats from human venous blood, incubated on a shaking plate at 4 °C overnight. You will get approximately $50–75 \times 10^6$ CD14+ cells (i.e., monocytes) from 500 mL blood.

2. Lymphocyte Separation Medium LSM 1077 (LSM; PAA, J15-004), precooled at 4 °C (*see* **Note 1**).

3. RPMI-1640, precooled at 4 °C.

4. Monocyte isolation buffer: Dulbecco's phosphate buffered saline (DPBS; without Ca^{2+} or Mg^{2+}) plus 2 mM EDTA, pH 7.4 and 5 mg/mL human albumin with low endotoxin (Sigma-Aldrich, A5843); sterile-filtered and precooled at 4 °C. Always prepare fresh before use.

5. Anti-CD14 MicroBeads, human (Miltenyi, 130-050-201). CD14 is strongly expressed on most monocytes and thus useful as a marker molecule for purification.

6. Cell separator: QuadroMACS™ Separation Unit (Miltenyi, 130-090-976) with a MACS MultiStand (Miltenyi, 130-042-303) can be used.

7. Cell separation columns and pre-separation filters: LS Columns (Miltenyi, 130-042-401) and Pre-Separation Filters (Miltenyi, 130-041-407) can be used.

8. Counting chamber.

9. 6-well plates.

10. 50 mL tubes (Falcon).

11. 2 mL tubes (Eppendorf).

12. Macrophage culture medium: RPMI-1640 plus the following additional components: 20 % (v/v) human serum (HS), 100 units/mL penicillin, 100 μg/mL streptomycin, 2 mM glutamine. The complete medium is sterile-filtered and pre-warmed at 37 °C.

2.2 Cell Culture and Media

1. Primary human macrophages are grown in 6-well plates to a density of approximately 1.5×10^6 cells/well.

2. Macrophage culture medium (*see* Subheading 2.1).

3. Starvation medium: macrophage culture medium without HS.

4. DPBS without Ca^{2+} or Mg^{2+}.

5. Alfazyme.

6. PP2 (Src tyrosine kinase inhibitor; Calbiochem): 10 mM in DMSO is used at a final concentration of 25 μM for 30 min [or prolonged up to 1 h in live cell imaging (*see* **Note 2**)], after approximately 2 h of serum starvation.

2.3 Preparation of Podosome-Enriched Cell Fractions

1. Lysis buffer A: 20 mM Tris–HCl, pH 7.4, 5 mM EDTA, 1 % Triton X-100, 1 mM sodium ortho-vanadate plus protease inhibitors (Complete Mini Protease Inhibitor, Roche Diagnostics) and phosphatase inhibitors (PhosSTOP Phosphatase Inhibitor Cocktail Tablets, Roche Diagnostics).

2. Lysis buffer B: 20 mM Tris–HCl, pH 7.4, 5 mM EDTA, 1 % SDS, 0.1 % sodium deoxycholate, 1 mM sodium ortho-vanadate plus protease and phosphatase inhibitors.

3. Laemmli sample buffer: 10 % glycerol, 2 % SDS, 60 mM Tris–HCl, pH 6.8, 5 % mercaptoethanol, 0.01 % bromophenol blue.

4. Phosphate buffered saline (PBS).

5. Cell scrapers.

6. Sonicator.

7. Pierce BCA protein assay kit from Thermo Scientific (*see* **Note 3**).

8. Primary antibody: phospho-Tyr mouse monoclonal antibody (PY99 from Santa Cruz) for specific detection of proteins containing phosphorylated tyrosine (Tyr) residues.

9. Secondary antibody: Horseradish peroxidase linked antibody (sheep anti-mouse from GE Healthcare).

10. SDS-PAGE/Western blot apparatus.

11. Whatman Protran nitrocellulose transfer membrane.

12. Pierce ECL Western blotting substrate from Thermo Scientific.

2.4 Immunofluorescence

1. Sharp-tipped forceps (*see* **Note 4**).

2. Autoclaved glass coverslips (12 mm diameter).

3. Phosphate buffered saline (PBS).

4. Fixation: 3.7 % (v/v) formaldehyde freshly diluted in PBS, from 37 % stock solution.

5. Permeabilization: 0.5 % Triton X-100 in PBS.

6. Washing solution: 0.05 % Triton X-100 in PBS.

7. Alexa Fluor488-labeled phalloidin to stain F-actin.

8. HCS CellMask Red stain (Invitrogen, #H32712) to stain cytoplasm and nuclei: 2 μg/mL, prepared according to manufacturer's instructions.

9. Fluorescent mounting medium: Mowiol (Calbiochem) containing DABCO (25 mg/mL; Sigma–Aldrich) as anti-fading reagent.

10. Nail polish to seal the coverslips on the microscope slides.

11. Microscope slides.

12. Microscope oil.

13. Microscopy: Images of fixed samples are acquired with a confocal laser scanning microscope with a 63× objective. We use Leica DM IRE2 with a Leica TCS SP2 AOBS confocal point scanner, equipped with an oil-immersion HCX PL Apo 63× NA 1.4 lambda blue objective.

14. Acquisition of images is performed with appropriate software. We use Leica Confocal Software.

15. Image processing and analysis are performed using ImageJ ver. 1.47b (http://rsbweb.nih.gov/ij/) [28] and two lab-developed macros described in detail later (*see* Subheading 3.5).

16. Obtained data are collected in Excel, and statistical analysis is performed with GraphPad Prism (*see* Subheading 2.7).

2.5 Transfection of Primary Human Macrophages by Electroporation

1. Neon® Transfection system (Life Technologies) (*see* **Note 5**). Supplied R-Buffer is used for resuspension of cells prior to transfection.

2. 1 μL of Lifeact-GFP at a concentration of 0.5 μg/μL in TE-buffer (10 mM Tris–HCl, pH 8.5, 0.1 mM EDTA).

3. Glass-bottom dishes (*see* **Note 6**).

2.6 Live Cell Imaging

1. Microscopy: Time lapse movies are acquired with a spinning disk confocal microscope. We use Nikon Eclipse Ti with the Ultra*VIEW* VoX system, Perkin Elmer, equipped with a Yokogawa CSU X1 spinning disk, an oil-immersion 60× Apo TIRF (corr.) objective, a 527 nm (W55) emission filter and a Hamamatsu EM-CCD C9100-50 camera. The microscope should be equipped with an environmental chamber to allow temperature, humidity and CO_2 control. Experiments are performed at 37 °C, 5 % CO_2, and a humid atmosphere (*see* **Notes 7** and **8**). Microscope control and image acquisition are

performed with appropriate software. We use Volocity 6.1.1 software (Perkin Elmer).

2. Microscope oil.

3. Movie processing and analysis are performed using ImageJ ver. 1.47b [28] and a lab-developed macro described in detail later (*see* Subheading 3.8) in combination with another, already available, macro called "Find Stack Maxima" (http://rsbweb.nih.gov/ij/macros/FindStackMaxima.txt).

4. Obtained data are finally analyzed using statistical software. We use Excel and GraphPad Prism.

2.7 Statistical Analysis

Data obtained from image analysis are collected in Microsoft Excel and analyzed in GraphPad Prism, using an unpaired nonparametric Kruskal–Wallis test followed by Dunn's Multiple Comparison test. $P < 0.05$ was considered as statistically significant (single asterisk), $P < 0.01$ as highly statistically significant (double asterisks).

3   Methods

3.1 Isolation of Primary Human Monocytes

Isolation and differentiation of primary monocytes is time- and cost-consuming. However, immortalized monocytic cell lines mostly form only a few, irregularly shaped podosomes, compared to the mostly uniform and numerous podosomes formed in primary human macrophages and are thus not ideal for subsequent statistical analysis.

Primary human monocytes can be isolated as CD14$^+$ cells from buffy coats of peripheral venous blood using a Ficoll gradient to separate monocytic cells from erythrocytes and plasma. In the presence of human serum or cytokines such as M-CSF, the isolated monocytes are then differentiated into macrophages over 6–7 days.

All steps should be performed in a laminar flow hood to avoid contamination. Make sure that all necessary reagents are cold and kept on ice during the whole procedure.

1. Precool a centrifuge with a rotor able to spin down solutions in 50 mL tubes at 4 °C. All the following centrifugation steps have to be performed at 4 °C and $450 \times g$ without brake.

2. Transfer the soluble part of the buffy coats from 500 mL human venous blood (ca. 60 mL) into 50 mL tubes.

3. Take three new 50 mL tubes and fill them each with 15 mL ice-cold LSM. Then carefully overlay the LSM with approximately 20 mL of the buffy coats. Try to avoid mixing of the two layers.

4. Spin for 30 min to separate lymphocytes from erythrocytes and plasma.

5. Tubes will now contain a gradient consisting of four layers. The bottom-most (red) fraction contains erythrocytes, followed by a clear LSM fraction. A white interphase containing the desired mononuclear cells separates the LSM fraction from the upper-most (yellow) blood plasma fraction.

6. Fill three new 50 mL tubes with 10 mL ice-cold RPMI-1640. (Use ice-cold RPMI-1640 for all subsequent steps.)

7. Aspirate the white interphases from the centrifuged tubes with serological pipettes and transfer them into the tubes containing the cold RPMI-1640. Fill up the tubes to 50 mL with RPMI-1640 to start a sequential washing process of the monocytes by gently resuspending the cell pellet each time (*see* **Note 9**).

8. Spin for 10 min.

9. Carefully discard the supernatants by aspiration with a serological pipette. Care must be taken because the cell pellets are not sticky and may slip along the tube wall.

10. Resuspend each pellet in 10 mL RPMI-1640 (*see* **Note 9**), combine all resuspended cells and split the solution into two 50 mL tubes. Fill up both tubes to 50 mL with RPMI-1640.

11. Spin for 10 min.

12. Discard the supernatants and resuspend each pellet in 10 mL RPMI-1640. Combine both solutions in a single 50 mL tube and fill it up to 50 mL with RPMI-1640.

13. Spin for 10 min.

14. Resuspend the pellet in 1.5 mL ice-cold monocyte isolation buffer. Transfer into a 2 mL tube and add 250 μL of anti-CD14 MicroBeads. Close the tube and mix gently by inverting three times. Incubate for 15 min on ice, to allow binding of the antibody-coupled beads to monocytes via the CD14 cell surface marker.

15. During this time, assemble the separation equipment consisting of holder, separation unit, separation column and pre-separation filter. Equilibrate the column and the pre-separation filter with 1 mL ice-cold monocyte isolation buffer.

16. Add the cell suspension to the column and let it run through completely.

17. Prepare a 50 mL tube with 10 mL RPMI-1640.

18. Add 3 mL monocyte isolation buffer to the column, remove the column from the separation unit and place it over the prepared 50 mL tube. Elute CD14-positive cells from the column by using the stamp provided in the kit.

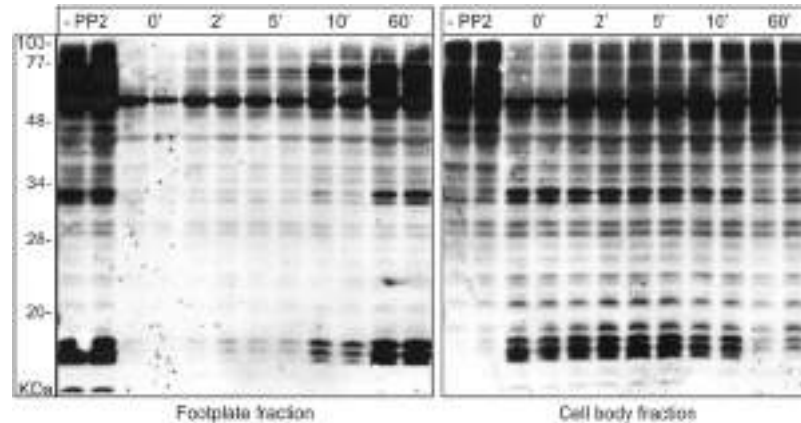19. Fill the tube to the 30 mL mark with RPMI-1640 and gently suspend the cells.

Fig. 2 Western blot analysis of podosome reformation. Western blots of macrophage lysates, developed using an anti-phosphotyrosine antibody (as proof of principle). *Left*: adhesive "footplate" fraction, *right*: cytosol and organelle fraction. Podosomes were disrupted by the use of the Src tyrosine kinase inhibitor PP2 (0 min), the inhibitor was subsequently washed out, and cells were differentially lysed at the indicated time points (0, 2, 5, 10, 60 min; two lanes for each condition). Note the successive recruitment of tyrosine-phosphorylated proteins from the cytoplasm into the podosome-containing footplate fraction. Molecular weight is indicated in kDa

20. Add an aliquot of the cell solution to a counting chamber, determine the cell number and seed the cells into 6-well plates at a density of 1.5×10^6 cells/well. If necessary, adjust the volume of the cell solution to approximately 1 mL/well with RPMI-1640.

21. Place the plates into a cell incubator at 37 °C and 5 % CO_2 for 2–4 h to allow the cells to settle and adhere. Then gently aspirate off the RPMI-1640 and add 1.5 mL of pre-warmed macrophage culture medium to each well.

22. Incubate the cells at 37 °C and 5 % CO_2 for at least 6 days to allow the development of monocytes into macrophages, which is induced by growth factors present in the human serum (*see* **Notes 10** and **11**).

3.2 Podosome Reformation Assay Using Podosome-Enriched Cell Fractions and Western Blotting

This section describes the biochemical analysis of podosome disruption and reformation, by preparation of podosome-enriched cell fractions, with subsequent Western blotting. This analysis requires the key step of differential cell lysis in order to "unroof" the cells, resulting in two different protein lysates: the "cell body" fraction, which contains cytoplasm, membranes, organelles, and cell debris, and the "footplate" fraction, which represents the adhesive membrane fraction and is enriched in podosomes [18].

This method, despite its apparent simplicity, allows one to monitor the recruitment of proteins to the footplate fraction during podosome reformation (here demonstrated for proteins enriched in phosphorylated tyrosine residues, Fig. 2).

1. 7 days cultured macrophages are grown in 6-well plates and starved for 2 h before PP2 treatment by exchanging macrophage culture medium with macrophage culture medium lacking HS (1 mL/well) (*see* **Note 12**).

2. During this period, pre-dilute the appropriate amount of PP2 in macrophage culture medium lacking HS (1 mL for each sample) to a final concentration of 25 μM; use the same procedure for control samples, but this time only with DMSO (as it is used as a dissolving agent for PP2).

3. Treatment of samples with PP2 to disrupt podosomes should start at different time points, to enable concomitant lysis of all samples. In this specific example (Fig. 2), chosen time points include 0, 2, 5, 10, and 60 min of reformation (*see* **Note 13**). The first sample to treat with PP2 is the 60 min reformation time point (30 min of PP2 treatment + 60 min of reformation = 90 min), then the reformation time point preceding it (10 min) and so on; the last time points are the control (with DMSO) and the 0 min reformation time point.

4. Podosome reformation is induced by carefully aspirating (*see* **Note 14**) the medium with PP2 and replacing it with macrophage culture medium for the intended reformation period.

5. Once all the samples are ready to be lysed differentially (to generate cell body and footplate fractions), carefully remove the medium from each well and wash the cells gently twice with PBS. After removal of PBS, add 600 μL of lysis buffer A/well to lyse cell bodies. After addition of lysis buffer A, place the plate immediately on ice to avoid protein degradation.

6. Gently shake the plate by hand for 30 s and rapidly check progression of cell lysis in phase contrast using a cell culture microscope. Onset of cell body lysis can be detected by the appearance of nuclei, cytoplasmic granules and cell debris in the lysis medium. Podosome-containing ventral membranes ("footplates") may be visible as opaque, light-scattering areas on the culture plate. Continue shaking on ice and periodically check the cells. Continue the treatment until all cell bodies are detached from the plate. Usually, after ca. 3 min, most of the cells are lysed.

7. At this point, the fraction containing cell bodies, cytoplasm, and nuclei can be removed and collected for consequent Western blotting. Remember to keep the plates on ice during all steps until the final sample collection. The remaining footplate fraction is now washed briefly twice with lysis buffer A to remove remaining cell debris. Solubilization of footplates is achieved by addition of 100 μL/well of lysis buffer B and thorough detachment of footplates with a cell scraper. Footplate fractions are collected for subsequent Western blotting analysis.

8. Sonicate the protein samples on ice for up to 10 s and 30 % of amplitude, mix them with the appropriate amount of Laemmli sample buffer and perform SDS-PAGE on 10–12 % polyacrylamide gels, loading equal volumes for the footplate and the cell bodies (*see* **Note 3**). Keep in mind that the protein concentration of the cell bodies is significantly higher than the footplate fraction (*see* **Note 3**). For this reason, fractions are lysed in different volumes of buffer (600 μL of lysis buffer A for cell bodies, compared to 100 μL of lysis buffer B for footplates).

9. The primary antibody (pY99) used as proof-of-principle (Fig. 2) in this experiment is against Tyr-phosphorylated proteins (1:1,000), with the secondary antibody being an anti-mouse horseradish peroxidase linked whole antibody (1:2,000). This allows simultaneous detection of a variety of tyrosine-phosphorylated proteins and illustrates the fact that podosomes are enriched in phosphotyrosine residues [14]. Of course, depending on the research question, a variety of different primary and secondary antibodies may be used.

3.3 Cell Culture and Coverslip Preparation for Podosome Reformation Assay Using Fixed Cells

This section describes how cultured macrophages are detached from culture dishes and seeded in a sub-confluent layer on coverslips or glass-bottom dishes. These seeded cell layers are then used to perform podosome reformation assays for fixed samples or for live cell imaging, respectively.

1. Coverslips should be sterilized before use and placed in a 6-well (one coverslip/well) plate.

2. After at least 6 days of culture (*see* **Note 11**), remove the media, wash twice with DPBS and then add 0.5–1.0 mL of alfazyme for 30 min (max. 45 min) at 37 °C.

3. After alfazyme incubation, add 0.5–1.0 mL/well of macrophage culture medium and collect the cells in a 50 mL tube prior to centrifugation ($450 \times g$ for 10 min).

4. Count the cells and seed approximately 60–70,000 cells/coverslip (80–100 μL) to generate a sub-confluent layer of macrophages (*see* **Note 15**).

5. After 30 min of incubation (37 °C, 5 % CO_2) to allow for sedimentation of cells, add 2 mL of pre-warmed macrophage culture medium per well.

3.4 Podosome Reformation Assay Using Fixed Cells and Immunofluorescence

This technique is based on the same principle as the sample preparation for podosome fractions (*see* Subheading 3.2), namely, podosome disruption by PP2 treatment, with subsequent podosome reformation by washout of the drug. However, as samples are then processed for immunofluorescence imaging, cells are plated on coverslips that are cultured in 6-well plates.

The advantages of using fixed cell samples include (1) the high number of cells that can be analyzed, yielding statistically robust parameters, and (2) the lack of need for a microscope equipped for live cell analysis.

1. Detach the cells and seed them on coverslips as described in Subheading 3.3.

2. Plan the time points for podosome reformation (for example, 0, 30, and 60 min) and proceed with the experiment as described in Subheading 3.2. This time cells will be only fixed, and not lysed, so it is not as important to perform the last step (in this case fixation) at the same time for all the samples (*see* **Note 16**).

3. Cells are fixed by transferring coverslips into wells containing freshly prepared 3.7 % (v/v) formaldehyde for 15 min at room temperature or ideally 37 °C (human primary macrophages are very sensitive to temperature changes) (*see* **Note 17**). After fixation, samples are washed three times (5 min each time) with PBS. Cells are permeabilized with 0.5 % Triton X-100 for 10 min at room temperature and washed again three times with 0.05 % Triton X-100 (5 min each).

4. Stain F-actin (labeling podosome cores) with Alexa Fluor488-labeled phalloidin (1:50) and cytoplasm with HCS CellMask Red stain both diluted in 0.05 % Triton X-100, for 30 min.

5. Wash coverslips three times with PBS (5 min each), dry coverslips by gentle contact with tissue to remove remaining liquid, and mount them with Mowiol (4 μL for a coverslip of 12 mm diameter) on microscope slides (cell side facing the slide). Seal samples by adding a layer of nail polish along the circumference of the coverslip (*see* **Note 18**).

6. Acquire fluorescent micrographs of podosomes and cell bodies. Depending on the quality and brightness of the staining, the ideal "standard" sample needs to have the following features (settings used for generation of Fig. 3 are given in brackets).

   - high magnification and resolution (oil-immersion HCX PL Apo 63× NA 1.4 lambda blue objective, 1,024 × 1,024 resolution and 1.5× zoom).

   - Low cell density/field of view (*see* **Note 15**).

   - Good signal to noise ratio to visualize bright and defined podosomes on dark background (pinhole airy 1 and 7 % 488 laser power).

   - Uniform and bright signal to visualize cell bodies on dark background (*see* **Note 19**) (pinhole 600 μm and 12 % 543 laser power).

The given settings can be adapted depending on the microscope parameters, the user needs and the quality of the staining. However, it is strongly suggested to keep the same settings, once defined, for the whole experiment, in order to enable a robust and statistically reliable image analysis.

3.5 Image Processing and Data Analysis of Fixed Samples

This section describes step-by-step the actions performed with ImageJ, which are assembled into a single macro using the "Record…" tool (Plugins > Macros > Record…). This analysis is based on the processing of images acquired in two channels (in this case red = cell body; green = podosomes), followed by merging the respective regions of interest (ROI), as shown in Fig. 3, yielding three different values: (A) area covered by each single cell, (B) number of podosomes in each single cell, (C) density of podosomes (here defined as number of podosomes/100 μm^2 of cell covered area).

In the first step, images acquired in the "cell channel" (HCS CellMask Red stain) are processed in order to get a final mask corresponding to all whole cells present in the respective field of view. For this purpose, it is important to reduce the background noise as much as possible, to ease the subsequent segmentation step, which enables recognition of individual cells as objects by the software. All settings can be adapted depending on the user needs and the quality of the staining, with settings used for the generation of images in Fig. 3 in brackets.

1. Open the "cell channel" image and calibrate the correct scale depending on the microscope settings used (Image > Properties…; if the "Global" box is checked, the software will keep the settings for the whole session, until it is closed).

2. Convert the image to 8-bit (Image > Type > 8-bit).

3. Reduce background noise by using the following tools: (*see* **Note 20**).

   (a) Smooth (Process > Smooth).

   (b) Gamma (here: 0.4) (Process > Math > Gamma…).

   (c) Median (radius used here: 4) (Process > Filters > Median…).

   (d) Gaussian Blur (sigma used here: 4) (Process > Filters > Gaussian Blur…).

4. Convert the image to black and white (Process > Binary > Make Binary) and then invert it (Edit > Invert).

5. Segment potentially adjacent objects (Process > Binary > Watershed). If you are satisfied with the output, you can proceed to the actual object analysis. In case the output is not satisfactory, adapt the previous settings to yield optimal results.

6. Highlight objects you are interested in by setting the expected size (in μm^2) and the circularity (0 = straight line, 1 = perfect circle) (Analyze > Analyze Particles…). In this step, you can
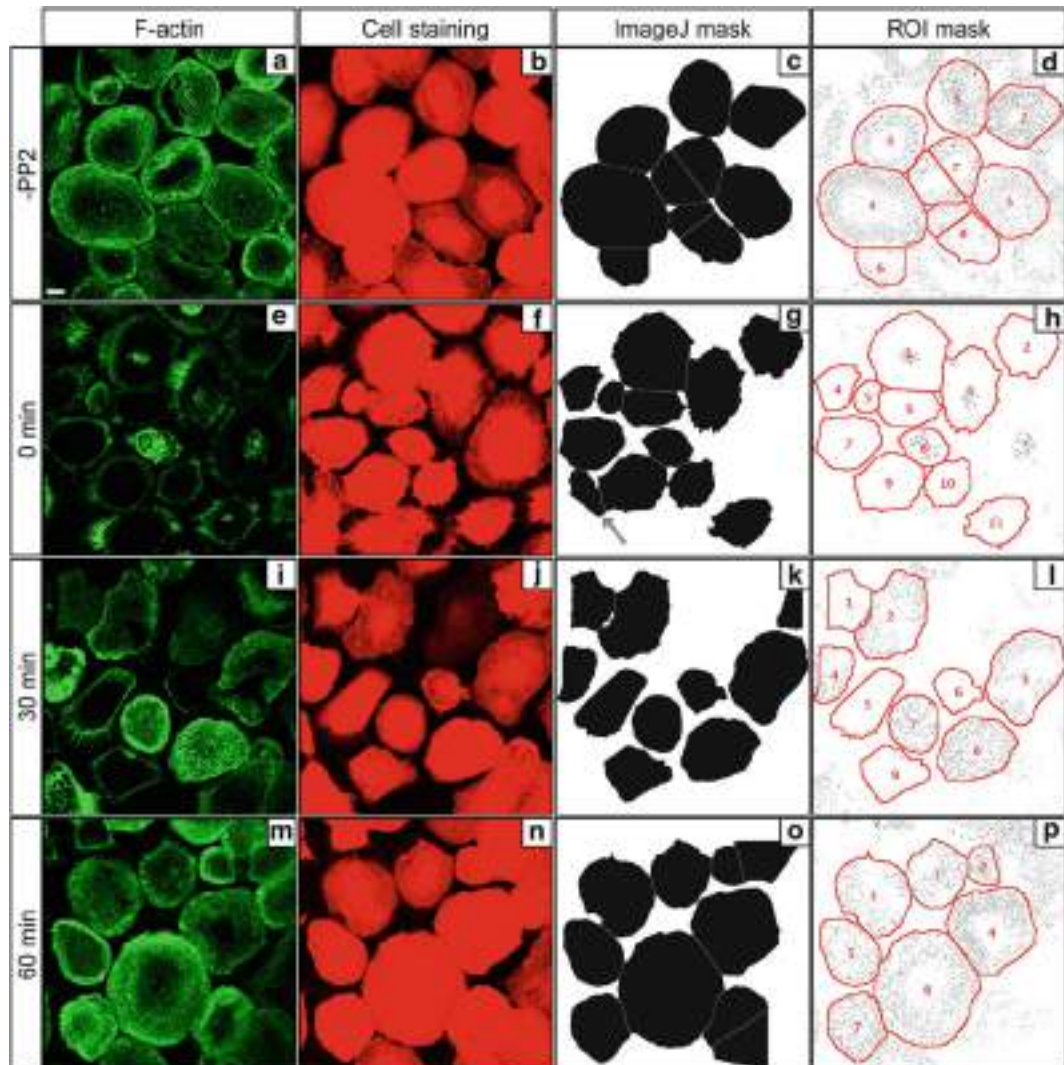
105

Fig. 3 Image analysis of podosome reformation using fixed samples. Gallery of confocal micrographs from macrophages stained for F-actin using Alexa488-labeled phalloidin to label podosomes (*green*; **a**, **e**, **i**, **m**), stained with CellMask to highlight individual cells (*red*; **b**, **f**, **j**, **n**), after application of the described ImageJ macro (*black*; **c**, **g**, **k**, **o**), and after using the ROI mask to correlate podosomes (*black dots*) with individual cells (*red outlines* and *numbers*; **d**, **h**, **l**, **p**). Images in *upper row* show untreated cells. *Lower rows* shows cells after 30 min treatment with PP2 to disrupt podosomes. Minutes after start of drug washout ($t = 0$ min) are indicated. Note that use of the ImageJ "ROI manager" tool allows the combination or deletion of ROI in case of oversegmentation (i.e., ROI 7 in **d** (*center*) is obtained by merging two segmented objects belonging to a single cell, while in **g**, a *grey arrow* indicates an object which was manually deleted, as it represents only a part of a cell not completely shown in the image. White scale bar = 10 μm

also check other options such as masks corresponding to the identified objects ("Show:Masks"), adding the obtained ROI to the ROI manager for further analysis ("Add to Manager"), and excluding incomplete objects identified on the edges of the image ("Exclude on edges").

106

7. Once the identified objects are recorded in the "ROI Manager", it is possible to modify them. This includes combining two segmented objects belonging to one single cell in case of oversegmentation (select the ROI that need to be merged, right-click and select the "OR (Combine)" function followed by "Add"; this will create a single new ROI that will include the previously selected ones, which have to be deleted individually) (*see* **Note 21**).

8. Set the values for calculation, for example cell area (Analyze > Set Measurements… > check only "Area"), then manually select all ROIs and click on "Measure". Save the obtained area values in a spreadsheet.

9. Recording all previous actions, including the settings used, will result in a macro that can be saved as a .txt file.

   ```
   run("8-bit");
   run("Smooth");
   run("Gamma…", "value=0.40");
   run("Median…", "radius=4");
   run("Gaussian Blur…", "sigma=4");
   run("Make Binary");
   run("Invert");
   run("Watershed");
   run("Analyze Particles…", "size=150-Infinity circularity=0.30-1.00 show=Masks clear exclude add");
   ```

   Once the ROIs corresponding to the cell positions are recorded, open the "podosome channel" (phalloidin stain) of the same image and run a series of actions which will allow highlighting and better definition of podosomes as individual, countable objects (Fig. 4).

10. Convert the image to 8-bit and smooth it (*see* **steps 2** and **3**).

11. Subtract the background (rolling here: 5) (Process > Subtract Background…).

12. Perform a gamma correction to increase the contrast (here: 1.30) (Process > Math > Gamma…).

13. Carefully convolve to further increase the contrast (here, a 5×5 matrix is used in which all elements are –1 except the central one, which is 30; the "Normalize Kernel" box has to be checked).

14. Convert the picture to black and white (Process > Binary > Make Binary).

15. Repeat **steps 5–6**, but this time use the "Analyze Particles" filter with the appropriate settings, enabling a better definition of podosomes (i.e., size = 0.10–50 μm² and circularity = 0.80–1.0). Choose only the option showing the masks (Show:Masks), without adding the results to the "ROI Manager".
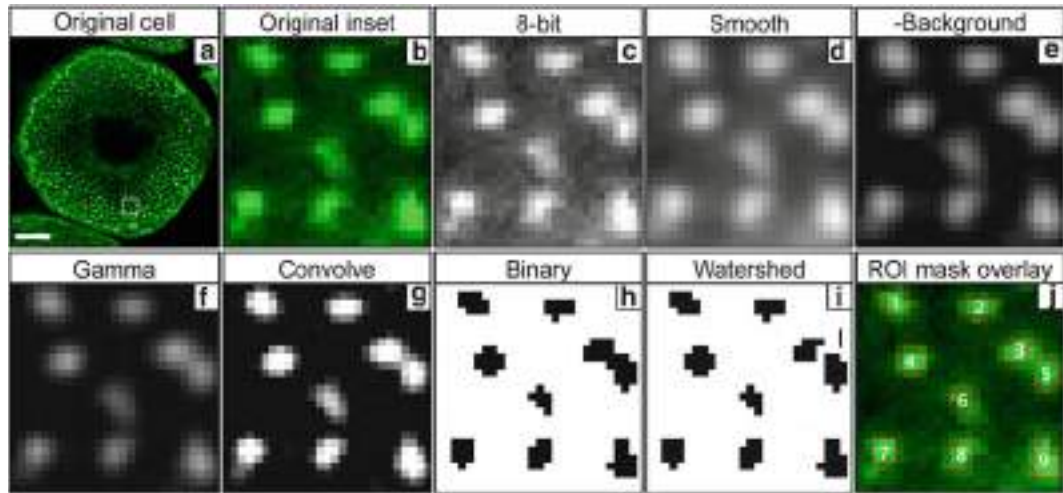
107

Fig. 4 Gallery of pictures showing the effects of the "podosome macro" step-by-step. The original picture (**b**; *inset* from image of complete cell in **a**) is first converted to an 8-bit image (**c**) and then smoothened (**d**). To allow for good detection of podosomes in the whole cell, it might be useful to increase the contrast by subtracting the background (**e**), performing the gamma correction (**f**) and the convolution (**g**). At the end of this process, podosomes are more easily detected by the software so that you can convert the picture to a binary image (**h**), ready to be watersheded (segmentation of touching objects; **i**). Note that the "watershed" step in (**i**) is able to separate a single detected object into two distinct podosomes (ROI *3* and *5*). The resulting ROI mask overlaying the original picture (**b**) is shown in (**j**). White scale bar = 10 μm; *White square inset* measures: 4.32 × 4.32 μm

16. Uncheck and recheck the "Show all" box in the "ROI Manager" to see the overlay of the cell ROI on the detected podosome mask.

17. Manually select a single cell ROI in the "ROI Manager" and use the "Find Maxima" tool (Process > Find Maxima…) to count the number of podosomes present in this ROI. Set "Noise tolerance" to 0 and "Output type" to "Count". The "Light background" box has to be checked.

18. **Step 17** can be fully automated for all of the cell ROI by adding respective instructions (here highlighted in bold) at the end of the "Podosomes" macro. The "Result" window will now show the number of podosomes detected in each cell ROI at the end of the list (keeping the same numbering order saved in the previous "Cell body" macro).

Recording all previous actions, including the settings used, will result in the complete macro, which can be saved as a .txt file.

```
run("8-bit");
run("Smooth");
run("Subtract Background…", "rolling=5");
run("Gamma…", "value=1.30");
run("Convolve…", "text1=[-1 -1 -1 -1 -1\n-1
-1 -1 -1 -1\n-1 -1 30 -1 -1\n-1 -1 -1 -1 -1\n-1
-1 -1 -1 -1\n] normalize");
```

```
run("Make Binary");
run("Watershed");
run("Analyze Particles…", "size=0.10-50 cir-
cularity=0.80-1.00 show=Masks display");
roiManager("Show None");
roiManager("Show All");
n=roiManager("count");
for (i=0; i<n; i++) {
roiManager("select", i);
run("Find Maxima…", "noise=0 output=Count light");
}
```

19. It is now possible to save the number of podosomes detected in each identified cell. These values, in combination with the values for cell area, can be used to calculate the three parameters described in the introduction to this section (A, B, C) and perform statistical analysis as shown in Fig. 5.

3.6 Transfection of Primary Human Macrophages by Electroporation

Sufficiently effective transfection of primary macrophages is so far only possible by electroporation (*see* **Note 5**); a mechanical process, where an electrical pulse is used to create temporary pores in cell membranes through which substances like DNA or RNA can pass into cells.

All steps should be performed in a laminar flow hood to avoid contamination.

1. On the day before live cell imaging (*see* **Note 22**), detach macrophages from two wells of a 6-well plate (obtained as described in Subheading 3.3) (*see* **Note 11**).

2. Take 1×10^5 cells for one transfection with the Neon™ Transfection System 10 μL Kit and resuspend in 12 μL R-buffer (pre-warmed at room temperature), supplied in the Kit.

3. Add 0.5 μg Lifeact-GFP (1 μL of 0.5 μg/μL) and mix by pipetting up and down 5–10 times. (Make sure that the added DNA solution does not exceed 10 % of the total volume.)

4. Load the solution with a Neon™ Pipette into a Neon™ Tip, also supplied in the Neon™ Transfection System 10 μL Kit. Ensure that there are absolutely no air bubbles in the loaded solution, as they will interfere with the transmission of the electrical current!

5. Plug the Neon™ Pipette with Neon™ Tip into position in the Neon™ Pipette Station with Neon™ Tube, filled with 3 mL E-buffer at room temperature. Select your transfection protocol on the device and press Start. We have optimized a protocol for primary human macrophages with two pulses of 1,000 V and 40 ms each.
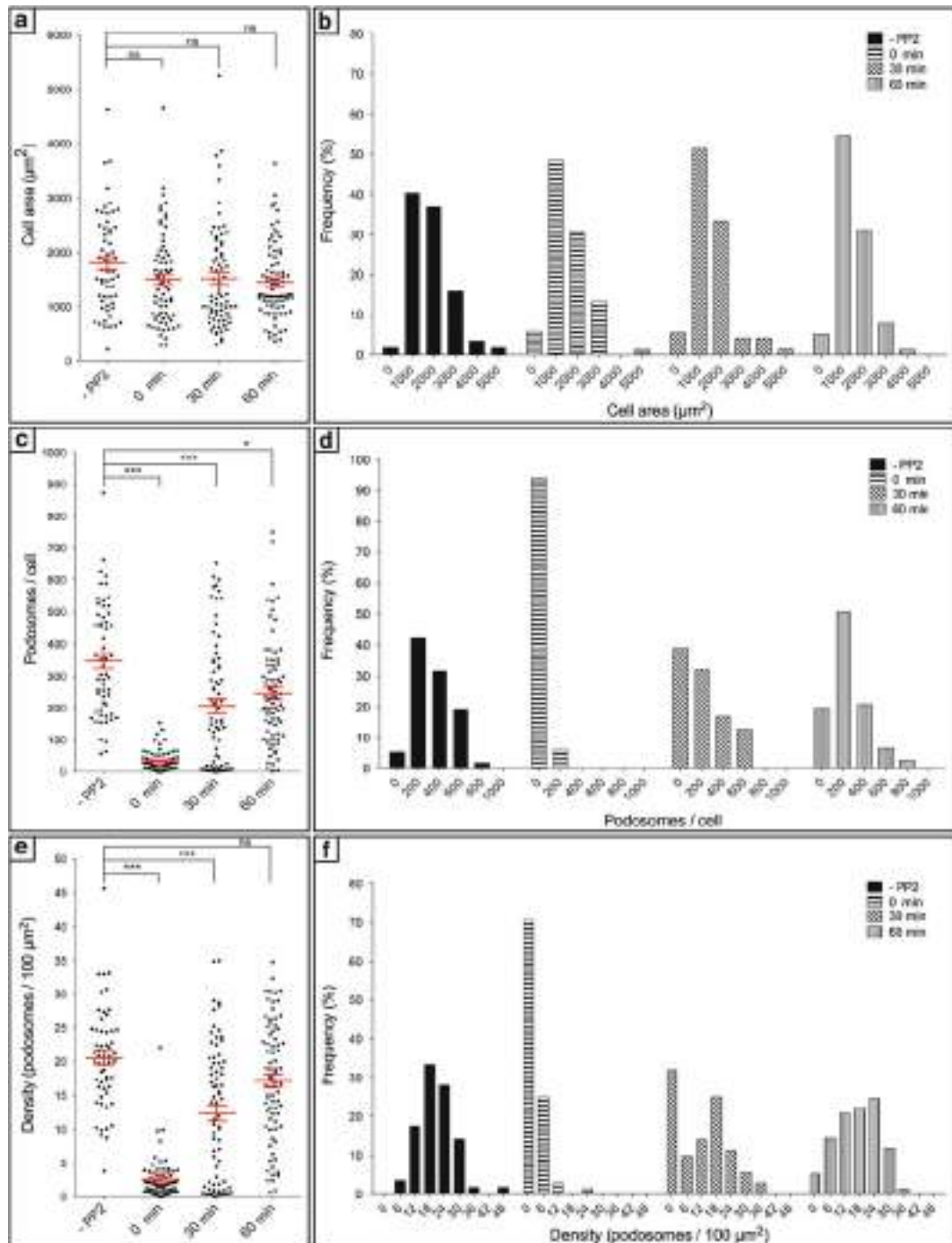
Fig. 5 Statistical analysis of podosome reformation using fixed samples. Measurements of (**a**, **b**) cell area, (**c**, **d**) number of podosomes per cell, and (**e**, **f**) density of podosomes. Each *dot* in (**a**, **c**, **e**) represents a value from a single cell, with mean values given ± SEM. (**b**, **d**, **f**) show respective frequency analyses of (**a**, **c**, **e**). Podosome density in (**e**, **f**) is given as (podosome number/100 μm²). Analyzed time points include 30 min before addition of Src tyrosine kinase inhibitor ("−PP2"), and 0, 30, and 60 min after the start of PP2 washout. Note that the high number of analyzed cells, coupled with frequency analysis of podosome numbers per cell reveals that the mean value for the 30 min time point in (**e**) is derived from a mixture of two cell subpopulations showing either numerous or almost no podosomes, as clearly visible in Fig. 3l (Color figure online)

6. Unplug the Neon™ Pipette and immediately transfer the transfected cells into a tube containing 100 μL macrophage culture medium pre-warmed to 37 °C. Mix the cells with the medium by gently pipetting up and down 5–10 times and transfer them to a glass-bottom dish for live cell imaging.

7. Place the dish in an incubator at 37 °C and 5 % CO_2 until you start the respective podosome reformation assay.

3.7 Podosome Reformation Assay Using Live Cell Imaging

Evaluating podosome reformation by live cell imaging enables the tracking of individual cells and their podosomes throughout the whole course of the experiment, yielding additional parameters including half times of podosome disruption and reformation, as well as the duration of the lag phase preceding podosome reformation (Fig. 6). Disadvantages include the need for a live cell microscope equipped with an environmental chamber, and the limited number of cells that can be analyzed. This assay thus displays different strengths and weaknesses compared to the analysis of fixed cell samples, and combining both setups is an ideal option.

1. Before the start of the experiment, equilibrate the environmental chamber in a humid atmosphere at 37 °C and 5 % CO_2 for at least 1 h (*see* **Note 8**).

2. Use cells transfected with Lifeact-GFP and seeded on glass-bottom dishes (as described in Subheading 3.6). Wash the cells two times with 1 mL of starvation medium (pre-warmed to 37 °C) and subsequently add 500 μL of starvation medium for 60–100 min to starve cells for a total period of at least 2 h. This starvation step makes the cells more susceptible to the PP2 treatment, allowing for lower doses of the drug and shorter incubation times (*see* **Note 2**). Place the cells into the equilibrated environmental chamber.

3. Prepare 1 mL of a 2× concentrated working solution of PP2 in starvation medium (= 50 μM) and at least 3 mL of washout medium (= macrophage culture medium). Place the solutions ready to use in not completely sealed vials (to allow pH-equilibration) in a nearby incubator, or even better in the environmental chamber.

4. Before imaging, place a drop of microscope oil on the (60×)-oil-immersion objective and the clean bottom of the live cell dish and fix the dish tightly on the stage. It is important that the dish does not move out of place during the imaging process, especially when solutions and media are added or removed.

5. Identify one or several cells (*see* **Note 23**) showing good expression of Lifeact-GFP and determine the optimal values for laser intensity, exposure time and camera settings for the time lapse imaging. While searching for appropriate cells, keep
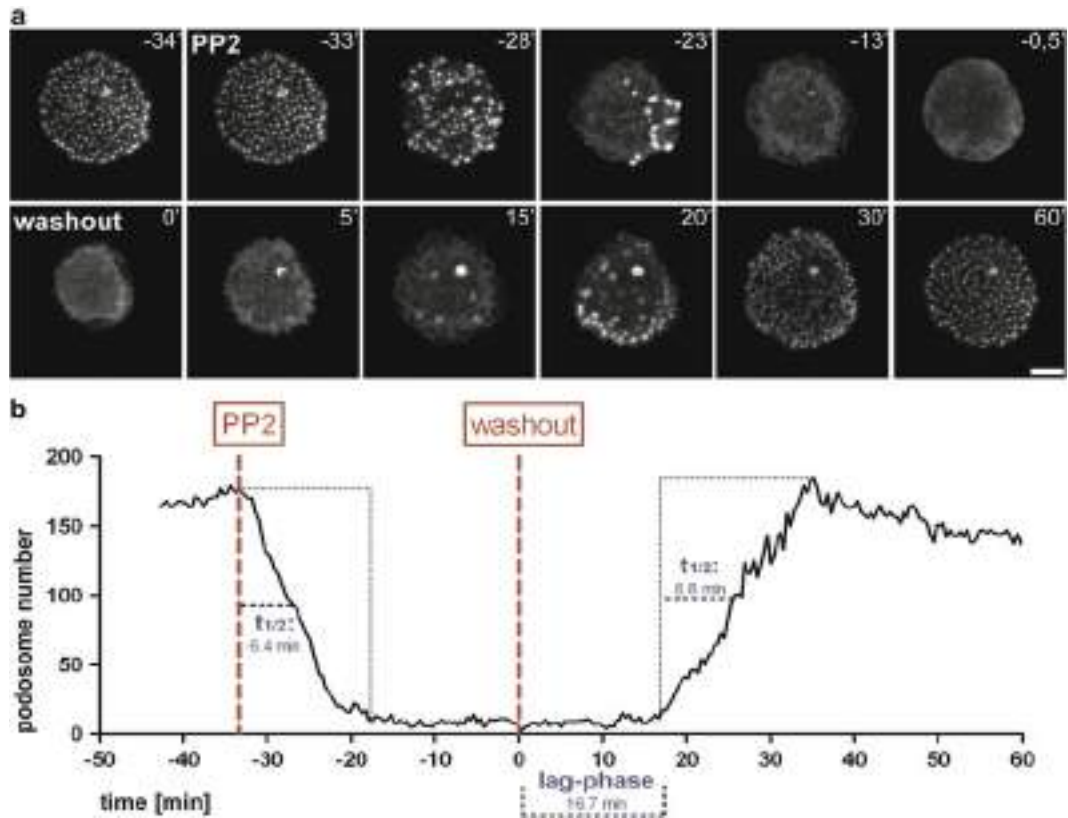
Fig. 6 Analysis of podosome reformation using live cell imaging. (**a**) Fluorescence micrographs of an 8 days cultured macrophage transfected with Lifeact-GFP. After transfection, cells were plated on a glass-bottom dish prior to serum starvation for 2 h. Time before and after washout of PP2 to start podosome reformation is given in minutes. Addition of PP2 to disrupt podosomes thus represents time point "−33′". Images were taken every 25 s. Scale bar: 10 μm. (**b**) Statistical evaluation of podosome disruption and reformation based on the live cell video of the cell shown in (**a**). Podosome number was measured by the described ImageJ macro and plotted over time using GraphPad Prism. Time points for addition of PP2 and washout of the inhibitor are indicated. Note that this analysis allows for the determination of several parameters, including the half times for podosome disruption and podosome reformation, as well as the duration of the lag phase until the start of podosome reformation, as indicated

in mind that high laser intensity and long exposure times lead to photobleaching and phototoxicity, resulting in a decrease in brightness and cell retraction (*see* **Note 24**).

6. Start the acquisition by taking an image every 15–30 s for 5–10 min. This acquisition rate is necessary because of the fast turnover and movement of podosomes. Keep in mind that podosomes have an average lifetime of about 2–12 min [7].

7. Stop the acquisition and add 500 μL of the 50 μM PP2 solution to the cells. Gently add and mix the PP2 solution with the starvation medium by carefully pipetting up and down three times. (timepoint 0 = start of PP2 treatment and of podosome disruption.)

8. Restart image acquisition immediately.

9. After 30 min, stop acquisition again for the washout of PP2. If not all of the podosomes have been disrupted, extend this period for up to 1 h (*see* **Note 2**). Carefully remove the starvation medium containing PP2 with a pipette tip from the edge of the live cell dish and gently add 1 mL of the washout medium also from this position. Repeat this step two times to ensure complete removal of the inhibitor-containing medium (=start of washout). Try to act fast to avoid loss of acquisition time, but treat cells gently, as the PP2 treatment makes them sensitive and prone to detachment.

10. Immediately resume image acquisition for 60 min.

3.8 Image Processing and Data Analysis of Live Cell Samples

This section describes the steps that enable the analysis of the recorded time-lapse videos, yielding parameters such as podosome numbers at each recorded time point, half times of podosome disruption and reformation, as well as duration of the lag phase preceding podosome reformation.

1. Open the sequence of recorded images as a TIFF-file stack in ImageJ.

2. As described in Subheading 3.5, it is necessary to initially enhance the image quality, which facilitates the subsequent analysis. The following ImageJ macro has been developed to optimize the contrast and the signal to noise ratio, also compensating for the unavoidable bleaching of specimens, to subtract the background and convert images to the required 8-bit format.

   ```
   run("Enhance Contrast", "saturated=0 use");
   run("Median…", "radius=1 stack");
   run("Subtract Background…", "rolling=50 stack");
   run("Gamma…", "value=1.50 stack");
   run("8-bit");
   ```

   Run this macro.

3. Next, run an already available macro called "Find Stack Maxima" (http://rsbweb.nih.gov/ij/macros/FindStackMaxima.txt). This macro performs the Process > Binary > Find Maxima command on all images in a stack. The only parameter that you have to adapt is "Noise tolerance", according to the quality of your image stack. To find the respective optimal value, take the output sequence of the first macro and test different values for "Noise tolerance" on individual images of the stack using the "Find Maxima" command. Make sure that the "preview point selection" box is checked, to analyze only the chosen image. It is recommended to compare the respective results for a few images from different time points of the assay, which allows a better estimation of the optimal value for "Noise tolerance" for

best detection of the podosomes in all different states of the experiment (usually, this is in the range of 5–20).

4. Run the "Find Stack Maxima" macro using the appropriate value for "Noise tolerance" and "count" for output type. This results in a chart, listing the number of podosomes for every single image of the stack. For checking the reliability of your analysis, choose "single points" for the output type, which results in an image showing all structures that have been identified by the software as dots.

5. Use Excel or GraphPad Prism to draw a graph depicting the number of podosomes in a single cell over the course of the whole experiments (Fig. 6b). This graph also allows determination of the half times for podosome disruption after PP2 addition and for podosome reformation after PP2 washout, as well as the duration of the lag phase between washout of the drug and the actual onset of the podosome reformation.

4   Notes

1. LSM 1077 is a separation solution made with Ficoll™ density gradient media. It is used for the separation of cells and subcellular components, which sediment during centrifugation. Mononuclear cells are recovered from the white interface separating the uppermost two fractions (*see* Subheading 3.1).

2. This can depend on the individual properties of primary cells from different donors. However, the PP2 treatment should not exceed 1 h, as this will lead to pronounced cell contraction.

3. It is not strictly necessary to measure protein concentration, as the same amount of cells has been used for all samples. However, keep in mind that the adhesive (here: "footplate") fraction contains much less protein (five- to tenfold) than the cell body fraction [29], and it may be necessary to adjust the loaded amounts of both fractions in order to reach comparable protein levels for subsequent detection.

4. The choice of forceps to correctly handle glass coverslips is important. Very sharp-tipped forceps can help in carefully lifting coverslips from parafilm or the bottom of 6-well plates.

5. Both the Neon™ Transfection system (Invitrogen) and the Amaxa Nucleofector® II (Lonza) are suitable for electroporation-based transfection of human macrophages and give similar transfection efficiencies (ca. 10–15 % for vector-based constructs; ca. 90–100 % for siRNA). Advantages of the Neon™ system include (1) better viability of cells, (2) faster expression of fusion proteins (as early as 3 h post transfection), (3) the necessity of only one single kit for all cell types (available in

two sizes, according to the volume of the cell suspension to be used), (4) easy and transparent adjustment of all electroporation parameters by the researcher.

6. Glass-bottom dishes are strongly recommended when using high numerical Aperture coverslip corrected objectives. It is best to take a glass coverslip No. 1.5 (=0.17 mm thickness), because most microscope objectives are designed for their use. If your objective has a correction collar to compensate for coverslip thickness variations, set it to 0.17 mm. We are using No. 1.5 glass-bottom live cell dishes from WillCo (# GWSt-3512) with a diameter of 12 mm.

7. A humid atmosphere is achieved by passing the 0.5 % CO_2 containing air through an air outlet into a bottle of water and from there into the environmental chamber.

8. The minimal technical prerequisites for live cell imaging of podosome reformation are an inverted epifluorescence or confocal microscope with an at least 60× objective. In addition, you will need an excitation and emission filter for GFP (or another filter, if Lifeact coupled to a different fluorophore is used), a camera and a shutter, which should be computer-controlled. Finally, an environmental chamber is necessary, to maintain a constant temperature of 37 °C and a CO_2 level of 5 % (to maintain the correct pH of $NaHCO_3$ buffered media). Both are important for preservation of the normal cell physiology, and cells will respond with contraction to variations in these parameters. If you are not able to supply your environmental chamber with CO_2, you can make use of HEPES buffered media, which do not require a controlled atmosphere. A perfect focus system is very helpful for constantly keeping the focus of cells/podosomes during image acquisition. If your microscope is not equipped with such a tool, make sure that the environmental chamber as well as the objective are well equilibrated at 37 °C by both a stage warmer and an objective heater in case of an objective with high numerical aperture. This will stabilize the Z-positioning over time.

9. It is important to resuspend cells gently during this step, as vigorous mixing and the creation of air bubbles may lead to random activation of cells, resulting in enhanced migration during cell culture.

10. As an alternative to whole human serum, you can also add macrophage colony-stimulating factor MCSF at 5 ng/mL in addition to 20 % dialysed fetal bovine serum [18]. This cytokine induces the differentiation of the isolated monocytic cells into macrophages [30].

11. Minimal time of culture is 6 days post purification of monocytic cells. The optimal time for using differentiated macrophages for podosome reformation is 7–9 days. Transfection efficiency

decreases after 9 days, however, cells may be used for up to 2 weeks of culture.

12. Using a 6-well plate is important in order to have all the samples ready to be lysed at the same time.

13. Time points can be varied, but should cover at least a 60 min period to allow for full reformation of podosomes.

14. It is important to perform this washing step gently, as macrophages are less adherent after the PP2 treatment due to the loss of their main adhesion structures (podosomes and focal adhesions).

15. For the image analysis, it is recommendable to generate a layer of clearly recognizable individual cells in order to simplify the segmentation step ("Watershed"). However, don't decrease the density too much, as cells may then lose their spread morphology.

16. Cell adhesion on glass coverslips is usually weaker compared to plastic surfaces. Aspiration of media may thus result in a substantial loss of cells. A gentler alternative is to rapidly transfer the coverslips to new cell culture wells, or dishes pre-filled with warmed medium (with or without PP2, depending on the step in the experiment). Use a vacuum pump for aspiration only after fixation of cells.

17. Transfer the coverslips to the fixative-containing well manually and make sure that remaining drops of medium on the coverslips are dripped onto a tissue before placing them in the fixative to not dilute the solution.

18. Sealing serves two purposes: coverslips are immobilized on the slide, and drying-out of samples is prevented. If stored at 4 °C in the dark, samples may thus remain usable for several months.

19. Macrophages contain a high amount of granules, which appear as dark spots on the red background of the cytoplasm and may thus interfere with the image analysis.

20. If your sample is uniformly stained (i.e., no visible granules) and if cells are clearly separate, you can skip the points described in Subheading 3.5, **step 3** and use only the "Smooth" tool.

21. If you don't have any cell body staining available, you can still draw the cell ROI manually, add them to the "ROI Manager" and follow the next points of the paragraph.

22. If your construct of interest shows good expression early after transfection, this step is also possible on the day of use. However, for Lifeact-GFP expression in macrophages, overnight is optimal.

23. If your microscope is equipped with an automated stage and respective software, videos of several individual cells can be acquired at the same time.

24. It is important to find a good balance between optimal resolution and a minimal effect of photobleaching and phototoxicity in order to obtain the best results of cells showing a physiological morphology, combined with sufficient and constant image quality. Thus, you have to minimize the energy level of the excitation light and/or laser power and the duration of exposure with the goal to not damage the cells and the fluorophore, but to achieve an image of sufficiently good resolution at the same time.

Acknowledgments

References

1. Gimona M, Buccione R, Courtneidge S, Linder S (2008) Assembly and biological role of podosomes and invadopodia. Curr Opin Cell Biol 20:235–241

2. Linder S, Wiesner C, Himmel M (2011) Degrading devices: invadosomes in proteolytic cell invasion. Annu Rev Cell Dev Biol 27:1 85–211

3. Saltel F, Daubon T, Juin A, Ganuza IE, Veillat V, Genot E (2011) Invadosomes: intriguing structures with promise. Eur J Cell Biol 90:100–107

4. Linder S (2007) The matrix corroded: podosomes and invadopodia in extracellular matrix degradation. Trends Cell Biol 17:107–117

5. Linder S, Nelson D, Weiss M, Aepfelbacher M (1999) Wiskott-Aldrich syndrome protein regulates podosomes in primary human macrophages. Proc Natl Acad Sci USA 96: 9648–9653

6. Burns S, Thrasher AJ, Blundell MP, Machesky L, Jones GE (2001) Configuration of human dendritic cell cytoskeleton by Rho GTPases, the WAS protein, and differentiation. Blood 98:1142–1149

7. Destaing O, Saltel F, Geminard J, Jurdic P, Bard F (2003) Podosomes display actin turn-over and dynamic self-organization in osteoclasts expressing actin-green fluorescent protein. Mol Biol Cell 14:407–416

8. Moreau V, Tatin F, Varon C, Genot E (2003) Actin can reorganize into podosomes in aortic endothelial cells, a process controlled by Cdc42 and RhoA. Mol Cell Biol 23:6809–6822

9. Burgstaller G, Gimona M (2004) Actin cytoskeleton remodelling via local inhibition of contractility at discrete microdomains. J Cell Sci 117:223–231

10. Lorenz M, Yamaguchi H, Wang Y, Singer RH, Condeelis J (2004) Imaging sites of N-WASP

activity in lamellipodia and invadopodia of carcinoma cells. Curr Biol 14:697–703

11. Monsky WL, Lin C, Aoyama A (1994) A potential marker protease of invasiveness, separase, is localized on invadopodia of human malignant melanoma cells. Cancer Res 54:5702–5710

12. Gimona M, Buccione R (2006) Adhesions that mediate invasion. Int J Biochem Cell Biol 38:1875–1892

13. Murphy DA, Courtneidge SA (2011) The "ins" and "outs" of podosomes and invadopodia: characteristics, formation and function. Nat Rev Mol Cell Biol 12:413–426

14. Linder S, Aepfelbacher M (2003) Podosomes: adhesion hot-spots of invasive cells. Trends Cell Biol 13:376–385

15. Mersich AT, Miller MR, Chkourko H, Blystone SD (2010) The formin FRL1 (FMNL1) is an essential component of macrophage podosomes. Cytoskeleton 67:573–585

16. Bhuwania R, Cornfine S, Fang Z, Krüger M, Luna EJ, Linder S (2012) Supervillin couples myosin-dependent contractility to podosomes and enables their turnover. J Cell Sci 125:2300–2314

17. Cox S, Rosten E, Monypenny J, Jovanovic-Talisman T, Burnette DT, Lippincott-Schwartz J, Jones GE, Heintzmann R (2012) Bayesian localization microscopy reveals nanoscale podosome dynamics. Nat Methods 9:195–200

18. Cervero P, Himmel M, Krüger M, Linder S (2012) Proteomic analysis of podosome fractions from macrophages reveals similarities to spreading initiation centres. Eur J Cell Biol 91:908–922

19. Zaidel-Bar R, Itzkovitz S, Ma'ayan A, Iyengar R, Geiger B (2007) Functional atlas of the integrin adhesome. Nat Cell Biol 9:858–867

20. Attanasio F, Caldieri G, Giacchetti G, van Horssen R, Wieringa B, Buccione R (2010) Novel invadopodia components revealed by differential proteomic analysis. Eur J Cell Biol 90:115–127

21. Dovas A, Cox D (2011) Signaling networks regulating leukocyte podosome dynamics and function. Cell Signal 23:1225–1234

22. Albiges-Rizo C, Destaing O, Fourcade B, Planus E, Block MR (2009) Actin machinery and mechanosensitivity in invadopodia, podosomes and focal adhesions. J Cell Sci 122:3037–3049

23. Destaing O, Block MR, Planus E, Albiges-Rizo C (2011) Invadosome regulation by adhesion signaling. Curr Opin Cell Biol 23:597–606

24. Boateng LR, Huttenlocher A (2012) Spatiotemporal regulation of Src and its substrates at invadosomes. Eur J Cell Biol 91:878–898

25. Starnes TW, Cortesio CL, Huttenlocher A (2011) Imaging podosome dynamics and matrix degradation (Chapter 9). Methods Mol Biol 769:111–136

26. Labernadie A, Thibault C, Vieu C, Maridonneau-Parini I, Charrière GM (2010) Dynamics of podosome stiffness revealed by atomic force microscopy. Proc Natl Acad Sci USA 107:1–10

27. Linder S, Hüfner K, Wintergerst U, Aepfelbacher M (2000) Microtubule-dependent formation of podosomal adhesion structures in primary human macrophages. J Cell Sci 113:4165–4176

28. Schneider CA, Rasband WS, Eliceiri KW (2012) NIH Image to ImageJ: 25 years of image analysis. Nat Methods 9:671–675

29. Kuo J, Han X, Yates JR III, Waterman CM (2012) Isolation of focal adhesion proteins for biochemical and proteomic analysis. Methods Mol Biol 757:297–323

30. Stanley ER, Berg KL, Einstein DB, Lee PSW, Pixley FJ, Wang Y, Yeung Y (1997) Biology and action of colony-stimulating factor-1. Mol Reprod Dev 46:4–10

DISCUSSION

1. Proteomic analysis of podosome fractions from macrophages reveals similarities to spreading initiation centres and identifies new podosome component.

Cells can interact with surrounding extracellular matrix by using a set of specific adhesion structures, such as focal contacts, focal adhesions, fibrillary adhesion [91] spreading initiation centers (SICs), podosomes and invadopodia, among others. They all have in common the same function, that is adhesion, however each structure also presents a unique combination of features like size, structure, dynamics, subcellular localization and additional functions (i.e. matrix degradation for podosomes and invadopodia) in order to provide cells with a wide range of flexibility. As a consequence, different cell-matrix contacts will also have specific molecular composition or "fingerprints".

In the past, many studies have focused on characterizing the proteomes of some cell-matrix contacts, such as focal adhesions [80-83], SICs [84] and invadopodia [85]. Focal adhesion proteins, for instance, have been shown to belong mostly to the family of adaptor proteins, adhesion receptors (i.e. integrins), actin binding proteins and actin regulators, kinases and phosphatases, and Rho GTPases together with their effectors GAPs (GTPase-activating protein) and GEFs (Guanine nucleotide exchange factors) [80].

Spreading initiation centers have been first described in 2004 as precursors of focal adhesions during very early stages of spreading, when other adhesion structures are not yet established [84]. They are mostly present in primary or non-tumor-derived cells where they regulate the rate of cell spreading [92].
Interestingly, SICs contain ribonucleic acids and numerous RNA binding proteins, such as FUS/TLS, hnRNP K and hnRNP E1, which normally are not presents in classical adhesion structures, in addition to very well established focal adhesion markers like vinculin and paxillin [84]. Moreover, each structure is surrounded by an actin sheath.

Thus SICs likely represent local protein factories producing the required components of focal adhesion very quickly and already in the correct place, as they normally form directly above and right before classical focal adhesions [84].

The invadopodia proteome has been described in 2010 and includes 58 proteins belonging to different functional classes including aerobic glycolysis and other metabolic pathways, protein synthesis, degradation and folding, cytoskeletal components and membrane-associated proteins [85].
In line with the relevant function of invadopodia in tumor invasion, the presence of glycolytic enzymes might be reconciled with the notion that many tumors have up-regulated glucose metabolism and a tendency to use glycolytic rather than respiratory energy production.

Surprisingly, despite the constantly increasing interest of the scientific community in the podosome field and the continuous developing of techniques in proteomics, a specific effort to identify the molecular fingerprint of podosomes and to compare it to other adhesion structures, by highlighting differences as well as similarities, had never been done.

In the first part of my PhD project I tried to address this point. Human primary macrophages represent one of the best cell model to study podosome proteome because most of their actin cytoskeleton is used to form podosomes, with only minor to null contributions from other adhesion structures [60].
By combining different techniques such as differential cell lysis [93], stable isotope labelling with aminoacids in cells culture (SILAC)[94-97], mass spectrometry and PP2-mediated disruption of podosomes [98] through inhibition of Src-family kinase activity, we were able to quantitatively compare macrophage protein lysates, enriched in podosomes, with analogous lysates, podosome-free.

From the overlap of three different replicates we generated a robust and reliable "consensus list" of 203 proteins (**Figure 9**).

This list represents a substantial description of the podosome proteome, although it is not complete, as some proteins already known and described as podosome component have been filtered out during the analysis, while others may be missing for technical limitations.
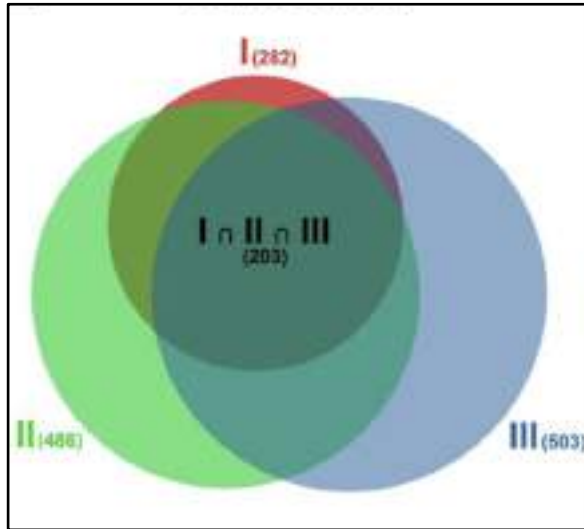
Figure 9. Podosome proteome overlaps [29].
Proteomic datasets from three different replicates (I-III) were compared using Venn diagrams. Each protein group has a specific color with number of detected proteins shown in brackets. The intersection of all three groups is shown in the middle as I ∩ II ∩ III and contains 203 proteins shared between all three datasets. This list is referred to as consensus list or podosome proteome from now on.

The validity and robustness of the experimental procedure was confirmed by the presence in the consensus list of 33 proteins already described as podosome component. Among them we found ARP 2/3 complex subunits, cofilin, CD44, coronin and gelsolin as F-actin core component together with vinculin, zyxin, talin-1, kindlin-3, β_2-integrin and myosin IIA as ring-related proteins. Other important proteins like CDC42, cortactin, WASP, MMP-9, among others, were only present in one or two datasets, thus filtered out from the overlap. In fact, if we consider all the proteins detected in the three replicates and not just those in common (i.e. overlap, consensus list) we identified 60 known podosome proteins, out of a total of 89 components described in the literature.

In general, the consensus list is mostly composed of proteins related to three main molecular functions: actin binding (i.e. cytoskeletal proteins), ATPase / GTPase activity (i.e. enzymes) and RNA binding (structural constituent of ribosomes) (**Figure 10**).

While the enrichment of the first two categories was expected because they comprise mostly cytoskeletal proteins, actin regulators with enzymatic activity (e.g. Rac1) and microtubule associated proteins (e.g. dynamin-2, several Rab proteins), the strong enrichment of ribosomal proteins was a surprise and drew immediately our attention, pointing to a potential contamination, due to experimental procedure, or to a previously unrecognized group of podosome components.
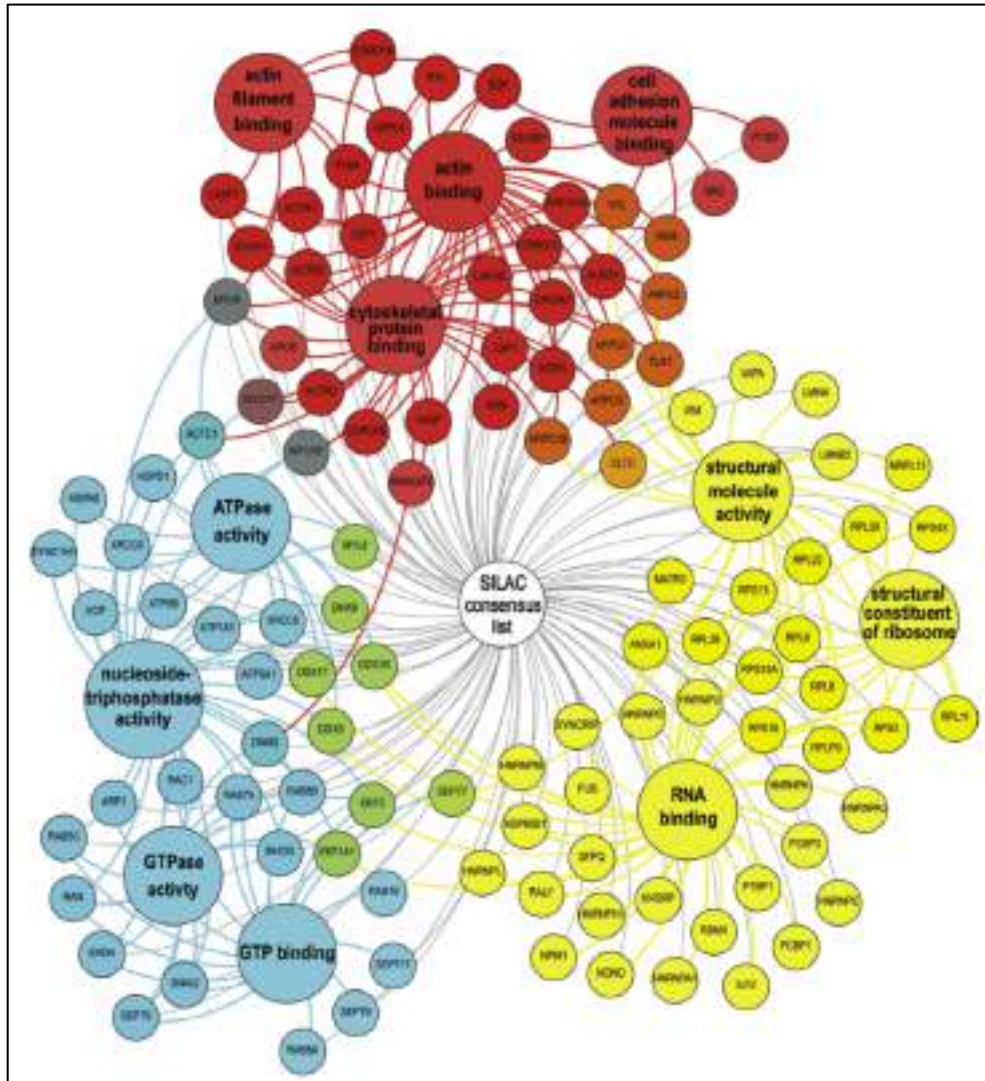
Figure 10. Network diagram of podosome proteome [29].
Proteins (gene name shown in small circles) from the consensus list have been grouped according to specific molecular function (large circles) and color-coded. Proteins belonging from more than one group have multiple connections and intermediate colors depending on the relative attribution to each group.

To test this hypothesis and as proof of principle, we evaluated the localization of two proteins picked up from the consensus list and not yet described as podosome component. We chose WDR1 from the group of actin binding proteins and hnRNP K as a representative for the newly identified group of RNA binding proteins.

WD repeat- containing protein 1 (WDR1) is a protein identified as an important cofactor of ADF/cofilin. It binds to both actin filaments and ADF/cofilin facilitating actin disassembly and turnover [99]. It is involved in cytokinesis as well as

chemotactic cell migration by restricting lamellipodial membrane protrusions to one direction via promoting cofilin activity [100]. As shown in the paper, WDR1 colocalizes with the F-actin core of podosomes, pointing to a potential role in the regulation of actin filament turnover.

Heterogeneous Nuclear Ribonucleoprotein K (hnRNP K) is known to bind to pre-mRNA in the nucleus and regulate its processing, stability and transport to the cytoplasm [101]. As shown by immunostaining and live cell imaging microscopy experiments performed in our lab, hnRNP K clearly colocalizes to podosome cores in addition to the canonical nuclear localization. We could therefore exclude the initial concerns about experimental "contamination" and confirm the potential importance of RNA binding proteins as additional components of podosome structure and / or regulators of podosome function. HnRNP K has also been found in the invadopodia proteome [85] as well as SICs proteome [84] and its direct interaction with N-WASP has been described in mouse embryonic fibroblasts [92]. Interestingly, N-WASP is also known as a key component of invadopodia [102], while its hematopoietic homologue WASp is essential for podosome formation and regulation in macrophages [60] and dendritic cells [61]. It is thus reasonable to speculate that hnRNP K has a role not only in the regulation of cell spreading rate, but also in the formation / regulation of podosomes and invadopodia, likely via interaction with (N)-WASP, although the potential localization of hnRNP K in invadopodia is still unknown.

In addition to podosome proteome description, we also compared the four proteomes to each other and noted that while focal adhesion, invadopodia and SIC proteomes share only few proteins with each other, the podosome proteome has specific overlaps with each group, pointing to an important intermediate role concerning the respective molecular machineries (**Figure 11**).

The overlap between podosomes and focal adhesions comprises 17 proteins, including 13 previously described podosome components such as filamin A, Arp2/3 complex subunits and cofilin, as well as adhesion proteins such as talin-1, vinculin and zyxin, in addition to the recently identified Lasp1 and potentially new candidates like CSRP 1 (cysteine and glycin rich protein-1), and SDCBP (syntenin 1).

The overlap between podosomes and invadopodia comprises 19 proteins, including Annexin A5, gelsolin, several heat shock proteins (HSP) and enzymes like glu-

cose 6-phosphate dehydrogenase or enolase-1 among others, whereas the overlap with SICs comprises mostly RNA binding proteins, like hnRNPs and 40S, 60S ribosomal proteins.

Moreover, 170 proteins out of the 203 of the podosome consensus list are potential novel components, of which 4 are shared with focal adhesions, 16 with invadopodia and 34 with SICs, in addition to 136 proteins only present in the podosome proteome because not yet identified in other adhesion structure proteomes.
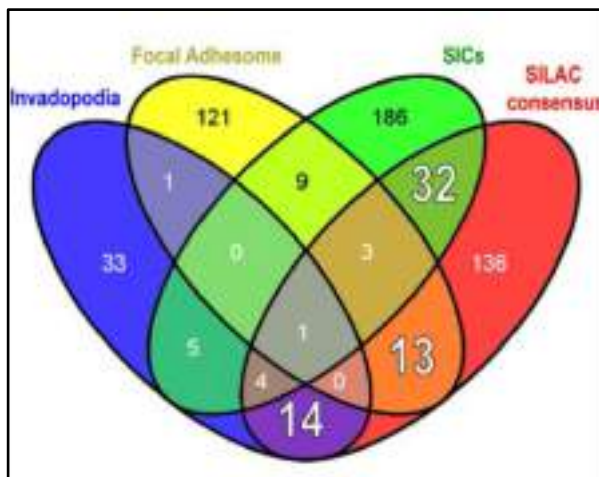

Figure 11. Venn diagram analysis of cell-matrix adhesion proteomes [29]. Comparison of podosome proteome with other cell-matrix contact proteomes. Note how podosome proteome is the only group (red group, SILAC consensus) showing extensive overlap with each other group (large digits). Digits indicate the number of proteins found in the specific overlap.

To recapitulate, by using proteomic approach we could show that podosomes share adhesion and structural proteins with focal adhesions, enzymatic/metabolic components with invadopodia and RNA-binding proteins with SICs. Interestingly, the presence of ribonucleoprotein complexes does not seem to be a contamination, but may rather represent a new podosome feature, a sort of ready-to-translate machinery useful for targeting protein production to specific subcellular compartments and for quickly providing macrophages with new batch of proteins, in case of acute stress or fast protein degradation.

In conclusion, the proteomic analysis that we described offers the possibility of 1) better understanding the common features shared by these structures as well as the protein machineries involved; 2) discovering new shared functions; 3) developing individual "molecular fingerprints" that allow clear distinction between the different types of matrix contacts.

2. LSP1 localizes to podosome cap and regulates macrophage migration and podosome mechanosensing.

Based on the podosome proteomic analysis described, we selected several proteins to screen as potential new components and, among them, decided to focus our attention on the most promising one according to the mass spectrometry score: lymphocyte-specific protein 1 (LSP1).

LSP1 is a protein isolated 30 years ago for the first time in B and T lymphocytes [103]. Since then, it has also been found in macrophages, neutrophils, dendritic cells and endothelial cells [87, 88, 104, 105].

In neutrophils and B lymphocytes, it localizes on the cytoplasmic face of the plasma membrane [106], whereas in endothelial cells, it is mostly present in the nucleus and decorates F-actin rich microfilaments in the cytoplasm [87, 107]. During our studies, it has also been shown, by another group, to co-localize with podosome F-actin cores in dendritic cells, where it also presumably interacts with ARP 2/3 complex and WASP [88].

Previous studies have described LSP1 as a crucial regulator of immune cells chemotaxis, recruitment to inflammation sites and phagocytosis [86, 88, 89, 108-111]. For instance, LSP1 overexpression is responsible for neutrophil actin dysfunction (NAD 47/89), an inherited disease where neutrophils have impaired ability to kill bacteria, despite an abundance of hair-like F-actin protrusions, and show reduced adhesion and motility, resulting in severe recurrent infections [112, 113]. In contrast, LSP1 deficiency leads to enhanced T cell migration and contributes to the development of rheumatoid arthritis [90].

LSP1 comprises 339 aminoacids and the structure can be ideally split in two subdomains with a similar number of residues: 1) the N-terminal half, highly acidic in composition, poorly conserved among species and putatively binding Ca^{2+}; 2) the C-terminal half, highly basic in composition, highly conserved among species and harbouring four F-actin binding sites, of which two are caldesmon-like domains (CI, CII; weak binding) and two are villin headpiece-like domains (VI, VII; strong binding). Interestingly, each isolated domain has the ability to bind F-actin in vitro, however only the cooperation between the two pairs (i.e. CI, CII and VI,

VII) seems to have biological relevance and preserve the ability to create the hair-like projections on the cell surface and the motility defect observed in NAD 47/89 [114]. In addition, LSP1 has also several serine and threonine residues that can be phosphorylated by kinases like MAPKAPK2 (MK2) or protein kinase C (PKC) [109, 110, 115-118], which are essential for chemotaxis regulation of immune cells.

Extending earlier data from dendritic cells [88], we found LSP1 not only colocalizing with podosome cores, but decorating especially the podosome cap and lateral/interconnecting actin filaments. Moreover, LSP1 was significantly enriched at the cell cortex and at the leading edge of migrating macrophages, where it preferentially localized at precursor rather than successors podosomes, pointing to a potential role in leading edge stabilization and migration.

Further confirmation for this hypothesis came from siRNA-mediated knockdown experiments, where depletion of LSP1 resulted in several effects on multiple levels, influencing individual podosomes, clusters of podosomes and overall cell dynamics. In particular, a reduction of about 50 % of protein levels is sufficient to shorten podosome lifetime and induce formation of multiple and highly dynamic clusters of podosomes that randomly move within the cell (**Figure 12**).

Usually, macrophages have only one cluster of podosomes which can be either in a dynamic steady state (i.e. resting cell with podosomes covering the whole ventral area) or move together with the leading edge of migrating cells, contributing to its stabilization (**Figure 12**).
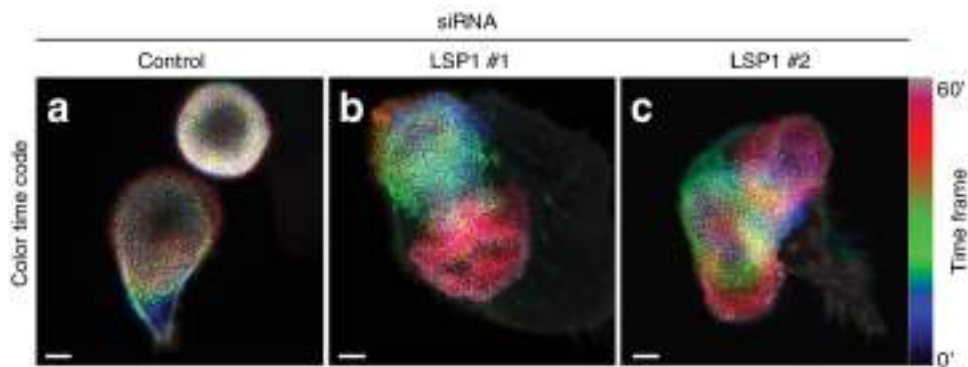

Figure 12. LSP1 depletion leads to enhanced mobility of podosome clusters [53].
Sequential frames from time lapse videos were progressively color-coded along the spectrum and merged in a single image. As consequence, static objects tend to be white, whereas moving objects acquire a rainbow-like pattern. To note, in (a) a typical resting cell (up-right) in comparison to a typical migrating macrophage moving along a vertical axis. Rainbow-colored podosome clusters in (b) and (c) indicate enhanced mobility.

Depletion of LSP1 destabilizes the whole podosome network and impairs the formation of a functional leading edge, producing a phenotype characterized by macrophages moving faster, but randomly, with formation of multiple leading edges. In addition, it is conceivable that reduction of LSP1 at the cell cortex can induce relaxation of cortical tension and improve the ability of the cell to deform and squeeze through ECM pores thus contributing to increase cell adhesion area and collagen I invasion observed in 2D and 3D settings, respectively.

These observations are in line with previous work, where leukocytes from LSP1-knockout mice show faster migration [119], whereas overexpression of the protein, typical of the neutrophil actin dysfunction syndrome (NAD47/89), leads to reduced motility of neutrophils [113], thus pointing to LSP1 as a negative regulator of immune cell migration.

As mentioned earlier, LSP1 localizes on top of the podosome core, i.e. the cap structure, and partially decorates unbranched actin fibers that extend along its side (i.e. lateral cables), connecting the actin core to adhesion proteins of the ring. These bundles of F-actin are also sites of myosin IIA localization, which allows them to contract [120]. The contractility of lateral cables together with actin polymerization, are responsible for the mechanosensing ability of podosomes, allowing them to oscillate perpendicular to the ventral plasma membrane and to exert a protruding force against it, in the range of several nN [75, 121, 122].

Consistent with these observations, we measured an increase in podosome oscillation activity upon LSP1 overexpression, whereas its depletion resulted in 50% less myosin IIA around the podosome core, with concomitant reduction of protrusion forces exerted by single podosomes, as measured by atomic force microscopy (AFM) (**Figure 13**).
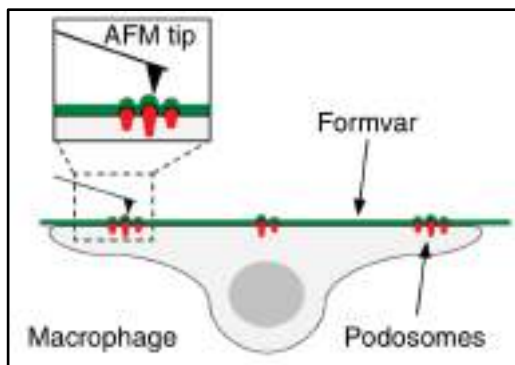

Figure 13. Principle of atomic force microscopy for measuring podosome protrusive forces [53].
Macrophage is seeded on a pliant substrate (Formvar) and turned upside down to allow a cantilever to probe protruding forces exerted by single podosomes.

From previous studies, LSP1 is known to have the ability to directly bind myosins, such as myosin 1e [111], however this does not seem to be the case with myosin IIA, where the interaction is mediated by F-actin, as we demonstrated by myosin immunoprecipitation experiments in the presence of Mg^{2+} /ATP, which reduce the amount of coprecipitated F-actin with concomitant reduction of LSP1, and myosin cosedimentation assays with pure proteins. We can therefore reason that depletion of LSP1 leads to concomitant reduction of myosin IIA, both at podosomes and the cell cortex, by decreasing the amount of F-actin bundles and, as a consequence, the number of myosin IIA molecules recruited.

In conclusion, we describe a new key role for LSP1 in regulating the mechanosensing activity of podosomes by ensuring the correct functionality of podosome lateral actin fibers. In addition, impairment of LSP1 activity is not only affecting dynamics of single podosomes, but also alters the stability of the whole podosome network and, in consequence, the overall migratory capability of macrophages.

3. LSP1 competes with supervillin for F-actin and myosin IIA regulators.

Similar to LSP1, supervillin localizes to the podosome cap and interacts with the same subset of myosin regulators (i.e. long myosin light chain kinase (L-MLCK) and calmodulin, but not ROCK1, ROCK2, RhoA, protein phosphatase 1 or 2), however both proteins show opposite distribution in cells, especially in migrating macrophages, with LSP1 enriched at precursors (i.e. leading edge), whereas supervillin is mostly confined at successor podosomes [79] (**Figure 14**).
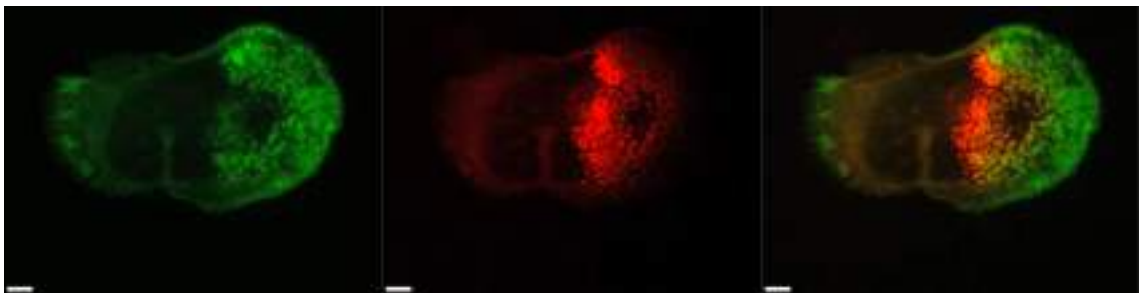

Figure 14. Differential distribution of overexpressed LSP1 (green) and supervillin (red) in a typical migrating macrophage moving on the horizontal axis [53].

They also differ in myosin IIA activation, with LSP1 inducing only moderate activity, whereas supervillin directly binds contractile myosin IIA and induces further activation, thus acting as a myosin hyper activator [79]. The preferential distribution of supervillin at successor podosomes leads to enrichment of active myosin IIA at this subset, which likely contributes to podosome dissolution, as observed previously in our lab [79].

Interestingly, LSP1 and supervillin not only share the interaction with the same subset of myosin regulators but can also compete for them. In fact, when both proteins are overexpressed in macrophages, we observe a concomitant redistribution of L-MLCK, calmodulin and Ser19-phosphorylated myosin light chain (pMLC, which is a direct indicator of myosin activity) from the leading edge, where LSP1 is mostly enriched, towards the trailing edge, where supervillin takes over. This competition contributes to generate distinct subcellular zones of different myosin IIA activity, in other words LSP1 and supervillin can induce and sustain a symmetry break in the cell by differentially regulating actomyosin contractility.

Normally resting macrophages are round-shaped and do not move, indicating that all the internal forces are dynamically counterbalanced. A symmetry breaking event represents a quick change of the internal equilibrium occurring at the macromolecular level right before the establishment of a specific polarization [123]. It is a complex process that involves many factors, such as the cytoskeleton, soluble factors and a wide range of proteins, all connected by intra- and extracellular signals. Interestingly, cells can polarize even in the absence of external stimuli, implying that the system normally operates close to instability threshold and thus is highly sensitive to minimal fluctuations [124]. Symmetry breaking is an essential process to generate functional polarization and sustain directed cell migration. In many cell types, it is normally achieved by differential recruitment of the myosin II isoforms A and B [125]. However, macrophages lack the isoform B, thus an alternative machinery, such as specific recruitment of myosin IIA regulators with different activities (i.e. LSP1 versus supervillin), becomes essential.

Recently, an interesting model has been proposed to describe migratory cell polarization and symmetry breaking. This model is based on the assumption that cells normally assemble and maintain two major F-actin networks that have differ-

ent organization and dynamics: branched filaments at sites of protrusion and contractile actomyosin bundles at cell cortex that has also the intrinsic feature to "sequester" and confine myosin [126].

These two networks locally compete for the same resource, that is G-actin, determining the degree of migratory cell polarity, with branched network pushing the edge outward, by actin nucleation, and circumferential actomyosin bundles pulling the edge inward [126]. Obviously, in such a model, myosin plays a pivotal role as it needs to be moderately active. In fact, extreme activation would lead to immobile cell with total inhibition of cell protrusion, whereas inactivation would result in formation of multiple edge protrusions and inefficient formation of single axis of polarity, an essential condition for functional migration [126].

According to this model of symmetry breaking, the formation of multiple protrusive sites (i.e. non-functional cell migration) observed in LSP1 knockdown conditions can be explained by strong reduction of cortical actomyosin contractility, being LSP1 an efficient actin bundler that normally supports moderate myosin IIA activity at the cell cortex. Further confirmation for this model come from rescue experiments using supervillin, which normally competes with LSP1 for F-actin. In absence of LSP1, supervillin is no longer confined to successor podosomes but can instead extend its range of action by localizing to precursors, and in general to the cell periphery, restoring an intermediate level of myosin activation, thanks to its capability of directly binding myosin IIA and regulators.

In conclusion, we provide detailed observations to describe how two actomyosin regulators, LSP1 and supervillin, which are localized to different subcellular compartments and differ in their ability to induce moderate or high myosin activity, respectively, can generate and sustain symmetry breaking in macrophages. However, one challenging question still remains open: what is driving the differential localization of the two actomyosin machineries that is responsible of symmetry breaking?

4. LSP1 regulation of actomyosin symmetry breaking through differential binding of actin isoforms.

Thinking about the molecular mechanism that leads to differential recruitment of LSP1 and supervillin and based on the observation that after depleting the cells of LSP1, overexpressed supervillin is not anymore confined in the usual compartment (i.e. successor podosomes), we decided to further investigate in the direction of the main common resource these two proteins compete for: F-actin.

Previous studies already showed actin isoforms having distinct cellular patterning in different cell types, such as fibroblasts, endothelial cells [52] and neurons [127].In macrophages we confirmed similar observations, with β-actin showing a clear decreasing gradient from the cell periphery or leading edge towards the cell centre or trailing edge, whereas α-cardiac actin having an inverse gradient. These distributions recall that of LSP1 and supervillin respectively (**Figure 15**).
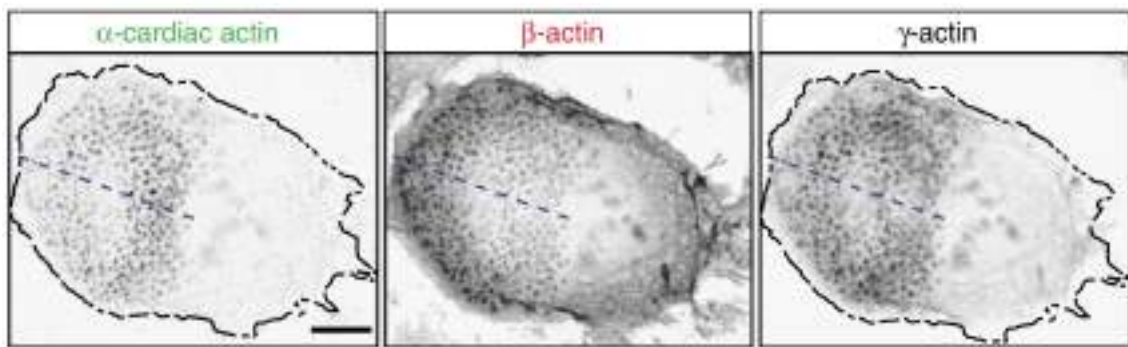

Figure 15. Differential distribution of endogenous actin isoforms (α-cardiac, β- and γ-cytoplasmic) in macrophages. To note, β-actin preferentially enriched at leading edge (precursor podosomes), while α-cardiac actin is preferentially enriched in the middle of the cell (successor podosomes) [53].

Interestingly, the presence of α-cardiac actin in a cell type other than its usual tissues of expression (i.e. muscles, especially heart) was only a partial surprise since we found it listed in the macrophage podosome proteome previously described. However, even in macrophages, this isoform keeps its high affinity for contractile structures such as those generated at successors podosomes by supervillin, which binds contractile myosin IIA and, by inducing its hyper activation, drives their dissolution [79]. In addition, we also tested the localization of γ-cytoplasmic isoform and

found a general cytoplasmic distribution with only a light to moderate gradient similar to that of β-actin.

Observations from microscopy analysis were further corroborated by in vitro experiments using pure proteins. In an F-actin cosedimentation assay, LSP1 was found to preferentially bind β-actin compared to approximately 50% less binding affinity for α-cardiac actin, whereas the three supervillin F-actin binding domains, analysed singularly, did not show any preference in binding specific F-actin isoforms.

Taking together data from microscopy and biochemistry, we could show that the differential distribution of LSP1 and supervillin is based on their different affinity for specific actin isoforms, namely β- and α-cardiac actin, which in macrophages are intrinsically distributed along inversely correlated gradients, mirroring those of LSP1 and supervillin.

Moreover, depletion of α-cardiac actin caused the redistribution of supervillin from successor podosomes to myosin IIA-positive filaments at the cell cortex. A possible reason is that supervillin, in absence of α-cardiac actin-rich successors and with β-actin-rich precursor podosomes already "occupied" by LSP1, could not bind any other F-actin structure than the myosin IIA-rich bundles underneath the cell cortex through its myosin IIA binding domain. In contrast, depletion of β-actin did not change significantly the distribution of LSP1 pointing to some other mechanism contributing to its specific enrichment at cell cortex and membranes.

Collectively, our data demonstrated that the actin isoform patterns form the basis for the differential localization of two actomyosin regulators, and their competition for F-actin isoforms is essential for the establishment and the regulation of actomyosin symmetry break in macrophages (**Figure 16**).
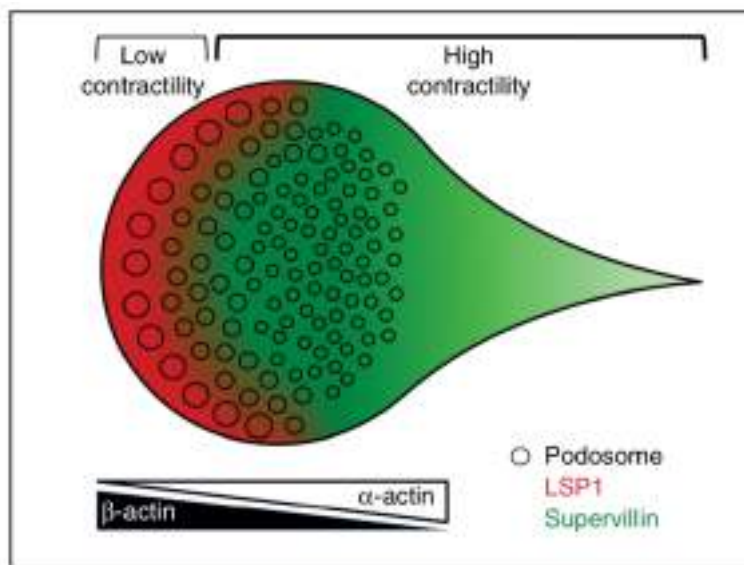
Figure 16. Model of actin isoform-based actomyosin symmetry break in macrophages [53].

Noteworthy, as described in the Introduction, different actin isoforms have also different biochemical properties that can confer specific physical features to filaments, based on their relative amount. In this way, actin isoform ratios within the cell, together with their specific molecular machinery associated (i.e. LSP1, supervillin and other actin binding protein with preferential affinity to specific isoform, such as cofilin [128] and profilin [129]) could also explain the different dynamics observed between podosome subpopulations, with β-actin-rich precursors being more prone to growth and fission and α-cardiac actin-rich successors being smaller and longer-lived.

In conclusion, our model opens up new interesting directions to further explore, such as defining the amino acid region of LSP1 responsible of its preferential binding to β-actin, and potentially provide a new general mechanism to describe actomyosin symmetry breaking in many other cell types that, like macrophages, have an intrinsic differential distribution of actin isoforms.

5. Podosome reformation in macrophages: assays and analysis.

As previously described, podosomes are highly dynamic adhesion structures with a lifetime of 0.5 to 14 minutes, a rapid internal actin turnover of 20-40 sec [63] and the additional ability to degrade extracellular matrix and sense the mechanical features of the surrounding environment [75]. The analysis of their dynamics can

provide insightful information about the functional role of novel components. Human primary macrophages represent an optimal system for the analysis of podosome dynamics because they constitutively form hundreds of podosomes and can thus provide large numbers and robust statistics, especially when investigated with imaging techniques. However, such large numbers cannot be fully exploited for statistics when the study is performed manually, because it is very time-consuming.

One way to investigate podosome dynamics is to induce their simultaneous dissolution and synchronized reformation by respectively adding PP2 and then washing it out. PP2 is a compound that can dissolve podosomes in a few minutes by inhibiting the activity of Src, the most important kinase involved in podosome regulation [60]. This assay can be paired with different other techniques, such as protein lysate preparation and analysis by Western blot or mass spectrometry, and microscopy imaging of fixed cells as well as living cells; each of these methods can address different questions and provide insightful information.

For instance, by imaging F-actin stained macrophages that have been previously fixed at specific time points during PP2 wash out, it is possible to compare the reformation curve of a certain treatment (e.g. knockdown) with the respective control and understand the reasons of potential differences. In particular, by using image analysis software it is possible to semi-automatically quantify parameters like single cell area, number of podosomes per cell and as consequence podosome density (i.e. podosomes / area). Obviously, raw images need to be "prepared" for proper podosome detection by applying a series of processing steps aiming to subtract background and highlight actual single podosomes in order to facilitate software-based detection; however, after some time spent in finding the best conditions for podosome detection, it is possible to set up an algorithm containing all the specific instructions and apply it to several dozens of images, thus gaining, in few minutes, hard numbers for robust statistic evaluation. All the instructions about image processing and podosome detection, which enable extensive analysis of podosome parameters, are collected in a macro that I developed for ImageJ software and described in detail in the protocol paper included in this thesis.

Similarly, by processing videos of PP2-mediated podosome disruption and consequent reformation in living cells, it is possible to gather information about half times of podosome disruption and reformation.

These image analysis-based tools, when used properly, can accelerate the investigation in the podosome field and provide robust statistics about the impact of certain component on the regulation of podosome dynamics.

Alternatively, PP2-mediated podosome disruption can also be used to compare macrophage protein lysates, enriched in podosomes, with analogous lysates, podosome-free [93]. Such a strategy was successfully used in combination with mass spectrometry to investigate macrophage podosome proteome [29].

REFERENCES

1.   Tauber, A.I. Metchnikoff and the phagocytosis theory. *Nat. Rev. Mol. Cell Biol.* **4**, 897-901 (2003).
2.   Varol, C., Mildner, A. & Jung, S. Macrophages: development and tissue specialization. *Annu Rev Immunol* **33**, 643-675 (2015).
3.   Lang, R.A. & Bishop, J.M. Macrophages are required for cell death and tissue remodeling in the developing mouse eye. *Cell* **74**, 453-462 (1993).
4.   Fantin, A. *et al.* Tissue macrophages act as cellular chaperones for vascular anastomosis downstream of VEGF-mediated endothelial tip cell induction. *Blood* **116**, 829-840 (2010).
5.   Ginhoux, F. & Jung, S. Monocytes and macrophages: developmental pathways and tissue homeostasis. *Nat Rev Immunol* **14**, 392-404 (2014).
6.   van Furth, R. & Cohn, Z.A. The origin and kinetics of mononuclear phagocytes. *J. Exp. Med.* **128**, 415-435 (1968).
7.   Zhao, Y., Zou, W., Du, J. & Zhao, Y. The origins and homeostasis of monocytes and tissue-resident macrophages in physiological situation. *J Cell Physiol* (2018).
8.   Gordon, S. & Taylor, P.R. Monocyte and macrophage heterogeneity. *Nat Rev Immunol* **5**, 953-964 (2005).
9.   Epelman, S., Lavine, K.J. & Randolph, G.J. Origin and functions of tissue macrophages. *Immunity* **41**, 21-35 (2014).
10.   Ginhoux, F. *et al.* Fate mapping analysis reveals that adult microglia derive from primitive macrophages. *Science* **330**, 841-845 (2010).
11.   Schulz, C. *et al.* A lineage of myeloid cells independent of Myb and hematopoietic stem cells. *Science* **336**, 86-90 (2012).
12.   Hashimoto, D. *et al.* Tissue-resident macrophages self-maintain locally throughout adult life with minimal contribution from circulating monocytes. *Immunity* **38**, 792-804 (2013).
13.   Lavin, Y., Mortha, A., Rahman, A. & Merad, M. Regulation of macrophage development and function in peripheral tissues. *Nat Rev Immunol* **15**, 731-744 (2015).
14.   Ginhoux, F., Schultze, J.L., Murray, P.J., Ochando, J. & Biswas, S.K. New insights into the multidimensional concept of macrophage ontogeny, activation and function. *Nat. Immunol.* **17**, 34-40 (2016).
15.   Mantovani, A. *et al.* The chemokine system in diverse forms of macrophage activation and polarization. *Trends Immunol.* **25**, 677-686 (2004).
16.   Sica, A. & Mantovani, A. Macrophage plasticity and polarization: in vivo veritas. *J. Clin. Invest.* **122**, 787-795 (2012).
17.   Lawrence, T. & Natoli, G. Transcriptional regulation of macrophage polarization: enabling diversity with identity. *Nat Rev Immunol* **11**, 750-761 (2011).
18.   Murray, P.J. Macrophage Polarization. *Annu Rev Physiol* **79**, 541-566 (2017).
19.   Martinez, F.O. & Gordon, S. The M1 and M2 paradigm of macrophage activation: time for reassessment. *F1000Prime Rep* **6**, 13 (2014).
20.   Biswas, S.K. & Mantovani, A. Macrophage plasticity and interaction with lymphocyte subsets: cancer as a paradigm. *Nat. Immunol.* **11**, 889-896 (2010).
21.   Mantovani, A., Allavena, P., Sica, A. & Balkwill, F. Cancer-related inflammation. *Nature* **454**, 436-444 (2008).

22. Yuan, A. *et al.* Opposite Effects of M1 and M2 Macrophage Subtypes on Lung Cancer Progression. *Sci. Rep.* **5**, 14273 (2015).

23. Mantovani, A. & Sica, A. Macrophages, innate immunity and cancer: balance, tolerance, and diversity. *Curr Opin Immunol* **22**, 231-237 (2010).

24. Ma, J. *et al.* The M1 form of tumor-associated macrophages in non-small cell lung cancer is positively associated with survival time. *BMC Cancer* **10**, 112 (2010).

25. Huber, F., Boire, A., Lopez, M.P. & Koenderink, G.H. Cytoskeletal crosstalk: when three different personalities team up. *Curr. Opin. Cell Biol.* **32**, 39-47 (2015).

26. Jekely, G. Origin and evolution of the self-organizing cytoskeleton in the network of eukaryotic organelles. *Cold Spring Harb. Perspect. Biol.* **6**, a016030 (2014).

27. Pollard, T.D. & Borisy, G.G. Cellular motility driven by assembly and disassembly of actin filaments. *Cell* **112**, 453-465 (2003).

28. Fujii, T., Iwane, A.H., Yanagida, T. & Namba, K. Direct visualization of secondary structures of F-actin by electron cryomicroscopy. *Nature* **467**, 724-728 (2010).

29. Cervero, P., Himmel, M., Kruger, M. & Linder, S. Proteomic analysis of podosome fractions from macrophages reveals similarities to spreading initiation centres. *Eur. J. Cell Biol.* **91**, 908-922 (2012).

30. Pollard, T.D., Blanchoin, L. & Mullins, R.D. Molecular mechanisms controlling actin filament dynamics in nonmuscle cells. *Annu. Rev. Biophys. Biomol. Struct.* **29**, 545-576 (2000).

31. Shekhar, S., Pernier, J. & Carlier, M.F. Regulators of actin filament barbed ends at a glance. *J. Cell Sci.* **129**, 1085-1091 (2016).

32. Bamburg, J.R. & Bernstein, B.W. Roles of ADF/cofilin in actin polymerization and beyond. *F1000 Biol. Rep.* **2**, 62 (2010).

33. Sun, H.Q., Yamamoto, M., Mejillano, M. & Yin, H.L. Gelsolin, a multifunctional actin regulatory protein. *J. Biol. Chem.* **274**, 33179-33182 (1999).

34. Rottner, K., Faix, J., Bogdan, S., Linder, S. & Kerkhoff, E. Actin assembly mechanisms at a glance. *J. Cell Sci.* **130**, 3427-3435 (2017).

35. Goley, E.D. & Welch, M.D. The ARP2/3 complex: an actin nucleator comes of age. *Nat. Rev. Mol. Cell Biol.* **7**, 713-726 (2006).

36. Goode, B.L. & Eck, M.J. Mechanism and function of formins in the control of actin assembly. *Annu. Rev. Biochem.* **76**, 593-627 (2007).

37. Schonichen, A. & Geyer, M. Fifteen formins for an actin filament: a molecular view on the regulation of human formins. *Biochim. Biophys. Acta* **1803**, 152-163 (2010).

38. Romero, S. *et al.* Formin is a processive motor that requires profilin to accelerate actin assembly and associated ATP hydrolysis. *Cell* **119**, 419-429 (2004).

39. Epelman, S. *et al.* Embryonic and adult-derived resident cardiac macrophages are maintained through distinct mechanisms at steady state and during inflammation. *Immunity* **40**, 91-104 (2014).

40. Baum, B. & Kunda, P. Actin nucleation: spire - actin nucleator in a class of its own. *Curr. Biol.* **15**, R305-308 (2005).

41. Winder, S.J. & Ayscough, K.R. Actin-binding proteins. *J. Cell Sci.* **118**, 651-654 (2005).

42. Herman, I.M. Actin isoforms. *Curr. Opin. Cell Biol.* **5**, 48-55 (1993).

43. Perrin, B.J. & Ervasti, J.M. The actin gene family: function follows isoform. *Cytoskeleton (Hoboken)* **67**, 630-634 (2010).

44. Shmerling, D. *et al.* Strong and ubiquitous expression of transgenes targeted into the beta-actin locus by Cre/lox cassette replacement. *Genesis* **42**, 229-235 (2005).

45. Tondeleir, D., Vandamme, D., Vandekerckhove, J., Ampe, C. & Lambrechts, A. Actin isoform expression patterns during mammalian development and in pathology: insights from mouse models. *Cell Motil. Cytoskeleton* **66**, 798-815 (2009).

46. Vedula, P. *et al.* Diverse functions of homologous actin isoforms are defined by their nucleotide, rather than their amino acid sequence. *Elife* **6** (2017).

47. Allen, P.G. *et al.* Phalloidin binding and rheological differences among actin isoforms. *Biochemistry* **35**, 14062-14069 (1996).

48. Bergeron, S.E., Zhu, M., Thiem, S.M., Friderici, K.H. & Rubenstein, P.A. Ion-dependent polymerization differences between mammalian beta- and gamma-nonmuscle actin isoforms. *J. Biol. Chem.* **285**, 16087-16095 (2010).

49. Condeelis, J. & Singer, R.H. How and why does beta-actin mRNA target? *Biol. Cell.* **97**, 97-110 (2005).

50. Kislauskis, E.H., Li, Z., Singer, R.H. & Taneja, K.L. Isoform-specific 3'-untranslated sequences sort alpha-cardiac and beta-cytoplasmic actin messenger RNAs to different cytoplasmic compartments. *J. Cell Biol.* **123**, 165-172 (1993).

51. Kashina, A.S. Differential arginylation of actin isoforms: the mystery of the actin N-terminus. *Trends Cell Biol.* **16**, 610-615 (2006).

52. Dugina, V., Zwaenepoel, I., Gabbiani, G., Clement, S. & Chaponnier, C. Beta and gamma-cytoplasmic actins display distinct distribution and functional diversity. *J. Cell Sci.* **122**, 2980-2988 (2009).

53. Cervero, P., Wiesner, C., Bouissou, A., Poincloux, R. & Linder, S. Lymphocyte-specific protein 1 regulates mechanosensory oscillation of podosomes and actin isoform-based actomyosin symmetry breaking. *Nat Commun* **9**, 515 (2018).

54. Linder, S. & Aepfelbacher, M. Podosomes: adhesion hot-spots of invasive cells. *Trends Cell Biol.* **13**, 376-385 (2003).

55. David-Pfeuty, T. & Singer, S.J. Altered distributions of the cytoskeletal proteins vinculin and alpha-actinin in cultured fibroblasts transformed by Rous sarcoma virus. *Proc. Natl. Acad. Sci. U. S. A.* **77**, 6687-6691 (1980).

56. Burgstaller, G. & Gimona, M. Actin cytoskeleton remodelling via local inhibition of contractility at discrete microdomains. *J. Cell Sci.* **117**, 223-231 (2004).

57. Moreau, V., Tatin, F., Varon, C. & Genot, E. Actin can reorganize into podosomes in aortic endothelial cells, a process controlled by Cdc42 and RhoA. *Mol. Cell. Biol.* **23**, 6809-6822 (2003).

58. Schachtner, H. *et al.* Megakaryocytes assemble podosomes that degrade matrix and protrude through basement membrane. *Blood* **121**, 2542-2552 (2013).

59. Johansson, M.W. *et al.* Eosinophils adhere to vascular cell adhesion molecule-1 via podosomes. *Am. J. Respir. Cell Mol. Biol.* **31**, 413-422 (2004).

60. Linder, S., Nelson, D., Weiss, M. & Aepfelbacher, M. Wiskott-Aldrich syndrome protein regulates podosomes in primary human macrophages. *Proc. Natl. Acad. Sci. U. S. A.* **96**, 9648-9653 (1999).

61. Burns, S., Thrasher, A.J., Blundell, M.P., Machesky, L. & Jones, G.E. Configuration of human dendritic cell cytoskeleton by Rho GTPases, the WAS protein, and differentiation. *Blood* **98**, 1142-1149 (2001).

62. Vincent, C., Siddiqui, T.A. & Schlichter, L.C. Podosomes in migrating microglia: components and matrix degradation. *J. Neuroinflammation* **9**, 190 (2012).

63. Destaing, O., Saltel, F., Geminard, J.C., Jurdic, P. & Bard, F. Podosomes display actin turnover and dynamic self-organization in osteoclasts expressing actin-green fluorescent protein. *Mol. Biol. Cell* **14**, 407-416 (2003).

64. Linder, S. Invadosomes at a glance. *J. Cell Sci.* **122**, 3009-3013 (2009).

65. Paterson, E.K. & Courtneidge, S.A. Invadosomes are coming: new insights into function and disease relevance. *FEBS J* **285**, 8-27 (2018).

66. Caldieri, G., Ayala, I., Attanasio, F. & Buccione, R. Cell and molecular biology of invadopodia. *Int. Rev. Cell Mol. Biol.* **275**, 1-34 (2009).

67. Kopp, P. *et al.* The kinesin KIF1C and microtubule plus ends regulate podosome dynamics in macrophages. *Mol. Biol. Cell* **17**, 2811-2823 (2006).

68. Linder, S. The matrix corroded: podosomes and invadopodia in extracellular matrix degradation. *Trends Cell Biol.* **17**, 107-117 (2007).

69. Linder, S. & Wiesner, C. Tools of the trade: podosomes as multipurpose organelles of monocytic cells. *Cell. Mol. Life Sci.* **72**, 121-135 (2015).

70. Seano, G. *et al.* Endothelial podosome rosettes regulate vascular branching in tumour angiogenesis. *Nat. Cell Biol.* **16**, 931-941, 931-938 (2014).

71. Labernadie, A., Thibault, C., Vieu, C., Maridonneau-Parini, I. & Charriere, G.M. Dynamics of podosome stiffness revealed by atomic force microscopy. *Proc. Natl. Acad. Sci. U. S. A.* **107**, 21016-21021 (2010).

72. van den Dries, K. *et al.* Dual-color superresolution microscopy reveals nanoscale organization of mechanosensory podosomes. *Mol. Biol. Cell* **24**, 2112-2123 (2013).

73. Walde, M., Monypenny, J., Heintzmann, R., Jones, G.E. & Cox, S. Vinculin binding angle in podosomes revealed by high resolution microscopy. *PLoS One* **9**, e88251 (2014).

74. Panzer, L. *et al.* The formins FHOD1 and INF2 regulate inter- and intra-structural contractility of podosomes. *J. Cell Sci.* **129**, 298-313 (2016).

75. Linder, S. & Wiesner, C. Feel the force: Podosomes in mechanosensing. *Exp. Cell Res.* **343**, 67-72 (2016).

76. Charras, G. & Sahai, E. Physical influences of the extracellular environment on cell migration. *Nat. Rev. Mol. Cell Biol.* **15**, 813-824 (2014).

77. Wiesner, C., Le-Cabec, V., El Azzouzi, K., Maridonneau-Parini, I. & Linder, S. Podosomes in space: macrophage migration and matrix degradation in 2D and 3D settings. *Cell Adh Migr* **8**, 179-191 (2014).

78. Evans, J.G., Correia, I., Krasavina, O., Watson, N. & Matsudaira, P. Macrophage podosomes assemble at the leading lamella by growth and fragmentation. *J. Cell Biol.* **161**, 697-705 (2003).

79. Bhuwania, R. *et al.* Supervillin couples myosin-dependent contractility to podosomes and enables their turnover. *J. Cell Sci.* **125**, 2300-2314 (2012).

80. Zaidel-Bar, R., Itzkovitz, S., Ma'ayan, A., Iyengar, R. & Geiger, B. Functional atlas of the integrin adhesome. *Nat. Cell Biol.* **9**, 858-867 (2007).

81. Zaidel-Bar, R. & Geiger, B. The switchable integrin adhesome. *J. Cell Sci.* **123**, 1385-1388 (2010).

82. Kuo, J.C., Han, X., Hsiao, C.T., Yates, J.R., 3rd & Waterman, C.M. Analysis of the myosin-II-responsive focal adhesion proteome reveals a role for beta-Pix in negative regulation of focal adhesion maturation. *Nat. Cell Biol.* **13**, 383-393 (2011).

83. Schiller, H.B., Friedel, C.C., Boulegue, C. & Fassler, R. Quantitative proteomics of the integrin adhesome show a myosin II-dependent recruitment of LIM domain proteins. *EMBO Rep* **12**, 259-266 (2011).

84. de Hoog, C.L., Foster, L.J. & Mann, M. RNA and RNA binding proteins participate in early stages of cell spreading through spreading initiation centers. *Cell* **117**, 649-662 (2004).

85. Attanasio, F. *et al.* Novel invadopodia components revealed by differential proteomic analysis. *Eur. J. Cell Biol.* **90**, 115-127 (2011).

86. Jongstra-Bilen, J. & Jongstra, J. Leukocyte-specific protein 1 (LSP1): a regulator of leukocyte emigration in inflammation. *Immunol. Res.* **35**, 65-74 (2006).

87. Petri, B. *et al.* Endothelial LSP1 is involved in endothelial dome formation, minimizing vascular permeability changes during neutrophil transmigration in vivo. *Blood* **117**, 942-952 (2011).

88. Prasad, A. *et al.* Slit2N/Robo1 inhibit HIV-gp120-induced migration and podosome formation in immature dendritic cells by sequestering LSP1 and WASp. *PLoS One* **7**, e48854 (2012).

89. Le, N.P., Channabasappa, S., Hossain, M., Liu, L. & Singh, B. Leukocyte-specific protein 1 regulates neutrophil recruitment in acute lung inflammation. *Am. J. Physiol. Lung Cell Mol. Physiol.* **309**, L995-1008 (2015).

90. Hwang, S.H. *et al.* Leukocyte-specific protein 1 regulates T-cell migration in rheumatoid arthritis. *Proc. Natl. Acad. Sci. U. S. A.* **112**, E6535-6543 (2015).

91. Adams, J.C. Cell-matrix contact structures. *Cell. Mol. Life Sci.* **58**, 371-392 (2001).

92. Yoo, Y., Wu, X., Egile, C., Li, R. & Guan, J.L. Interaction of N-WASP with hnRNPK and its role in filopodia formation and cell spreading. *J. Biol. Chem.* **281**, 15352-15360 (2006).

93. Gringel, A. *et al.* PAK4 and alphaPIX determine podosome size and number in macrophages through localized actin regulation. *J Cell Physiol* **209**, 568-579 (2006).

94. Ong, S.E. *et al.* Stable isotope labeling by amino acids in cell culture, SILAC, as a simple and accurate approach to expression proteomics. *Mol. Cell. Proteomics* **1**, 376-386 (2002).

95. Blagoev, B. *et al.* A proteomics strategy to elucidate functional protein-protein interactions applied to EGF signaling. *Nat. Biotechnol.* **21**, 315-318 (2003).

96. Ong, S.E. & Mann, M. A practical recipe for stable isotope labeling by amino acids in cell culture (SILAC). *Nat. Protoc.* **1**, 2650-2660 (2006).

97. Mann, M. Functional and quantitative proteomics using SILAC. *Nat. Rev. Mol. Cell Biol.* **7**, 952-958 (2006).

98. Linder, S., Hufner, K., Wintergerst, U. & Aepfelbacher, M. Microtubule-dependent formation of podosomal adhesion structures in primary human macrophages. *J. Cell Sci.* **113 Pt 23**, 4165-4176 (2000).

99. Fujibuchi, T. *et al.* AIP1/WDR1 supports mitotic cell rounding. *Biochem. Biophys. Res. Commun.* **327**, 268-275 (2005).

100. Kato, A. *et al.* Critical roles of actin-interacting protein 1 in cytokinesis and chemotactic migration of mammalian cells. *Biochem. J.* **414**, 261-270 (2008).

101. Sun, X., Haider Ali, M.S.S. & Moran, M. The role of interactions of long non-coding RNAs and heterogeneous nuclear ribonucleoproteins in regulating cellular functions. *Biochem. J.* **474**, 2925-2935 (2017).

102. Yamaguchi, H., Pixley, F. & Condeelis, J. Invadopodia and podosomes in tumor invasion. *Eur. J. Cell Biol.* **85**, 213-218 (2006).

103. Jongstra, J., Tidmarsh, G.F., Jongstra-Bilen, J. & Davis, M.M. A new lymphocyte-specific gene which encodes a putative Ca2+-binding protein is not expressed in transformed T lymphocyte lines. *J. Immunol.* **141**, 3999-4004 (1988).

104. Jongstra, J., Ittel, M.E., Iscove, N.N. & Brady, G. The LSP1 gene is expressed in cultured normal and transformed mouse macrophages. *Mol. Immunol.* **31**, 1125-1131 (1994).

105. Li, Y., Guerrero, A. & Howard, T.H. The actin-binding protein, lymphocyte-specific protein 1, is expressed in human leukocytes and human myeloid and lymphoid cell lines. *J. Immunol.* **155**, 3563-3569 (1995).

106. Klein, D.P., Jongstra-Bilen, J., Ogryzlo, K., Chong, R. & Jongstra, J. Lymphocyte-specific Ca2+-binding protein LSP1 is associated with the cytoplasmic face of the plasma membrane. *Mol. Cell. Biol.* **9**, 3043-3048 (1989).

107. Liu, L. *et al.* LSP1 is an endothelial gatekeeper of leukocyte transendothelial migration. *J. Exp. Med.* **201**, 409-418 (2005).

108. Wang, C. *et al.* Modulation of Mac-1 (CD11b/CD18)-mediated adhesion by the leukocyte-specific protein 1 is key to its role in neutrophil polarization and chemotaxis. *J. Immunol.* **169**, 415-423 (2002).

109. Wu, Y. *et al.* MAPKAPK2-mediated LSP1 phosphorylation and FMLP-induced neutrophil polarization. *Biochem. Biophys. Res. Commun.* **358**, 170-175 (2007).

110. Anand, A.R. *et al.* HIV-1 gp120-induced migration of dendritic cells is regulated by a novel kinase cascade involving Pyk2, p38 MAP kinase, and LSP1. *Blood* **114**, 3588-3600 (2009).

111. Maxeiner, S. *et al.* Crucial role for the LSP1-myosin1e bimolecular complex in the regulation of Fcgamma receptor-driven phagocytosis. *Mol. Biol. Cell* **26**, 1652-1664 (2015).

112. Howard, T.H., Hartwig, J. & Cunningham, C. Lymphocyte-specific protein 1 expression in eukaryotic cells reproduces the morphologic and motile abnormality of NAD 47/89 neutrophils. *Blood* **91**, 4786-4795 (1998).

113. Zhang, Q., Li, Y. & Howard, T.H. Human lymphocyte-specific protein 1, the protein overexpressed in neutrophil actin dysfunction with 47-kDa and 89-kDa protein abnormalities (NAD 47/89), has multiple F-actin binding domains. *J. Immunol.* **165**, 2052-2058 (2000).

114. Zhang, Q., Li, Y. & Howard, T.H. Hair-forming activity of human lymphocyte specific protein 1 requires cooperation between its caldesmon-like domains and the villin headpiece-like domains. *Cell Motil. Cytoskeleton* **49**, 179-188 (2001).

115. Jongstra-Bilen, J., Janmey, P.A., Hartwig, J.H., Galea, S. & Jongstra, J. The lymphocyte-specific protein LSP1 binds to F-actin and to the cytoskeleton through its COOH-terminal basic domain. *J. Cell Biol.* **118**, 1443-1453 (1992).

116. Matsumoto, N., Kojima, S., Osawa, T. & Toyoshima, S. Protein kinase C phosphorylates p50 LSP1 and induces translocation of p50 LSP1 in T lymphocytes. *J. Biochem.* **117**, 222-229 (1995).

117. Carballo, E., Colomer, D., Vives-Corrons, J.L., Blackshear, P.J. & Gil, J. Characterization and purification of a protein kinase C substrate in human B cells. Identification as lymphocyte-specific protein 1 (LSP1). *J. Immunol.* **156**, 1709-1713 (1996).

118. Huang, C.K., Zhan, L., Ai, Y. & Jongstra, J. LSP1 is the major substrate for mitogen-activated protein kinase-activated protein kinase 2 in human neutrophils. *J. Biol. Chem.* **272**, 17-19 (1997).

119. Jongstra-Bilen, J. *et al.* LSP1 modulates leukocyte populations in resting and inflamed peritoneum. *Blood* **96**, 1827-1835 (2000).

120. van den Dries, K. *et al.* Interplay between myosin IIA-mediated contractility and actin network integrity orchestrates podosome composition and oscillations. *Nat Commun* **4**, 1412 (2013).

121. Bouissou, A. *et al.* Podosome Force Generation Machinery: A Local Balance between Protrusion at the Core and Traction at the Ring. *ACS Nano* **11**, 4028-4040 (2017).

122. Luxenburg, C., Winograd-Katz, S., Addadi, L. & Geiger, B. Involvement of actin polymerization in podosome dynamics. *J. Cell Sci.* **125**, 1666-1672 (2012).

123. Huang, S. Where to Go: Breaking the Symmetry in Cell Motility. *PLoS Biol.* **14**, e1002463 (2016).

124. van der Gucht, J. & Sykes, C. Physical model of cellular symmetry breaking. *Cold Spring Harb. Perspect. Biol.* **1**, a001909 (2009).

125. Vicente-Manzanares, M., Newell-Litwa, K., Bachir, A.I., Whitmore, L.A. & Horwitz, A.R. Myosin IIA/IIB restrict adhesive and protrusive signaling to generate front-back polarity in migrating cells. *J. Cell Biol.* **193**, 381-396 (2011).

126. Lomakin, A.J. *et al.* Competition for actin between two distinct F-actin networks defines a bistable switch for cell polarization. *Nat. Cell Biol.* **17**, 1435-1445 (2015).

127. Cheever, T.R. & Ervasti, J.M. Actin isoforms in neuronal development and function. *Int. Rev. Cell Mol. Biol.* **301**, 157-213 (2013).

128. De La Cruz, E.M. Cofilin binding to muscle and non-muscle actin filaments: isoform-dependent cooperative interactions. *J. Mol. Biol.* **346**, 557-564 (2005).

129. Larsson, H. & Lindberg, U. The effect of divalent cations on the interaction between calf spleen profilin and different actins. *Biochim. Biophys. Acta* **953**, 95-105 (1988).

LIST OF FIGURES

LIST OF ABBREVIATIONS

2D	Two dimensions
3D	Three dimensions
ADF	Actin depolymerizing factor
ADP	Adenosine diphosphate
AFM	Atomic force microscopy
ARP	Actin-related protein
ATP	Adenosine triphosphate
Ca^{2+}	Calcium
Cc	Critical concentration
CD44	Cluster of differentiation 44
Cdc42	Cell division control protein 42
CMP	Common myeloid progenitor
CSRP1	Cysteine and glycine rich protein 1
DAD	Diaphanous autoregulatory domain
DID	Diaphanous inhibitory domain
ECM	Extracellular matrix
FH	Formin homology
FMNL1	Formin like 1
GAP	GTPase activating protein
GEF	Guanine-nucleotide exchange factor
hnRNP	heterogeneous ribonucleoprotein
HSP	Heat-shock protein
IL	Interleukin
IL-1R	Interleukin 1 receptor
INF	Interferon
INF2	Inverted formin 2
KO	Knockout
L-MLCK	Long myosin light chain kinase
LPS	Lipopolysaccharide
LSP1	Lymphocyte-specific protein 1
Mg^{2+}	Magnesium
mM	Millimolar
MMP	Matrix metalloproteinase

mRNA	Messenger ribonucleic acid
N-WASP	Neuronal Wiskott-Aldrich syndrome protein
NAD	Neutrophil actin dysfunction
nN	Nanonewton
NPF	Nucleation-promoting factor
PIP$_2$	Phosphotidylinositol 4,5-bisphosphate
PKC	Protein kinase C
pMLC	phospho myosin light chain
PP2	4-amino-5-(4-chlorophenyl)-7-(dimethylethyl)pyrazolo[3,4-*d*]pyrimidine
PRR	Pattern recognition receptor
ROCK	Rho kinase
SDCBP	Syndecan binding protein
SIC	Spreading initiation centres
SILAC	Stable isotopes labeling by amino acids in cell culture
siRNA	Small interfering ribonucleic acid
TAM	Tumor associated macrophages
Th1-Th2	T helper cell
TLR	Toll like receptor
TNF	Tumor necrosis factor
UTR	Untranslated region
WASH	Wiskott-Aldrich syndrome protein and scar homolog
WASP	Wiskott-Aldrich syndrome protein
WAVE	WASP family Verprolin-homologous protein
WD repeats	Tryptophan-aspartic acid repeats
WDR1	WD repeat domain 1
WH2	Wiskott-Aldrich homology 2
ZBP1	Zipcode binding protein 1
μM	Micromolar

DECLARATION ON OATH

I hereby declare, on oath, that I have written the present dissertation on my own and have not used other than the acknowledged resources and aids.

Hamburg 21.03.2018   _____

                                                                         Pasquale CERVERO

ACKNOWLEDGEMENT

I would like to express my sincere gratitude to Prof. Stefan Linder for the continuous support during my PhD study and related research. A person with strong helpful attitude and always open to discussion.

Genuine thanks go to Elisabeth Genot for believing in me in the first place and recommending me to Prof. Linder, without her I wouldn't be here defending my thesis.

Many thanks to all the T3Net Marie Curie supervisors for sharing their great knowledge and fellows for all the moments we experienced beyond research.

A big thank you to Andrea and all the lab mates who always supported me and made me feel like at home; I'm honoured to have met you.

All my love goes to my wife Rossella, who patiently and heavily supported (and still supports) me during all these years and my little big smile Luis Lorenzo, you both are the joyful thoughts of my life.

Last but not least I would like to thank very much my father Luigi, my mom Cira and my sister Emilia for their continuous and unconditional support, motivation and love throughout my life, and my friends for their precious help and invaluable friendship.